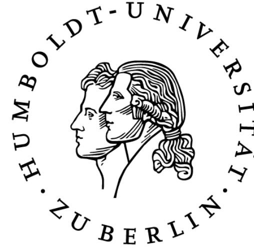

Growth and characterization of phosphorus-doped silicon for photovoltaic application directionally solidified under the influence of different process conditions

– Dissertation –

zur Erlangung des akademischen Grades
doctor rerum naturalium (Dr. rer. nat.)
im Fach: Physik, Spezialisierung: Experimentalphysik

eingereicht an der
Mathematisch-Naturwissenschaftlichen Fakultät der
Humboldt-Universität zu Berlin

von

M.Sc. Iryna Buchovska

Präsidentin der Humboldt-Universität zu Berlin:
Prof. Dr.-Ing. Dr. Sabine Kunst

Dekan der Mathematisch-Naturwissenschaftlichen Fakultät:
Prof. Dr. Elmar Kulke

Gutachter/innen:
1. Prof. Dr. Thomas Schröder
2. Prof. Dr. Marisa Sabatino
3. Prof. Dr. Norbert Koch

Tag der mündlichen Prüfung: 8 November 2021

Abstract

Current demands of the energy market require a constant decrease in cost of solar power, including through improving the efficiency of solar cells. A promising way to increase the efficiency of solar cells is to use phosphorus-doped crystalline n-type Si substrates. However, the yield of n-type material in the desired resistivity range is much lower compared to that of similar grown p-type crystals due to a more inhomogeneous dopant distribution over the crystal length. This phenomenon is caused by the smaller segregation coefficient of phosphorus in the silicon melt, leading to a significant increase of phosphorus concentration during the solidification process. Since base resistivity affects final solar cell performance, the research described in this thesis is focused on homogenization of resistivity profiles along phosphorus-doped directionally solidified multicrystalline silicon (mc-Si) ingots for PV application.

Resistivity of bulk Si crystals is defined by dopant concentration. The incorporation of phosphorus, which is used as a donor dopant in crystalline silicon, is determined by various transport mechanisms in the silicon melt as well as at the solid-liquid and liquid-gas interfaces. Since phosphorus has higher vapour pressure than silicon, incorporation thereof into mc-Si ingot is not only defined by segregation but also strongly influenced by its evaporation from the silicon melt surface. The analytical study conducted within the framework of the thesis is focused on phosphorus transport in the silicon melt, at the crystal-melt interface, at the melt surface and in the gaseous phase above the melt, as well as the influence of various process parameters on these mechanisms.

The experimental study was conducted in directional solidification furnace of G1 size equipped with KRIST*MAG*® heater-magnet module, which can produce heat and magnetic fields at the same time. Three process parameters were identified to have the most dominant influence on phosphorus distribution in multicrystalline ingots: melt mixing, furnace ambient gas pressure and gas flow above the melt.

Since travelling magnetic field (TMF) is known to be an effective method to control the flow of semiconductor melts, particular attention was given to its action mechanism. It was shown that enhanced melt mixing induced by TMF intensifies evaporation of phosphorus from the free melt surface. This effect takes place during melt homogenization phase as well as during solidification process and increases with the strength of the magnetic field. It was found that variations in strength of

TMF could be used to control the phosphorus distribution along the ingot's length. Weak TMF provokes more uniform dopant distribution and results in decreased ingot resistivity at the initial stages of crystallization, while strong TMF has more prominent effect on phosphorus evaporation that leads to the increase of resistivity towards the ingot's end. Moreover, it was experimentally confirmed that the application of a traveling magnetic field with two overlapping frequencies flattens the solid-liquid interface, which is beneficial for the stable growth of elongated crystal grains.

The results of experiments demonstrated that chamber gas pressure has the most significant influence on phosphorus transport out of all process parameters considered in the study. Reduction of ambient gas pressure leads to significantly intensified phosphorus evaporation from the free melt surface and increases the resistivity of the solidified ingot, especially towards its end. Low overall pressure increases detachment of the crucible coating, which increases the probability of adhesion of the ingot to the crucible and ingot cracking, and at the same time leads to higher interstitial oxygen concentration in the ingot.

Theoretical calculations showed that variation in purging gas flow has no noticeable influence on phosphorus transport during typical DS process, which was experimentally confirmed.

The findings obtained during the study were used for the adjustment of the typical G1 growth recipe. Weak and strong traveling magnetic fields with two overlapping frequencies and reduced total gas pressures as a function of the crystallization process were implemented. Conventional G1 mc-Si ingots grown using this recipe show more uniform resistivity distribution than those grown using a typical one. Resistivity variation was reduced to 55% and met the target range of 3.0 – 1.0 Ω·cm set by market specification.

The developed recipe was successfully replicated for directional solidification seeded growth. The G1-size high-performance multicrystalline (HPM) ingot grown according to the developed recipe also showed a more uniform resistivity distribution along the ingot's length.

Kurzfassung

Die aktuellen Anforderungen des Energiemarktes bedürfen einer ständigen Senkung der Kosten für Solarstrom. Ein vielversprechender Weg zur Effizienzsteigerung von Solarzellen ist die Verwendung von phosphordotiertem, kristallinem n-Typ Si-Substratmaterial. Allerdings ist die Ausbeute an n-Typ-Material im gewünschten Widerstandsbereich viel geringer als bei ähnlich gezüchteten p-Typ-Kristallen, verursacht durch eine viel inhomogenere Dotierstoffverteilung über die Kristalllänge. Das ist auf den kleinen Segregationskoeffizienten von Phosphor in der Siliziumschmelze zurückzuführen, der eine deutlich zunehmende Phosphorkonzentration während des Erstarrungsprozesses verursacht. Da der Basiswiderstand einen Einfluss auf die endgültige Solarzellenleistung hat, werden in dieser Arbeit Möglichkeiten zur Homogenisierung von Widerstandsprofilen entlang von phosphordotierten, gerichtet erstarrten, multikristallinen Silizium (mc-Si) Blöcken für PV-Anwendungen untersucht.

Der spezifische Widerstand von Si-Volumenkristallen wird durch die Dotierstoffkonzentration definiert. Der Einbau des als Donator in kristallinem Silizium wirkenden Phosphors wird durch verschiedene Transportmechanismen in der Siliziumschmelze sowie an der fest-flüssigen und flüssig-gasförmigen Grenzfläche bestimmt. Da Phosphor einen höheren Dampfdruck als Silizium aufweist, wird sein Einbau in den mc-Si-Block nicht nur durch Segregation bestimmt, sondern ist auch stark von der Verdampfung beeinflusst. Die im Rahmen der Dissertation durchgeführte analytische Untersuchung konzentriert sich auf den Phosphortransport in der Siliziumschmelze, an der Grenzfläche zwischen Kristall und Schmelze, an der Schmelzenoberfläche und in der Gasphase oberhalb der Schmelze sowie auf den Einfluss verschiedener Prozessparameter auf diese Mechanismen.

Die experimentelle Studie wurde in einem Züchtungsofen für die gerichtete Erstarrung der Blockgröße G1 durchgeführt. Dieser ist mit einem KRIST*MAG*®-Heizmagnetmodul ausgestattet, das in der Lage ist, Wärme und Magnetfelder gleichzeitig zu erzeugen. Es wurden drei Prozessparameter identifiziert, die den stärksten Einfluss auf die Phosphorverteilung in multikristallinen Blöcken haben: die Durchmischung der Schmelze, der Gesamtgasdruck in der Anlage und der Gasfluss über der Schmelze.

Da ein wanderndes Magnetfeld (TMF) bekanntermaßen eine effektive Methode zur Steuerung der Strömung von Halbleiterschmelzen ist, wurde dessen Wirkmechanismen besondere Aufmerksamkeit gewidmet. Es konnte gezeigt werden, dass eine durch ein TMF induzierte starke Durchmischung der Schmelze die Verdampfung von Phosphor von der freien Schmelzoberfläche verstärkt. Dieser Effekt tritt sowohl während der Homogenisierungsphase der Schmelze, als auch während des Erstarrungsprozesses auf und nimmt mit der Magnetfeldstärke zu. Variationen in der Stärke der TMF sind sinnvoll, um die Phosphorverteilung entlang der Barrenhöhe zu beeinflussen. Ein schwaches TMF bewirkt eine gleichmäßigere Dotierstoffverteilung und führt zu einem verringerten spezifischen Widerstand des Blocks in den Anfangsstadien der Kristallisation, während ein starkes TMF einen signifikanten Effekt auf die Phosphorverdampfung hat und zu einem Anstieg des spezifischen Widerstandes zum Ende des Blocks hin führt. Darüber hinaus wurde experimentell bestätigt, dass die Anwendung des Wandermagnetfeldes mit zwei sich überlagernden Frequenzen die fest-flüssige Grenzfläche ebnet, was für das stabile Wachstum von länglichen Kristallkörnern vorteilhaft ist.

Die Ergebnisse der Experimente zeigten, dass der Gasdruck in der Anlage von allen betrachteten Prozessparametern den stärksten Einfluss auf den Phosphortransport hat. Die Verringerung des Gasdrucks führt zu einer deutlich verstärkten Phosphorverdampfung von der freien Schmelzenoberfläche und erhöht damit den spezifischen Widerstand des erstarrten Blocks, vor allem gegen dessen Ende hin. Ein niedriger Gesamtdruck verstärkt eine Ablösung der Tiegelbeschichtung, was die Wahrscheinlichkeit des Anhaftens des Blocks an den Tiegel sowie die Rissbildung im Block erhöht, und führt gleichzeitig zu einer deutlichen Erhöhung der interstitiellen Sauerstoffkonzentration im Block.

Theoretische Berechnungen zeigten, dass die Variation des Spülgasflusses keinen merklichen Einfluss auf den Phosphortransport während des typischen DS-Prozesses hat. Das wurde experimentell bestätigt.

Die während der Studie gewonnenen Erkenntnisse wurden für die Optimierung der typischen G1-Wachstumsrezeptur verwendet. Darin implementiert sind schwache und starke Wandermagnetfeldern mit zwei sich überlagernden Frequenzen und verringerte Gesamtgasdrücke in Abhängigkeit des Kristallisationsprozesses. Die mit diesem Rezept gezüchteten G1 mc-Si Blöcke zeigen eine gleichmäßigere Widerstandsverteilung als solche, die mit einem typischen Rezept gezüchtet wurden. Die Widerstandsvariation wurde auf 55 % verringert und erfüllte den von der Marktspezifikation vorgegebenen Zielbereich von 3,0 - 1,0 Ω·cm.

Die entwickelte Rezeptur wurde erfolgreich für die gerichtete Erstarrung mit Keimvorgabe übertragen. Die nach der entwickelten Rezeptur gezüchteten high-performance multikristallinen (HPM) Blöcke der Größe G1 weisen ebenfalls eine gleichmäßigere Widerstandsverteilung entlang der Blockhöhe auf.

Table of Contents

Abstract I

Kurzfassung III

Table of Contents V

Abbreviations and Symbols IX

List of abbreviations IX
List of constants X
List of symbols X

1. Introduction **1**

1.1. Motivation and objectives 1
1.2. Outline of the thesis 4

2. Fundamental principles of directional solidification **7**

2.1. Directional solidification method 7
2.2. Crucible and coating 11
2.3. Melt flow and convection 14
2.4. Growth front and growth rate 17
2.5. Gas flow and melt surface 19
2.6. Segregation of dopants and impurities 21
2.7. Grain boundaries and dislocations 27
2.8. Types of material 29

3. Phosphorus in crystalline silicon ingot and melt **33**

3.1. Doping of silicon 33
3.2. Chemical and electrical properties of phosphorus in silicon 35
3.3. Homogenous resistivity distribution 38
3.4. Phosphorus transfer 40
3.4.1. Modification of Gulliver-Scheil equation 40
3.4.2. Mass transfer coefficient 42
3.4.3. Transfer in the bulk melt 43
3.4.4. Transfer in the boundary layer at the melt surface 43

3.4.5. Transfer at the melt surface ... 44
3.4.6. Transfer in the gas ambient ... 46

4. Melt flow control by magnetic fields ... 49
4.1. Magnetic fields in crystal growth ... 49
4.2. Travelling magnetic fields ... 52
4.3. Fundamentals of travelling magnetic fields ... 55

5. Equipment and methodology ... 59
5.1. KRIST*MAG*® technology ... 59
5.2. DS furnace with KRIST*MAG*® heater-magnet module ... 61
5.3. Supporting numerical modelling ... 63
5.4. Characterization methods ... 64
5.4.1. Four-point probe (FPP) method ... 64
5.4.2. Microwave-detected photoconductivity (MDP) ... 66
5.4.3. Fourier-transform infrared spectrometry (FTIR) ... 67
5.4.4. Lateral photovoltage scanning (LPS) ... 67
5.4.5. Photoluminescence (PL) imaging ... 68
5.4.6. Near-infrared transmission (NIR) imaging ... 69
5.4.7. Glow discharge mass spectrometry (GDMS) ... 69

6. Growth experiments ... 71
6.1. Growth setups ... 71
6.1.1. G1 setup ... 71
6.1.2. 4×G0 setup ... 73
6.2. Process preparation ... 75
6.2.1. Crucible and coating ... 75
6.2.2. Charge composition ... 76
6.3. Experimental conditions ... 78
6.3.1. Growth process ... 78
6.3.2. Two-component TMF ... 82
6.3.3. TMF marking of the solid-liquid interface ... 83
6.4. Sample preparation ... 85

7. Influence of TMF on phosphorus evaporation in 4×G0 setup ... 87
7.1. Verification of setup symmetry ... 88
7.2. Constant TMF stirring ... 91
7.3. Variable TMF stirring ... 100
7.4. Conclusion ... 102

8. Tailoring of resistivity profiles for G1 mc-Si ingots ... 105
8.1. TMF at early stages of crystallisation ... 109
8.2. Intensification of TMF at later stages of crystallisation ... 116
8.3. Gas flow ... 122

8.4. Chamber pressure 124
8.5. Material properties 134
8.6. Conclusion 141

9. Process replication for G1 HPM ingots 143

10. Summary and Outlook 149
10.1. Summary 149
10.2. Outlook 152

Appendix 153

Bibliography 159

List of Figures 181

List of Tables 187

Publications and Contributions 189

Acknowledgments 193

Selbständigkeitserklärung 195

Abbreviations and Symbols

List of abbreviations

AC	alternating current
AMF	alternating magnetic field
BPS	Burton, Prim and Schlichter theory
BSF	back surface field
c-Si	crystalline silicon
CCz	continuous Czochralski
CMF	cusp-shaped magnetic field
CSL	coincident site lattice
Cz	Czochralski
DC	direct current
DS	directional solidification
DSL	diluted Sirtl light
FPP	four-point probe
FSF	front surface field
FTIR	Fourier-transform infrared spectroscopy
FZ	float zone
GDMS	glow discharge mass spectrometry
HEM	heat-exchanger
HIT	heterojunction with intrinsic thin layer
HMF	horizontal magnetic field
HPM-Si	high-performance multicrystalline silicon
IBC	ion implanted cell
IR	infrared
LPS	lateral photovoltage scanning
mc-Si	multicrystalline silicon
MDP	microwave-detected photoconductivity
µ-PCD	microwave-detected photoconductive decay

NIR	near-infrared
OLS	ordinary least square
ppm	particles per million
ppmw	particles per million by weight
PL	photoluminescence
PV	photovoltaic
PVA	polyvinyl alcohol
RMF	rotating magnetic field
SoG	solar grade
TMF	travelling magnetic field
VGF	vertical gradient freeze
VMF	vertical magnetic field

List of constants

$e = 1.602 \cdot 10^{-19}$	elementary charge	[C]
$k_B = 1.38 \cdot 10^{-23}$	Boltzmann constant	[J/K]
$\mu_0 = 4\pi \cdot 10^{-7}$	magnetic constant	[H/m]
$P_0 = 101325$	standard atmospheric pressure	[Pa]
$R = 8.314$	ideal gas constant	[J/mol·K]

List of symbols

A	melt surface area	[m^2]
α	evaporation coefficient	[−]
$\vec{B}$	magnetic induction	[T]
C	species concentration	[$atoms/m^3$]
$C_{s,l}$	species concentration in solid, liquid	[$atoms/m^3$]
D	diffusion coefficient	[m^2/s]
d	distance between induction coils	[m]
d_p	distance between probes	[m]
$\overline{\Delta}$	convecto-diffusive parameter	[−]
$\vec{E}$	electric field intensity	[V/m]
σ	electrical conductivity	[$\Omega^{-1}m^{-1}$]
η	dynamic viscosity	[Pa·s]
$\vec{F}_L$	Lorentz force density	[N/m^3]
f	frequency	[Hz]
ϕ	phase shift	[grad]
G^0	Gibbs free energy of evaporation	[J/mol]
g_s	fraction of solidified material	[−]

γ	activity coefficient of dopant in the melt	[–]
γ^0	Henrian activity coefficient in the melt	[–]
ΔH_L	latent heat	[J/kg]
I	electrical current	[A]
I_{eff}	total effective AC of TMF	[A]
J	flux of species	[$s^{-1}m^{-2}$]
$\vec{J}$	current density	[A/m^2]
K	total mass transfer coefficient	[m/s]
K_e	mass transfer coefficient of evaporation	[m/s]
K_g	mass transfer coefficient in gas phase	[m/s]
K_m	mass transfer coefficient in bulk melt	[m/s]
K_s	mass transfer coefficient at melt surface	[m/s]
k	wave number	[m^{-1}]
k_0	equilibrium segregation coefficient	[–]
k_{eff}	effective segregation coefficient	[–]
λ	wavelength	[m]
$\lambda_{s,l}$	thermal conductivity in solid, liquid	[W/m·K]
M	molecular weight	[kg/mol]
m^*	effective mass of charge carriers	[kg]
μ	mobility of charge carriers	[m^2/V·s]
μ_r	relative magnetic permeability	[–]
N	number of windings in induction coil	[–]
N_A	acceptor concentration	[atoms/m^3]
N_D	donor concentration	[atoms/m^3]
Nu	Nusselt number	[–]
n	electron carrier concentration	[atoms/m^3]
n_i	intrinsic carrier concentration	[atoms/m^3]
ν	kinematic viscosity	[m^2/s]
ω	angular frequency	[rad/s]
P	pressure	[Pa]
p	hole carrier concentration	[atoms/m^3]
p^0	standard vapour pressure	[Pa]
p^s	surface partial pressure	[Pa]
$p^{s,e}$	equilibrium surface partial pressure	[Pa]
Pe	Peclet number	[–]
q	heat flux	[W]
R	average radius of induction coil	[m]
r	atomic radius	[m]
ρ	resistivity	[Ω·m]
$\rho_{s,l}$	density of solid, liquid	[kg/m^3]
δ	thickness of boundary layer	[m]

δ_D	thickness of diffusion boundary layer	[m]
δ_{BPS}	thickness of BPS boundary layer	[m]
δ_{TMF}	penetration depth of TMF-induced Lorentz force	[m]
T	temperature	[K], [°C]
$\nabla T_{s,l}$	thermal gradient in solid, liquid	[K], [°C]
τ	lifetime of charge carriers	[s]
V	volume	[m^3]
$\vec{v}_{dr}$	drift velocity of carriers	[m/s]
U	voltage	[V]
$\vec{u}_{gas}$	gas velocity above the melt	[m/s]
$\vec{u}_{melt}$	flow velocity of the melt	[m/s]
$\vec{u}_{surf}$	surface velocity of the melt	[m/s]
$\vec{v}_{gr}$	growth rate	[m/s]
X	species mass content	[-]
x, y, z, r	coordinates	[m]
Z	Lorentz force coefficient	[N/A^2]

CHAPTER 1

Introduction

1.1. Motivation and objectives

In recent years, the diminishing stock of fossil fuels and their harmful environmental impact have urged humanity to shift the energy supply towards renewable sources, which are more sustainable and environmentally friendly. In this regard, the principle of the direct conversion of light into electrical energy captures a particular attention. Over last decades, the photovoltaic (PV) industry has become a strong player in the renewable energy segment and exhibited an impressive annual growth. According to European Photovoltaic Industry Association, the added capacity of PV installations in 2019 was not only higher than that for all fossil fuel and nuclear power generation combined, it also saw nearly twice as much power installed as wind, and more than all renewables together [EPI20]. The total worldwide capacity of installed PV systems increases every single year (Figure 1.1.) and in 2019 has summed up in 634 GW, which makes up 2.6% of the global electricity production. Different forecasts scenarios predict that the amount of globally installed PV systems will reach the level of 1.18 – 1.68 TW by 2024.

The most dominant material used as a substrate in PV solar cells is crystalline silicon (c-Si). According to the annual market reports, more than 95% of PV market is constantly taken by c-Si based technologies [Phi20]. Crystalline silicon conquered such a high place on the market due to its abundance in the earth's crust, high level of safeness, easiness in handling, exceptional absorption characteristics,

efficient purification by classical crystallization processes, and a huge number of mature technologies for solar cell fabrication.

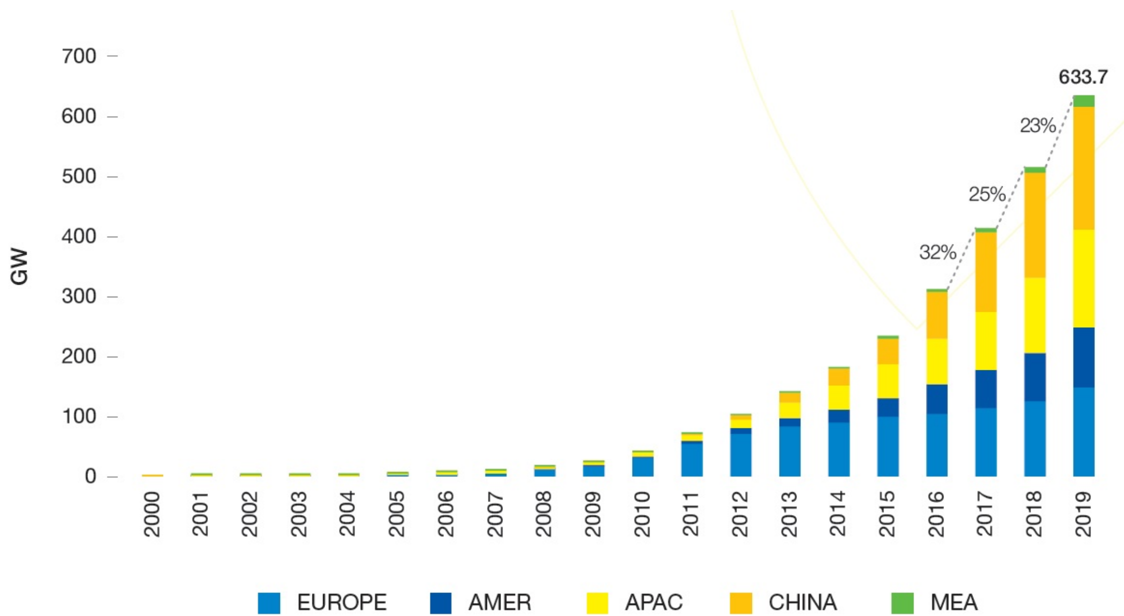

Figure 1.1.: Evolution of the worldwide installed PV capacity [EPI20].

Although monocrystalline silicon produced by Czochralski (Cz) and float zone (FZ) processes shows superior structural properties and purity, their growing process is rather complex and costly. Since solar cells can tolerate higher amount of impurities and higher defect levels, multicrystalline silicon (mc-Si) arouse a great interest in PV industry. Mc-Si material is characterized by the presence of grain boundaries in the bulk that separate grains with different crystallographic orientation. The most common crystallization process used for production of multicrystalline silicon is directional solidification (DS). The quality of mc-Si is somehow lower than that for monocrystalline silicon that results in reduction of solar cell efficiency. However, this material has an advantage of relatively easy and cheap production process, which makes mc-Si the leading material on PV market with a dominant share of total world production for the decades.

In order to remain competitive on the energy market, PV manufacturers must follow the cost reduction strategy in terms of price per Wp, which means to decrease the production cost of materials or/and to improve the performance of solar cells [Pow12]. Therefore, the efficiency of solar cells has continuously increased over the last years. Figure 1.2. gives the chart of record efficiencies for different types of PV solar cells measured in laboratory conditions. Nowadays, monocrystalline-silicon-based cells without concentrator reach the record value of about 26%, while mc-Si-based cells show the level of 23%.

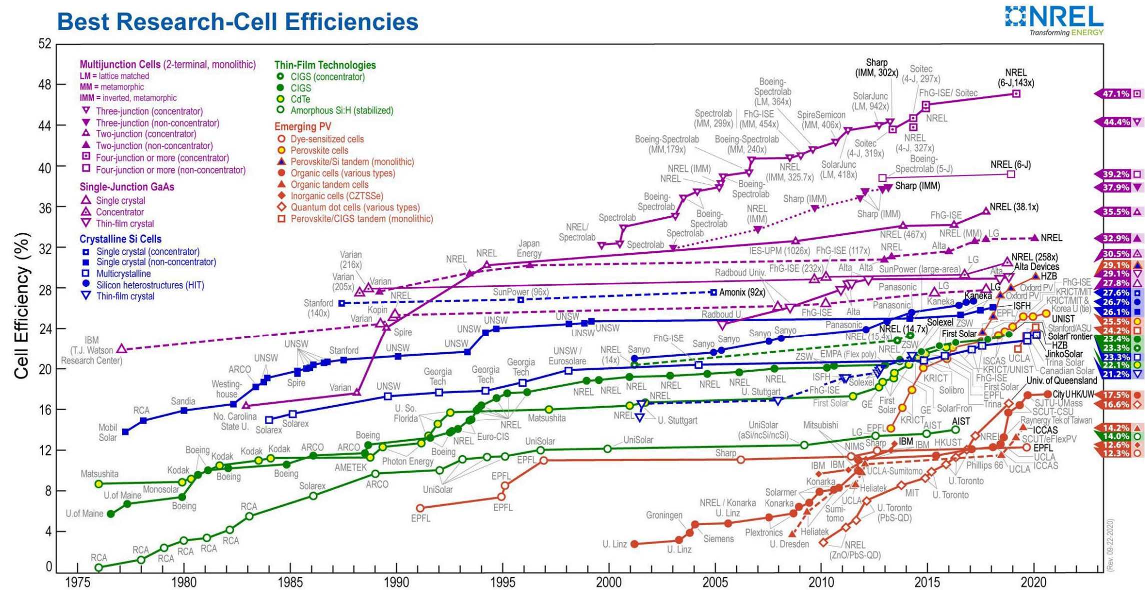

Figure 1.2.: Solar cells efficiency chart [NRE20].

The enlargement of solar cell efficiency is realized through improvement of c-Si material quality and development of new solar cell designs. Since many years, solar cells based on p-type boron-doped c-Si wafers have been a PV standard. This is due to the fact that emitter formation, which for n-type wafers is realized through boron diffusion process, requires higher temperatures compared to phosphorus diffusion for p-type cells. This process was very complicated to perform on industrial scale at the dawn of PV industry. Even now, with significant improvements in technologies of solar cell fabrication, the cost of solar modules based on n-type c-Si substrates is somewhat higher than those based on p-type ones. Nevertheless, n-type c-Si material has a number of advantages over p-type c-Si. These are the absence of light-induced degradation related to boron-oxygen defects [Glu01], greater tolerance to key metal impurities [Mac04] and higher charge carrier lifetime [Mic13]. The above-mentioned advantages allow reaching higher solar cell efficiencies for solar cells based on n-type Si wafers, hence to achieve lower price per Wp despite the higher cost of solar modules. The gain in monocrystalline solar cell efficiency due to switching from p-type to n-type is equal to 1-3% absolute [ITR20].

During the last decade, n-type cell concepts for industrial use have been successfully reported. They include different types of front surface field (FSF) rear emitter cells, back surface field (BSF) front emitter cells, heterojunction with intrinsic thin layer (HIT) cells and ion implanted (IBC) cells [Reh13, Ais15]. Nowadays, these concepts are dedicated to monocrystalline silicon and their market share in c-Si based technologies is only about 5%. However, the shift of PV market to n-type based technologies accelerates and is expected to reach at least 30% by 2030 [ITR20]. Until recently, mc-Si wafers were not involved in this progress, since

this type of material was considered to have too many structural defects and its potential for significant gain in efficiency from n-type cell concepts was doubtful, even though n-type quasimono wafers produced by DS were successfully utilized as n-type monocrystalline material, since their properties in many ways are similar [Jay14]. However, the development of high-performance multicrystalline material (HPM), which exhibits low defect density, arouse the interest of its utilization in n-type-based cell concepts. During the last years a few cell designs for n-type mc-Si were introduced and claimed to reach record efficiencies for multicrystalline based devices, e.g. 21.9% efficiency was reported by Fraunhofer ISE in 2017 [Ben17] and 23.81% efficiency reported by Canadian Solar in 2020 [Pic20]. This indicates that n-type mc-Si is a promising substrate material for high-efficiency solar cells.

Although n-type c-Si material has a superior quality, there are also some disadvantages compared to p-type material doped with boron. Owing to segregation of phosphorus in silicon, c-Si ingots have a non-uniform axial dopant profile, thus significant discrepancy of resistivity along the ingot's length. It is well known that base resistivity has an influence on final solar cell performance [Ric17b, Reh13, Sol15]. Hence, high wafer-to-wafer resistivity variation might be a concern for regular industrial solar cell manufacturing, since it decreases production yield and increases costs. Many industrial manufacturers adjust their solar cell process for resistivity variation as narrow as ±50% from the target value, nevertheless aiming at ±5% [Top14, Mih08]. A pronounced effect of phosphorus segregation during crystallization process brings additional difficulties for cell manufacturing, since resistivity of cell substrates vary by a factor of 10, which is at least 4 times higher variation compared to boron doped p-type material [Sol15]. Therefore, there is a high need for specific solutions that will help to obtain relatively homogeneous axial resistivity profile along the height of phosphorus-doped silicon ingots.

The problem of inhomogeneous resistivity profile for monocrystalline Cz-material is already solved by continuous Czochralski (CCz) technique [Ans93, Fic01]. However, a similar solution for directional solidification method has not been found yet. Since the properties of crystalline material grown by DS are dependent on growth process conditions, it is expected that dopant distribution can also be influenced in this way. The aim of this work is to study the effect of various DS process parameters on resistivity distribution in mc-Si ingots and to find a suitable solution for its homogenization. The study comprises a fundamental research as well as an experimental investigation.

1.2. Outline of the thesis

In Chapter 2 the fundamentals of directional solidification are reviewed. In the first part of the chapter, the main principles of the growth technique are given in

order to introduce the method of multicrystalline silicon manufacturing. The following parts describe various processes and phenomena, taking place during directional solidification of silicon, including mass and heat transport, kinetics and fluid dynamics. Finally, the influence of different process parameters on material quality and characteristics is discussed.

Chapter 3 is dedicated to the properties of n-type crystalline silicon doped with phosphorous. Particular attention is given to the behaviour of phosphorus in silicon melt and its transport during directional solidification process. The detailed analysis of transport mechanisms provides insight into the most promising direction of the research described in the following chapters.

One of the tools successfully used in the experimental work described in this thesis is travelling magnetic field (TMF). Chapter 4 gives an overview of its application for bulk growth of semiconductor materials and provides the perspectives of TMF utilization for influencing the process conditions of directional solidification of silicon, namely melt flow, dopant transport and shape of solid-liquid interface.

The equipment used for crystallization of mc-Si material studied in this work is described in Chapter 5. Main emphasis lies on KRIST*MAG*® technology, which provides many opportunities for crystal growth within a broad range of process conditions [Fra07]. In addition, the methods of numerical simulation supporting experimental study are also briefly discussed. At the same time, a number of techniques applied for characterisation of the grown ingots is introduced. The utilised methods provide a comprehensive analysis of electro-physical, chemical and structural properties of investigated material.

Chapter 6 describes the conditions and peculiarities of the growth experiments conducted within this study. Two sequential stages for comprehensive investigation of n-type mc-Si material are introduced, which consist of preliminary evaluation of investigated parameters in a newly developed 4×G0 setup and detailed parameter study within subsequent scale-up to G1 size. Besides the characteristics of both setups, the temperature profiles of experimental growth processes and utilization of two-component TMF are outlined. Furthermore, the technique to mark the solid-liquid interface with TMF is presented.

In Chapter 7, the principal possibility to influence resistivity of phosphorus-doped multicrystalline ingots by application of travelling magnetic field is investigated. The research is performed on G0 scale and comprises enhanced melt mixing with TMF of constant current amplitude as well as TMF of variable current profile. A parameter study addresses the influence of TMF strength on phosphorus evaporation and dopant segregation. The experimental results are complimented with numerical analysis. The phenomena observed in this research are discussed and basic relations between process parameters and the measured data are derived.

The research described in Chapter 8 is focused on influence of various process parameters on resistivity distribution in conventional phosphorus-doped mc-Si of G1 size. At the beginning, a theoretical evaluation of different transport mechanisms for the G1 DS system is performed and the most suitable candidates from process parameters are chosen for the experimental study. The influence of every chosen process parameter on resistivity distribution as well as on other material properties are experimentally investigated and supported by numerical simulation. In addition, the obtained results are complimented with numerical analysis. Finally, all findings are summarised in the adjusted growth recipe that provides an improved resistivity profile in G1 phosphorus-doped ingots.

In Chapter 9, the optimized growth recipe developed in Chapter 8 is replicated for seeded DS growth of G1 HPM-Si ingots. Similarities and differences in process application and material characteristics between conventional mc-Si and HPM material are revealed and discussed.

In Chapter 10, all results are being summarized and evaluated. In the end, the outlook on future strategies on adjustment of the developed growth process for phosphorus-doped mc-Si ingots and its subsequent replication to a larger scale is given.

CHAPTER 2

Fundamental principles of directional solidification

2.1. Directional solidification method

Directional solidification is an established method widely used in welding and metallurgy, which owning to its high repeatability and scalability is one of the most popular techniques for production of metal and semiconductor ingots [Cap10]. In this method, the melt is placed in a resistant container (crucible) and subsequently solidified from bottom to top. Solid silicon feedstock material might be either molten in a separate container and then poured into the growth crucible for solidification, or molten and solidified in the same growth crucible. In the former case the technique is called mould casting [Aut78], in the latter case – regular DS.

The principles of directional solidification were first described by Tammann in 1914 [Tam14] and further complemented by Stöber in 1925 [Sto25]. The method consist of controlled vertical shifting of the temperature profile with constant gradient from bottom to top within the crucible filled with melt [Sch00]. In such a way the solidification of the melt is realized. A principal sketch of directional solidification process is given in Figure 2.1. The temperature shifting can be fulfilled by one of three approaches. The first one is Bridgman technique named by its inventor [Bri25, Sto36]. It consists of mechanical movement of the crucible with melt in relation to the temperature field of a fixed furnace. The second approach is heat-exchanger method (HEM), which implies extracting heat through the bottom of the crucible [Vie74]. And the third one is vertical gradient freeze method (VGF)

firstly described by Ramsperger and Malvin [Ram27]. This solidification process is achieved by moving a vertical temperature gradient in relation to the melt either by moving the furnace or, preferably, by moving the temperature gradient inside the furnace. Normally, in case of VGF growth, the crucible as well as the heaters do not move and their positions are fixed. In contrast, the power of the heaters is changed in such a way that a vertical temperature gradient moves. The advantage of HEM and VGF over the Bridgman method is that a crucible with melt is located in a fixed position during solidification; hence the crystal growth is not disturbed by the movement of the system.

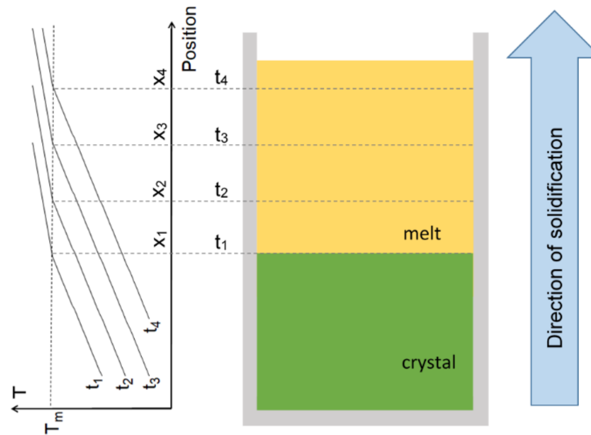

Figure 2.1.: Sketch of the temperature profiles (left) for different time steps ($t_1 < t_2 < t_3 < t_4$) with positions (x_1, x_2, x_3, and x_4) of the solid-liquid interface (at temperature of melting point $T < T_m$) during directional solidification of silicon melt placed in a crucible (right).

A traditional DS process does not imply seeding from monocrystalline crystal; hence, material fabricated by this method is characterized by multicrystalline structure with crystallites (grains) of size the order of mm to cm and columnar development along the direction of solidification. The very first casting of multicrystalline silicon in graphite crucible was reported already in 1913 by Allen [All13]. Early multicrystalline casting of silicon for PV application was done in graphite moulds by Fischer and Pschunder in 1976 [Fis76]. The development of DS process and corresponding equipment started in mid-1970s and evolved into a mature technology by early 2000s [Nar10]. Nowadays in PV industry, silicon is molten and grown in one and the same crucible which has a square shape in order to simplify the post-treatment and reduce material losses while cutting silicon ingots into standard square wafers required for solar cells. Crystallisation process takes place in a DS furnace, which utilizes either VGM, or HEM, or Bridgman technique, or combination of them. There is a variety of DS furnaces for PV application suitable both for industrial application and research purposes on a lab-scale, which are available from different suppliers [Osb10, Chu11, Lan15].

Dimensions of mc-Si ingots are selected in such a way to optimally fit the industrial standard of solar wafers, which is 156×156 mm^2. The horizontal cross-section of an ingot is square-shaped and its sides contain an integer number of standard wafer sizes that is represented in so-called generation number. E.g., the ingot, which after mechanical post-treatment has a cross-section of 156×156 mm^2, is suitable only for one standard solar wafer and is called Gen1 (generation 1). The ingot with twice-larger square sides of 312×312 mm^2 after post-treatment is called Gen2 (generation 2) and contains four standard wafer sizes. It has to be kept in mind that the size of as-grown ingots are something larger, since the quality of the material at the ingot rim is not sufficient for solar cell production due to contamination from crucible and has to be removed. Hence, the typical dimensions of cross-section for as-grown G1 and G2 ingots are 220×220 mm^2 and 380×380 mm^2, respectively. The height of ingots is optimised for each generation to comply with sufficient material quality (not too tall) and attractive production cost (not too short). Nowadays, PV industry successfully works with mc-Si ingots as large as Gen6 and Gen7 with weight up to 1200 kg, and showing productivity up to 6.5 kg/h [Lan16, ITR20]. Moreover, ingots of G8 size and 1650 kg weight have also been industrially produced and demonstrated [Che12]. However, Gen1 ingots with as-grown size of 22×22×13 cm^3 and weight of 15 kg are still widely used for research purpose.

Despite the different implementations of DS method and variety of materials used in the process, the main steps and phases of the growth cycle are common for all the variations of the method. Prior a growing process itself, silicon feedstock together with necessary dopants is placed in a pure heat-resistant crucible. In industrial production, solar-grade (SoG) polysilicon is normally used as a feedstock. The crucibles typical for utilisation in solar industry are made of quartz or fused silica. Since liquid silicon is known to react with quartz material of the crucible, which leads to dissolution of impurities from a crucible into a melt and sticking between a silicon ingot and a crucible, special coatings have been developed to reduce or better avoid these effect (see Chapter 2.2).

There are different designs of industrial and laboratory DS equipment, but they all have very similar approach to crystallization and rather comparable design. The example of a lab-scale DS furnace is presented in Figure 2.2.

A crucible with feedstock material and necessary dopants is placed inside the furnace. Both melting and crystallization of silicon take place at elevated temperatures at which the crucible becomes soft. Therefore, additional mechanical support (so-called susceptor) is required to be placed tightly around a crucible both to prevent its deformation and to fit into the rectangular heater configuration. A special cover is placed on the top of this susceptor-crucible setup in order to reduce a direct contact of furnace atmosphere with the free melt surface and reduce contamination of the melt with impurities. The susceptor-crucible-cover setup is

surrounded by heaters on the sides (sometimes also at the top and at the bottom), and connected to a heat-exchanger at the bottom. The entire configuration is called a hot zone. Most parts of a furnace are made of carbon materials (isostatically pressed graphite, graphite felts, carbon composites, carbon fibres etc.). The heaters are surrounded by heat insulation, which separates the hot zone from furnace surroundings, reduces undesired heat losses and limits radial thermal gradients in the system. The whole system is enclosed in a water-cooled chamber and filled with an inert atmosphere (usually argon) with controlled pressure and inlet/outlet gas flow.

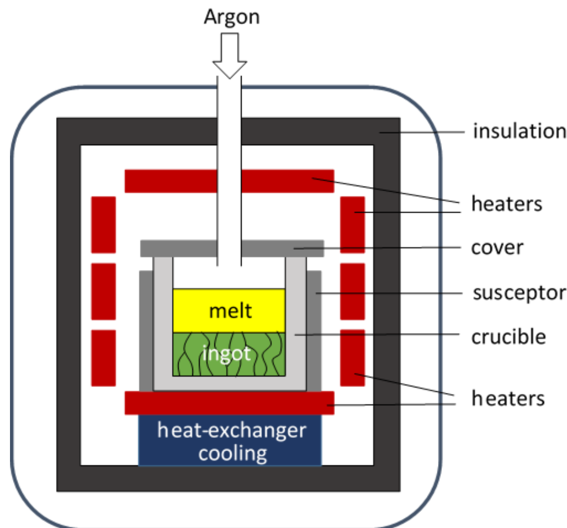

Figure 2.2.: Sketch of a lab-scale directional solidification furnace.

The design of heaters and heat-exchanger must ensure accurate control of temperature gradients inside a hot zone during the process. Industrial furnaces mostly use resistance heaters supplied with AC current, where the heating is performed by radiation transfer from induction coils. However, induction heating with water-cooled coils are also used is some furnace designs. The quantity of heaters may likewise vary from one up to several. A larger quantity allows more accurate and sophisticated control of heat and temperature fields during the growing process. Some furnaces are also equipped with additional installations like cooling systems under a heat-exchanger, movable insulations, shifting partition blocks around the heaters, crucible-to-heater travelling mechanism etc. [Lan15]. All these installations provide complementary control of temperature gradients and growth conditions.

At the beginning of the standard DS process all heaters run at high power to heat the silicon feedstock above the melting temperature of 1414°C (Table 10.1. in Appendix) and ensure its complete melting. At this stage, neither additional cooling nor particular temperature gradients are required. However, in case of specific process for HPM-Si or quasi-mono silicon (see Chapter 2.7) a certain part of silicon material on the bottom inside the crucible must be kept unmolten. In this instance, either bottom cooling or low heat input must be applied to preserve the required

material from melting. After the melting, is over the solidification phase takes place. For this purpose, the melt is imposed to a vertical temperature gradient in such a way to keep the liquid bottom colder than the top. When the temperature at the crucible bottom drops below the melting point of silicon, the conditions for the nucleation are reached and the first solidification layer is formed. The layer consists of numerous crystallites, which compete with each other while growing upwards, parallel to the direction of solidification, and results in multicrystalline structure. The whole system is gradually cooled down by creating a vertical temperature gradient along the direction of crystallization. At the same time, the top of the crucible must remain liquid at the temperature above the melting point, implying the thermal gradient inside the crucible must be appropriate to enable the ingot to grow from the bottom towards the top until totally crystallized. The growth rate of mc-Si ingots is typically 10-20 mm/h. During the whole crystallisation process, the vertical temperature gradients are created by manipulation of power supplied by heaters, heat extraction from the crucible bottom, smart isolation placement and crucible to heater positioning.

Due to the high temperature inside the furnace and aggressiveness of silicon melt, the direct and accurate temperature measurement of the melt and the crystal are greatly complicated. The experimental measurements are normally performed with pyrometers and thermocouples located in different parts of the furnace. However, the solution for precise measurements inside the melt so far is not available.

After the crystallisation, the silicon ingot is gradually cooled down to the room temperature and extracted from the furnace. The whole growth cycle depends on the size of the furnace and the ingot. E.g. for 15 kg (G1) ingot it takes about 50 h, where melting reaches up to 20 h and solidification about 10-20 h. In case of 450 kg (G5) ingot, the growth cycle is about 60-70 h, with similar duration of melting and duration of solidification is typically 30-40 h. The further steps of production chain include sawing of the ingot into 156×156 mm^2 square blocks and their subsequent slicing into wafers of typically 180 µm thickness.

The most critical and sophisticated aspects of DS process include the design of a hot zone for enabling proper growth conditions, the control of nucleation process at the crucible bottom, the proper temperature gradients, the applied cooling rate etc.

2.2. Crucible and coating

The prevalent material for crucibles to use in directional solidification process for manufacturing mc-Si is fused silica. This material has a number of advantages compared to alternative ones. First of all, the chemical properties of silica are

resembling to silicon, specifically high level of purity and low contamination, as composing its elements are silicon and oxygen. However, some impurities present in silica are harmful for mc-Si quality and its performance in solar cells [Kva09, Sch14]. These are mainly metals, which deteriorate the minority carrier lifetime of silicon and result in low conversion efficiency of solar cells [Col12, Col13]. Another reason for popularity of silica are mechanical and thermal qualities, which perfectly meet the requirements of DS process for silicon: good mechanical strength, high resistance to thermal shock, sound isolation and elevated softening point [Lan15]. In addition, this material has a moderate price.

However, a low cost of fused silica does not bring a significant benefit, as it cannot be used in DS process more than a single time. The main reason lies in the structural properties. Before the usage at room temperature, fresh fused silica material has a glassy structure. Yet during the growth cycle a crucible experiences major heating, greater than the melting point of silicon. In the phase of heating, when the temperature elevates beyond 1200 ˚C, silica undergoes the process of sintering and starts to devitrificate by changing its microstructure [Col34, Mar08, Cam17]. At first, the thermal stress can be easily released by banding and shrinking. However, during the melting phase, when the temperature reaches 1450 ˚C, devitrification greatly accelerates and the crucible structure transforms into β-cristobalite, which is rather rigid and not prone to plastic deformations. Finally, on the stage of cooling β-cristobalite turns into α-cristobalite when the system reaches the temperature of 275 ˚C [Mar08, Lan15, Cam17]. This phase transformation leads to crucible expansion, which can provoke its breakage. However, even if the crucible after the process is not broken, its second usage is not possible due to α-cristobalite microstructure of silica.

Despite all the advantages of fused silica, there are also some peculiarities that need additional technological solutions. One of these is sticking of silicon to a crucible during solidification. Not only does it make difficult to remove the ingot out of the crucible after the process. Since silica and silicon have different thermal expansion coefficients (e.g. at 400℃ thermal expansion coefficients for fused silica and silicon are 0.6×10^{-6} K^{-1} and 4.0×10^{-6} K^{-1} [Oka84], respectively), shrinking during the cooling phase can easily provoke ingot cracking when a crucible and ingot stuck to each other. In addition, direct contact of molten silicon with silica crucible leads to elevated diffusion and crucible dissolution, hence contamination of mc-Si with oxygen and high risk of crucible destruction and melt leakage. In order to avoid these effects, a special coating material is applied on the inner surface of the crucible prior loading it with feedstock. The most common material to be used as a coating for silica crucibles is silicon nitride Si_3N_4.

Silicon nitride powder is mixed into suspension with aqueous solution of organic adhesive and evenly spread over the crucible surface in a thin layer of hundreds microns. The uniformity of coating is extremely important as it assures its sufficient

firmness, durability and detachment properties. Therefore, the homogeneity of suspension, the size of the particles, the viscosity of solution as well as spraying technique must be thoroughly controlled. Moreover, the thickness of the coating layer has to be carefully chosen, since too thin coating might fail to protect a crucible from the contact with silicon, and too thick coating is prone to peeling off crucible walls. It must be also taken into account that the most common area in terms of sticking is the contact line between the melt meniscus and the crucible wall, therefore an extreme stability and strength of coating in this part of crucible is highly needed. The explanation lies in reaction between melt and crucible with subsequent formation of silicon monoxide, which acts as a barrier for silicon on its way towards the crucible [Dre10, Cam17]. Since silicon monoxide partially discharged to the gas at the meniscus contact line, the chance of sticking at this specific area is significantly higher. Moreover, the pressure in the furnace chamber during solidification process affects the intensity of gas evaporation, consequently the stability of coating.

A coated crucible is left to dry with subsequent firing in a clean muffle furnace in order to remove any remains of water, organic adhesive and to sinter the coating. The duration of firing also has an influence on coating performance. Brynjulfsen showed that wettability of silicon nitride coating by silicon is influenced by the coating thickness and oxygen concentration of the coating. The oxygen concentration increases with duration of firing, and the higher the oxygen level, the larger the wetting angle becomes [Bry10].

Element, ppm	B	P	Al	Fe	Ca	Ti	Ni	Mn	O	C
Crucible			<1100	<100	<100	<100	<1	<3		
Si_3N_4			<10	<5	<5	<3	<3	<3	<1.5	
SoG Si	<0.05	<0.1	<0.05	<0.05	-	-	<0.01	-	<5	<5

Table 2.1.: Concentration of impurities in crucible, Si_3N_4 and SoG silicon [Col12, Deg12, Lan15, Ols08].

Since contamination of mc-Si at elevated temperatures is fairly intensive, only high purity silicon nitride powder is used for DS process. An additional advantage of using silicon nitride coating is that its purity is vastly higher than the one for fused silica, consequently the coating protects mc-Si ingot against contamination from the crucible. For comparison typical values of impurities present in industrial silica crucibles, Si_3N_4 and SoG silicon are listed in Table 2.1.

Yet, the amount of impurities both in crucibles and in coating materials, especially metals, is one of the key factors that defines the quality of mc-Si ingot

[Gey05, Kva09, Kwa12]. Even high purity silica and silicon nitride is the source of significant contamination of silicon. Transition metals such as Fe, Cu, Ni and Co show high solubilities and diffusivities in liquid silicon and tend to accumulate along the grain boundaries [Buo06b]. Moreover, metallic impurities from crucible and coating easily diffuse into solid silicon at elevated temperatures during crystallization process. All these result in low minority carrier lifetime in so-called red-zone, the parts of the ingot that are close to the crucible (bottom, sides, corners), as well as inclusions and precipitates located on grain boundaries [Buo06a, Nae09]. The thickness of the red-zone depends on process parameters. Figure 2.3. shows a μ-PCD minority carrier lifetime map of a Gen5 mc-Si ingot with a representative red-zone. Consequently, the bottom and the side parts of mc-Si ingots have extremely low quality, which is insufficient for PV application, and have to be removed before slicing the ingot into wafers.

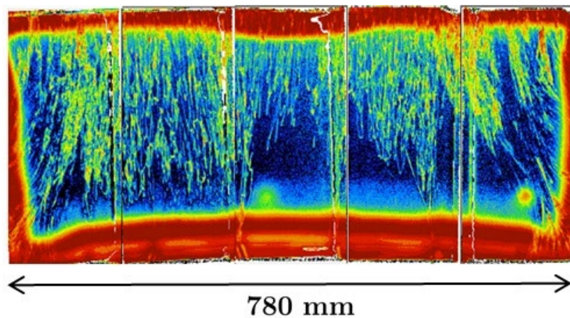

Figure 2.3.: Typical minority carrier lifetime map of a central vertical cut from Gen5 mc-Si ingot. The red color corresponds to low lifetime areas [Buc11].

It is also worth mentioning that during the process, some part of crucible coating is dissolved in silicon melt and built into the silicon crystal as the ingot grows [Rei10]. Si_3N_4 particles are incorporated in mc-Si in the form of filaments, which in turn serve as a nucleation sites for SiC precipitates [Rak05]. These compounds are extremely harmful both for mc-Si post-treatment and solar cell performance (see Chapter 2.5). Therefore, process conditions for directional solidification must be carefully selected in order to avoid dissolution of silicon nitride coating.

2.3. Melt flow and convection

Although the ingot growth is initiated by intentionally applied vertical thermal gradients, certain radial temperature gradients are also present in the system. Depending on the design of DS furnace, these gradients can have different values and pattern [Fra00]. In standard DS furnaces, the heat during crystallization process is supplied through the top heaters and the side heaters at the upper part of crucible walls. At the same time, the heat is exhausted through the bottom of the crucible and the lower part of crucible walls. Therefore, in the upper part of the melt, the temperature of the melt near the crucible walls is higher than that in

the central area at the same height, while in the lower part of the melt near the crystallization front the temperature of the melt in the central part is higher than that near the crucible walls. These radial temperature gradients lead to the liquid density variation, which results in movement of the silicon melt during solidification. In a traditional directional solidification process, there are two main phenomena that provoke this movement. The first one is buoyancy forces (so-called natural convection) that is caused by a horizontal temperature gradient between the colder areas and warmer areas of the melt. The second phenomena is Marangoni effect, which is related to differences in surface tension between colder and warmer regions of the free melt surface. Altogether, the melt motion is generated by the heat flow and the latent heat released to the melt at the solid-liquid interface during growth, and is tightly coupled with the shape of solid-liquid interface, as the melt flow can change the heat flow to the interface, and at the same time is also dependent on its shape [Viz07, Bel13a].

In classical DS process, natural convection of the silicon melt is rather low. The melt velocities depend of the size of the melt and process conditions. In general, for the systems of G1 to G5 size the magnitude lays in the range of $(1-10)\times10^{-3}$ m/s [Viz07, Tre10, Dro13]. This convection has a strong influence on distribution of impurities and inclusions in the melt, hence in crystallized mc-Si ingot [Bel10, Gar12, Bel13b]. This is especially important for oxygen and carbon, which main sources are the crucible and the carbon-reach components of the hot zone [Rei10, Nak13].

Due to the high temperature and the high chemical activity of silicon melt, direct measurements of the melt flow during DS process by velocimetry methods is highly complicated. Therefore, the most important and reliable information about melt convection can be estimated from numerical simulation and computer modelling of the growth process, as well as indirect analysis of impurity distribution in the grown ingot. Numerical simulation shows that the convection of the melt during crystal growth consists of two flow areas coupled with each other: the lower and the upper vortices [Ten10, Nie11] (see Figure 2.4). Both vortices are symmetrical to the central vertical axis of the furnace and correspond to different convection mechanisms. The lower vortices are caused by buoyancy depending on the shape of solid-liquid interface, and the upper ones are provoked by the Marangoni effect. At the beginning of crystallization, the volume of the silicon melt is large, thus the influence of the lower vortices is stronger than the one of the upper vortices. It was experimentally shown that these vortices promote impurities, such as carbon, SiC and Si_3N_4, to accumulate near the centre of the ingot [Ten10, Li13]. However, as the volume of the melt decreases due to solidification, the temperature difference between solid-liquid interface and the melt surface gets smaller and natural convection becomes less pronounced and is gradually overgrown by Marangoni flows. At the end of solidification, Marangoni convection is dominant and forces

the melt at the surface to flow from the crucible walls towards the centre due to surface tension, while heading the opposite direction at the solid-liquid interface. In this area, SiC and Si_3N_4 impurities are tend to be pushed from the ingot centre to the sides.

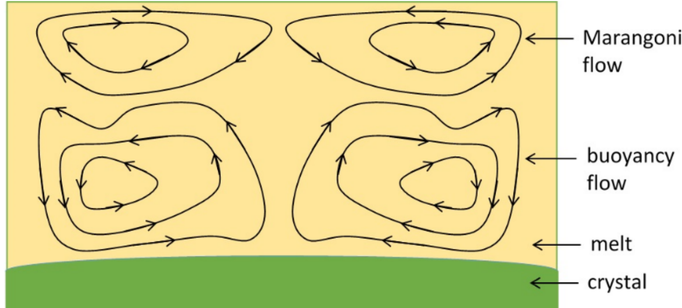

Figure 2.4.: Sketch of natural melt flow during directional solidification of silicon.

For ingots with large feedstock charge and melt area, the magnitude of temperature gradients rises and convective flows become more pronounced and influential. Since melt convection is a key factor in segregation and precipitation of impurities, it is highly important to control it. Furthermore, as the melt flow have significant impact on solid-melt interface, the unfavourable flow direction can cause undesirable growth conditions. All these obstacles must be avoided. Therefore, the effective method to dump undesirable convection and enhance favourable flow is one of the main objectives for successful DS process.

As the melt convection is greatly dependent on heat flows, it is in principle possible to control both natural and Marangoni flows by hot zone design and heat management. Nakano at all showed that sophisticated heat supply through side heaters could change the flow pattern of upper vortices and even totally annihilate Marangoni effects [Nak13]. However, a more effective way to influence melt convection is the use of external forces. Numerous successful attempts to effect fluid convection were performed by different research groups using various approaches and techniques, including mechanical stirring [Dum12], vibrations [Zha10], rotation rate variations [Bel11], electrical currents [Bly97] and magnetic fields [Rud09]. Application of mechanical stirring during directional solidification of G2 60 kg ingot proved to increase convection of silicon melt and significantly intensify the segregation of carbon and metallic impurities [Alb13]. Injection of a direct current during the crystallization process can also be successfully used to make the marking of solid-liquid interface by Peltier effect [Cab15]. Ultrasound and low frequency vibrations noticeably reduce the thickness of the diffusion boundary layer [Ubb12]. Radial direct electric current can also be successfully used for melt stirring and influencing the distribution of impurities in semiconductors [Wan06]. The increased melt flow induced by electromagnetic fields was shown to be beneficial for segregation process [San12] and will be discussed further in details.

Among the numerous methods to influence melt flow by external forces, the application of magnetic fields is of the most promising to assure optimal growth conditions. The application of travelling magnetic fields (TMF) was successfully tested both in the lab and on industrial level. It was proved that TMF has a positive influence on growth of G5 mc-Si ingots as large as 640 kg [Kud13]. The melt flow induced by TMF showed downward direction near the crucible walls, which is profitable for stability of crucible coating. The induced mixing not only has an influence on the pattern of a melt flow, but also on the shape of solid-liquid interface, and results in slightly convex curative at the rim. The grown ingot showed excellent properties with regard to low dislocation density, high minority carrier lifetime and particularly no bulk inclusions. The effect of magnetic fields on melt flow and ingot quality will be further discussed in Chapter 4.

2.4. Growth front and growth rate

The control of growth front (solid-liquid interface) is an important factor in manufacturing of crystalline material of a high quality. The shape of growth front affects the size and the crystallographic orientation of grains, the pattern of grain boundaries, as well as thermal stresses and the amount of structural defects in multicrystalline material. The most common approach is to keep the growth front flat, as it assures stable growth of vertically prolonged columnar grains and sufficient relaxation of stresses [Lan15]. In contrast, concave shape of solidification front implies parasitic nucleation on side walls of the crucible with subsequent propagation of grains inclined to horizontal direction. In this case, columnar grains, which grow in unparalleled directions, ultimately meet and collide that results in mechanical stress and generation of undesired defects [Che10]. Taking the above into account, it is preferable to keep a solid-liquid interface slightly convex close to the crucible rim, since it is unfavourable for the parasitic nucleation of grains at the side walls. The shape of solid-liquid interface is determined by the thermal heat flux in the melt and in the crystal. In order to obtain a flat growth front it is crucial to keep heat flow strictly vertical from the top to the bottom of a hot zone and to avoid any temperature gradients along the solid-liquid interface, which are normally present in real DS systems. In this case the thermal stress is minimized, which is a mandatory condition for a low dislocation density in the grown crystal. This approach can be implemented by hot zone modification, e.g., effective crucible insulation [Yeh10] or introduction of additional construction elements such as side blocks or partition insulators [Lan95, Lan12a]. It is worth to be mention that the precise control of solid-liquid interface is particularly important in the case of seeded growth of HPM-Si and quasi-mono silicon.

Metal impurities from the crucible and its coating are prone to solid diffusion into silicon crystal at elevated temperatures that deteriorates the material quality. In order to reduce the time of the contact between the solidified material and the crucible, it is preferable to increase the growth rate. In addition, a short process cycle reduces the cost of mc-Si material, which is one of the main tasks in industrial production. However, due to conditions at the solid-liquid interface, the growth rate is limited. Therefore, ingots grown at elevated solidification rates are prone to rapid and uncontrolled nucleation; hence exhibit higher level of defects and dislocations. For the case of solidification from the melt, the growth rate is limited by transport of the latent heat [Uwa15]. The transport of heat is performed by heat conduction in the material and melt convection. Therefore, the growth rate depends on vertical temperature gradients and the cooling rate. The heat transfer is influenced by the difference in heat conductivities in solid and liquid material. The heat conductivity of solid silicon is smaller than the one of the silicon melt (Table 10.1. in Appendix). The growth rate is determined by the heat flux balance and is described as following [Fle74]:

$$v_{gr} = \frac{q_l - q_s}{\Delta H_L \rho_s} = \frac{\lambda_s \nabla T_s - \lambda_l \nabla T_l}{\Delta H_L \rho_s} \tag{2.1}$$

Where v_{gr} indicates the growth rate, ΔH_L the latent heat, q_s and q_l the heat fluxes, ρ_s and ρ_l the densities, λ_s and λ_l the thermal conductivities, ∇T_s and ∇T_l the temperature gradients at solid-liquid interface for the solid and the liquid silicon, respectively. The growth rate is limited to the case of $\nabla T_l = 0$.

$$v_{grMAX} = \frac{\lambda_s \nabla T_s}{\Delta H_L \rho_s} \tag{2.2}$$

In order to ensure maximum growth rates, the latent heat released at the solid-liquid interface and the heat transported from the melt to the interface have to be effectively removed. Which means that fast crystal growth is possible only when the vertical thermal gradients in the ingot are larger than the ones in the melt (Figure 2.1). For temperature gradients typical for directional solidification, the maximum possible growth rate lays in the range of 10 cm/h.

It also has to be keep in mind that an elevated growth rate results in supercooling, following supersaturation of the melt with carbon, silicon carbide, nitride precipitation, and generation of defects, which was observed in several studies [Sch12, Tre10]. On the opposite, a moderate growth rate prevents supercooling and uncontrolled nucleation, as well as ensures stable growth of columnar vertical grains. It is also has to be mention that high growth rates result in introduction of higher thermal stresses in the grown ingot, which subsequently

leads to increased dislocation density in mc-Si material. Furthermore, the shape of solid-liquid interface is also defined by solidification rate. The latent heat, which is released during solidification, cannot be promptly exhausted in case of high crystallization rate, hence leads to concave solidification front and inferior crystal structure. It is commonly considered that uniform material quality requires moderate and constant growth rate throughout the whole crystallization phase. Therefore, in order to obtain mc-Si ingots of appropriate quality and ensure stable growth conditions, the growth rate is normally kept in the range of 1-2 cm/h.

2.5. Gas flow and melt surface

During directional solidification, not all impurities are incorporated into the ingot through simple diffusion or segregation processes. The most abundant elements in multicrystalline silicon ingot are carbon and oxygen. The mechanism of their incorporation is rather complex and involves a series of chemical reactions and transportation routes [Gao10, Kak15] which are shown in Figure 2.5.

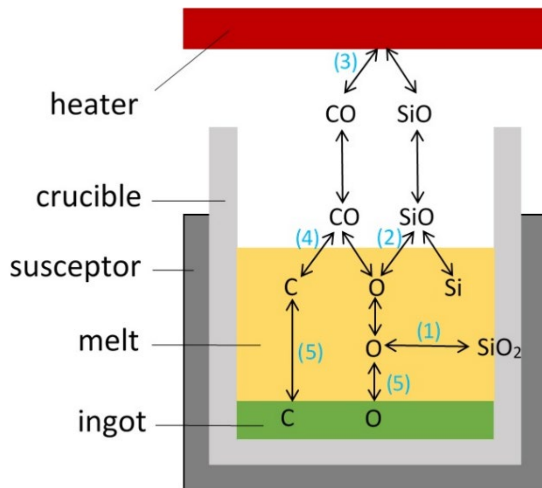

Figure 2.5.: Incorporation of oxygen and carbon into a mc-Si ingot during DS.

At elevated temperatures during silicon melting and crystal growing, silicon diffuses through crucible coating and starts to dissolve silica crucible. Oxygen and silicon atoms penetrate into the melt and the dissolved oxygen is further transported by the melt flow. On the way to the melt surface, oxygen reacts with liquid silicon and transforms into gaseous silicon monoxide compound, which evaporates from the melt surface as soon as reaches it [Gao10].

$$SiO_{2(s)} + Si_{(l)} = 2SiO_{(g)} \tag{2.3}$$

At this stage, it is highly important that SiO gas be taken away from the system by outgoing gas flow. If the gas flow above the melt is not effective in removing of

evaporated silicon monoxide, it will react with graphite components of the furnace and produce gaseous CO.

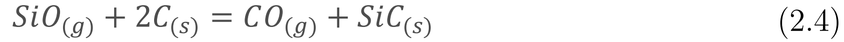

$$SiO_{(g)} + 2C_{(s)} = CO_{(g)} + SiC_{(s)} \tag{2.4}$$

Silicon carbide formed in this reaction will typically stay on graphite elements creating a lasting layer (so-called graphite siliconizing process). If no cover is used above the melt surface, some SiC particles can also be introduced into the melt and subsequently incorporated into the mc-Si ingot. However, even though SiC pollution from this source is relatively low, pure carbon is easily introduced into the melt through the second compound from the above-described reaction, carbon monoxide. CO is transported back to the melt surface by diffusion and/or convection and dissociates thereat reintroducing both carbon and oxygen.

$$CO_{(g)} = C_{(m)} + O_{(m)} \tag{2.5}$$

Finally, C and O atoms are captured into the solid phase as the ingot grows. Despite of a coupled mechanism of introduction to the melt, carbon and oxygen atoms are differently distributed in the ingot. As the main source of oxygen is the surface of the crucible in direct contact with the melt, its rate of diffusion is proportional to the area of the contact, hence it decreases as the ingot grows and the melt volume decreases. At the same time, the evaporation of oxygen through silicon monoxide compound from the melt surface stays constant during the whole solidification process. Therefore, oxygen concentration decreases towards the top of the ingot. In contrast to oxygen, carbon is introduced through the melt surface; hence, its concentration increases as the ingot grows.

It is also worth mentioning that the silica crucible has a contact with the graphite susceptor on the outer surface, which can also result in a similar to the abovementioned reactions that does not involve transport in the gaseous phase [Gao11].

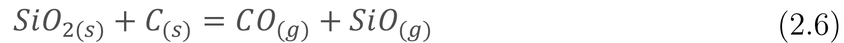

$$SiO_{2(s)} + C_{(s)} = CO_{(g)} + SiO_{(g)} \tag{2.6}$$

However, the exact mechanisms of the compounds transport to the melt in this case are not clear yet.

Due to the above-described transport mechanisms, carbon and oxygen are the most abundant impurities in multicrystalline and their amount. Oxygen is incorporated into silicon crystals as an interstitial atom, while carbon is introduced as a substitutional atom. In case no specific solutions for interrupting the particle transport are applied during the growth process, the concentrations of oxygen and carbon atoms in most contaminated areas of mc-Si ingot can be as high as 10 ppm.

Even though carbon is introduced into the melt as a solute atom, when its concentration in the silicon melt exceeds the range of 100 ppm and reaches the solubility limit (Table 2.2), it starts to precipitate in the form of silicon carbide. When the precipitation is high, these precipitates can be easily transported by the melt to the solid-liquid interface and incorporated into the ingot as SiC particles. SiC inclusions are extremely harmful for the quality of PV silicon. First of all, they cause a wire breakage during slicing of ingots into blocks and wafers [Du07]. Secondly, SiC particles result in severe ohmic shunts in solar cells [Bau07, Ric17a]. Similar to carbon, oxygen can also create O_x precipitates when its concentration exceeds solubility limit (Table 2.2). However, this limit for oxygen is much higher than for carbon, so that such high oxygen values are rarely observed in mc-Si. Nevertheless, even atomic O is greatly undesired in silicon crystals. E.g., in boron-doped c-Si, which is an industrial standard for PV market, oxygen is prone to create B_2O complexes that lead to light-induced degradation of solar cells during operation [Sch03].

Therefore, in order to obtain high-quality mc-Si material, carbon and oxygen concentrations must be carefully controlled. One of the effective techniques is the usage of crucible cover, which cuts the back diffusion of CO and reduces carbon. However, it has to be kept in mind, that material of this cover must be rather inert [Gao13, Bel14, Ten14]. The other method is the reduction of SiO-CO transport through the gaseous phase by effective species evacuation with purging gas flow. It was shown by many research groups that accelerated and/or tailored argon flow above the melt surface can significantly reduce the level of C, O and SiC in mc-Si ingots [Liu17]. In addition, purging gas flow has a certain influence on other volatile compounds evaporating from the melt surface. These mechanisms will be further discussed in Chapter 3.3.

2.6. Segregation of dopants and impurities

The quality of mc-Si material strongly depends on both its structure and foreign elements incorporated into a crystal. Foreign species might be introduced either intentionally in order to obtain certain properties (e.g., dopants), or due to pollution during the crystal growth. The incorporation is realised either by diffusion in the solid state after crystallisation, or by capturing at the solid-liquid interface during solidification. In the latter case, there are two possible mechanisms of capturing. The first one is irregular incorporation of relatively large particles that are brought to the interface by the melt flow. The second mechanism is segregation – gradual embedding of solute elements, which are distributed in the bulk melt. This section describes the segregation phenomena for closed systems (i.e. no additional source of elements or melt and no mechanisms of extraction of species during the process)

and considers neither diffusion in the solid material nor irregular capturing of inclusions.

The nature of segregation lies in different solubility of foreign elements in the solid and in the liquid phase. Depending on which one is higher, the solute will be pushed into either phase at the solid-liquid interface. This phenomena results in enrichment or depletion of solutes in the melt, hence to their non-uniform distribution in the ingot as it grows. The most pronounced effect is observed in the axial direction, since the melt is solidified hitherwards, and leads to the gradual increase or decrease of impurity/dopant concentration along the ingot's length.

In thermodynamic equilibrium, when the growth rate is zero, the solute concentration in the solid and in the liquid phase is C_s and C_l, respectively. Their ratio at solid-liquid interface defines equilibrium segregation coefficient k_0,

$$k_0 = \frac{C_s(x=0)}{C_l(x=0)} = \frac{C_s^0}{C_l^0} \tag{2.7}$$

where x is the distance from interface, C_s^0 and C_l^0 are the solute concentrations at the interface in the solid and in the liquid phase, respectively.

k_0 depends solely on the nature of the solute and the medium species, and not on the crystal growth process parameters or hydrodynamic melt properties [Gli11]. When the ingot is grown at a slow rate and the solute is evenly distributed in the melt, it can be assumed that the growth takes place at thermodynamic equilibrium. If $k_0 < 1$, solute atoms preferably stay in the melt rather than build into the solid phase. After solidification of the first portion of the melt, the concentration of solute species in the crystal will be smaller than the one in the melt, hence the remaining concentration in the liquid phase increases. Over time of solidification, the melt becomes enriched with solute atoms. Consequently, the concentration of the solute atoms incorporated into the solid phase also increases as the ingot grows, since the ratio of concentrations in the solid and in the liquid phase is constant at every single moment. For $k_0 > 1$, the solute concentration in the solid is larger than in the liquid, hence the concentration in the ingot decreases over the progress of solidification. The former situation is more common than the latter one, therefore further discussion will be illustrated with the case of $k_0 < 1$. The case of $k_0 > 1$ follows analogical mathematical procedures.

The transport of solutes in the melt and at the solid-liquid interface is defined by two main mechanisms – diffusion and convection. Both these mechanisms must be taken into account while describing the incorporation of elements during crystal growth [Cam86].

As during crystal growth solute atoms at the solid-liquid interface are rejected into the melt, their concentration in the melt near the interface rises while building a solute boundary layer with the thickness of δ. The concentration of solute within

this boundary layer decreases from its equilibrium value at the interface $C_l(x=0)=C_l^0$, to a lower value in the bulk melt $C_l(x=\delta)=C_l^\infty$. The thickness of the boundary layer depends on melt convection. If melt mixing is very fast and effective (so-called perfect mixing), the solute atoms redistribute evenly in the melt and the boundary layer does not build up at all. In the absence of any convection, the boundary layer is purely diffusive and in DS process might be as large as 1 mm. In the presence of non-perfect melt convection, δ is normally reduced below 0.1 mm [Ost15]. Figure 2.6. illustrates the concentrations of solute in the vicinity of the solid-liquid interface and within the boundary layer for three cases: perfect mixing, no convection (pure diffusion) and coupled effect of diffusion and convection (convecto-diffusive case).

In the presence of both diffusion and convection in the melt, it is still possible to use the relation of the solid to the liquid concentration of solute element in the form of effective segregation coefficient k_{eff},

$$k_{eff}=\frac{C_s(x=0)}{C_l(x>\delta)}=\frac{C_s^0}{C_l^\infty} \tag{2.8}$$

where C_l^∞ corresponds to the solute concentration in the liquid phase beyond the boundary layer. For the case of perfect melt mixing the boundary layer disappears $\delta\to 0$ and the effective segregation becomes equilibrium one $k_{eff}\to k_0$.

The distribution of solute atoms in a convecting melt with a moving growth front is described by the convection-diffusion equation [Ost15]

$$\frac{\partial C_l}{\partial t}+\vec{u}_{melt}\cdot\vec{\nabla}C_l=D\nabla^2 C_l+\vec{v}_{gr}\cdot\vec{\nabla}C_l \tag{2.9}$$

with D to be the diffusion coefficient, $\vec{v}_{gr}$ the growth rate, and $\vec{u}_{melt}$ the velocity of the melt flow.

Gulliver [Gul22] and Scheil [Sch42] solved this equation under the conditions of local equilibrium for the case of perfect mixing. In this approach, the solute distribution in crystallized ingot C_s with progressing growth was deducted to be

$$C_s(g_s)=k_0C_0(1-g_s)^{k_0-1} \tag{2.10}$$

where g_s is the fraction of solidified material and C_0 initial solute concentration in the melt before solidification started.

Tiller et al. [Til53] considered (2.9) for the opposite limiting case of pure diffusion with no convection, so that derived an approximate solution of

$$D\frac{\partial^2 C_l}{\partial x^2}+\vec{v}_{gr}\frac{\partial C_l}{\partial x}=0 \tag{2.11}$$

with boundary conditions for $x = 0$

$$D\left(\frac{\partial C_l}{\partial t}\right)_{x=0} = -\vec{v}_{gr}(C_l^0 - C_s) = -\vec{v}_{gr}(1-k_0)C_l^0 \tag{2.12}$$

and for $x = \infty$

$$C_l = C_l^\infty \tag{2.13}$$

The solution for the pure diffusion case was found to be

$$C_s(x) = C_0\left[1 + \frac{1-k_0}{k_0} exp\left(-x\frac{v_{gr}}{D}\right)\right] \tag{2.14}$$

The first attempt to combine both limiting cases in the model, which takes into account both diffusion and convection in the melt, was done by Burton, Prim and Schlichter in their BPS theory [Bur53]. With the assumption of one-dimensional solute segregation and introducing the solute boundary layer, they found a fundamental relationship which connects D, v_{gr}, k_0, and δ with k_{eff}

$$k_{eff} = \frac{k_0}{k_0 + (1-k_0)exp\left(-\delta_{BPS}\frac{v_{gr}}{D}\right)} \tag{2.15}$$

and derived the solute distribution in the ingot to have the same character as Gulliver-Scheil equation (2.10) substituting k_0 with k_{eff}

$$C_s(g_s) = k_{eff}C_0(1-g_s)^{k_{eff}-1} \tag{2.16}$$

It has to be mentioned that in this model δ_{BPS} does not correspond to the real physical thickness of the boundary layer, but is the adoption parameter that defines diffusive and convective shares at the solid-liquid interface. At the same time, Wilson [Wil78] determined the diffusion boundary layer for purely diffusive case to be

$$\delta_D = \frac{C_l^0 - C_l^\infty}{-\left(\frac{\partial C_l}{\partial x}\right)_{x=0}} = \frac{D}{v_{gr}} \tag{2.17}$$

that can be successfully extended to the convecto-diffusive case. Here, the effective segregation coefficient k_{eff} depends on the physical thickness of the boundary layer

δ, the growth rate v_{gr}, and the flow velocity at the interface rate u_{melt} [Ost92]. It is convenient to introduce a non-dimensional convecto-diffusive parameter [Gar90]

$$\overline{\Delta} = \frac{\delta}{\delta_D} = \frac{\delta v_{gr}}{D} = 1 - exp\left(-\delta_{BPS}\frac{v_{gr}}{D}\right) \tag{2.18}$$

which value lies between 0 and 1. The pure diffusion corresponds to $\overline{\Delta} = 1$, the perfect mixing to $\overline{\Delta} = 0$. The values in between quantitatively define the share of diffusive and convective influences on the solute transport. Using this parameter the effective segregation coefficient can be written as follows

$$k_{eff} = \frac{k_0}{1 - (1 - k_0)\overline{\Delta}} \tag{2.19}$$

For the pure diffusive transport the effective segregation coefficient turns to be $k_{eff} = 1$, for the case of perfect mixing $k_{eff} = k_0$.

The solute distribution in the ingot for three representative cases of perfect mixing (2.10), pure diffusion (2.14) and convecto-diffusive transport (2.16) are demonstrated in Figure 2.6.

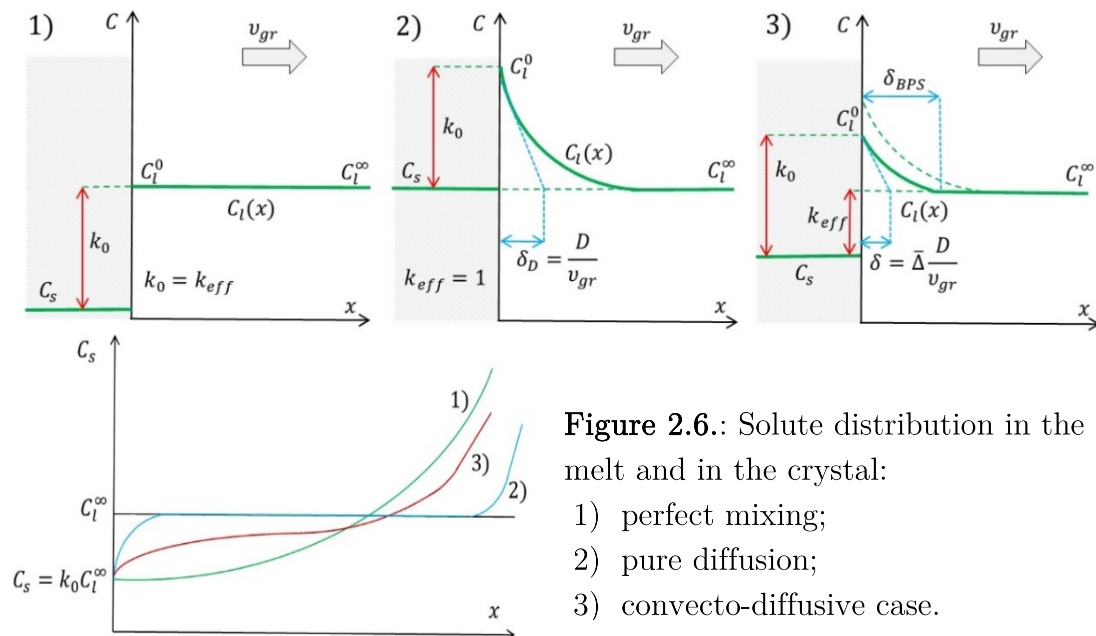

Figure 2.6.: Solute distribution in the melt and in the crystal:
1) perfect mixing;
2) pure diffusion;
3) convecto-diffusive case.

All the above-described analytical derivations are made by using a row of simplifications and assumptions. However, the governing convection-diffusion equation is not solvable in real systems. In engineering practice, phenomenological solutions must be adopted with the usage of empirical relationships obtained from experimental results. While considering complex crystal growth problems one must take into account unsteady growth conditions, e.g. rate/flux relationships,

fluctuations in growth rates, solute reactions with encapsulation material etc. These conditions consider the effective segregation coefficient to be variable. Experimental results performed by many research groups enabled the development of numerous empirical correlations [Ost15]. The effective segregation coefficient for directional solidification determined from these correlations [Inc90, Cen15] provides better accuracy and compliance with real systems:

$$k_{eff} = \frac{k_0}{1 - (1 - k_0)Pe/[Nu^{1.4} + Pe^{1.4}]^{1/1.4}} \tag{2.20}$$

where Nu stays for the heat and mass transfer coefficients called Nusselt number, and Pe for the dimensionless interface velocity called Peclet number. These correlations and dependencies are used in global simulations to create the detailed segregation model and consider heat and mass transfer, as well as melt and gas convection [Liu06].It also needs to be mentioned that many systems have not perfectly planar but curative solid-liquid interface. Therefore, their horizontal cross section actually includes areas solidified at different time, hence belonging to different solidified fraction g. This effect is called lateral segregation and is quite pronounced in melts with curved interface.

As it was shown, the distribution of species in mc-Si ingots depends on their solubility in silicon melt as well as segregation and diffusion coefficients. The typical values for most common impurity elements in PV c-Si are given in Table 2.2. Light elements such as C, O and N are the most abundant impurities in mc-Si. In previous sections, it was already discussed that the source of oxygen and nitrogen are silica crucible and nitride coating, and carbon comes from the graphite parts through the gas phase and back diffusion. The pollution of silicon melt with these elements takes place during the entire time of crystallization. The quantity of C and N is often so high that reaches solubility limit and concludes in compound formation. Since phenomenological equations of BPS or Gulliver-Scheil are valid only for closed systems, i.e. they do not consider the cases where solutes precipitate or are introduced into the system during the process, these equations are not applicable for light elements. However, segregation coefficients give basic understanding of these impurities distribution, i.e. concentration of C and N increases and concentration of O decreases towards the top of the ingot. The source of metal contamination is crucible and coating material as well as silicon feedstock. In principle, due to extremely low segregation coefficients these impurities are effectively segregated to the very top of mc-Si crystal, which can be observed in low minority carrier lifetime in the uppermost part of the ingot (see Figure 2.3).

Element	Segregation Coefficient	Diffusivity [cm^2/s]	Solubility [$atoms/cm^3$]
B	0.80 [Joh12]	2.4×10^{-4} [Kod63]	6.0×10^{20} [Tru60]
P	0.35 [Joh12]	5.1×10^{-4} [Kod63]	1.3×10^{21} [Tru60]
O	1.25 [Yat73]	3.6×10^{-4} [Eng92]	2.2×10^{18} [End79]
C	0.07 [Noz70]	3.5×10^{-4} [Eng92]	5.1×10^{18} [Rei10]
N	7.0×10^{-4} [Yat73]	4.1×10^{-4} [Eng92]	5.7×10^{18} [Rei10]
Al	2.0×10^{-3} [Kod63]	7.0×10^{-4} [Kod63]	2.0×10^{19} [Tru60]
Fe	1.5×10^{-5} [Col11]	1.2×10^{-6} [Col11]	1.2×10^{13} [Col11]
Cu	4.0×10^{-4} [Joh12]	8.0×10^{-5} [Col11]	1.1×10^{17} [Col11]
Cr	3.1×10^{-6} [Col11]	3.6×10^{-7} [Col11]	1.7×10^{12} [Col11]
Ni	8.0×10^{-4} [Lan15]	1.6×10^{-5} [Col11]	3.5×10^{16} [Col11]
Ti	3.5×10^{-5} [Col11]	7.6×10^{-11} [Col11]	$(1–7)\times10^{10}$ [Col11]

Table 2.2.: Segregation coefficient, diffusivity and solubility for typical species in silicon.

Besides impurities incorporated into crystalline material due to pollution, multicrystalline silicon ingots also contain dopants – foreign species intentionally introduced into the melt in order to obtain certain material properties. PV c-Si is typically doped with boron or phosphorus, which ensure specific electrical conductivity essential for functioning of p-n junction in solar cells. Industrial standard for electrical resistivity of mc-Si wafers is 3.0 – 1.0 Ω·cm which corresponds to concentrations in the order of 10^{15} – 10^{16} $atoms/cm^3$. As dopants are introduced deliberately together with feedstock material and their concentration in the melt is significantly lower than solubility limit, their distribution in crystallized material can be successfully described with analytical convecto-diffusive model of segregation. The aim of this thesis is the study of distribution and segregation of phosphorus in mc-Si and will be discussed in details in further chapters.

2.7. Grain boundaries and dislocations

Although the technology for the production of multicrystalline silicon is relatively simple and cheap, the material quality demonstrates many imperfections. These include not only pollution with inclusions and impurities, but also unavoidable for mc-Si extended structural defects, such as randomly oriented grain boundaries and dislocations. These extended defects are found in high densities in

mc-Si materials and have a considerable impact on solar cell properties. E.g., they interact with mobile impurities and precipitates during crystal growth and cooling, and store the majority of them [Buo06a, Buo06b]. Some of these impurities, such as Ti, Cr, Ni, Cu and Fe, have a deteriorative effect on the minority carrier lifetime of mc-Si material, hence solar cell performance [Col11]. Fast-diffusion metals, which decorate extended defects, might be successfully removed with phosphorus gettering during solar cell processing. However, this procedure is not effective against other groups of metals and precipitates at grain boundaries [Col11].

One of the main flaws of mc-Si compared to monocrystalline Si is numerous dislocations. Dislocations and their clusters are active recombination centres deteriorating the performance of solar cells [Ara06, Moe05]. In mc-Si ingots dislocations nucleate at the solid-liquid interface during solidification and behind the growth front during the growth run and the cooling of ingot down to 800°C [Coc11, Lan15]. The main sources for nucleation of dislocations are grain boundaries [Ryn11, Tak10] and precipitates, such as SiC or Si_3N_4 [Sch12], due to lattice distorted stress concentration around them. However, some part is also nucleated at the crucible walls. In contrast to grain boundaries, dislocations have the ability to migrate in crystalline material. Hence, once generated, they can multiply, annihilate or rearrange in energetically favourable structures [Fra50, Nak11, Val01]. As the ingot grow dislocations rapidly multiply due to plastic deformation under thermal stress and create clusters. The stress needed to nucleate dislocations is rather high and lies in the range of 0.1 – 5.0 GPa [Rab10]. However, the stress required to move and multiply dislocations that were nucleated during growth is much lower and is found to be around 9 MPa [Tsa91]. Dislocations generated during cooling are rarer to be found in crystallised material than those nucleated during crystallisation, since their ability to multiply is smaller. In mc-Si ingots, dislocations are typically found in densities of 10^4-10^6 cm^{-2} [Gas17, Lan15]. However, in localized areas, the density can reach values as high as 10^8 cm^{-2} and their bundles can extend over a few centimetres [Erv13, Gas17].

Mc-Si material consists of elongated grains extending through the height of ingot, with the size ranging from a few millimetres to a few centimetres. The grains that build up an ingot have different crystalline orientations and are separated by interfaces called grain boundaries, which affect the ingot quality, hence the performance of solar cells [Yan80, Fuj06a, Wan09]. The density of dislocations in crystalline material depends on the grain orientations and the type of grain boundaries; hence, these have a significant impact on material properties, e.g., mechanical and electrical characteristics [Usa10, Wue10, End02].

According to the angle between crystalline orientation of neighbouring grains (misorientation angle) and the arrangement of atoms at the interface, grain boundaries are classified into two main categories. The boundaries between two grains that share coincident sites are called coincident site lattice (CSL) grain

boundaries. Σ-value defines the degree of fit, corresponding to the reciprocal density of coincident sites. CSL grain boundaries show low interfacial energies and high degrees of coherency. These boundaries is normally considered to have higher resistance to the cutting stress, lower influence on material electrical properties, and lower ability to collect impurities and precipitates [End02, Sto10]. Σ3 grain boundaries, or twins, are a particular case of CSL boundary. They show significantly lower dislocation density and do not act as recombination centres for charge carriers [Che05, Sto10]. The second group are random grain boundaries, which considerably deviate from the CSL configurations. They have low degrees of coherency and high interfacial energies. The deviation from the ideal CSL misorientations leads to introduction of dislocations in the grain boundary [Usa10].

Therefore, it is very important for mc-Si material quality to assure high content of grains with favourable orientation and favourable grain boundaries, which must be performed through careful control of nucleation and grain growth. It was proved that this control could be fulfilled by slow cooling and smart management of the shape of solid-liquid interface [Lan15].

2.8. Types of material

Due to negative influence of dislocations and grain boundaries of unfavourable orientations on multicrystalline material quality, defect engineering is one of the most important research directions. Several techniques have been proposed to limit the generation of dislocations and grain boundaries during ingot growth, including dendritic casting [Fuj06b], noncontact crucible method [Nak12], high-performance multicrystalline material (HPM-Si) [Lan12b] and quasi-mono technique [Cun08]. The two latter are most successfully used in PV industry, and nowadays are the most widespread material on the market besides conventional multicrystalline material.

Quasi-mono c-Si

Quasi-mono technique aims at avoiding grain growth, thus eliminating grain boundaries. The goal is to grow ingots with monocrystalline structure. The most suitable approach to obtain the desired quality is seeded-growth. The technology was firstly presented and patented in 2006 by Stoddard [Cun08, Sto06, Sto08]. The approach is performed by arranging nucleation on a large piece of monocrystalline material (seed). The seed is placed on the bottom of the crucible with polycrystalline feedstock put above and the top part of the seed is molten together with the feedstock. When the growing starts, the seed material acts as a nucleation

site and the orientation of the growing crystal is imposed by this mean. As the ingot solidifies, monocrystalline material grows from bottom to top.

The seed-growth seems to be easy to implement. However, successful seeding procedure requires fulfilment of certain conditions. First of all, it is needed to organize the melting phase in such a way that not the entire seed but only its top part is molten while the bottom part is kept solid. This condition is fulfilled by either sophisticated control of heat input or additional cooling at the crucible bottom. The procedure is complicated by the fact that the solid-liquid interface cannot be observed during the process. The selection of suitable seed thickness is also crucial for securing the seeding across the curved solid-liquid interface.

Although the modern quasi-mono technology assures large ingots with monocrystalline structure across almost the entire ingot, there are still many technical challenges to overcome. The difficulties in mechanical treatment and the lack of sufficiently large monocrystalline seeds makes it necessary to pave the bottom of large crucibles with seeds of G1 size. This pattern provokes the generation of dislocations at the seed-joints with their subsequent multiplication and cascade propagation into the crystal as it grows. In addition, the seed-joints as well as the crucible walls are the origin of parasite grains nucleating thereat [Tre12, Erv14, Eks15]. However, the recent development has been very successful to prevent these problems by utilizing careful seed arrangement and deliberate inducing certain grain boundaries that suppress the growth of parasitic grains [Jou13, Hu15], e.g. large-angle tilt junctions by rotating the seed around the <100> axis [Wu16].

Another notable challenge for quasi-mono material is a significantly enlarged red-zone at the bottom of the ingots clearly seen on lifetime maps, which is about twice larger than that for conventional mc-Si. It is believed to be induced by back-diffusion of iron from the silica crucible into the monocrystalline seeds during melting stage [Gao12, Zho14]. Several research groups already demonstrated that this problem might be hopefully solved with special diffusion barrier layers applied to the crucible [Hug11, Hsi14, Tre15, Tre20].

High-performance mc-Si

Another widespread approach in DS technology focuses on lowering the average dislocation density in crystalline material and is called high-performance mc-Si. It was found that relatively small grains with uniform structure and random grain boundaries are less prone to generate dislocations and show the best uniformity of lifetime as well as superior solar cell efficiency [Lan12b, Yan13, Buc12]. This random structure is achieved by a better control of the nucleation phase or by seeded-growth. Seeded-growth is performed in a similar way as for quasi-mono technique, but instead of monocrystalline material in this case the layer of small silicon chips and chunks are used as seeds to ensure small uniform grains to be

nucleated [Lan13]. While using such small seeds, the ingot composed of smaller grains and containing almost no dislocation cluster can be easily obtained.

Low defect density was shown to be related to stress relaxation at the grain boundaries. It was shown that in the early stages of ingot growth, dislocation clusters are located in intragrains, and mostly disappear when these grains are overgrown by others. Therefore, further multiplication of dislocations is successfully terminated. At the latter stages, when the grains become larger, more defects are introduced, but they are localized in smaller grains surrounded by larger ones. During crystallization, the ingot always experiences thermal stress, since silicon expands as it solidifies. The generation of dislocations during plastic deformation is an effective way to relax the stress. Since in HPM material the stress is concentrated in small defective grains, the stress can be easily relaxed. Consequently, the massive propagation of dislocations in large grains is significantly smaller as compared to that in the case of conventional mc-Si growth [Lan12c, Yan13]. However, on the late stages of growth, more dislocations are observed also in the large grains and they are more prone to further multiplication because less grain boundaries are available to stop them. Therefore, the existence of many grain boundaries and small grains are crucial for HPM technique, since these provide a sufficient space for thermal stress to be relaxed and for small defective grains to be overgrown by the grains with better structure [Lan15, Lan16].

It has to be mentioned that fine silicon chunks are not the possible only way to perform the seeded-growth of HPM-Si ingots. Different research groups reported the successful seeding of HPM-Si structure with the use of notched crucibles [Li11, Buc17] and rough crucible coating [Kie18].

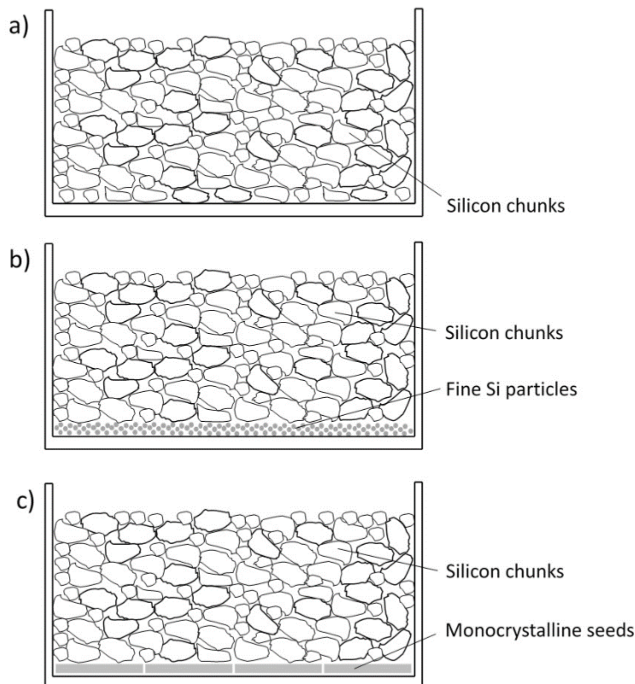

Figure 2.7.: Crucible loading for nucleation of different types of crystalline material:
a) conventional mc-Si;
b) high-performance mc-Si;
c) quasi-mono c-Si.

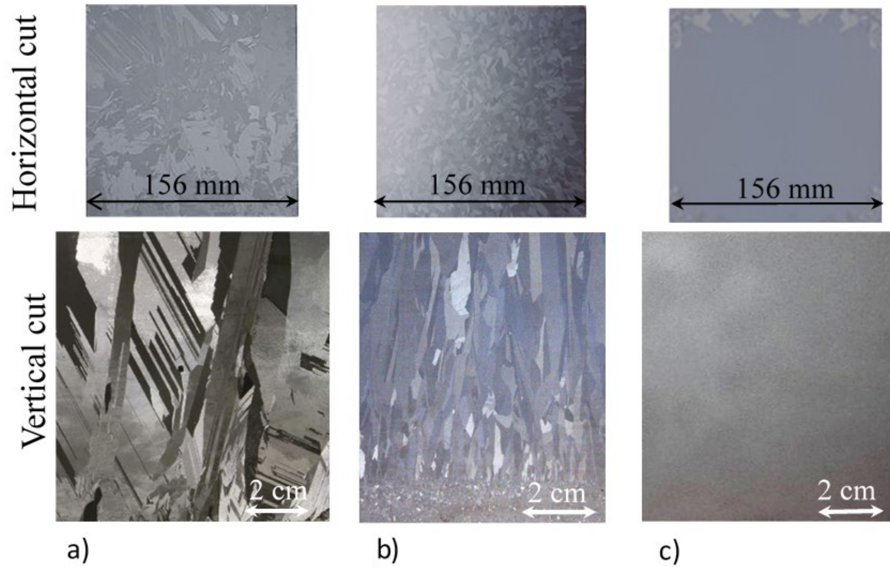

Figure 2.8.: Grain structure of different types of crystalline material in vertical and horizontal cross-section: a) conventional mc-Si; b) high-performance mc-Si; c) quasi-mono c-Si.

Figure 2.7. illustrates the schematic arrangement of seeded-growth for conventional multicrystalline material, HPM-Si and quasi-mono material. The crystalline structure of three types of directionally crystallized material is given in Figure 2.8. Conventional mc-Si ingot consist of columnar grains with the size up to a few centimetres, while HPM-Si show more organized and elongated crystallites of significantly smaller size about few millimetres. At the same time, quasi-mono material demonstrated homogenous monocrystalline structure with rare parasite grains of different orientation on the periphery. As these three types of DS-material require rather different growth conditions, especially in the initial phases, and demonstrate different crystalline quality, it is crucial to understand that any alteration or modification of the growth process must take into account these peculiarities and should be verified for each material independently.

CHAPTER 3

Phosphorus in crystalline silicon ingot and melt

3.1. Doping of silicon

Nearly all photovoltaic energy conversion devices, including those based on crystalline silicon, utilise semiconductors in the form of p-n junction. In order to be used as a substrate for the production of solar cells, crystalline silicon has to be intentionally doped with acceptor or donor elements to acquire a certain level of conductivity.

Doping is a technique used to vary the number of charge carriers (electrons and holes) in semiconductors. Silicon, which belongs to group IV in the periodic table, has four valance electrons that participate in covalent bonds between four neighbouring silicon atoms in the crystalline lattice structure. In the simplest case, doping elements substitute silicon atoms in lattice cells. If a silicon atom is substituted with the element from group V (e.g. phosphorus, arsenic, antimony), which atoms have five valence electrons, it forms covalent bonds with the four valence electrons of silicon, and thus the unit cell acquires an additional electron in the conduction band. This situation is called n-type conductivity. In case of doping with elements from group III (e.g. boron, aluminium, gallium), which atoms have only three valance electrons, the unit cell obtains a hole, the absence of an electron, which is called p-type conductivity. In such a manner, the balance of electrons and holes in the silicon crystal lattice can be shifted by doping [Mar03]. The illustration

of mechanism of silicon doping with phosphorus (n-type) and boron (p-type) is given in Figure 3.1.

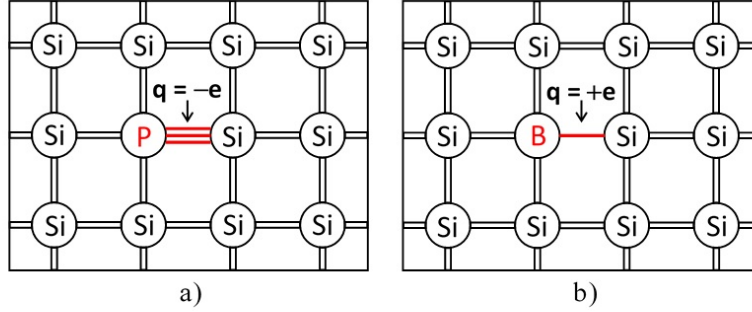

Figure 3.1.: Sketch of silicon crystal lattice with incorporated dopants: a) n-type, b) p-type.

N-type dopants increase the conductivity of semiconductors by increasing the number of available electrons. Analogically, p-type dopants increase conductivity by increasing the number of holes present. In doped material, the concentration of one carrier type is always higher than that of the other. The type of carrier with the higher concentration is called a majority carrier, while the lower concentration carrier is called a minority carrier. The number of carriers in the conduction and valence band, which exist without any external excitation, is called the equilibrium carrier concentration. For majority carriers, the equilibrium carrier concentration is equal to the intrinsic carrier concentration (without doping) plus the number of free carriers added by doping. In most situations the doping in semiconductor is several orders of magnitude larger than the intrinsic carrier concentration, thus the number of majority carriers is approximately equal to the doping. In equilibrium conditions, the number of minority and majority carriers is expressed by the law of mass action [Pie96]:

$$np = n_i^2 \tag{3.1}$$

where n_i is the intrinsic carrier concentration, and n and p are the concentrations of electron and holes, respectively. The majority and minority carrier concentrations for a p-type material are given as

$$n = N_D, \qquad p = \frac{n_i^2}{N_D} \tag{3.2}$$

Similar for an n-type material

$$p = N_A, \qquad n = \frac{n_i^2}{N_A} \tag{3.3}$$

with N_D and N_A to be the concentration of donor and acceptor atoms accordingly. Thereby, the number of minority carriers decreases as the doping level increases.

However, the symmetric equations do not mean that the impact of donors and acceptors into conductivity of silicon is equal, since the mobility of electron and holes is different. In the general case of both charge carriers present in a semiconductor material, its resistivity and conductivity are described with the following expression [Mar03].

$$\rho = \frac{1}{\sigma} = \frac{1}{e(\mu_n n + \mu_p p)} \tag{3.4}$$

where ρ is the resistivity of material, σ its conductivity, e the charge of electron, and μ_n and μ_p mobility of electrons and holes, respectively. The mobility is the parameter indicating how readily carriers may move in the presence of an electric field, which generally defines as

$$\mu = \frac{v_{dr}}{E} = \frac{e\tau}{m^*} \tag{3.5}$$

with v_{dr} to be the drift velocity of carriers, E the electric field intensity, τ the lifetime of charge carriers, and m^* their effective mass, which is different for electrons and holes (electrons are lighter than holes). Furthermore, charge carrier mobility strongly depends on the doping, temperature and operating point of the device (injection level) and may change by an order of magnitude. Increasing the doping in nearly all cases decreases the mobility because additional dopant atoms act as defects, which increase scattering of carriers in the material. In general, the mobility will remain relatively constant until a given doping is reached, and then decrease to another level.

Such a complex interaction between charge carriers cannot be expressed in simple phenomenological expressions and requires computer simulations and development of empirical models for the impact of doping and other parameters. Commonly used empirical solutions are called the Caughey-Thomas expressions and take into account numerous effects and interactions of charge carriers in a semiconductor bulk material [Cau67, Dor81].

3.2. Chemical and electrical properties of phosphorus in silicon

Crystalline silicon for photovoltaic purpose is normally doped with boron for obtaining p-type conductivity and with phosphorus for n-type conductivity. The

characteristic values for segregation coefficient, diffusivity and solubility of boron and phosphorus in liquid silicon are given in Table 2.2. In principal, there are also arsenic and antimony from group V in the periodic table that also can provide n-type conductivity. The choice of phosphorus is conditioned by its high availability, relatively low price and advantageous distribution in silicon. For instance, antimony has a significantly lower segregation coefficient than that for phosphorus ($k_0 = 0.023$ for Sb versus $k_0 = 0.35$ for P [Eng92, Joh12]), thus it is pushed to the very top of mc-Si ingots and its concentration in the main part of silicon material is rather low and unevenly distributed. In contrast to antimony, the segregation coefficient of arsenic is similar to that for phosphorus ($k_0 = 0.30$ for As and $k_0 = 0.35$ for P [Eng92]). However, the usage of arsenic in industrial-scale production is greatly complicated with its toxicity and health hazards.

Although phosphorus has the highest segregation coefficient is silicon among all elements from group V, hence the most uniform distribution along the c-Si ingot's length, it is still somehow lower than that for boron ($k_0 = 0.80$ for B [Eng92]). In addition, as it was already mentioned in the previous chapters, the impact of n-type and p-type dopants have different influence on silicon resistivity due to different mobility of electron and holes. The relationship between resistivity and dopant concentration for the cases of phosphorus- and boron-doped crystalline silicon can be derived from empirical relations [Dor81, Thu80a, Thu80b] and is illustrated in Figure 3.2.

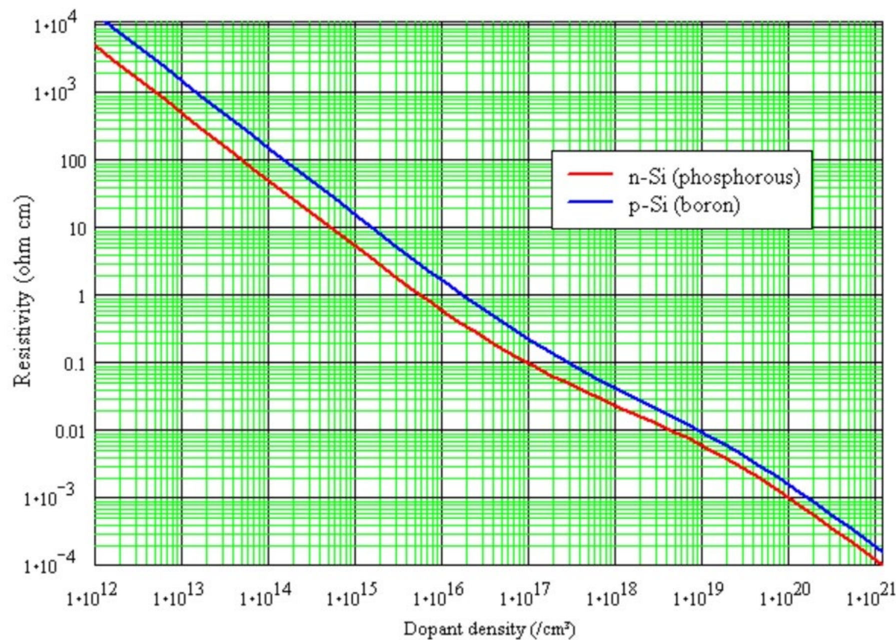

Figure 3.2.: The relationship between resistivity and dopant concentration for crystalline silicon doped with boron and phosphorus [PVE20].

The PV industry standard for mc-Si resistivity is 3.0 – 1.0 Ω·cm. Even though real DS growth is not performed in a closed system, it is possible to evaluate the necessary concentration of dopants in the silicon melt and solidified ingot using the Gulliver-Scheil equation and the empirical relationships between dopant concentration and resistivity. The distribution of resistivity along the height of mc-Si ingot in the cases of boron and phosphorus doping is presented in Figure 3.3. The calculations were done aiming the PV standard resistivity and resulted in necessary dopant concentrations in the silicon melt to be 8.4×10^{15} cm^{-3} and 4.1×10^{15} cm^{-3} for boron and phosphorus, respectively. It can be easily seen that n-type mc-Si ingots doped with phosphorus show significantly broader resistivity distribution than p-type mc-Si ingots doped with boron (3.1 – 0.1 Ω·cm for n-type and 2.0 – 0.9 Ω·cm for p-type). It also has to be mentioned that this level of dopant concentration is significantly lower than solubility limit of phosphorus in silicon melt 1.5×10^{21} cm^{-3}, thus the risk of its precipitation is negligible.

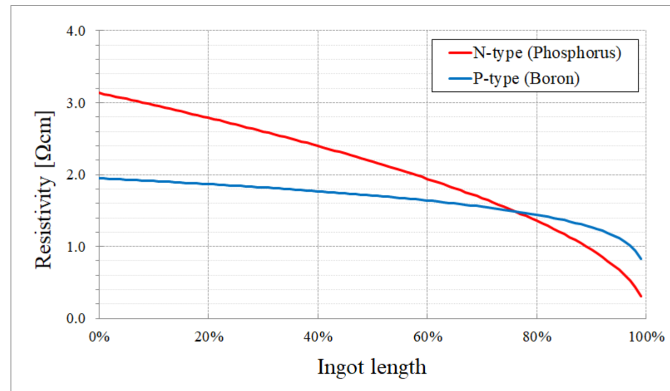

Figure 3.3.: Resistivity distribution along the ingot's length for multicrystalline silicon doped with boron and phosphorus.

In contrast to most intentional dopant elements and impurities in silicon melt, phosphorous has the ability to evaporate intensively from the silicon melt surface even at relatively low temperatures. In principal, any dissolved elements with a vapour pressure higher than silicon can be expected to evaporate. The information about vapour pressure of the solute can be successfully used as a guidance for efficiency of its evaporation [Eng92]. The vapour pressure of pure substances with temperature is given in Figure 3.4. Numerous research works on the removal of phosphorus from the silicon melt under vacuum conditions have been reported by different research groups and proved the efficiency of the process [Zhe10, Zhe11, Saf12, Shi17, Zha17]. Directional solidification of silicon is normally performed not in vacuum but at pressures of about 0.5 bar. However, even in these conditions the evaporation of phosphorus is still noticeable [Jia14, Li18].

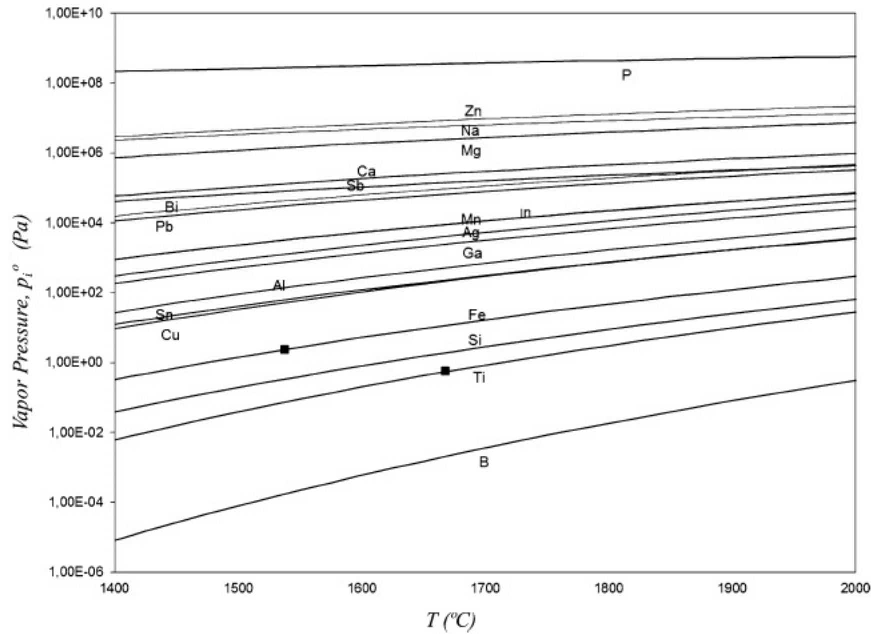

Figure 3.4.: The vapour pressure of pure substances with temperature. Solid symbols indicate melting points [Saf12].

The thermodynamics of phosphorus in molten silicon was particularly described by Miki et al [Mik96]. It was shown that in concentrations typical for PV mc-Si, monatomic phosphorus vapour is dominant in the gas phase, while the component P_2 becomes significant only above 50 ppmw. From Figure 3.4 it can be seen that vapour pressure of silicon at the silicon melting point 1414°C is about 9 order of magnitude higher than that for phosphorus in typical concentrations, thus indicates the ability of phosphorus to evaporate from the silicon melt [Lop12, Saf12].

Thereby, in directional solidification of n-type silicon doped with phosphorus, the effect of solute evaporation must be considered together with solute segregation that makes the classical Gulliver-Scheil inapplicable in the general case.

3.3. Homogenous resistivity distribution

As it was mentioned in previous sections, due to high segregation of phosphorus in silicon, crystallized mc-Si ingots have non-uniform axial dopant profile, and consequently significant discrepancy of resistivity along the ingot's length, which brings additional difficulties for cell manufacturing [Sol15]. Therefore, there is a high need for specific solutions that will help to obtain relatively homogeneous axial resistivity profile along the height of phosphorus-doped silicon ingots.

In classical DS growth the distribution of phosphorus in solidifying ingot can be sufficiently described with the BPS equation (2.16). Since segregation coefficient of phosphorus is less than 1, it is constantly pushed into the liquid phase as the ingot

grows and slowly enriches the melt, which makes its uniform distribution impossible if the growth is performed in a large closed system that experiences constant melt convection. Consequently, this effect can be avoided when performing crystal growth in a half-open system, which implies constant or periodical supply/removal of dopant.

One of the ways to reduce resistivity variation along the ingot's length, which is relatively easy to implement in conventional crystal growth, is compensational doping. This method consists of simultaneous doping of feedstock material with phosphorus and acceptor elements with low segregation coefficient (e.g. Al, Ga), and is widely used while working with silicon feedstock of lower quality [For13]. However, additional doping elements might have a harmful effect on Si-material properties (deterioration of minority carrier lifetime, formation of recombination centers, spot shunting etc.) and are not desirable in crystalline silicon (c-Si) material for high-efficiency solar cells. It is preferable to keep only one doping element (phosphorus) in c-Si material while making its axial distribution, hence resistivity, more homogeneous.

The approach of a half-open system is realized in pioneering research for a continuous Czochralski process (CCz) [Ans93, Fic01]. A uniform dopant distribution is ensured by periodical feeding, where undoped feedstock is added while crystal grows. Since the melt is enriched with dopant while ingot grows, undoped feedstock constantly dilutes it in such a way that the dopant concentration in the melt remains unchanged throughout the whole process. This method is very effective for obtaining monocrystalline ingots with homogeneous quality along the whole height, and by now, it has become a mature technology widely utilized in industry. Recent reports for this technique show impressive results for n-type material both on ingot and cell level [Xu15, Xu16]. However, it also meets some specific difficulties, e.g. problems with material structure (cavities, loss of dislocation-free growth etc.), high oxygen content and higher cost compared to mc-Si.

Nevertheless, similar solutions for mc-Si process are still missing. The approach used in CCz cannot be simply reproduced in DS. On the one hand, during Cz growth the melt experiences significantly higher temperature gradients than those for DS process; hence melt flow dynamics are rather different. On the other hand, continuous doping and feeding for DS require a specific approach for melt homogenization, ensuring of equilibrium conditions and ingot evacuation during the growth. The isolated researches in this direction show that continuous feeding during DS is a sophisticated process that requires major and costly reconstruction of growth equipment and is still on the initial stage of development [Leh16, Kre17].

However, there is another approach for creating a half-open growth system, which might result in uniform dopant distribution, namely removing an excessive dopant from enriched melt by evaporation. Since phosphorus volatilizes above

silicon melt, it might be possible to control dopant concentration by evaporation. This fact is used for purification of highly contaminated silicon by vacuum refining [Wei07, Saf12, Jia14]. It was proved that enhanced melt stirring during vacuum refining could significantly increase evaporation of phosphorus from the melt surface, and thus improve the efficiency of purification [Kar18]. Porrini et al. showed that noticeable evaporation of phosphorus from silicon melt surface is observed during Cz process, and the limiting factor is insufficient dopant transport through the melt to the melt-gas interface, which is defined by the melt convection [Por17].

Nevertheless, so far this method has never been intentionally used in silicon crystal growth for resistivity homogenization. But it is reasonable to expect that controlled evaporation of phosphorus from silicon melt surface during DS might be an effective way to influence resistivity distribution along the ingot's length, and that some process parameters can have a noticeable effect on phosphorus evaporation. In addition, intentional influence on melt convection and impurity transport during crystallization process can alter dopant transport from melt volume to solid-liquid interface and change the effective segregation coefficient of phosphorus, which is an additional instrument for affecting resistivity distribution in n-type mc-Si ingots.

3.4. Phosphorus transfer

3.4.1. Modification of Gulliver-Scheil equation

The Gulliver-Scheil equation assumes that crystallization takes place in a closed system with no additional source of dopants and no mechanisms of extraction of dopants during the process, and that the final concentration profile is the only result of the segregation of elements initially present in the silicon feedstock. In the case of directional solidification of silicon doped with phosphorus, this assumption does not hold, as the phosphorus evaporates from the melt surface and leaves the system. In order to account this effect, a certain modification of for the Gulliver-Scheil equation must be built. Similar modifications were done by different researches for oxygen, calcium, sodium, copper, manganese as well as for phosphorus [Xi07, Dad13a, Jia14, Ren15, Zhe16, Zha17, Li18].

A schematic diagram of phosphorus transport during directional solidification is depicted in Figure 3.5. The evaporation of phosphorus follows first-order kinetics [Saf12, Shi17], which means that the evaporation rate is proportional to its concentration in the melt. The flux of dopants J that is transferred from solid-liquid interface out of the system is given as

$$J = KC_l \tag{3.6}$$

where C_l is the concentration of phosphorus in the silicon melt and K the mass transfer coefficient [Eng92].

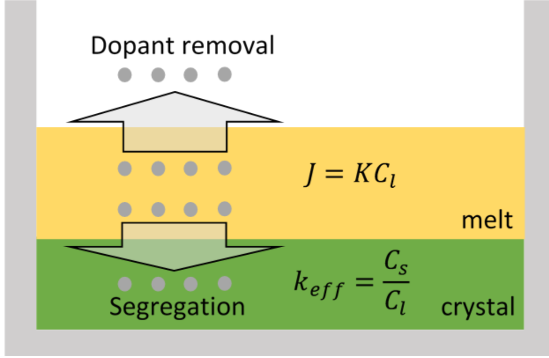

Figure 3.5.: Schematic diagram of phosphorus transport during directional solidification process.

In the absence of evaporation, the solute conservation equation for dopant, which is transferred from the silicon melt to the crystal, can be written as follows

$$(C_l - C_s)dV_s = V_l dC_l \tag{3.7}$$

with C_l and C_s to be the concentration of phosphorus in the melt and in the ingot, respectively, V_l and V_s the volume of liquid and solid silicon, respectively. In the case of phosphorus evaporation, the equation takes the form

$$(C_l - C_s)dV_s - KC_l A dt = V_l dC_l \tag{3.8}$$

where A is the melt surface area. After dividing both parts by V_l and taking into account the relation (2.8) for C_l and C_s, it is transformed to

$$(C_l - k_{eff}C_l)dg_s - \frac{K}{v_{gr}}C_l dg_s = (1 - g_s)dC_l \tag{3.9}$$

where g_s is the fraction of solidified material and v_{gr} the solidification rate. After integrating, the concentrations of phosphorus in the silicon melt and in the ingot can be expressed as follows

$$C_l(g_s) = C_0(1 - g_s)^{k_{eff} + \frac{K}{v_{gr}} - 1} \tag{3.10}$$

$$C_s(g_s) = k_{eff}C_0(1 - g_s)^{k_{eff} + \frac{K}{v_{gr}} - 1} \tag{3.11}$$

with C_0 to be initial phosphorus concentration in the melt before solidification started.

This modified equation can be successfully used for valuation of any volatile dopant distribution in multicrystalline silicon ingots. The nature and properties of evaporation process are described with the mass transfer coefficient K.

3.4.2. Mass transfer coefficient

To understand which parameters have an influence on the mass transfer coefficient it is necessary to consider the mechanisms of phosphorus migration. The main stages of phosphorus transport in the silicon melt during directional solidification are shown in Figure 3.6.

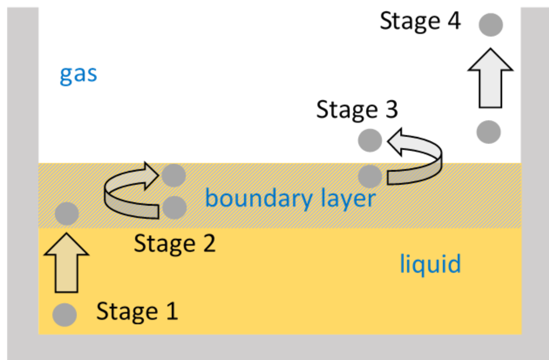

Figure 3.6.: Schematic model of phosphorus removal from the silicon melt during directional solidification process.

The removal of phosphorus can be divided into four stages [Zhe11, Saf12, Jia14]:

1) Mass transport of the dopant from the melt to the boundary layer at the melt surface.
2) Mass transport through the boundary layer at the melt surface.
3) The evaporation of dopant at the melt free surface.
4) Mass transport of the evaporated dopant in the gaseous phase.

This model does not take into account neither back-transport of phosphorus from gas to the melt nor its diffusion into crucible.

Since the removal of phosphorus from molten silicon is a continuous process, the dopant flaxes at each stage must be equal to those in the others. Thus, the total mass transfer coefficient can be presented by:

$$K = \left(\frac{1}{K_m} + \frac{1}{K_s} + \frac{1}{K_e} + \frac{1}{K_g}\right)^{-1} \tag{3.12}$$

where K_m, K_s, K_e, and K_g are mass transfer coefficients for bulk melt, surface boundary layer, evaporation and gas phase, respectively.

Depending on growth conditions and process parameters of directional solidification process, some of these three steps may become the rate-controlling for dopant removal while the others can be neglected, which can be determined by evaluation of the total mass transfer coefficient and the mass transfer coefficients at each step. The process parameters that have an influence on the phosphorus migration in each step will be considered in the following sections.

3.4.3. Transfer in the bulk melt

In classical directional solidification process, the dopant transport in the bulk melt is defined mainly by buoyancy and Marangoni convection. It depends on the velocity of the melt u_{melt} and the pattern of the melt flow. The magnitude of the mass transfer coefficient in the bulk melt K_m can be evaluated for each DS process by numerical simulation, which takes into account the specific melt flow parameters of the system. In case the melt mixing is significant enough to ensure homogeneous distribution of phosphorus across the bulk melt, K_m is not considered to be the rate-controlling step in phosphorous removal. However, when the dopant concentration is not uniform, the mass transfer at this stage has a noticeable influence on the total mass transfer coefficient.

3.4.4. Transfer in the boundary layer at the melt surface

The migration process in the liquid boundary layer in the vicinity of gas-liquid interface is different from that in the bulk melt. The transport of phosphorus in the liquid boundary layer is defined by diffusion and convection mechanisms. The flux of dopants J_m that is transferred through gas-liquid interface is given as

$$J_s = K_m(C_l - C_l^{ms}) \tag{3.13}$$

where C_l and C_l^{ms} are the concentrations of phosphorus in the bulk melt and at the melt surface, respectively.

The kinetic of phosphorus transport in the vicinity of the melt surface can be described by Machlin theory [Mac60], which uses a rigid flow model to characterize the behaviour of the melt in the vicinity of reaction surfaces, and is successfully used for the mass transfer calculations in the vacuum refining of molten metals as well as phosphorus evaporation from silicon melt [Saf12, Zhe10]. According to this theory the mass transfer coefficient through the liquid boundary layer can be written as

$$K_s = \sqrt{\frac{8D_P u_{surf}}{\sqrt{\pi A}}} \tag{3.14}$$

with D_P to be the diffusion coefficient of phosphorus in liquid silicon, u_{surf} the surface velocity of the melt and A the melt surface area. The diffusivity of solute elements is liquids strongly depends on the melt temperature T and can be estimated with the Stock-Einstein equation modified by Engh [Eng92].

$$D_P = \frac{k_B T}{4\pi\eta_{Si} r_P} \sqrt{\frac{M_P + M_{Si}}{2M_P}} \tag{3.15}$$

where k_B is the Boltzmann constant, M_P and M_{Si} the molar masses of phosphorus and silicon, respectively, r_P the atomic radius of phosphorus and η_{Si} the dynamic viscosity of silicon melt, which also depends on the temperature and can be obtained from the following relation [Sat03]

$$\lg \eta_{Si}\,[mPa \cdot s] = -0.727 + \frac{819}{T[K]} \tag{3.16}$$

It can be seen that the mass transfer coefficient depends on temperature, surface melt velocity and the melt surface area. Since in directional solidification the melt surface area is constant and the changes of the surface melt velocity are not significant, the major rate-controlling parameter on this stage of phosphorus transport is temperature, and the mass-transport coefficient increases with the increase of the temperature.

3.4.5. Transfer at the melt surface

The flux of dopants J_e on the stage 2), where the chemical evaporation takes place, is described by Herz-Langmuir-Knudsen equation [Har82, Ozb86]. Using complex derivations from regular solution model for the dilute solutions of silicon binary melts it can be described as

$$J_e = \frac{\alpha(p_P^{s,e} - p_P^s)}{\sqrt{2\pi M_P R T}} \tag{3.17}$$

where R is the ideal gas constant, $p_P^{s,e}$ the equilibrium partial pressure of phosphorus near the melt surface, p_P^s the partial pressure of phosphorus near the melt surface and α the so-called evaporation coefficient that is attributed to the surface

contamination. The value of α is smaller than 1. However, for clean melts, which is the case for PV multicrystalline silicon, it is assumed that $\alpha = 1$.

The mass transfer coefficient of evaporation for this transfer stage can be written as follows [Wan11, Saf12, Shi17]

$$K_e = \frac{\alpha(p_P^{s,e} - p_P^s)}{C_l^{ms}\sqrt{2\pi M_P RT}} \tag{3.18}$$

The parameter $p_P^{s,e}$ is given as

$$p_P^{s,e} = \frac{p_P^0 \gamma_P M_{Si}}{\rho_l^{Si}} C_l^{ms} \tag{3.19}$$

with p_P^0 to be the standard vapour pressure of phosphorus and γ_P the activity coefficient of phosphorus in the silicon melt. Phosphorus in low concentrations, which are typical for PV c-Si, follows Henry's law. Hence, it can be assumed that activity coefficient is equal to Henrian activity coefficient of phosphorus in silicon melt γ_P^0, which is $\gamma_P^0 = 0.4522$ [Saf12]. It has to be kept in mind that the density of liquid silicon ρ_l^{Si} and standard vapour pressure p_P^0 are dependent on the temperature. Different research groups investigated the behaviour of these parameters. Mukai et al. give the empirical relation for density as follows [Muk00]

$$\rho_l^{Si}[kg/m^3] = 2520 - 0.325(T[K] - 1687) \tag{3.20}$$

The standard vapour pressure for phosphorus is normally expressed by Clausius-Clapeyron equation with the following coefficients [Wan11]

$$\lg p_P^0\,[Pa] = 9.965 - \frac{2740}{T[K]} \tag{3.21}$$

Miki et al discovered that in the temperature range 1723-1848 K the equilibrium partial pressure is related to the Gibbs free energy changes of phosphorus evaporation [Mik96]. The changes of Gibbs free energy can be calculated from the empirical relation [Shi17]

$$\Delta G^0[J/mol] = 387000(\pm 2000) - 103(\pm 10)T[K] \tag{3.22}$$

For the reaction that reached thermodynamic equilibrium it can be written as follows

$$\Delta G^0 = -RTln\left(\frac{p_P^{s,e}}{P_0}\frac{1}{\gamma_P X_P^{ms}}\right) = -RTln\left(\frac{p_P^{s,e}}{P_0}\frac{\rho_l^{Si}}{\gamma_P M_P C_l^{ms}}\right) \quad (3.23)$$

where P_0 is the standard atmospheric pressure and X_P^{ms} mass content of phosphorus on the melt surface.

At the same time the partial pressure of phosphorus p_P^s depends on $p_P^{s,e}$ and chamber pressure P [Zhe10]. It is always smaller than equilibrium partial pressure and decreases with the reduction of the chamber pressure; hence, according to (3.18) the mass transfer coefficient increases as the chamber pressure goes down. When the process takes place in vacuum, p_P^s becomes negligible and the evaporation reaches its maximum rate:

$$K_{eMAX} = \frac{\alpha p_P^{s,e}}{C_l^{ms}\sqrt{2\pi M_P RT}} = \frac{\alpha\gamma_P P_0}{\rho_l^{Si}} exp\left(-\frac{\Delta G^0}{RT}\right)\sqrt{\frac{M_P}{2\pi RT}} \quad (3.24)$$

Suchwise, the evaporation mass transfer coefficient as well as the mass transfer coefficient in the melt depends on the temperature and phosphorus concentration at the melt surface, and is also significantly affected by ambient gas pressure.

3.4.6. Transfer in the gas ambient

Mass transfer of the evaporated dopant in the gas ambient is mostly defined by convection mechanisms, since directional solidification process utilizes relatively strong purging gas flow, which makes the gaseous diffusion mass transfer negligible. Therefore, the flux of evaporated phosphorus in the gas phase can be expressed as [Har82]:

$$J_g = \frac{u_{gas} p_P^0}{RT} \quad (3.25)$$

where u_{gas} is the gas velocity above the melt. Similar, the mass transfer coefficient in the gaseous phase will be written as follows

$$K_g = \frac{u_{gas} p_P^0 \gamma_P M_{Si}}{RT\rho_l^{Si}} \quad (3.26)$$

In directional solidification process, the gas ambient consists mainly of argon and its typical flow rate above the melt is in the range of 10-100 l/min depending on the size of the ingot. This means that the process of phosphorus evacuation is rather fast; hence, the dopant transfer in the gas ambient is not the rate-controlling stage

in dopant transport. However, in certain process conditions when the melt experiences strong flow at the surface and the chamber pressure is significantly low, i.e. the evaporation of phosphorus is very intensive, the transfer of dopant in the gas phase might become the limiting factor [Saf12].

Overall, the influence of each mass transfer stage must be separately evaluated for every DS process taking into account specific process conditions. Different combinations of temperature gradients, ambient pressure as well as melt and gas flow are able to shift the rate-controlling step to either one and make the others negligible.

CHAPTER 4

Melt flow control by magnetic fields

4.1. Magnetic fields in crystal growth

Conventional directional solidification process is characterized by significant temperature gradients, which induce melt convection by differences in buoyancy force. With increasing of melt dimensions, temperature gradients also increase. In large DS systems, they can be so significant that the convective flow changes from laminar to time-dependent. This type of flow can easily provoke undesirable fluctuations at the solid-liquid interface that lead to local disturbances in dopant distribution, precipitation of impurities and changing of interface shape, hence generation of dislocations. Therefore, the control of melt convection plays a crucial role in the optimization of silicon crystal growth. The use of external force fields during crystal growth is an effective way to perform this control.

The application of external force fields generally pursues three goals [Viz15, Fra20]. The first one is to control the shape and morphology of solid-liquid interface. The second goal is the damping of undesirable fluctuations and turbulence in melt convection i.e. like in a Cz-configuration. And the third goal is the improvement of melt mixing to ensure homogeneous distribution of dopants in the melt and to avoid constitution supercooling. The method for generation of the force fields has to fulfil the main requirements for crystal quality. Namely, to withstand high temperatures, to keep the impermeability of the growing furnace, and to ensure the high purity of the grown crystal. A comprehensive overview of bulk crystal growth under the influence of external force fields in the context of different techniques and approaches has been done by Rudolph and Kakimoto [Rud09]. The methods widely

used in bulk crystal growth can be divided into three categories: mechanical, electrical and magnetic force fields.

Mechanical methods for controlled melt stirring include the variety of different approaches, such as rotation of the crucible and/or crystal, periodically reversed or accelerated rotation of the crucible, and vibrations, either low range ones applied to the crucible or high range ones induced by submerged transducer. The main advantage of mechanically induced stirring is that these methods can be applied to any type of melts regardless their magnetic and electrical properties. However, the scale-up of these methods for large square melts meets significant challenges and has not been performed yet.

The properties of most molten semiconductors is similar to liquid metals. In particular, their electrical conductivity is in the range of liquid metals [Bus13]. An electrically conductive melt, which moves within a magnetic field, is exposed to Lorentz forces. Therefore, the application of magnetic fields has been proved an effective tool for influencing the melt flow in semiconductor melts. There are two principally different approaches for application of magnetic fields: steady magnetic fields and nonsteady magnetic fields.

Steady magnetic fields

Steady magnetic fields create no movement in a static melt. They only have an influence on existing melt flow generated by other forces, such as buoyancy or Marangoni. The acting Lorentz force in this case is directed in the opposite direction to the movement of the melt, which results in artificial enhancement of the effective melt viscosity, hence in dumping the melt convection. It was demonstrated that steady magnetic field could be successfully used to terminate the convective turbulence in the melt and thereby to improve the microscopic homogeneity of the dopant distribution in the crystal [Che66, Kim82]. There are three different types of steady magnetic fields widely used in bulk crystal growth of semiconductor materials – vertical magnetic field (VMF), horizontal magnetic field (HMF), and cusp-shaped magnetic field (CMF) [Frie07, Rud09, Viz15]. The latter is generated by two magnetic coils with opposite currents.

Although steady magnetic fields are successfully used in Czochralski crystal growth to obtain low-oxygen ingots [Amm05], their application to directional solidification technique is less interesting since multicrystalline material of high quality implies enhancement of melt convection rather than dumping. Additional difficulty in working with steady magnetic fields is that the necessary intensity for this type of fields lies in the range of 200-500 mT, which requires fairly large and strong magnets.

Nonsteady magnetic fields

In contrast to steady magnetic fields, nonsteady ones induce the movement of the melt themselves by creating potential differences and thus eddy-currents in an electrically conductive melt according to Faraday's law of induction. The melt flow is dependent on distribution of Lorentz forces, which are defined by the product of the eddy-current density and the external magnetic field. Thus, unsteady magnetic fields are able not only to dump the natural convection but also to induce and intensify the desired melt motion, therefore to provide a permanent control of the melt flow. The controlled enhancement of the melt motion can be successfully used for improving the melt mixing and stabilisation of heat and mass transport as well as for sophisticated modification of the shape of the solid-liquid interface and the segregation of dopants [Frie07, Viz15]. In comparison to steady magnetic fields, nonsteady ones require significantly lower magnetic flux densities to neutralize natural convection. However, their penetration depth is limited.

The most popular types of nonsteady magnetic fields used in semiconductor bulk growth are alternating (AMF), rotating (RMF) and travelling magnetic fields (TMF). They are defined by the geometry of the inductor and the phase shift. The arrangement of the electro-magnetic coils for the generation of different types of nonsteady magnetic fields is depicted in Figure 4.1.

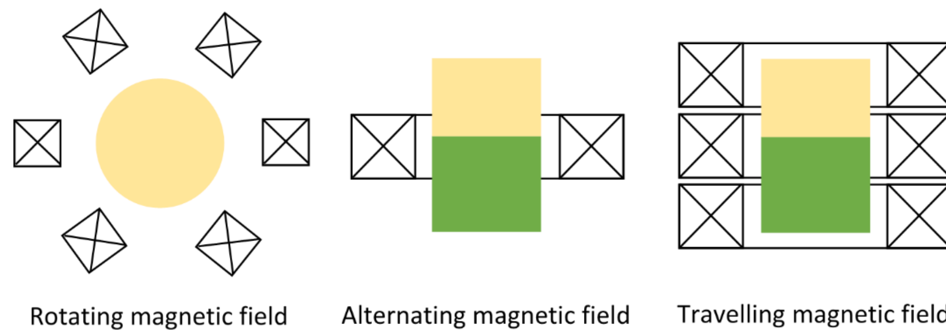

Figure 4.1.: The arrangement of the electro-magnetic coils for the generation of different types of nonsteady magnetic fields.

Rotating magnetic field

Rotating magnetic field is generated by three azimuthally displaced coil pairs with a phase shift of 120°. In such a way, a rotating transversal magnetic field with a determined angular frequency is created in the horizontal plane. RMF induces an azimuthal Lorentz force, which creates a primary azimuthal flow. There is also a secondary meridional flow, which arises due to the imbalance of the centrifugal force and the radial pressure gradient in the boundary layers at the top and bottom

surfaces. The meridian flow consists of two toroidal parts and is one order of magnitude smaller than the primary azimuthal flow [Frie07, Viz15].

The meridional flow is used to influence the shape of the solid-liquid interface by decreasing its curvature or even creating a w-shape [Dol97]. Furthermore, the combination of azimuthal flow and meridional flows helps to reduce temperature fluctuations in the melt and to improve mass transport [Fis99].

Alternating magnetic field

An alternating magnetic field is generated by one or several electro-magnetic coils vertically arranged around the crucible containing melt. The coils are simultaneously fed by an alternating current with no phase shift. The generated Lorentz forces are directed perpendicular to the side surface and result in flow pattern consisting of two tori [Rud09, Viz15].

It was shown that application of AMF during Vertical Bridgeman growth can enhance the melt mixing and stabilize the radial segregation profile along the ingot's length [Mit06]. In addition, several studies prove that AMF is able to keep the deflection of the solid-liquid interface at reasonably constant values [Ste04, Mit06].

Travelling magnetic field

The traveling magnetic field system consists of several electro-magnetic coils, which are arranged vertically one over the other at the side of the melt, or e.g. as spirals for bottom and top heaters. The coils are fed by an alternating electric current with certain amplitude, frequency and phase shift. The resulting magnetic field introduces an upward or downward travelling Lorentz force in the melt, which results in a toroidal flow pattern. The detailed description of TMF influence on the semiconductor melt is given in the following sections.

4.2. Travelling magnetic fields

Travelling magnetic fields already proved to be a promising option for providing a melt flow control during directional solidification. In comparison to other types of nonsteady magnetic fields, it has a number of advantages, such as relatively low flux densities achievable without ferromagnetic cores, simultaneous generation by furnace heaters, flexible flow directions, a negligible heat generation and relatively large penetration depth [Dad12, Fra20].

The flow of silicon melt under the influence of TMF is defined by superposition of the Lorentz force field and buoyancy forces. Since the shape of the growth front is defined by the varying heat fluxes in the melt, travelling magnetic fields may

have a significant influence on the shape of the solid-liquid interface. The Lorentz force field creates an axisymmetric meridional flow, which, depending on its parameters, can accelerate or diminish the natural convective flow near the solid-liquid interface.

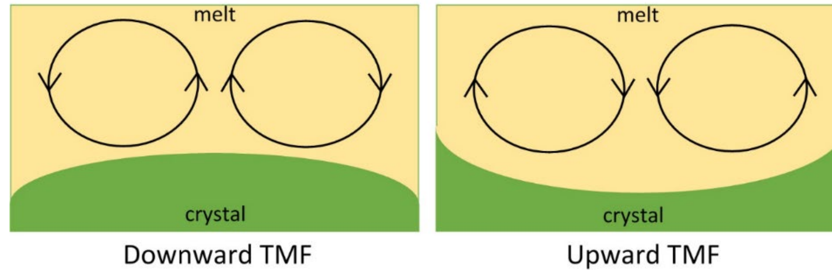

Figure 4.2.: The shape of solid-liquid interface and flow patterns for directional solidification under the influence of TMF with various orientations.

When the strength of magnetic field increases and the Lorentz force exceeds the buoyancy force, the natural convection couples with the meridional single vortex flow induced by the TMF [Nie11]. The flow induced by magnetic field transports liquid at high temperature from the top of the bulk melt towards the liquid-solid interface and thus decreases the temperature gradient inside the melt. Once the high temperature liquid reaches the interface, it provokes a partial remelting of the solid. Depending on the flow patterns, the hot liquid can be brought to the solid-liquid interface either in the centre of the ingot (upward TMF) or near the crucible walls (downward TMF) (Figure 4.2.) In such a way, the flow patterns in the melt influence the shape of solid-liquid interface [Dro12]. If in the absence of external force fields the solid-liquid interface of the ingot is perfectly flat, then upward TMF results in a concave interface, while downward TMF leads to a convex one. However, in the real DS systems the temperature of the crucible walls near the solid-liquid interface is somehow lower than that in the centre of the bulk melt at the same height, which causes the natural concave shape of the solid-liquid interface. Therefore, in real melts an upward TMF noticeably increases both the deflection of the interface and the thermal stresses, while downward TMF decreases thermal stresses and makes the interface flatter [Sch04].

By influencing the shape of the solid-liquid interface travelling magnetic fields also affect dopant segregation. With a flattened interface by downward TMF, radial dopant segregation decreases too [Lyu04]. Numerical studies also show that the direction of the melt flow in the vicinity of the solid-liquid interface has a large influence on radial segregation [Gra08]. In the case of solely natural convection, the radial thermal gradients over a concave interface provoke the melt flows from the periphery that meet in the centre of the interface and create a solute concentration peak along the crystal vertical axis [Pri07]. The downward TMF can potentially

intensify this effect, while the upward one can reverse the flow along the solid-liquid interface and remove the concentration peak.

On the other hand, too strong TMF can also disturb the growth of the crystal. If the Lorentz forces overgrow a critical value, intensive convection can lead to significant temperature fields in the melt and thus asymmetries in the melt flow. Numerical modelling shows that these instabilities occur when the dimensionless TMF forcing parameter exceeds the ratio value of the buoyancy to viscous force in the melt [Gra09, Dad13b]. In this case, the melt flow changes from laminar to unsteady, the flow velocities oscillate, the crystal growth is disturbed, and thus the crystallised material acquires numerous striations and dislocations.

Several research groups report promising results about effectiveness of travelling magnetic field applied to directionally solidified silicon in rectangular crucibles. Numerical simulations for mc-Si of Gen4 size show that it is possible to obtain various flow pattern depending on the direction and strength of TMF, which can both dump and enhance the melt mixing during the crystal growth [Dro10, Dro12, Dad13a, Viz13]. Excellent results about the utilization of double-frequency TMF have been obtained through numerical simulation [Dro11]. This novel approach is performed by application of a summary magnetic field composed of two oppositely directed TMF with different strength, frequencies and phase shifts. Such a combination generates various penetration depth and horizontal velocity profiles for each component. It was demonstrated that compared to a single-frequency TMF, a double-frequency TMF creates a more intensive flow in the bulk melt and a weak flow in the periphery, which prevents crucible walls and coating from dissolution and destruction. In principal, a double-frequency TMF enables shifting the maximum of the Lorentz force into an arbitrary position in the melt.

The experimental work for directionally solidified mc-Si also show a positive effect of TMF on crystal quality [Kie11a, Kie11b, Kie12a]. It was demonstrated that TMF can be used to influence the melt convection and adjust the shape of the solid-liquid interface, and it is assumed to reduce the thickness of the diffusion boundary. A downward TMF allows obtaining a convex interface, and the optimized conditions of magnetic field enable growing of Gen1 size ingots free of SiC and Si_3N_4 inclusions. Similar results were reported for a Gen5 multicrystalline silicon ingot grown under the influence of TMF in a large industrial-scale furnace [Kud13]. Effective melt mixing and careful control of the interface shape performed by TMF resulted in multicrystalline material of high quality without any undesired inclusions throughout almost the whole volume of the ingot.

4.3. Fundamentals of travelling magnetic fields

For derivations of the main relations between parameters of travelling magnetic field influencing the silicon melt during directional solidification, it is needed to consider the principal arrangement of TMF coil system. Figure 4.3. depicts the geometry of the vertically arranged electro-magnetic coils which induce the travelling magnetic field. The system consists of three identical coils, each of them has an even number of windings N, the average radius R, and the distance between the coils is d. When the coils are fed with alternating current having a phase shift ϕ between neighbouring coils, they induce an upward or downward Lorentz force field. The phase shift defines the direction of current flowing through each coil, and hence the direction of the travelling Lorentz field.

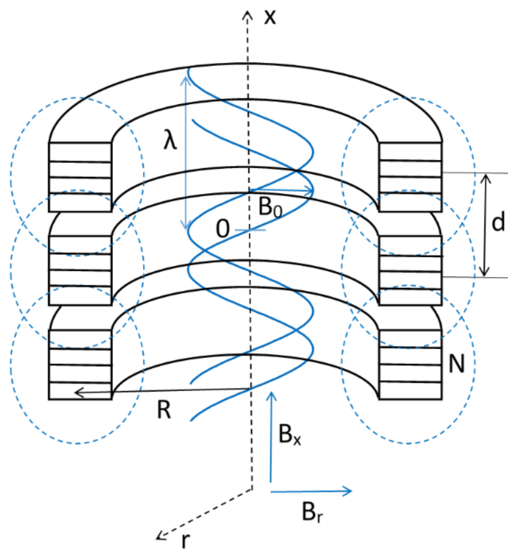

Figure 4.3.: Sketch of a TMF coil system with three axially arranged coils.

The axisymmetric travelling magnetic field $\vec{B}$ induced in the coil can be described as a continuous travelling wave. Owing to radial symmetry of the system, it is convenient to express the wave in cylindrical coordinates (r, φ, x) using a radial and an axial component with a phase shift $\pi/2$ [Dad12]:

$$\vec{B} = B_x \cdot \vec{e}_x + B_r \cdot \vec{e}_r \tag{4.1}$$

$$\vec{B} = B_x \cdot \left(\sin(\omega t - kx) \cdot \vec{e}_x + \frac{rk}{2} \cos(\omega t - kx) \cdot \vec{e}_r \right) \tag{4.2}$$

where B_0 is the amplitude of magnetic induction, ω the angular frequency, and k the wave number. The wavelength λ of the TMF can be written as follows

$$\lambda = \frac{2\pi d}{\phi} = \frac{2\pi}{k} \tag{4.3}$$

The amplitude B_0 defines the strength of the travelling magnetic field and can be expressed with geometrical characteristics of the coil system by superpositioning the components of magnetic induction $\vec{B}$ for each coil along the x axis [Gla14]:

$$B(x, r = 0) = B_x(x) = \left| \sum_{n=1}^{3} B\big(x + d(n-2)\big) e^{i(n-1)\phi} \right| \tag{4.4}$$

$$B(x, r = 0) = \left| B(x - d) + B(x) \cdot e^{i\phi} + B(x + d) \cdot e^{2i\phi} \right| \tag{4.5}$$

The magnitude of the magnetic field strength for a current-carrying circular coil system can be expressed with the Biot-Savart law on the symmetry axis perpendicular to the closed inductor loop [Lan07b]. The total field of the coil consisting of N windings located close to each other is the sum of the fields created by each winding:

$$B(x) = N \cdot I \cdot \frac{\mu_0}{2} \cdot \frac{R^2}{(R^2 + x^2)^{3/2}} \tag{4.6}$$

where I is the electric current and μ_0 the magnetic constant. Using equations (4.5) and (4.6) one can define the amplitude of travelling magnetic field created in the centre of the coil system:

$$B_0 = B(x = 0) = N \cdot I \cdot \frac{\mu_0}{2R} \cdot \left| \frac{R^3}{(R^2 + d^2)^{3/2}} + e^{i\phi} + \frac{R^3}{(R^2 + d^2)^{3/2}} \cdot e^{2i\phi} \right| \tag{4.7}$$

If a nonsteady magnetic field is applied to the melt with a relatively high electrical conductivity, it provokes the opposing eddy currents in the melt, which leads to the exponential diminishing of the applied field within the near-crucible melt area [Viz15]. This is a well-known skin effect that is characterised with δ_{TMF}, the penetration depth of the magnetic field into the melt:

$$\delta_{TMF} = \sqrt{\frac{2}{\mu_0 \mu_r \sigma \omega}} \tag{4.8}$$

where σ and μ_r are the conductivity and the relative magnetic permeability of the melt, respectively. If the penetration depth is significantly larger than the characteristic size of the melt, the magnetic field penetrates into the melt volume

without any alterations. In the case when the penetration depth is much smaller than the size of the melt, the magnetic field penetrates only into the limited volume of the melt near the crucible walls, because the field quickly diminishes due to the high conductivity of the melt. As it can be seen from the equation (4.8), the penetration depth increases with decreasing the frequency. Thus, high-frequency magnetic fields induce the Lorenz forces in the vicinity of crucible walls, while low-frequency fields penetrate into the bulk melt.

In order to derive analytical relations for the Lorentz fields induced by TMF, it is reasonable to employ Grants and Gerbeth model [Gra04]. The model implies the following assumptions. The wavelength of the travelling magnetic field is normally significantly larger than the typical dimensions of the melt. Hence, the induced currents in the melt can be neglected assuming that the TMF frequencies are rather low. Therefore, the penetration depth of TMF in this case is supposed to be relatively large. In addition, the velocity of the travelling magnetic field is supposed to be much larger than the velocity of the melt flow.

According to the Faraday's law of induction, a time-dependent magnetic field induces an electric field $\vec{E}$.

$$\vec{\nabla} \times \vec{\mathrm{E}} = -\frac{\partial \vec{\mathrm{B}}}{\partial t} \tag{4.9}$$

In cylindrical coordinates for the considered coil system, the electric field is characterized only by the azimuthal component:

$$\vec{\mathrm{E}} = E \cdot \vec{\mathrm{e}}_{\varphi} \tag{4.10}$$

The induced electric field creates an electrical current in the melt according to the Ohm's law. The current density $\vec{j}$ is also described only by the azimuthal component [Lan07b]:

$$\vec{\mathrm{j}} = \sigma_{melt} \vec{\mathrm{E}} = B_0 \frac{r\omega\sigma}{2} \cos(\omega t - kx) \cdot \vec{e}_{\varphi} \tag{4.11}$$

Each element of the melt volume experiences the Lorentz force with a force density field $\vec{F}_L$ given as

$$\vec{\mathrm{F}}_L = \vec{\mathrm{j}} \times \vec{\mathrm{B}} \tag{4.12}$$

Lorentz force density generated by the induced current can be derived from the equations (4.1) and (4.11) [Gla14] as

$$\vec{\mathrm{F}}_L = \begin{pmatrix} B_0^2 \cdot \frac{r\omega\sigma}{2} \cdot \cos(\omega t - kx) \cdot \sin(\omega t - kx) \\ 0 \\ B_0^2 \cdot \frac{r\omega\sigma}{2} \cdot \cos^2(\omega t - kx) \end{pmatrix} \tag{4.13}$$

The integrating of the obtained expression over the oscillation period gives the final relation for the Lorentz force density induced by the travelling magnetic field, which appears to have only the axial component [Lan07b].

$$\vec{\mathrm{F}}_L = F_{L\,x} \cdot \vec{\mathrm{e}}_x = B_0^2 \cdot \frac{r^2\omega\sigma k}{8} \cdot \vec{\mathrm{e}}_x \tag{4.14}$$

The direction of the Lorentz force induced by TMF is defined by the phase shift. The example for upward and downward direction near the crucible walls is given in Figure 4.2. In small crucibles with symmetrical boundary conditions, the force field induces two axisymmetric meridional vortices. In the case of large melts with small asymmetries, the vortices change their shape to the toroidal one.

The strength of the Lorentz force decreases exponentially in radial direction from the crucible walls towards the melt centre and can be written as following [Dro11]:

$$F_L = F_L^{max} \cdot exp\left({}^{-x}/_{\delta_{TMF}} \right) \tag{4.15}$$

The force value is dependent on the frequency of the travelling magnetic field as well as on its amplitude value. It is also more convenient to describe it with the amplitude value of the electric current flowing through the coil system, rather than the magnetic induction:

$$F_L \sim B_0^2 \cdot \omega \sim I_0^2 \cdot \omega \tag{4.16}$$

Thereby, there are three parameters of travelling magnetic field that have the most significant influence on the acting Lorentz forces – the amplitude of the alternating current, the frequency of TMF and the phase shift between the neighbouring coils. The alternating current amplitude changes the magnitude of the Lorentz force, while the phase shift is able to change not only the strength but also the direction of the force field. However, TMF frequency has the most complex influence on its characteristics, as it affects the magnitude and the direction of Lorentz forces, the penetration depth and the spatial distribution of the field. Therefore, the magnetic field frequency has the biggest potential for changing the melt convection [Viz13, Gla14, Yu18].

CHAPTER 5

Equipment and methodology

5.1. KRIST*MAG*® technology

Directional solidification of mc-Si is normally realised in standard growth equipment showed in Figure 2.2. In order to utilize travelling magnetic fields for this type of furnaces it is needed to install external electro-magnetic coils outside the growth chamber (Figure 5.1a.) However, such an approach is ineffective for generation of required Lorentz force density in the melt. The distance between the coils and the melt is relatively large [Fra20]. Furthermore, there side heaters, insulation and chamber walls located between the melt and the coil weaken the effect of the magnetic field. Taking into account the large distance and the skin effect, the generated magnetic field has to be rather strong to cover all the losses in the system. According to rough evaluation only about 10% of the original flow density reaches the melt, and the rest is dissipated [Rud08]. Therefore, the utilisation of travelling magnetic fields in such a configuration is energy consuming and expensive, hence the approach must be improved.

One of the most promising way to improve the configuration of TMF for crystal growth pullers is the adjustment of heaters. The first ones to propose the combination of heater and electro-magnetic coil were Fujimori and Ayusawa in the patent of 1970 [Fuj70]. They described a vertical meander-type heater fed by a three-phase alternating current. Three delta-connected heater segments were situated around the melt and simultaneously supplied heat and RMF through the phase shift between the heater segments.

In 2003 Mühe et al. patented a heater-magnet setup, which was based on the same principal and combined the generation of heat and travelling magnetic field at a time [Mue03]. The heater consisted of three coupled vertically stacked graphite coils and was fed simultaneously with a direct and alternating current. Both are responsible for supplying heat, while only the latter for magnetic field. A three-phase alternating current with a phase shift of 120° created a longitudinal TMF. The described setup allowed efficient utilization of generated magnetic flow density. However, such an arrangement also had some disadvantages. Namely, the phase shift between three coils was fixed and could not be chosen freely. Furthermore, the coils were coupled, which made it impossible to adjust the power of each heater independently and to create the necessary vertical temperature gradients in the melt. Thus, the utilization of this configuration for directional solidification of high quality multicrystalline silicon was complicated.

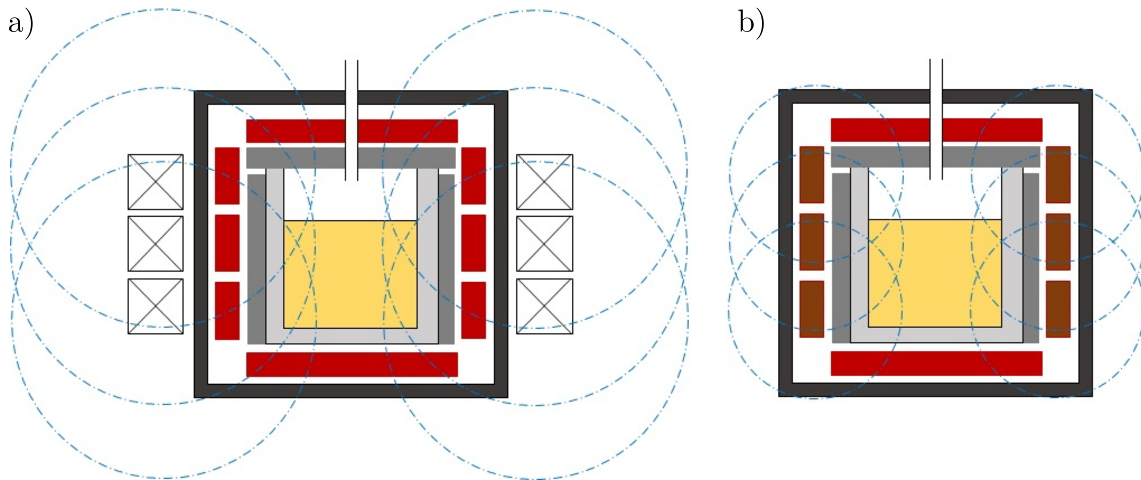

Figure 5.1.: a) Conventional DS furnace with additional external coils for TMF generation; b) DS furnace equipped with KRIST*MAG*® heater-magnet module.

The concept of combined heater-magnet approach was further developed in KRIST*MAG*® technology [Rud08]. Numerous improvements described in many patents [Zie07, Lan07a, Fra07, Bue08, Lan12d] resulted in the development of the so-called heater-magnet module. The principal arrangement of a DS furnace equipped with the heater-magnet module compared to a conventional one with external electro-magnetic coils is given in Figure 5.1. This module can be effectively used to upgrade the conventional Cz, VGF and DS growth equipment for utilizing together with travelling magnetic field. The heater-magnet module is supplied with a unique power unit and control system containing an integrated intelligent power system SKiiP. It enables the feeding of graphite coils with a direct and alternating current independently from one another, so that the heat and travelling magnetic field are generated simultaneously. The configuration of additional resistive heaters

is remained unchanged. The phase shift of the alternating current between the coils is not fixed and can be set individually, as well as current amplitude and frequency. The direct current through each coil can be controlled independently, which allows adjusting the desired temperature gradients in the system at every stage of the growth process. The DC-coupled steady magnetic fields generated in three coils are weak and can be neglected.

An additional advantage of the KRIST*MAG*® heater-magnet module is the possibility of using a two-component TMF [Dro11]. The approach is realized through superposition of two alternating currents with different frequencies. Each one can have its own phase shift and amplitude. Owning to a different skin depth, which depends on frequency, the lower frequency TMF can penetrate deeper inside the melt than the higher frequency one. Therefore, the former induces the Lorentz force in the whole melt, while the latter is concentrated mainly at the crucible walls. The resulting force acting in the melt is the sum of both forces. With careful adjustment of parameters for both magnetic fields, it is possible to achieve optimal melt flow conditions for ensuring a preferable shape of the solid-liquid interface while preserving the integrity and stability of crucible coating.

Thereby, the KRIST*MAG*® heater-magnet module has several advantages when compared to conventional growth configurations with external coils and previously developed combined heater-magnet modules. The generation of heat and travelling magnetic field is energy efficient and is realised in such a way that thermal and convective configuration of the system can be optimized separately without sacrificing either of them. A large space for altering many variable parameters of magnetic field enables developing the ideal conditions for convection control. In addition, the heater-magnet module is able to provide two-component TMF consisting of two alternating currents with different phase shifts, frequencies and amplitudes.

5.2. DS furnace with KRIST*MAG*® heater-magnet module

The DS furnace used for experiments in this work is equipped KRIST*MAG*® heater-magnet module. The picture and the layout of the furnace is given in Figure 5.2. The DS configuration of the KRIST*MAG*® heater-magnet module and its utilization for ingot growth is described in the patent of Kiessling et al. [Kie12b]. The module consists of three vertically stacked rectangular coils connected around the perimeter. Each coil has an integer number of spirally arranged windings. All the geometric parameters of the coils are optimally adjusted to the furnace hot zone.

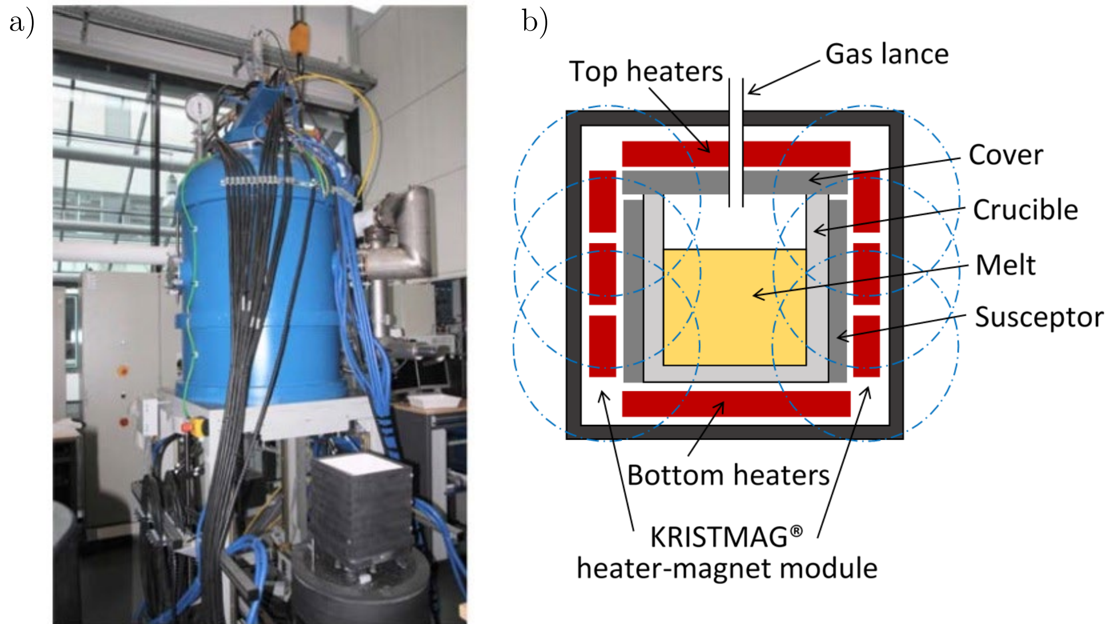

Figure 5.2.: a) Image of KRIST*MAG*® G1 size DS furnace; b) Layout of KRIST*MAG*® DS setup.

The furnace is designed for growing of multicrystalline silicon ingots of G1 size. The heater-magnet module consists of three rectangular side-heaters that produce heat and TMF at the same time. The module is able to create the magnetic fields with effective currents up to I=130 A and frequencies in the range of f=10-600 Hz. The phase shit can be changed in the range of ϕ=0-360°. All parameters in every heater can be set independently from another, which enables a broad range of adjustments for different process conditions, including the utilisation of two-component TMF with different frequencies, amplitudes and phase shifts. Additionally, the hot zone is equipped with resistive heaters, three at the top and three at the bottom, which are used exclusively for heating. All nine heaters are made of graphite and operate independently for the effective control of temperature gradients and power input. The insulation material between the heaters and the furnace chamber are made of graphite, carbon fibre and graphite felt, which are optimized for the growth temperature above 1414 ˚C.

Twelve thermocouples are situated inside the furnace at fixed positions (one at each of nine heaters, one directly under the crucible, and two at the sides) and are used for control and observation of the process as well as for security reasons. The furnace is also equipped with a pyrometer focused at the melt surface, which is used only for indicating the transition between the liquid and the solid states of silicon.

The furnace utilizes argon as the working gas and is equipped with pressure controllers for pressure ramping or keeping it at a desired value. The working pressure can be set in the range of to P=2-1100 mbar. A thin lance made of inert ceramic material is used for the inlet argon flow during the growth process and is

located in the centre of the hot zone directly above the melt. The flow rate can be kept constant during the whole process as well as changed in the desired manner.

A crucible with silicon feedstock is loaded into the furnace from the bottom. A sectional graphite susceptor is tightly placed around the crucible to prevent its deformation and provide additional mechanical support. A silicon carbide cover is placed on the top of the susceptor-crucible setup in order to avoid contamination of the melt with impurities from surrounding environment. The cover contains two holes. One hole is located in the centre serves as a viewing port for a pyrometer. The second one is situated at a distance of 2 cm from the centre and is designed specifically for a gas-inlet lance. The gas outlet is performed through the square openings at the rim of the cover.

The growth process is operated by a control software. A preliminarily developed recipe with respective heater powers, ambient pressure, purging gas flow and TMF parameters for each growing step are loaded into the control software before the process. During growth, all process parameters are set and changed automatically to the desired values. However, the manual control over the process can be taken at any time.

5.3. Supporting numerical modelling

In order to analyse the results obtained in growth experiments and to develop the optimal parameters of travelling magnetic field that enable the desired melt convection and solute transport, a number of numerical models for different system and process configurations were made.

The modelling focused on the development of TMF parameters for variable melt convection were conducted by Dr. Natascha Dropka from IKZ Berlin. Quasi steady-state axisymmetric simulations and transient 3D simulations were performed using the commercial software CrysMAS and ANSYS Workbench, respectively, for various magnetic parameters (frequencies, phase shifts and current magnitudes). The transport phenomena occurring during directional solidification in the presence of TMF were calculated by using the equations of continuity, Navier Stokes with the Boussinesq approximation, energy balance and Faraday's law of induction together with the Ohms law [Viz15]. The Lorentz force density of the double-frequency TMF was obtained using superposition principle, i.e. superposition of Lorentz forces densities corresponding to single-frequency TMFs. In all simulations, a stepwise methodology was applied.

In case of 2D simulations, first, a temperature field with a fixed solid-liquid interface was simulated, while neglecting melt convection; in the second step, the buoyancy driven melt flow with an interface tracking was modelled; finally, magnetically driven flow was simulated also with the interface tracking. In case of

3D simulations, the results of global thermal and flow analyses provided boundary conditions for the local simulation of the melt flow. Radiative heat transfer in the furnace was described by the discrete transfer radiation method. Effects of turbulence were taken into account by using the of $k\omega$ SST model. Buoyancy driven flow was used as an initiation for magnetic driven flows and as a benchmark for comparison.

The modelling focused on the analysis of dopant distribution obtained in growth experiments were conducted by Dr. Kaspars Dadzis from IKZ Berlin. The 3D Lorentz force distribution in the melt generated by the TMF was calculated by finite-element GetDP module with the use of time-harmonic A-V formulation. The coupled problem of melt flow, crystallization interface motion, and dopant transport including segregation was simulated with an unsteady 3D solver in finite-volume package OpenFOAM. The crystallization motion was modelled according to heat balance.

5.4. Characterization methods

Multicrystalline material grown within this research work was characterized with respect to its electronic, physical and structural properties. The measurements were performed by various methods described below.

5.4.1. Four-point probe (FPP) method

One of the most important parameters to be analysed in this research work is resistivity, since resistivity distribution in n-type phosphorus-doped ingots is the focus of this thesis. The electrical resistivity ρ for all ingots was measured on grinded longitudinal cuts using the four-point probe (FPP) method. This is a simple technique widely used in characterisation of semiconductor materials [Sch06].

The measurement device is depicted in Figure 5.3. It consists of four probes located on one straight line at the same distance d_p one from another. An electrical current I passes between the outer probes and through the sample surface due to their low resistance. The inner probes have a comparatively high resistance and therefore are used to measure the voltage U between the outer probes. The magnitude of current is constant and controlled by the power source, while the measured voltage changes depending on the resistivity of the sample. Thus, the resistivity can be determined according to the Ohm's law

$$\rho = \frac{2\pi d_p U}{I} \tag{5.1}$$

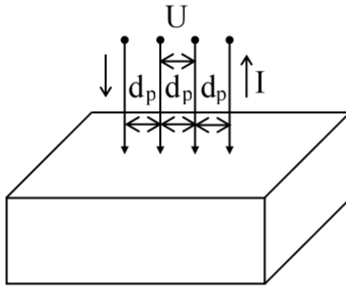

Figure 5.3.: Sketch of four-point probe setup.

It has to be kept in mind that silicon material that has relatively high concentration of oxygen is prone to contain oxygen precipitates. These are oxygen compounds of various nature and properties. Some of these precipitates are called thermal donors, since they are electrically active and contribute addition electrons into silicon conduction band, thus distort original resistivity of silicon samples. Nevertheless, electrically active thermal donors can be easily destroyed in the temperature range 300-550°C [Wru79]. The technology of solar cells manufacturing contain certain steps under temperatures up to 900°C. Hence, thermal donors are destroyed during production of solar cells and do not affect the performance of the devices. However, the accurate resistivity measurement of silicon samples requires the absence of thermal donors.

Despite the fact that directional solidification provides relatively low oxygen concentration in silicon ingots and thermal donors are normally not observed in multicrystalline silicon, for the sake of accuracy all silicon samples were exposed to low-temperature annealing prior resistivity measurements in order to destroy possibly existing thermal donors. The procedure was carried out in a clean muffle furnace for 1 hour at 800°C with rapid cooling down to room temperature afterwards.

After FPP measurements, resistivity for selected samples was additionally measured by eddy-current method [Hag90]. The data obtained by both methods were identical within a measurement error, which confirms that the applied FPP method provides reliable resistivity results for mc-Si material.

Since phosphorus concentration in experimental ingots is significantly lower than solubility limit, the measured resistivity data can be successfully used for determination of dopant concentration by applying standardized relations for semiconductor silicon [Thu81]. In order to verify the applicability and accuracy of the described procedure for investigated mc-Si material, 5 selected samples were examined by Hall method [Pau58]. The obtained data confirmed that the mobility of charge carriers in mc-Si samples corresponds to the one used in standardized relations within a measurement error. Hence, the phosphorus concentration derived from resistivity data can be considered reliable.

It has to be mentioned that derivation of dopant concentration of such a low magnitude from resistivity is much more accurate that any methods of analytical

chemistry. The reason lies in low errors of measurement for FPP method compared to analytical ones and certain difficulties for sample preparation for the latter.

5.4.2. Microwave-detected photoconductivity (MDP)

The minority carrier lifetime of semiconductor material is the average time, which a carrier can spend in an excited state after electron-hole generation before it recombines. This is one of the most important characteristic parameters for PV crystalline silicon. It is defined by recombination rate of charge carriers, which in turn depends on their concentration [Pie96]. In general, the lifetime is a very complex parameter since it takes into account different mechanisms and types of recombination, and it is difficult to distinguish them one from another. However, the lifetime of crystalline silicon material is an indicator of the efficiency of a solar cell produced from this material. Therefore, it is highly important to investigate the grown ingots with regard to the minority carrier lifetime.

The mapping of minority carrier lifetime τ for all ingots was performed on grinded nonpassivated longitudinal cuts by microwave-detected photoconductivity (MDP) method [Sch10]. The method is based on the evaluation of sample photoconductivity by measurement of its microwave absorption during and after the excitation with a rectangular laser pulse. The principal of MDP measurements is displayed in Figure 5.4.

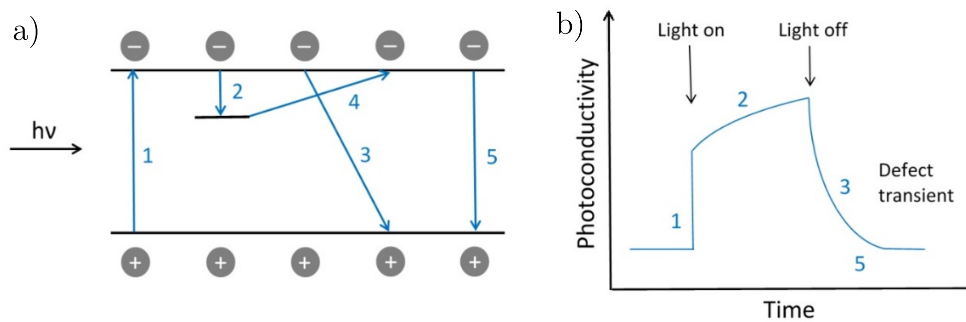

Figure 5.4.: The principal of MDP measurement:
a) energy scheme of the measurement; b) measurement signal.

The sample is illuminated with a laser, which generates free charge carriers in the conduction band (1). The energy levels induced by traps are filled with the excited charge carriers (2). When the external illumination is switched off, the excited free carriers from conduction band recombine over a certain time (3) while carriers from trap energy levels reemit an excess energy (4) with subsequent recombination, which is somehow shifted in time (5). The microwave absorption of the sample is measured during the whole time of excitation and relaxation. The

time at which the signal decays in e times is defined as the minority carrier lifetime τ.

The duration and the magnitude of laser illumination can be set to various values in order to obtain the best accuracy and gain more information [Cue04]. It is well known that the measured lifetime strongly depends on the injection level (i.e. the intensity, laser power, laser wavelength, illumination area etc.) Therefore, in order to make the measured values comparable, all the samples were investigated while using the same measurement settings: laser wavelength 980 nm, laser power 140 mW, laser spot 1 mm and pulse duration 1 ms.

5.4.3. Fourier-transform infrared spectrometry (FTIR)

A significant part of oxygen and carbon contamination in multicrystalline silicon ingots is present in the single atomic state. Carbon substitute silicon atoms in lattice cells as substitutional point defect C_s, while oxygen is normally located in interstitial positions O_i. Such a structural peculiarity makes it possible to detect these elements through their chemical bonds in crystalline lattice (Si-O-Si for oxygen and Si-C for carbon) with spectrometric methods.

In Fourier-transform infrared spectrometry (FTIR) method, a monochromatic laser beam of IR spectrum is transmitted through the sample. The intensity of both incident and transmitted beam are detected for each wavelength band in the beam spectrum. Silicon is transparent at IR wavelengths, while interstitial oxygen and substitutional carbon in the crystal lattice vibrate at frequencies 1107 cm^{-1} and 605 cm^{-1}, respectively. Some part of the transmitted light at these frequencies is absorbed by contaminations, which can be detected by the FTIR spectrometer. The absorption depends linearly on the sample thickness and concentration of impurities. By using verified reference samples and standardized relations for FTIR technique, it is possible to define the concentrations of C_s and O_i in silicon samples.

The concentrations of oxygen and carbon were defined with FTIR technique [Key04] on 2 mm thick both side polished vertical cuts. The measurements were performed by Mike Pietsch from IKZ Berlin. The calibration factor of $1.0 \cdot 10^{17}$ cm^{-2} was used for carbon and $3.14 \cdot 10^{17}$ cm^{-2} for oxygen. The resistivity of the measured samples was always higher than 0.1 $\Omega \cdot cm$, which is the limit of FTIR spectrometer operation for n-type material due to free charge carrier absorption.

5.4.4. Lateral photovoltage scanning (LPS)

The shape of solid-liquid interface strongly depends on melt convection and heat transport during solidification process. Unfortunately, there are no mature methods that are able to detect this parameter in situ in standard DS furnaces. However,

the shape of solid-liquid interface can be visualized on grown ingots by specific electro-physical methods, e.g. lateral photovoltage scanning (LPS) [Lue97].

The LPS method is based on the ability of charge carriers to drift in electrical field. The investigated sample is placed between two Ohmic contacts on its opposite sides, while its upper surface is illuminated with a laser of energy exceeding the band gap. Laser illumination excites free charge carriers, which diffuse into the bulk of the sample. If the sample has an internal electrical field due to resistivity gradient in the lateral direction between the Ohmic contacts, it will provoke an additional lateral drift motion (current) of the charge carriers, so that this field is compensated by their space charge. The lateral charge displacement leads to a small potential difference (1 μV) between the contacts, which can be measured by a phase-sensitive AC detection system. The magnitude of this voltage depends on the lateral resistivity gradient.

In such a way, the LPS method is able to visualise local resistivity inhomogeneities (so-called striations) in longitudinal direction of the sample [Buc20]. Since dopants are distributed uniformly along the solid-liquid interface at any given time, the mapping of striations grants the possibility to track the shape of the growth front. Normally striations are the result of accidental fluctuations of the growth process. However, these fluctuations might be provoked deliberately in order to create striations, and thus to mark the solid-liquid interface at a certain stage of solidification. Moreover, by creating several markers with striations at predefined times, it is possible to determine the growth rate at different growth stages with simple dividing the distance between the markers by time when they were made.

All G1 size ingots were deliberately marked with striations during growth and measured by LPS method. The investigation was performed on grinded vertical cuts in longitudinal direction. The Ohmic contacts were made by GaIn tinning solder.

5.4.5. Photoluminescence (PL) imaging

Photoluminescence imaging is a popular technique for characterisation of crystalline silicon. It is particularly suited for the detection of shallow-level defects, but can be also applied in other applications. PL imaging allows the characterisation of a large variety of material properties by simple detecting bulk recombination properties of silicon material. The surface of a silicon sample is illuminated with an optical source/laser with the photon energy larger than the band gap energy of silicon, which excites free charge carriers. The subsequent recombination of the excited carriers leads to the emission of luminescence due to their band-to-band transitions. The image of the luminescent emission is taken by a CCD camera. The rate of spontaneous emission via band-to-band transitions is

connected to physical parameters, such as the quantity of charge carriers, the minority carrier lifetime, the splitting of the quasi-Fermi energies etc. [Tru12]

In such a way, photoluminescence images contain complex information about material properties of the measured sample, ranging from bulk and surface recombination properties, to crystal structure, bulk lifetime, quality limiting impurities etc. The PL imaging was performed on mechanically polished nonpassivated longitudinal cuts for each investigated ingot.

5.4.6. Near-infrared transmission (NIR) imaging

Since silicon is transparent in infrared spectrum, it is convenient to use IR transmission spectroscopy for the detection of impurities and inclusions that absorb the light in this spectrum. A fast and inexpensive method that utilizes this feature is near-infrared (NIR) transmission imaging in the spectrum from 0.7 to 1 μm. The high intensity NIR source illuminates the sample with lower photon energy than the band gap of silicon. The long wavelength light passes through the crystalline structure of silicon, and is scattered and absorbed at crystal defects and faults. The image of the light, which goes through the sample, is recorded by a short wavelength IR line scan camera. As the result, the NIR image depicts macro-defects in crystalline structure, such as cracks, cavities and inclusions. With this method, it is possible to visualise the location and the size of SiC and Si_3N_4 inclusions.

Near-infrared transmission imaging of 2 mm thick polished longitudinal cuts from selected ingots was performed by Christian Kranert from IISB Fraunhofer, Erlangen.

5.4.7. Glow discharge mass spectrometry (GDMS)

In order to evaluate the contamination of the grown ingots with metals, selected G1 size ingots were analysed by means of analytical chemistry, namely glow discharge mass spectrometry (GDMS). The detailed description of the method can be found elsewhere, e.g. [Qua17, Sab14]. Representative samples for the analysis where taken from 5 equidistant positions along the central vertical line at longitudinal cuts of selected ingots. The investigation included the content of impurities, such as sodium Na23, magnesium Mg24, aluminium Al27, potassium K39, calcium Ca44, scandium Sc45, titanium Ti47, chromium Cr52, manganese Mn55, iron Fe56, cobalt Co59, nickel Ni60, copper Cu63, zirconium Zr90, molybdenum Mo98, tantalum Ta181 and tungsten W184. In addition, the concentrations of dopants: boron B11, phosphorus P31 and arsenic As73 were also measured, in order to evaluate the applicability of indirect dopant determination

from resistivity data. GDMS analysis was carried out by Gagan Paudel at the Department of Material Science and Engineering at NTNU Trondheim (Norway).

CHAPTER 6

Growth experiments

6.1. Growth setups

The experimental research was performed in two stages. The main part of the research was dedicated to the study of various process parameters on resistivity distribution across mc-Si ingot and crystalline material properties. This study was performed on G1 size ingots, since the process has many similarities to those conducted in industrial scale. However, in order to evaluate the fundamental dependencies between process parameters and material properties a preliminary research on the smaller scale is highly preferred. The preliminary study was dedicated to the TMF influence on phosphorus dopant distribution and was realized in so-called G0 ingots, which are significantly smaller than the ones sufficient for manufacturing of standard size PV wafer.

6.1.1. G1 setup

The fundamental research on the influence of various process parameters (TMF intensity, ambient pressure and gas flow) on resistivity distribution in multicrystalline silicon ingots as well as on their structural, electrical and physical properties was performed in G1 size scale. The ingots were grown in traditional G1 setup placed inside the G1 KRIST*MAG*® hot zone. The layout of the setup is showed in Figure 6.1.

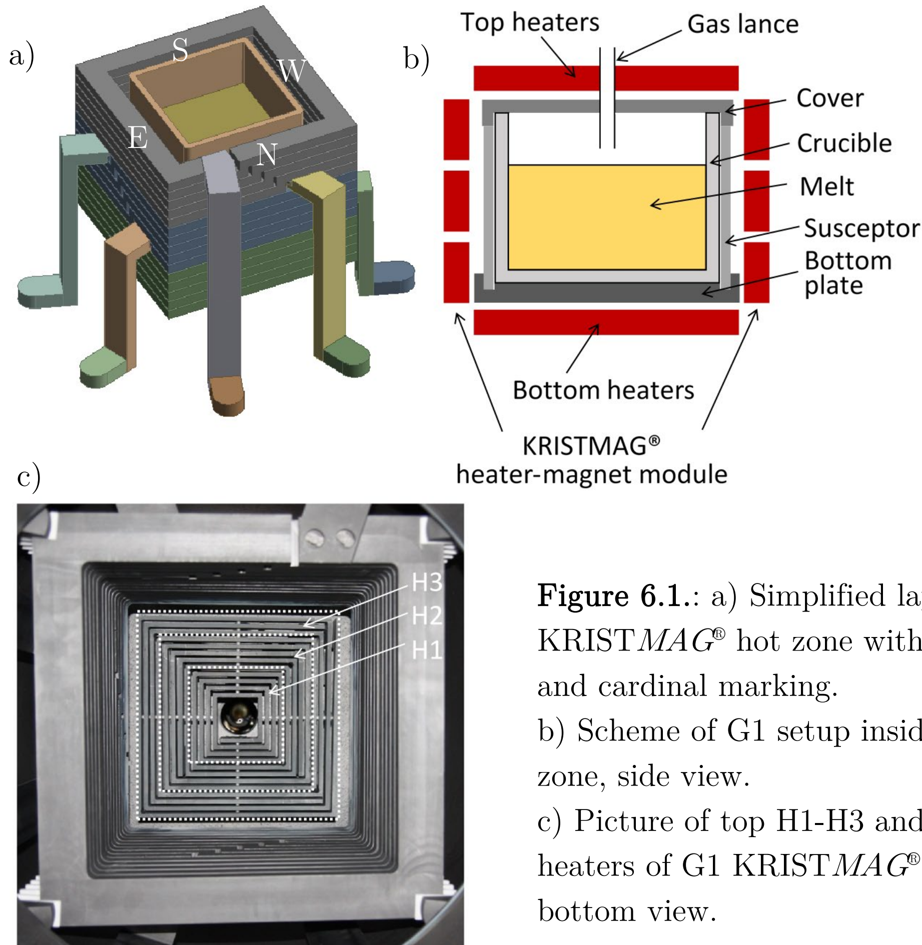

Figure 6.1.: a) Simplified layout of G1 KRIST*MAG*® hot zone with G1 setup and cardinal marking.
b) Scheme of G1 setup inside G1 hot zone, side view.
c) Picture of top H1-H3 and side heaters of G1 KRIST*MAG*® hot zone, bottom view.

The hot zone consists of three top (H1-H3) and three bottom (H7-H9) resistive graphite heaters performed in the 4-angle spirangle shape and placed one inside the other. The heater-magnet module comprises three graphite side heaters (H4-H6) of 4-angle spirangle shape located one above the other. Since the symmetry of the thermal fields inside the hot zone is mostly disturbed by bus bars, the bus bars connecting the side heaters to the power supply are situated at three different sides of the heaters. In order to follow up the discrepancies in system symmetry, all sides of the hot zone are marked according to the principal of cardinal directions: east, west, north and south (E, W, N, S).

The G1 rectangular crucible is placed in the centre of the graphite plate above the bottom heaters and tightly surrounded with a G1 graphite susceptor. The susceptor consists of four demountable side sections connected with each other with graphite screws. The demountable design is preferred over the solid one, since it provides the necessary gaps for thermal expansion during the solidification process, thus prevents the graphite construction from cracking. In order to reduce the contamination of silicon melt with graphite, a rectangular cover made of silicon carbide is placed above the crucible and the susceptor. The cover contains two round holes. The one in the centre serves as a viewing port for melt surface

observation with a pyrometer. The second neighbouring hole is used for the ingoing argon flow supplied through the ceramic lance. The openings at the rim of the cover realize the outgoing argon flow. The picture of the G1 setup is showed in Figure 6.2.

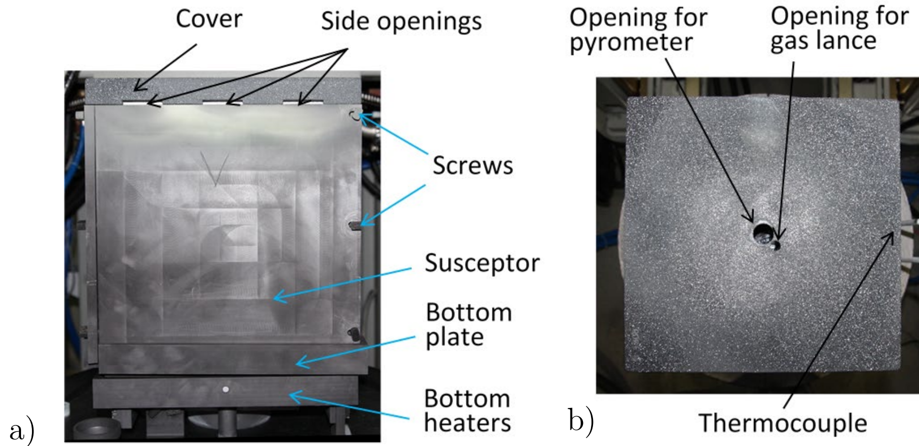

Figure 6.2.: a) G1 set up, side view; b) SiC cover, top view.

The G1 setup enables growing of G1 ingots with dimensions of 22×22×12 cm^3 and weight of 14 kg. The growth recipe for G1 ingots was based on power input control. Power input control is preferred of the temperature control, since it allows regulation of the used current per coil. The thermocouple and pyrometer measurements were used for observation of growth progression as well as for indication of the transition between liquid and solid phases. The power profile was generated on the basis of the previous experimental processes performed in the same G1 setup that resulted in the ingot growth rate of 1 cm/h. The respective heater powers as well as TMF, pressure and gas flow parameters were loaded into the control software and controlled thereby. The powers, magnetic fields, pressure and gas flow characteristics were ramped automatically to the set values. The adjustment of the set values was realized manually during the growth process in case it was needed.

6.1.2. 4×G0 setup

Before the detailed and accurate study of mc-Si material properties in different process conditions it is needed to evaluate the principal possibility to influence these properties by a fundamentally new approach. For this purpose, it is convenient to perform the test runs for relatively small ingots. Such an approach has a number of advantages, including short time-saving crystallization process and cost-effective post-treatment. For the purpose of additional research benefits, the G1 KRIST*MAG*® hot zone was supplemented with a specially developed 4×G0 setup

consisting of four individual symmetric rectangular susceptors. The layout of the setup is shown in Figure 6.3. Each of the rectangular susceptors consists of four demountable side sections made of graphite, which are tightly placed around a small G0 rectangular crucible. G0 susceptors are symmetrically located in the four corners of a standard larger G1 graphite support. No specific covers above quartz crucibles were used for individual G0 ingots. The whole setup used one large G1 SiC cover enabling common gas ambient for all G0 ingots. The gas inlet in the cover was slightly off-centre (Figure 6.2.b). The gas outlet was implemented through symmetrical openings along the rim of the graphite support, which is expected to form comparable gas flow in every G0 crucible directed from the inner towards the outer corner, and minimizes the influence of crucibles on one another.

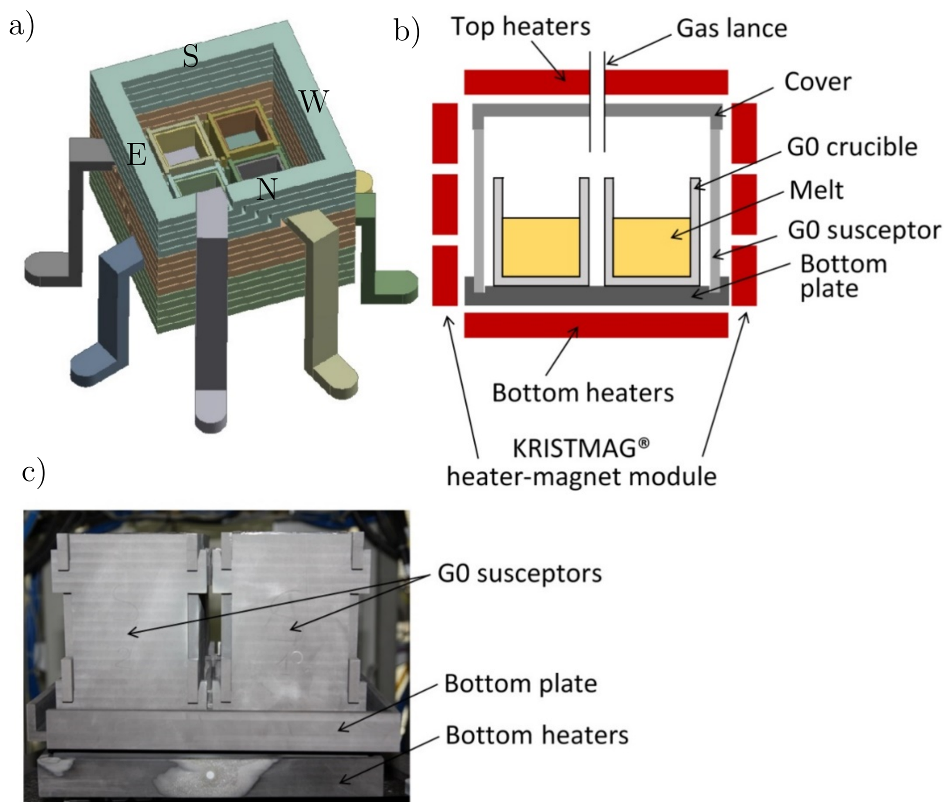

Figure 6.3.: a) Simplified layout of G1 KRIST*MAG*® hot zone with 4×G0 setup and cardinal marking. b) Scheme of the 4×G0 setup inside the G1 hot zone, side view. c) Picture of the 4×G0 setup, side view.

Such a 4×G0 setup enables the simultaneous growth of four G0 size ingots with dimensions of 80×80×60 mm^3 and weight of 0.9 kg. The symmetrical location and identical design of the individual supports assure nearly equal growth conditions in each crucible, such as heat profile, growth rate, temperature gradients, gas pressure and Lorentz forces. This peculiarity gives an opportunity to grow four ingots with various feedstock composition while keeping the same process parameters without the risk of process-to-process fluctuations.

However, it has to be taken into account that such a design of the setup also has certain disadvantages compared to the traditional G1 setup. Since the furnace is equipped with only one pyrometer focused at the centre of the system, it is not possible to observe the melt surface of either ingot, consequently this method of process control is not applicable for the 4×G0 setup. In addition, the volume of silicon melts is significantly smaller than the cumulative size of graphite supports, and the distances between the crucibles and thermocouples are larger than that for the case of G1 setup. These factors make the process control by thermocouples data less accurate and the entire 4×G0 system more sensitive to process fluctuations. Nonetheless, these disadvantages are not critical for rough estimation of the influence of TMF on phosphorus behaviour during directional solidification of silicon ingots, since the quality of multicrystalline material is not the focus of the study on this stage.

Similar to G1 processes, the growth recipe for 4×G0 setup was based on power input control. The observation of growth progression and indication of liquid-solid phase transition was performed solely by temperatures measured with thermocouples. The power profile was generated by numerical modelling in order to assure the ingot growth rate of 1 cm/h and subsequently improved by experimental crystallization processes.

6.2. Process preparation

6.2.1. Crucible and coating

The G1 growth was performed in G1 fused silica crucibles with inner dimensions of 220×220×266 mm^3 and wall thickness of 12-16 mm manufactured by Vesuvius. The crucibles for G0 ingots were made of quartz by Glasbläserei Müller. G0 crucibles had the inner dimensions of 80×80×80 mm^3 and the wall thickness of 10 mm. Before the utilization in the growth process all crucibles were coated with Si_3N_4 to prevent silicon ingots from sticking to crucibles as well as to avoid contamination of mc-Si material with metals contained in fused silica. In order to minimize the pollution of silicon melt, only high purity Si_3N_4 from H.C. Stark was used for crucible coating. Since silicon nitride is supplied in the form of fine powder with particle size of 1-3 µm, the direct coating with dry Si_3N_4 is not possible and should be performed through liquid suspension with subsequent drying. The suspension used for the coating was based on distilled water containing PVA for sufficient adhesion to the crucible walls. The concentration of PVA was chosen in such a way, so that the coating also adheres to very smooth surface like that for G0 crucibles. The received solution mixed with the Si_3N_4 powder and mechanically stirred until heterogeneous state of chemical suspension. The resulting suspension

was evenly spread all over the inner surface of the crucibles with an air gun. In order to avoid the peeling of the coating off the crucible walls, the coating was performed stepwise by sequential application of three thin layers for G1 crucibles and four layers for G0 crucibles. After spraying of each layer the crucible was left to rest at the room temperature until dry. During spraying, particular attention was given to crucible corners and wall junctions, since these parts of crucibles are especially hard to reach. The thickness of the coating was randomly controlled by a contactless OptiSense profilometer by photothermal measurement method. The total thickness of the applied coating was always in the range between 100 and 150 µm. After the final spraying the residual water and PVA was removed by firing. The firing of the crucibles was carried out in a clean muffle furnace. The firing profile was chosen in such a way that it assures successful removal of residual moisture, but prevents crucible phase transition happening above 1200°C [Col34, Mar08, Cam17]. Another purpose of this high temperature treatment is the sintering and oxidation of the applied coating [Bry10]. In order to avoid the thermal shock and cracking of the crucibles, the temperature ramp up and cool down were realized in a slow manner of 200°C/h. The described technique and recipe were proved to ensure a stable coating that withstands the entire solidification process and prevents the contact between the crucible and silicon melt. In order to eliminate any influence of the differences in coating quality on the characteristics of mc-Si ingots, all G1 and G0 crucibles were coated with the identical suspension as well as sprayed and fired in the identical way. Thus, any differences in the properties of multicrystalline material produced within one experimental set (e.g. minority carrier lifetime, oxygen concentration, resistivity distribution etc.) are induced solely by growth process conditions.

6.2.2. Charge composition

High purity polysilicon chunks were used as feedstock for every ingot charge. The resistivity of the polysilicon feedstock was larger than 1000 Ω·cm, thus did not have an influence on final resistivity of doped mc-Si ingots. Since the volumetric density of solid charge strongly depends on the size and shape of polysilicon chunks, the composition of the charge must be chosen carefully to fit the dimensions of the crucible. Therefore, three groups of polycrystalline material with identical bulk properties and different size distribution were used for charge composition: fine (0-15 mm), small (5-45 mm) and large (35-150 mm). In order to minimize the influence of charge composition on melting process and mc-Si material quality, the share of each feedstock group in every ingot charge was equal. The feedstock was placed into the crucible in alternating layers of different chunk size that provide the most compact material packaging and the highest volumetric density.

It is greatly important to prevent crucible coating from scratching with sharp chunk edges during charge loading and melting. It has to be kept in mind that polysilicon chunks melt at different rates depending on their size and location inside the crucible. At a certain stage after the charge is partially molten, the unmolten chunks start to move due to buoyancy and gravity and might damage the coating and even the crucible. Therefore, the protective 5 mm layer of fine polysilicon pieces was placed on the bottom of every crucible before packing of large chunks, and either small or smooth chunks were laid out at the walls of the crucibles. Moreover, both silica and quartz crucible are tend to expand and change their shape under the influence of elevated temperatures at the feedstock melting stage. The parts mostly susceptible to the shape distortion are crucible corners and wall junctions. Hence, it is highly important to keep these areas free of large chunks in order to avoid high mechanical stresses and the risk of crucible cracking. Figure 6.4. illustrates G1 and 4×G0 setup loaded with polysilicon before the process. For the growth of conventional mc-Si ingots each G1 crucible was loaded with 14 kg of polysilicon feedstock, while G0 crucibles contained 0.9 kg of polysilicon.

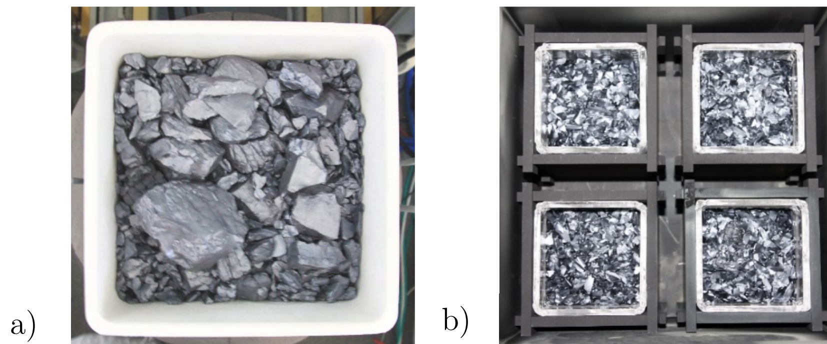

Figure 6.4.: a) G1 crucible with 14 kg of polysilicon feedstock; b) 4×G0 setup with four G0 crucibles each filled with 0.9 kg of polysilicon feedstock.

Besides the polysilicon feedstock, each ingot charge also contained phosphorus dopant. Since the direct usage of phosphorus is complicated by its high partial pressure, silicon material doped with large quantity of phosphorus was used as a doping substance instead of pure phosphorus. Moreover, the utilisation of highly-doped silicon is preferable for small multicrystalline ingots, since due to the ease of dosing it gives more stable results when low dopant quantities are required. All ingots grown within this research work were doped with the same highly-doped silicon of uniform phosphorus concentration. The concentration of phosphorus in doping material was defined in previous growth experiments by reverse calculations from resistivity distribution using standardized empirical relations for semiconductor silicon [Thu80a]. The exact quantity of phosphorus added into ingot charges was chosen in such a way to be close to the market specification for c-Si wafers, which is of 3.0 – 1.0 Ω·cm. The amount of highly-doped silicon added to

each ingot was either varied or kept constant depending on the parameter study. In order to assure equal experimental conditions for all processes, the doping material was placed into the centre of the charge at 60-70% of crucible height.

Figure 6.5.: Seeding layer of fine polysilicon chunks placed on the bottom of G1 crucible for the growth of an HPM ingot.

The final set of experiments in this research work was dedicated to the replication of the developed growth recipe on the crystallisation of high-performance mc-Si ingots. HPM experiments were performed only in G1 size. The above-described sequence of crucible loading was supplemented with the sick uniform seeding layer of fine silicon chunks with the total weight of 2 kg placed on the bottom of the crucible (Figure 6.5). Hence, the crucible charge for HPM ingots summed up to 16 kg. Since the complimentary material serves mainly as a seeding layer and does not contribute noticeably to the amount of the silicon melt, the quantity of phosphorus dopant used in HPM experiments was the same as in conventional multicrystalline G1 ingots.

The detailed charge composition and doping for the growth experiments conducted within this research work is presented in the following chapters.

6.3. Experimental conditions

6.3.1. Growth process

The growth recipes were based on numerical modelling and previous processes conducted in G1 KIST*MAG*® setup, and implied process control by power ratio of nine heaters that ensure thermal gradients resulting in the ingot growth rate of 1 cm/h. After the loading and closing the furnace, the chamber was pumped down to the level of 10^{-3} mbar with subsequent filling with argon. The procedures of pumping and filling was repeated at least three times for removing any dust and impurities brought to the system during the loading. In order to eliminate the residual water introduced by outer atmosphere and guarantee the dryness of the graphite parts, the chamber was subjected to annealing at 500-700°C in vacuum for

12 hours and subsequent gaseous evacuation by sequential pumping and purging with argon. Before the start of the growth process, the chamber was filled with argon up to the working pressure of 600 mbar.

During the entire growth process, the temperatures and thermal gradients inside the chamber were controlled by twelve thermocouples located in fixed positions inside the hot-zone. Figure 6.6. shows the typical temperature profile of G1 process measured by the thermocouple TC-1 located at the central top heater H1 and the thermocouple TC-B located at the centre of the crucible bottom. Additionally, in the case of G1 process, the condition of the melt surface was observed by pyrometer Pyro.

The DS growth process consists of five main phases:

a) Heating the chamber to the temperature slightly above the melting point of silicon (1414 ˚C).
b) Melting the charge at constant temperature.
c) Keeping the melt at the temperature above the melting point for homogenization.
d) Solidification at a certain cooling rate by creating a vertical temperature gradient within a crucible.
e) Cooling the solidified ingot to the room temperature.

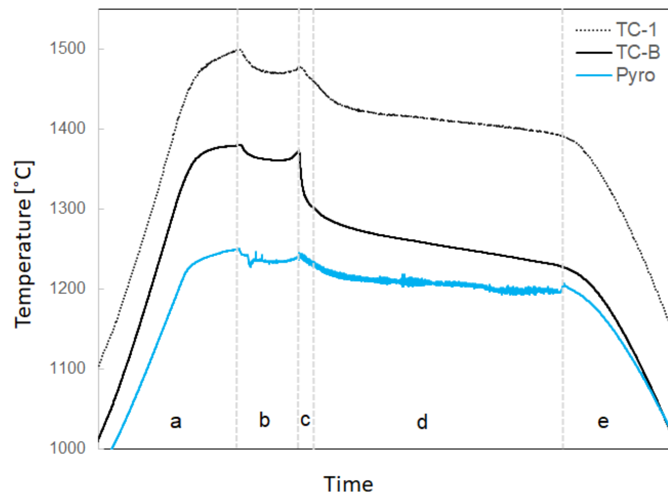

Figure 6.6.: Typical temperature profile of G1 DS process measured by the upper thermocouple TC-1 and the lower thermocouple TC-B, supplemented by pyrometer Pyro observing the melt surface. a) Heating; b) melting; c) homogenization; d) solidification; e) cooling.

During the heating phase, the temperature in the furnace was gradually raised by the constant power input from all nine heaters. Although the configuration of thermal fields does not have a significant impact on material heating and melting, it is preferable to keep a vertical thermal gradient in the system already at this

stage, since such an approach makes the transition from the melting to the crystallisation phase smoother and faster. The temperature measured by the upper thermocouple increases rapidly to the value above the melting point of silicon. The temperature at the lower thermocouple rises much slower, since the heat supplied by heaters is absorbed by silicon.

When the temperature at the lower thermocouple approaches the melting point of silicon, the power input from all the heaters are slightly lowered and kept at this level for the entire melting stage. This decrease in power input is performed for the purpose of making the melting process slower, thus more controllable, and the temperature profile more sensitive to the changes of the melting condition. At this moment, the temperatures indicated by both thermocouples slightly decrease, since the impact of irradiation from neighbouring heaters becomes smaller. Nevertheless, the constant heat input is kept somehow superior to the heat output, thus is sufficient to melt the feedstock inside the crucible. While the charge absorbs the heat and slowly melts, the temperature at the lower thermocouple stays constant close to the melting point. Silicon feedstock does not melt rapidly and the whole melting stage takes from several minutes (for G0 ingots) up to an hour (for G1 ingots). Large pieces of silicon melt slower than small ones and the melt goes down to the crucible bottom due to gravity. Therefore, after a while larger pieces will be immersed into the melt and even floating on the melt surface. When the sufficient amount of the feedstock is molten, the liquid silicon appears at the top of the charge and can be detected by the pyrometer. It has to be mentioned that the absolute values indicated by the pyrometer do not correspond to the real temperature of the surface melt. Nevertheless, the intensive fluctuation of pyrometer data indicates the presence of the melt at the top of the feedstock, although does not guarantee that the entire charge is molten. Since the first pieces are molten, the charge absorbs heat for melting rather than for heating (heat of fusion). Therefore, the temperature at the lower thermocouple does not change dramatically up to the moment when the whole silicon charge is molten. The rapid increase in the temperatures measured by thermocouples is the signal that the entire feedstock is molten and starts to heat above the melting point, since the material already consumed more heat than needed for melting. At this point, the process is switched to the next stage.

When the entire feedstock is molten, the bottom heaters are switched off in order to exhaust the heat through the bottom of the crucible, while the heat profiles of the top and side heaters are set in such a way to create the vertical temperature gradient inside the hot zone. At this stage, in some experiments the travelling magnetic field is switched on. During a certain time, the entire content of the crucible remains liquid and is subjected to the convection of different intensity due to buoyancy and TMF. This phase is called homogenization and lasts until the melt at the bottom of the crucible starts to solidify. The duration of homogenization phase depends on the cooling rate and the heat consumed by the charge after the

melting. In different experiments, this phase lasted from 15 minutes up to two hours. The vertical thermal gradient and the cooling rate were kept constant during the entire crystallization phase. In all experiments is resulted in the growth rate in the range of 1.0 – 1.2 cm/h.

In large rectangular industrial ingots, the last part to crystallize is the corners of the ingot. However, in smaller lab-scale furnaces it is not always the case. In both G0 and G1 ingots, the last-to-freeze part is slightly shifted from the centre of the ingot surface. Similar to the melting phase, the pyrometer data can be used for the indication of the surface solidification. The vanishing of fluctuations and the sharp peak of the pyrometer signal point out that the surface observed by the pyrometer is solid, although do not guarantee that the entire surface is crystallized. After the solidification of the entire charge is over and the last part of the melt is crystallized, the thermocouples experience the rapid decrease in temperature at the same heat exhaust rate, which means all silicon is solid, since the system released the entire heat of fusion. It has to be mentioned that in the case of 4×G0 setup the pyrometer cannot be used for the observation of the melt surface and the temperature control is performed solely by thermocouples, hence it is not possible to indicate the appearance of the first melt and the first solid state.

Although the ingot is fully crystallized, it still cannot be rapidly cooled down at this stage, since silicon is extremely fragile at this temperature and rapid cooling provokes cracking and breakage of material [Che08]. Therefore, the next phase of annealing and slow cooling is extremely important. Not only do these prevent the ingot from breaking, but also help to release thermal stresses acquired during crystallization and temper dislocations. On the other hand, keeping the solid ingot at elevated temperatures for significant amount of time is also undesirable, since fast-diffusive impurities from crucibles and coating (e.g. metals) penetrate into silicon at these conditions. The ingot cooling is kept at a constant and relatively low rate, and lasts for 14-15 hours.

The entire growth cycle depends on the size of the ingot. For 14 kg G1 ingot it takes about 45 h, where melting reaches up to 20 h and solidification lasts 12 h. In the case of 4×G0 setup, the growth cycle lasts about 40 h, with similar duration of melting and solidification to be 6 h.

When the system is cooled down to the room temperature, the furnace is opened and the crucible is taken out. Both quartz and fused silica pass through irrevocable β- to α-cristobalite phase transformation during the growth process that provokes deformation and shrinking [Mar08], which makes them unsuitable for the repeatable use. Due to the carefully developed Si_3N_4 coating the sticking between the ingot and crucible is completely avoided. The crucible is carefully broken, the broken parts are removed, and the silicon ingot is released for further investigated.

The HPM process is very similar to the crystallization of conventional multicrystalline Si ingots, although contains certain differences in the melting and

homogenization steps. In order to ensure the seeding layer to stay solid during the melting phase and to serve as a nucleation site at the beginning of crystallization, the bottom heaters were used neither at the heating nor at the melting phase, and their power input was compensated by the side and top heaters. The process control was realised through the temperature profiles measured by the thermocouples at the side heaters. The transition from the melting to the cooling phase was performed before the rapid increase of the temperature. The exact moment was defined by the absolute temperature values measured by thermocouples TC-4, TC-5 and TC-6 located at the side heaters.

During preliminary experiments, the suitable growth recipes were developed for three various types of DS processes: conventional multicrystalline G0 ingots in 4×G0 setup, conventional multicrystalline G1 ingots, HPM G1 ingots and quasi-mono G1 ingots. These recipes imply the predetermined power input from each of nine heaters during every process phase and provide the optimal heat profiles resulting in growth rate of 1.0-1.2 cm/h. Every experimental run conducted within this research work used one of the described recipes depending on the type of multicrystalline ingots. The duration of the melting and crystallization phases might slightly vary and were determined using the data measured by the thermocouples and pyrometer. In such a way, the influence of heat input on the final results were minimized. The parameters and configuration of TMF, chamber pressure and purging gas flow were set to different values depending on parameter study and will be described in the following sections.

6.3.2. Two-component TMF

In order to receive a preferable solid-liquid interface and protect the crucible coating from dissolving, only two-component TMF fields were used in this research work [Dro11]. Superposition of two opposite travelling TMFs with different frequency, and therewith different penetration depths in the melt, enables shifting of maximum of the Lorentz force magnitude away from the crucible wall towards the bulk melt. The suitable parameter combination for the components of TMF were chosen during previous experiments supported by numerical simulation. The summary Lorentz force density induced by both components were estimated analytically by a simple 1D model. The Lorentz force density distribution for single-frequency TMF perpendicular to a solid boundary was calculated as an exponential decay function of the skin depth, and hence the frequency of the TMF. The summary Lorentz force density of the double-frequency TMF was obtained by applying the superposition principle. Depending on the parameters of each component, their superposition produces horizontal profiles of Lorentz force density being upwards- or downward-directed at the wall and followed by a maximum in the direction of the crucible centre. When using two frequencies it is possible to

shift the Lorentz force density maximum from the wall to the desired position in the bulk melt. The shift of the maximum strongly depends on the ratio of the component intensities and their frequencies.

The optimal parameters of two-component TMF for the utilisation in G1 KRIST*MAG*® was defined to consist of upward TMF with frequency $f_1 = 20$ Hz and downward TMF with frequency $f_2 = 200$ Hz. The penetration depth of TMF components are $\delta_{TMF1} = 10.3$ cm and $\delta_{TMF2} = 3.3$ cm. The corresponding phase shifts were determined to be $\phi_1 = +90°$ and $\phi_2 = -90°$, respectively, while the ratio of the current amplitudes was kept at I_1/I_2=10. Figure 6.7. depicts schematic distribution of the Lorentz force density perpendicular to the crucible side wall for the double-frequency TMF with the defined optimal values. The TMF with such a configuration minimize the melt motion near the crucible walls, thus prevents the crucible coating from dissolving.

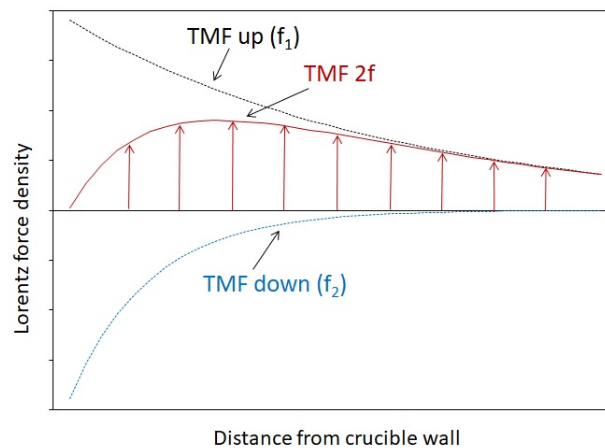

Figure 6.7.: Lorentz force density distribution for the double-frequency TMF consisting of two components with opposite directions.

The TMF used for the melt stirring within this research work consisted of two components with the above-mentioned parameters. The parameter study was focused on the influence of the intensity of the TMF on resistivity distribution in multicrystalline ingots. Thus, the varying parameters in experimental processes were the amplitude of the alternating current and the duration of TMF stirring at different segments of the ingot growth.

6.3.3. TMF marking of the solid-liquid interface

One of the most important parameters to be controlled during directional solidification is the shape of solid-liquid interface. Unfortunately, there are no mature methods for measuring or defining this parameter, neither in situ nor in the ingots after the growth. The effective method of the indirect measurements is the defining of solid-liquid interface position through the dopant profiles. During

directional solidification, dopants tend to segregate in the direction of growth, while their concentration stays uniform at the solid-liquid interface at each time point. Thus, isolines drawn in resistivity maps can be successfully used to track the position and shape of the solid-liquid interface. Although the accuracy of resistivity measurements is not sufficient to define the smallest details of interface curvature, dopant striations induced by temperature fluctuations have the same nature and character as resistivity isolines and are normally much easier to detect by DSL etching, IR transmission or LPS.

When the growth process is stable, microsegregation is significantly reduced, thus striations are difficult to be find. However, the deliberate alteration of the growth process can induce the formation of artificial striations. Since TMF applied during the crystal growth has an influence on the melt convection and heat transfer, it becomes a very effective tool to mark the solid-liquid interface. Rapid alteration of TMF parameters lead to the responding temperature variation at the interface. This could result either in temporary enhancement of solidification or in partial back-melting. When the intensity of TMF is rapidly increased, hot liquid from the melt surface is brought to the interface resulting in a partial back-melting of the solid upper layer. Once the intensity of the TMF is switched again to the previous lower value, the vertical thermal gradient in the melt increases and the interface is cooled down to the previous temperature. These rapid alterations induce noticeable dopant striations depicting the solid-liquid interface. Moreover, the interface marking made by TMF can be used as an efficient method for the accurate defining of the ingot growth rate. The growth rate can be easily calculated using the distance between two markers made at the defined moments of crystal growth.

The solid-liquid interface of all conventional multicrystalline ingots grown within this study were marked with TMF at different stages of solidification. The marking was realised through the rapid increase in the intensity of two-component travelling magnetic field. At the defined solidification stage, the effective current of the TMF was increased to the elevated value within 30 seconds, and then, returned to the previous level within 10 minutes. This time is sufficient to induce back-melting distinguishable by LPS without disturbing the entire growth process. The frequencies, phase shift and ratio of the current amplitudes were kept unchanged. In order to induce distinguishable striations, the intensity of the TMF applied for the marking should be significantly higher than the one used during the growth process. Therefore, the effective current of TMF markers was twice higher than the one used for melt stirring. Clearly distinguishable striations induced by these markings were revealed by LPS measurements. The pattern of the measured striations enable the determination of both the solid-liquid interface shape and the growth rate at different stages of solidification. However, it has to be kept in mind that due to different melt velocity the back-melting near the crucible walls is greatly reduced. Therefore, TMF marking at ingot edges is normally not visible.

It has to be mentioned that no marking was applied during the growth of HPM ingots, since process fluctuations induced by marking are strong enough to disturb the growth of crystallites and destroy the desired structure of HPM material.

6.4. Sample preparation

All the ingots after the growth were subjected to visual inspection and cutting for further investigation. In order to ensure that the measured parameters and characteristics of the grown ingots represent their bulk properties, the scheme of ingot cutting and sample preparation must be carefully considered. Although the G1 KRISMAG® furnace is considered to have 4-fold rotational symmetry in the first approximation, some peculiarities of the hot zone and setup design, such as positions of the heater bus bars, off-centre gas lance, non-uniform deterioration of the components etc. make the system slightly asymmetric. The asymmetry of the resulting heat fields acting inside the hot zone can be observed by the position of the last-to-freeze part on the ingot surface – in all G1 ingots it was slightly shifted from the centre to the south side of the setup.

In order to avoid the influence of the system asymmetry and make the measured data comparable to each other, all G1 ingots were cut along the same central line in west-to-east direction. Figure 6.8.a illustrates the cutting scheme of G1 ingots.

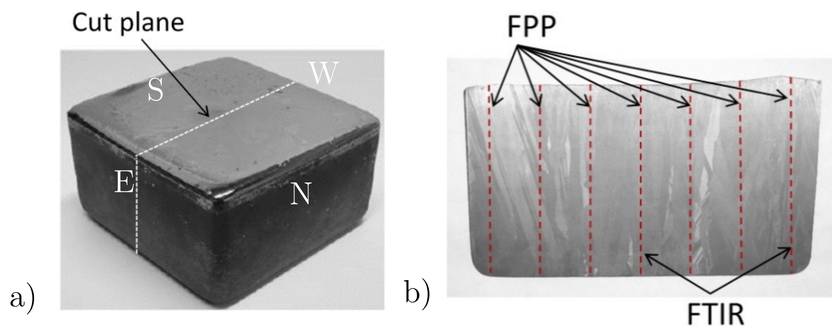

Figure 6.8.: a) Cutting scheme and b) measurement pattern for G1 ingots.

In contrast to G1 setup, G0 ingots grown within 4×G0 setup possessed 2-fold rotational symmetry, since they were located in the corners of the system. In order to avoid edge effects and evaluate the average bulk material properties, all G0 ingots were cut diagonally, perpendicular to the symmetry plane. The cutting scheme of G0 ingots are shown in Figure 6.9.a.

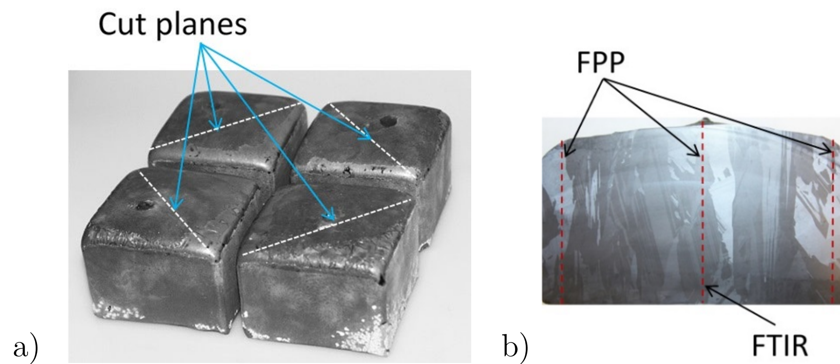

Figure 6.9.: a) Cutting scheme and b) measurement pattern for G0 ingots.

Several longitudinal samples were taken along the cut planes and used for parameter characterization. LPS, MDP, PL and IR transmission measurements were made on the entire surface of the sample in the form of 2D maps, while FPP and FTIR measurements were performed along the central and side vertical lines (Figure 6.8.b and Figure 6.9.b). For selected G1 ingots resistivity profiles were measured along 30 equidistant vertical lines providing 2D resistivity mapping. In order to avoid the influence of surface damages on measurement procedures, the most surface-sensitive measurements were made prior to least sensitive, e.g. PL mapping was performed after FTIR measurements.

CHAPTER 7

Influence of TMF on phosphorus evaporation in 4×G0 setup

In this chapter, the principal possibility to influence resistivity of phosphorus-doped multicrystalline ingots by application of travelling magnetic field is investigated. Since large systems are subjected to complex influences of numerous factors, it is preferable to evaluate the basic trends at G0 scale. In addition, smaller ingots give an opportunity to obtain effective and low-cost data for parameter studies in short times.

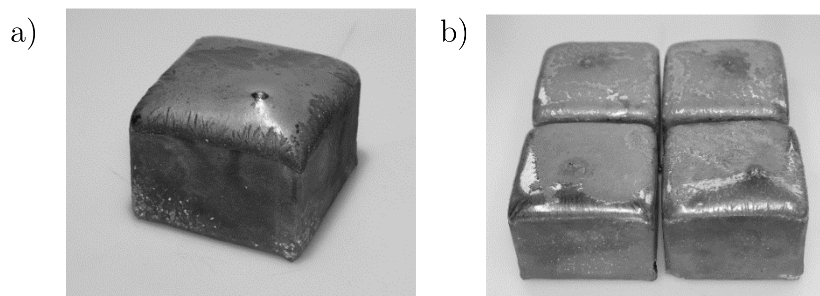

Figure 7.1.: a) G0 ingot of 80×80×60 mm^3 size. b) 4 G0 ingots grown in 4×G0 setup.

Within the framework of this research, 21 G0 multicrystalline ingots with dimensions of 80×80×60 mm^3 and weight of 0.9 kg were successfully grown within 9 growth sets with utilization of 4×G0 setup. The study was focused on the correlation between the intensity of melt stirring induced by TMF and evaporation of phosphorus from the melt surface. Nearly all ingots were grown under the

influence of two-component travelling magnetic fields with various amplitudes of alternating current, while other parameters were kept identical: frequencies $f_1 = 20$ Hz and $f_2 = 200$ Hz, phase shifts $\phi_1 = +90^\circ$ and $\phi_2 = -90^\circ$, ratio of current amplitudes $I_1/I_2 = 10$. In order to eliminate the influence of other factors, all experiments were conducted under the same process conditions, such as heat input, cooling rate, chamber pressure, purging gas flow, annealing etc. The growth recipe was developed in the set of preliminary experiments and implied the predetermined power input from each of nine heaters during every process phase. The resistivity of the grown ingots was measured by FPP method along the central and side lines of grinded longitudinal cuts (Figure 6.9). The detailed charge composition and process conditions for the growth experiments conducted within this research work are presented in Table 10.2. in Appendix.

7.1. Verification of setup symmetry

4×G0 setup provides growing of four G0 ingots in identical corner positions marked as -/1, -/2, -/3 and -/4 (Figure 7.2.a). Although the setup should secure equal growth conditions for all positions with regard to magnetic, temperature and heat profiles, the G1 furnace is not perfectly symmetric. Some asymmetry in power supplies, gas inlet/outlet, cooling system etc. may have various effects on ingots grown in different positions. All ingots grown in the same position within different experiments can be compared appropriately. However, objective comparability of ingots grown in different positions within 4×G0 setup is not obvious. Yet, it is not clear whether discrepancy of parameters between different ingot positions is significant enough to affect dopant transport or might be neglected.

Indeed, careful numerical simulation shows that characteristics of G1 furnace equipped with 4×G0 setup are noticeably uneven in terms of hot zone construction and power supply, thus the system exhibits asymmetric properties with respect to thermal fields. Figure 7.2.b illustrates temperature distribution within four G0 crucibles in the end of the melting phase while using the previously developed G0 growth recipe. Melts in positions -/1 and -/2 experience higher temperatures than those in positions -/3 and -/4. Therefore, growth conditions, and hence, material properties of ingots grown within one process might vary.

In order to verify the comparability of all four G0 crucible positions within the 4×G0 setup and its influence on the axial doping distribution in the ingots, the four G0 size ingots were grown in one set (Group A) using the developed growth recipe. Initial phosphorus concentration in every ingot was identical (indicated in Table 7.1.) and chosen in the way to provide resistivity in the range standard for PV specification. Target resistivity is the expected resistivity range calculated from the quantity of dopant added to the feedstock by using the Gulliver-Scheil equation

(2.10) with equilibrium segregation coefficient of phosphorus to be $k_0 = 0.35$. Double-frequency TMF with constant total effective AC magnitude $I_{eff} = 40$ A was applied during melt homogenization and solidification stages. TMF marker with total effective current of $I_{eff} = 80$ A was applied at the point of 2 h after the start of crystallization. The chamber pressure and argon flow were set to 600 mbar and 6.0 l/min, respectively, and kept constant throughout the entire process.

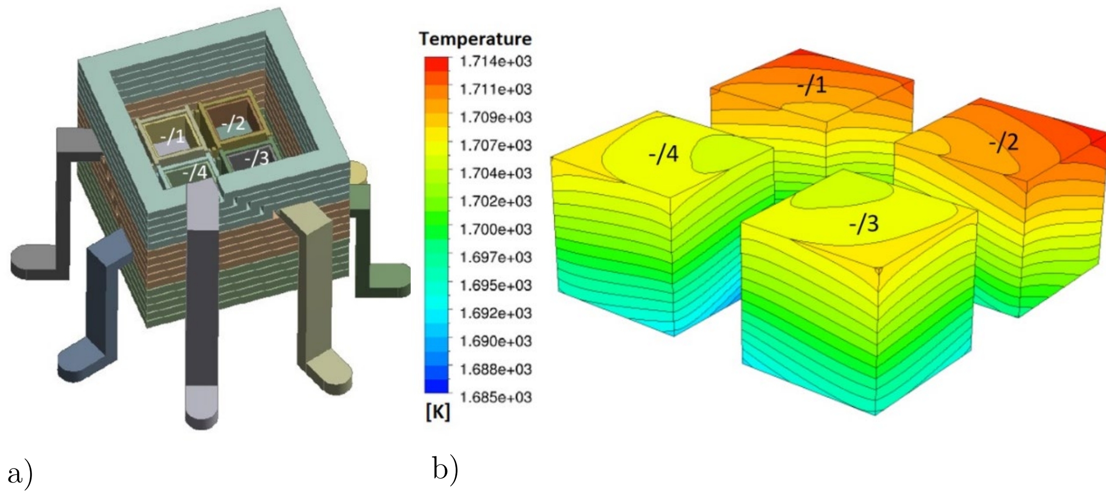

Figure 7.2.: a) Four ingot positions within the 4×G0 setup. b) Temperature distribution within 4×G0 setup in the end of the melting phase obtained by 3D numerical simulation.

Ingot position	C_0, concentration of phosphorus in ingot charge, [cm^{-3}]	Target resistivity range, [Ω·cm]
-/1, -/2, -/3, -/4	5.5×10^{15}	2.5 – 0.8

Table 7.1.: Phosphorus concentrations used in crucible charges for ingots in Group A.

The grown ingots were analysed and compared one with another. First of all, all four ingots had identical appearance, did not experience growth disturbances and had sufficiently flat crystallization front and columnar grain structure (Figure 6.9 and Figure 7.1.b). The grain structure characteristics prove that the developed 4×G0 setup enables proper conditions for successful DS growth of four mc-Si ingots at a time.

LPS images of longitudinal cuts are shown in Figure 7.3. They reveal similar crystal pattern and slightly concave solid-liquid interface for all four G0 ingots. Although the shape of the interface is not ideally optimal for securing mc-Si material with low dislocation density, the perfection of crystal structure is not the

aim of the research at this stage. The position of the marker applied during the growth process slightly differs in each of the four individual G0 ingots and corresponds to the isotherms obtained with numerical simulation. Due to the uneven thermal fields expected from numerical simulation, the solidification process in each crucible starts and ends at different time even in case the growth velocity is the same. Thus, the homogenization time is dependent on crucible position. Considering that the ingot growth rate is in the range of 1.0 cm/h, 1 cm of ingot's length corresponds to 1 hour of crystallization. From the position of the marker in LPS images, it can be concluded that crystallization of the ingots A1/3 and A1/4 starts about 0.5 hour earlier than that for the ingot A1/2 and nearly 1 hour earlier than for the ingot A1/1. Hence, the duration of homogenization for A1/1 is 30 minutes longer than for A1/2 and 1 hour longer than for A1/3 and A1/4.

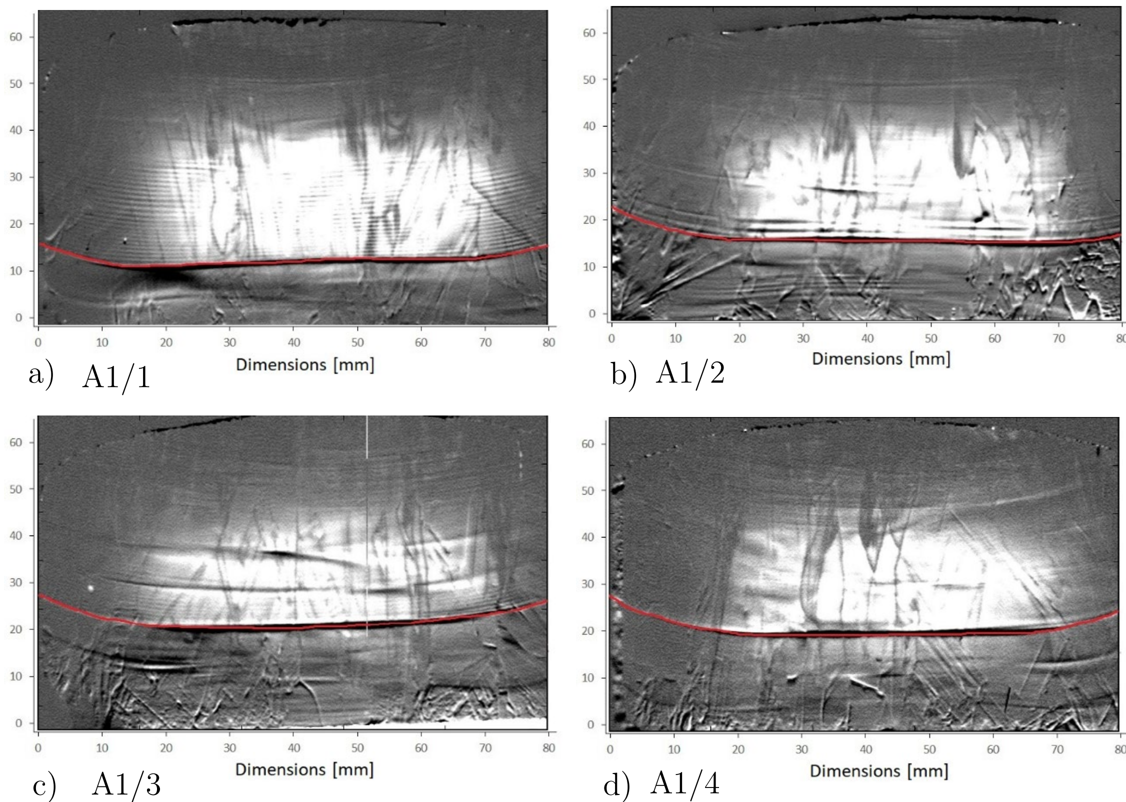

Figure 7.3.: LPS images for G0 ingots grown in different positions within 4×G0 setup in A1 set: a) A1/1, b) A1/2, c) A1/3, d) A1/4. TMF marker is indicated with the red curve.

The distribution of resistivity along the central vertical axis of G0 ingots is depicted in Figure 7.4. Systematic measurement error of FPP setup in the major part of measured resistivity range was less than 2%. It can be seen that the four ingots have significant discrepancies even though they were doped with the same quantity of phosphorus. Resistivity distributions along the side axis of these ingots have the same character as for the central one. It is obvious that despite equal

process data and materials, resistivity values differ more than in the range of measurement error. This can only be explained if the growth conditions in each G0 crucible are not equal. Since the ingots A1/1 and A1/2 which experience higher temperatures and noticeably longer homogenization time than those for A1/3 and A1/4 also show considerably higher resistivity, it is reasonable to assume that phosphorus evaporates already during the homogenization phase, which might be one of the reasons of different axial dopant distributions. Another reason for various intensity of phosphorus evaporation in different ingot positions is asymmetrical construction of gas inlet, which is slightly shifted from the centre towards ingot A1/1 and provokes different ambient gas flow above four melts. This is an important conclusion for evaluating further results, since only ingots grown in the same position can be evenly compared one with another.

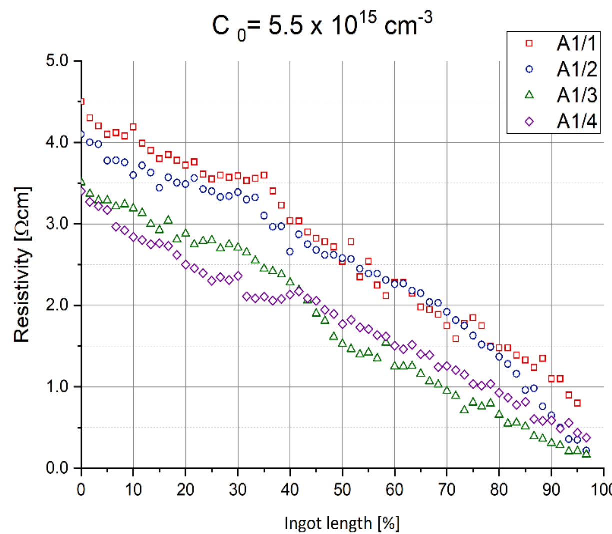

Figure 7.4.: Resistivity distribution along the central vertical axis of G0 ingots grown in different positions within 4×G0 setup in A1 set. All the ingots were doped with equal quantity of phosphorus $C_0 = 5.5\times10^{15}$ cm^{-3}.

7.2. Constant TMF stirring

After the verification of symmetry, the research was focused on the distribution of phosphorus in mc-Si ingots grown under the influence of TMF with constant parameters. Within this study, the group of three experimental sets of G0 size mc-Si ingots was grown (Group B consisting of B0, B1 and B2 sets). In order to investigate the effect of melt stirring on different ranges of resistivity, each set consisted of four G0 ingots grown within one 4×G0 setup and was doped with different quantity of phosphorus. For all the three growth sets, ingots with the same dopant level were always located in the same positions within the 4×G0 setup. The

quantity of dopants used in G0 ingots are indicated in Table 7.2. Target resistivity is the expected resistivity range calculated from the quantity of dopant added to the feedstock by using of the Gulliver-Scheil equation (2.10) with equilibrium segregation coefficient of phosphorus to be $k_0 = 0.35$.

Ingot position	C_0, concentration of phosphorus in ingot charge, [cm^{-3}]	Target resistivity range, [Ω·cm]
-/1	5.5×10^{15}	2.5 – 0.8
-/2	1.0×10^{16}	1.5 – 0.5
-/3	2.5×10^{16}	0.6 – 0.2
-/4	6.0×10^{16}	0.3 – 0.1

Table 7.2.: Phosphorus concentrations used in crucible charges for ingots in Group B.

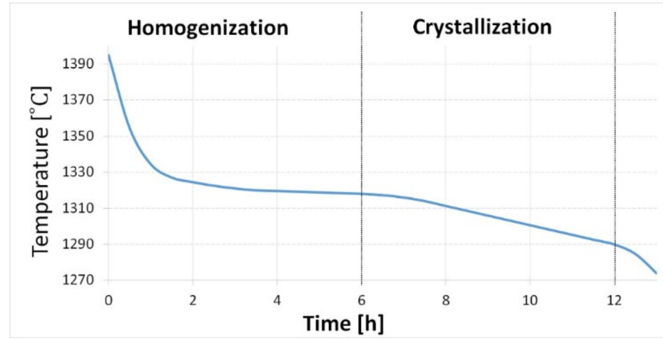

Figure 7.5.: Typical temperature profile of DS process conducted in 4×G0 setup measured by the lower thermocouple TC-B.

Every set used the same growth recipe based on the predetermined power input from each heater during every process step and implied the growth rate in the range of 1.0 cm/h. In order to allow sufficient phosphorus evaporation, the duration of melt homogenization was deliberately prolonged and made comparable to the one for ingot crystallization. The typical temperature profile for G0 process is shown in Figure 7.5. Each set was exposed to travelling magnetic field of different strength: B0 (no magnetic stirring), B1 (weak magnetic stirring), and B2 (strong magnetic stirring). In every experiment within Group B the current amplitude of TMF was kept constant during melt homogenization and ingot crystallization. Since the Lorentz force induced by magnetic field is a quadratic function of current amplitude (4.16), it is convenient to evaluate the magnitude of the acting force through artificial parameter Z:

$$F_L = I_{eff}^2 \cdot Z \tag{7.1}$$

In order to make the following scale-up from G0 to G1 size easier, the travelling magnetic field applied for G0 experiments consisted of two components with configuration previously developed for G1 process. The parameters of TMF used for each set is given in Table 7.3. and the profile of TMF intensity is shown in Figure 7.6. The chamber pressure and argon flow were set to 600 mbar and 6.0 l/min, respectively, and kept at these values throughout the entire process.

Experimental set	I_{eff}, [A]	F_L, [N]	I_1/I_2	f_1 [Hz]	f_2 [Hz]	ϕ_1	ϕ_1
B0	0	0	–	–	–	–	–
B1	40	1600 Z	10	20	200	+90°	–90°
B2	70	4900 Z	10	20	200	+90°	–90°

Table 7.3.: TMF parameters used during growth process in the experimental sets of Group B.

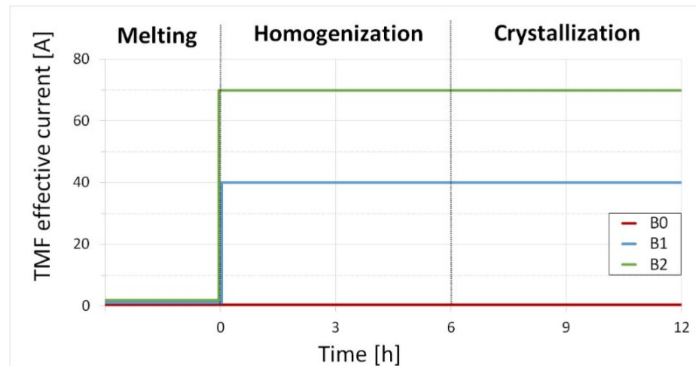

Figure 7.6.: TMF intensity profiles used in the experimental sets of Group B.

Magnitudes of TMF current for both B1 and B2 sets were selected from the range of parameter sets according to the results of numerical simulations in such a way that Lorentz force promotes more intensive melt stirring than provided by natural thermal convection. An example of simulated TMF stirring for the case of B1/2 crucible at the end of the melting phase is given in Figure 7.7. For the set B2 the Lorentz force affecting the melt was approximately three times higher than that for B1. The simulated Lorentz force density for B1 and B2 sets is shown in Figure 7.8. It can be seen that the pattern of the streamlines is identical for both cases and the difference lies solely in the force magnitude. The same is valid for the melt velocity streamlines. Thus, the melt flow for the case of B1 and B2 sets has the same pattern but different magnitudes.

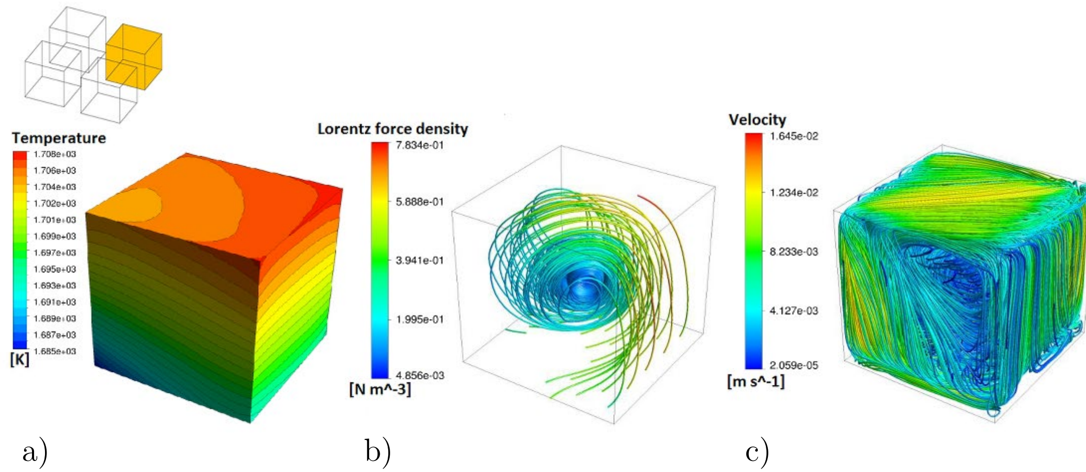

Figure 7.7.: Typical results of 3D numerical simulation for TMF driven flow in silicon melt at the end for the melting phase for G0 ingot B1/2: (a) temperature, (b) Lorentz force density streamlines induced by TMF, (c) velocity streamlines for summarized melt flow driven by natural convection and TMF.

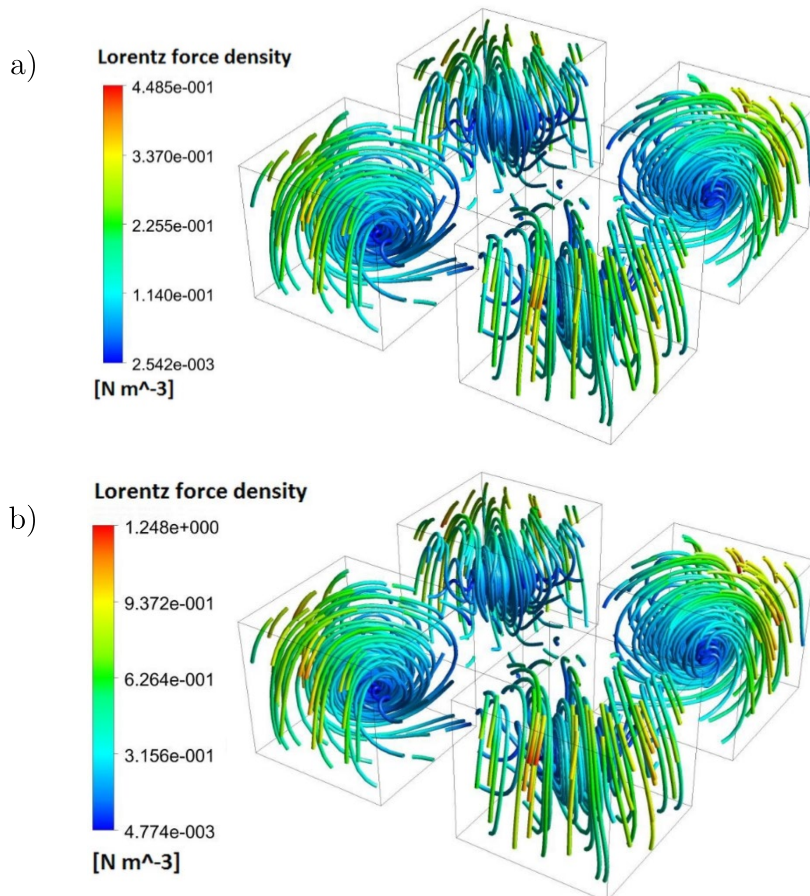

Figure 7.8.: Lorentz force density streamlines induced by TMF obtained by 3D numerical simulation for (a) B1 and (b) B2 sets.

Numerical simulation shows that 4×G0 setup ensures radial temperature gradient above 0.5 Kcm-1, which is sufficient for intensive melt mixing [Dro13]. Assuming complete melt mixing, the expected phosphorus distribution was calculated using the Gulliver-Schell equation (2.10) for each of the four ingots with respective concentration C_0 within every experimental set and an equilibrium segregation coefficient of phosphorus $k_0 = 0.35$. The obtained dopant distribution was further utilized for target resistivity calculation using the Klaassen model for majority carrier mobility of electrons and holes [Kla92].

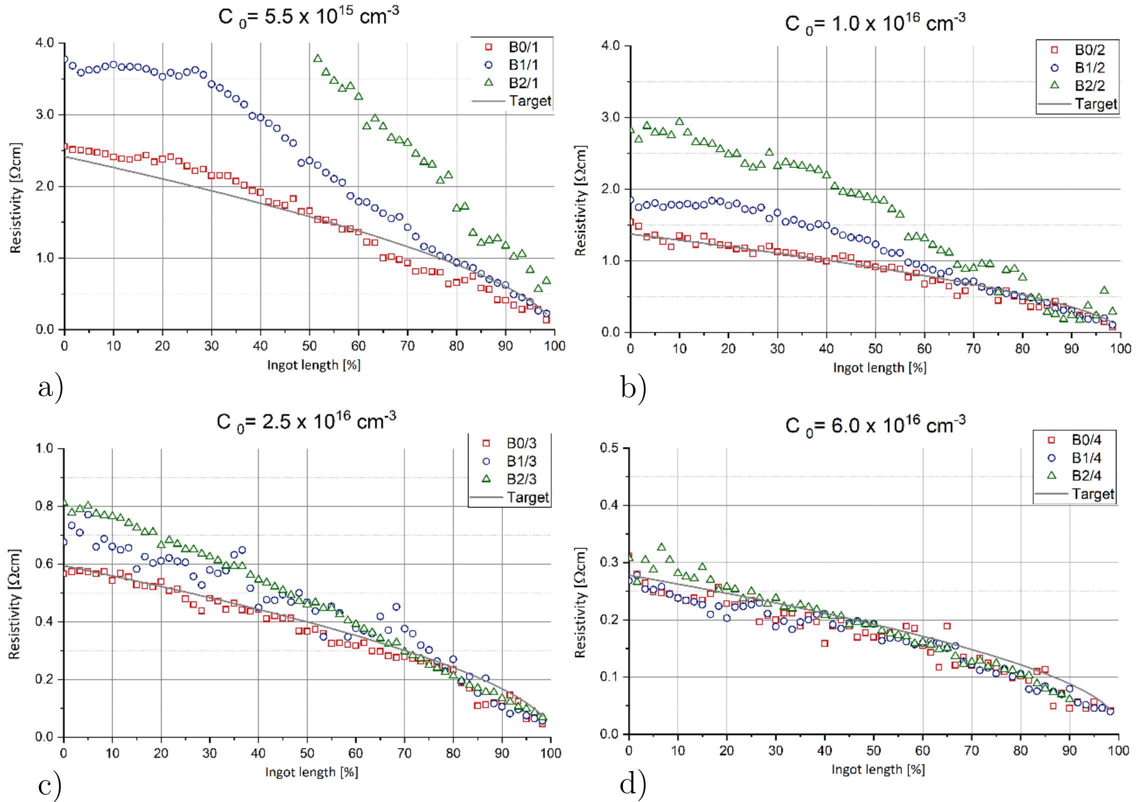

Figure 7.9.: Resistivity distribution along the central vertical axis of the ingots grown in different positions within 4×G0 setup in three experimental sets (B0, B1, B2): a) -/1, b) -/2, c) -/3, d) -/4.

As already explained, in conducted experiments resistivity distribution can only be compared for those ingots, which were grown in the same position, and which have the same dopant concentration. Therefore, the resistivity measured along the central vertical axis and the target resistivity were compared one with another for each of four doping levels (Figure 7.9). It can be seen that in the absence of magnetic stirring (B0) the measured resistivity is similar to the target one regardless the initial dopant level. This is a surprising result since in DS growth melt convection is only driven by radial temperature gradients. Since the real growth takes place in an open system, out and in-transport of elements might be

the reason for similar curves. However, this is very unlikely because the theoretical curves are alike to all considered cases, thus in- and out-transport should be very similar in all cases resulting in different impact on the resistivity. From that one can conclude that the mixing has to be complete even if no TMF was applied. This is only possible if the radial temperature gradients are big enough to ensure strong natural convection and hence, complete mixing.

In the case of TMF melt stirring, all ingots exhibit a certain increase in measured resistivity, which is considered to be caused by evaporation of phosphorus and a lower concentration of dopant-related charge carriers in crystallized material. This effect is more obvious for the ingots which were grown with lower dopant level in positions -/1 and -/2, for which phosphorus concentration in ingot charge was lower than that for -/3 and -/4. The experiments conducted within Group B cannot decisively explain whether the low increase in resistivity for -/3 and -/4 ingots is caused by ingot position with lower temperatures or the reason is high dopant concentration in ingot charge. However, it can be seen that the difference between target and measured resistivity increases when more intensive melt stirring is applied. This implies that enhanced melt stirring induced by TMF leads to the increase of phosphorus mass transfer coefficient in the bulk melt. In other words, the transport of dopant to the melt surface is enhanced and more phosphorus can evaporate resulting in lower dopant concentration in the ingot, hence its higher resistivity.

At this point, it has to be mentioned that resistivity distributions along the side axis of ingots have the same character as for the central one. Thus, it confirms that the change in axial resistivity profile is not caused by spatial redistribution of dopant inside the ingots. It is also worth noting that some measured data cannot be taken into account as reliable. Since the FPP setup used for resistivity measurements was calibrated for resistivity range of 0.2 – 5.0 Ω·cm, all the values outside of this range experience significantly higher measurement error.

As one can see in Figure 7.9, TMF mixing has an influence on phosphorus evaporation. Hence, distribution of phosphorus in crystallized ingots must be investigated in respect to TMF-based evaporation. For this purpose, experimental resistivity data from Figure 7.9. were utilized to derive phosphorus concentration with the use of standardized relations for semiconductor silicon [Thu80a]. The obtained distribution of dopant was plotted, and it clearly shows that enhanced melt stirring leads to reduced phosphorus concentration along the entire ingot's length regardless the initial quantity of dopant in an ingot's charge (Figure 7.10). Since phosphorus distribution along the ingot's length show very similar curves, one can conclude that the segregation coefficient of phosphorus is not significantly influenced.

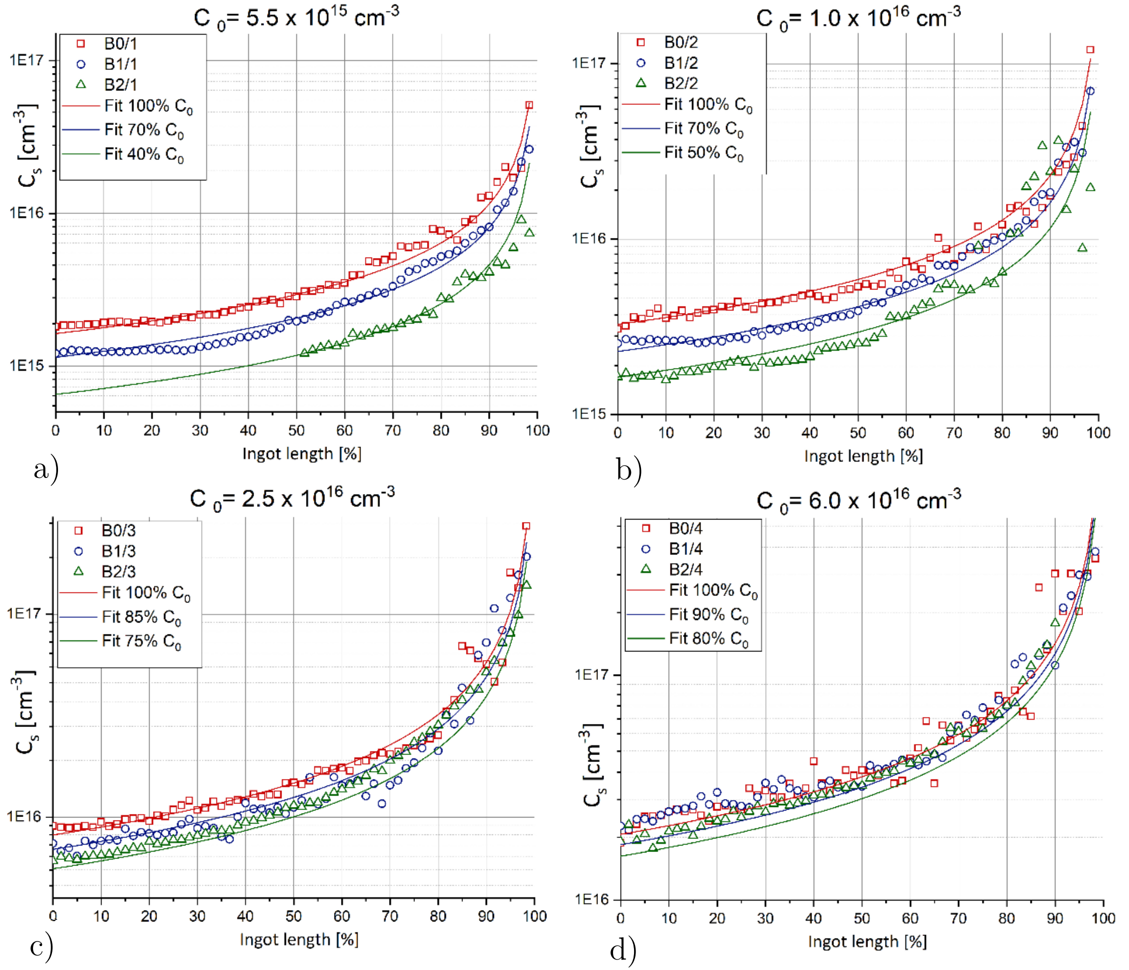

Figure 7.10.: Distribution of phosphorus concentration along the ingot's length for ingots grown in different positions within 4×G0 setup in three experimental sets (B0, B1, B2): a) -/1, b) -/2, c) -/3, d) -/4. The discrete points correspond to the data derived from measured resistivity (Figure 7.9). The solid curves are numerical fitting corresponding to a modified Gulliver-Scheil equation (7.2.)

In order to evaluate the level of phosphorus loss due to evaporation, a segregation model for dopant distribution for every ingot was built through curve fitting with the help of ordinary least square (OLS) method by linear regression in log-log scale. The model is described by the modified Gulliver-Scheil equation [Xi07, Li18]:

$$C_s(g_s) = k_x C_x (1 - g_s)^{k_x - 1} \tag{7.2}$$

where k_x and C_x are variable parameters of segregation coefficient and phosphorus concentration, respectively, which express the deviation of investigated system from the classical Gulliver-Scheil model.

The calculated curve fitting is in a good agreement with experimental data up to solid fraction of $g_s = 0.80$. Fitting procedure showed that the same trends suit

C_s distribution for all the ingots in the limit of measurement and method errors. Numerical fitting shows that the optimal curves correspond to a certain value of C_s parameter, which is lower than C_0, while k_x parameter for all twelve ingots is calculated to be equal to equilibrium segregation coefficient $k_0 = 0.35$. This indicates that the investigated system is equal to Gulliver-Scheil model for dopant concentrations somehow lower than that initially placed into the ingot charge. Thus, some part of dopants placed into the charge is lost before crystallization starts, but during solidification process, the system can be considered as a closed one in first approximation where no evaporation takes place. In other words, in G0 DS process conducted under the influence of constant TMF, silicon melt experiences a certain loss of phosphorous prior to rather than during crystallization phase, namely during charge melting and melt homogenization. Presumably, the process of phosphorus evaporation from the melt surface also takes place during solidification phase. However, in the investigated case the quantity of evaporated dopant during crystal growth is negligible compared to that for melting and homogenization. It can be explained by the fact that duration of the melt homogenization was deliberately prolonged and made equal to the duration of crystallization. Moreover, the melt surface temperature during solidification is lower by about 50 K than that during homogenization, which results in decreased partial vapour pressure by a factor of 2 [Mik96] and significantly reduces dopant evaporation. It is also worth mentioning that intensity of stirring decreases as the ingot grows and the melt height decreases, which reduces stirring-dependent dopant loss.

Ingot position	C_0, concentration of phosphorus in ingot charge, [cm^{-3}]	C_x as a fraction of initial doping	
		B1 (weak stirring)	B2 (strong stirring)
-/1	5.5×10^{15}	70%	40%
-/2	1.0×10^{16}	70%	50%
-/3	2.5×10^{16}	85%	75%
-/4	6.0×10^{16}	90%	80%

Table 7.4.: Concentration of phosphorus left in the melt after homogenization calculated from experimental data for ingots in Group B.

The value of C_s parameter was calculated to be different for various ingots and as a matter of convenience was expressed in the fraction of initial dopant concentration in a charge C_0 (summarized data are presented in Table 7.4). Depending on doping level and the intensity of melt stirring, C_s was found to be equal to values between 40% C_0 (for B2/1) and 90% C_0 (for B1/4). As it was already

mentioned, the construction of gas inlet/outlet minimizes the possibility of phosphorus evaporated from one crucible to be transported to other crucibles. All four melts experience evaporation of phosphorus and the most pronounced effect is observed for crucibles with the lowest concentration of dopant, which confirms that no cross-pollution was present. However, it cannot be definitely asserted that cross-influence of melts on each other was fully eliminated. In such a way, from these experimental data it is not possible to evaluate appropriately the dependence between quantity of evaporated phosphorus and its initial concentration in a charge, inasmuch as ingots with different doping were grown in various positions within 4×G0 setup, hence experienced different process conditions and possibly some minor influence of neighbouring ingots. Nevertheless, due to comparability of ingots with identical doping one with another, it can be concluded that more intensive TMF melt stirring leads to higher phosphorus evaporation regardless ingot position and initial quantity of phosphorus in the charge. Depending on doping level, the loss of phosphorus may be as high as 60% C_0 (for B2/1). This means that TMF with constant Lorentz forces, as it was applied in this study, has mainly an influence on the initial phosphorus concentration, but not on segregation mechanism.

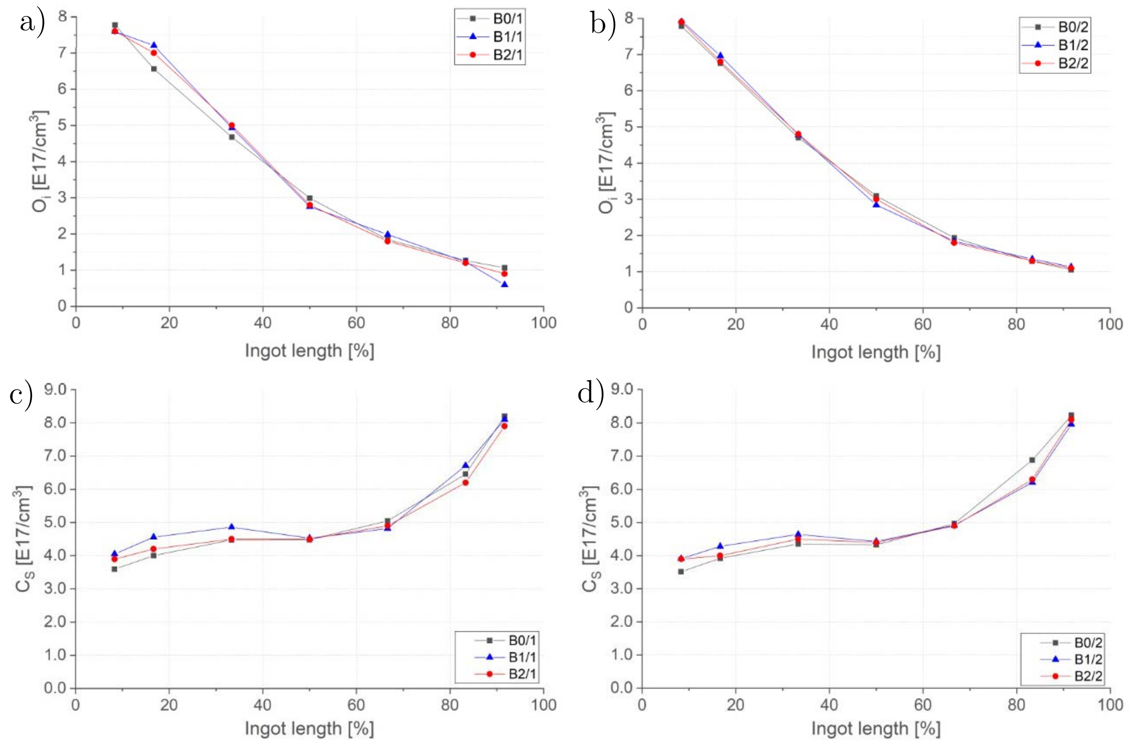

Figure 7.11.: Distribution of O_i and C_s along the central vertical line for ingots grown in positions -/1 and -/2 in experimental sets of Group B: a) O_i for -/1, b) O_i for -/2, c) C_s for -/1, d) C_s for -/2.

Concentrations of interstitial oxygen and substitutional carbon for ingots grown in positions -/1 and -/2 measured by FTIR are given in Figure 7.11. It can be seen that the obtained data were similar for all ingots within a measurement error, which allows to exclude the influence of different oxygen transport on experimental results. Ingots from positions -/3 and -/4 were not measured due to their low resistivity, which are not suitable for FTIR method.

7.3. Variable TMF stirring

In order to examine the influence of TMF melt stirring at different stages of crystal growth, the group of five experimental sets of G0 size mc-Si ingots was grown (Group C consisting of C1, C2, C3, C4 and C5 sets) using two-component travelling magnetic field of variable intensity. For the purpose of minimisation of the cross-influence between neighbouring crucibles, each set consisted of one G0 ingot doped with the same quantity of phosphorus. Since the most pronounced effect of TMF on phosphorus distribution in the experiments conducted for ingots in Group B was observed for ingots grown in position -/1, it was decided that for all growth sets in Group C, G0 ingot is always located in the same position -/1 within the 4×G0 setup and the quantity of dopant placed in every ingot charge is equal to that for -/1 position in Group B sets (Table 7.2). Every set used the same power input recipe as the ones described in previous section, including the prolonged homogenization phase (Figure 7.5). Each set was exposed to two-component travelling magnetic field of variable strength and constant frequencies, phase shifts and current amplitudes ratio. Except for the total effective AC magnitude, the parameters of TMF were identical to those used for the sets in Group B (Table 7.3). The profile of TMF intensity used for each set is given in Figure 7.12. The chamber pressure and argon flow were set to 600 mbar and 6.0 l/min, respectively, and kept constant throughout the entire process.

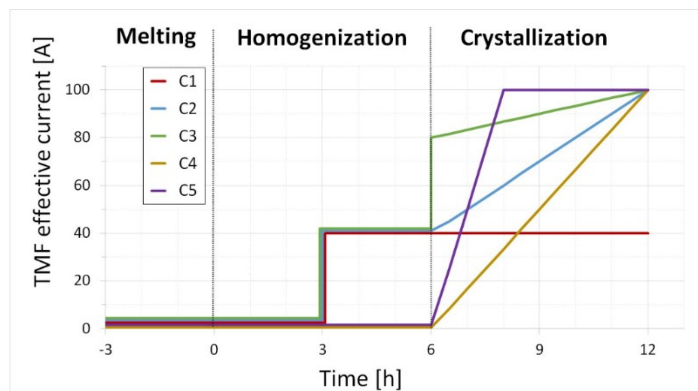

Figure 7.12.: TMF intensity profiles used in the experimental sets of Group C.

The grown ingots were analysed and compared one with another. The distribution of resistivity along the central vertical axis of G0 ingots is depicted in Figure 7.13. Systematic measurement error of FPP setup in the major part of measured resistivity range was less than 2%.

It can be seen that in contrast to the ingots grown within Group A and Group B experiments, resistivity distribution for the ingots of Group C follow the trends, which significantly differ from those for classical BPS and Gulliver-Scheil theories and sometimes remind of exponential behaviour (C1/1 and C2/1). It can be explained by numerous side effects induced by size inconsistency between G1 furnace and G0 ingot, which become more visible in case of growing only one G0 ingot per run. Although the utilization of the obtained resistivity data for the improvement of the dopant segregation model developed in the previous section is greatly complicated, these data can be successfully used for the qualitative analysis of TMF influence at different stages of crystal growth.

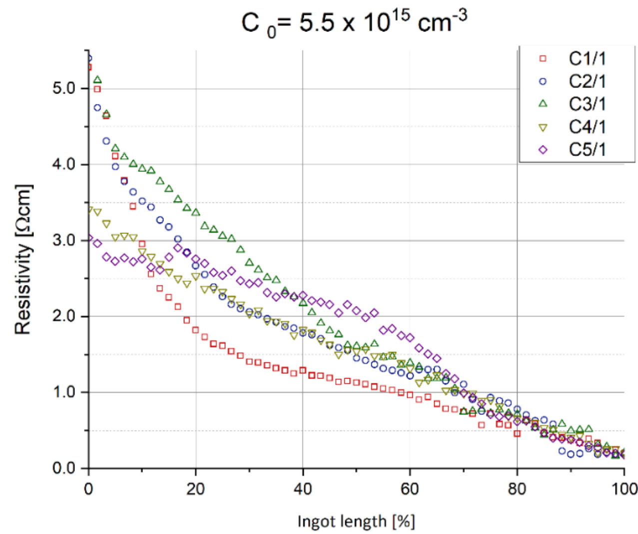

Figure 7.13.: Resistivity distribution along the central vertical axis of G0 ingots grown in position -/1 within 4×G0 setup in the experimental sets of Group C. All the ingots were doped with equal quantity of phosphorus $C_0 = 5.5\times10^{15}$ cm^{-3}.

Ingots which experienced TMF melt stirring already during melt homogenization (C1/1, C2/1 and C1/3) show higher resistivity at the start of crystallization than those which were subjected to TMF influence only during solidification (C4/1 and C5/1). This finding proves the assumption made for experiments in Group B that significant phosphorus evaporation takes place already at homogenization phase. Phosphorus evaporation during crystallization phase is also evidential and follows the same dependence between evaporation and stirring intensity (Figure 7.12 and Figure 7.13). Comparing resistivity distribution for the ingots with the same mixing conditions during homogenization (C1/1 with C2/1

and C1/3, C4/1 with C5/1) it can be concluded that evaporation of phosphorus intensifies with the increase of TMF strength. Moreover, gradual intensification of the melt mixing in the middle of the growth process leads to more homogeneous resistivity distribution along the ingot's length (C4/1 and C5/1). The results obtained for the ingots grown within Group C show that variable melt stirring induced by travelling magnetic field, which is applied throughout the crystallization phase, can be successfully used to flatten resistivity distribution along the ingot's length.

The model developed for the experimental sets in Group B does not explain the behaviour of dopant along the last 20% of ingot's length in Group C. Regardless of melt stirring intensity, the resistivity at the end of all ingots exhibits the same behaviour with nearly identical low values. The explanation lays in the specific pattern of the melt flow during solidification of the last portion of material. At the end of crystallization, the volume of silicon melt becomes critically small and both natural convection and magnetic mixing are inferior to surface effects, which dramatically changes fluid dynamics, hence mass transport in the system. Moreover, the size of G0 ingots is considerably smaller than that for G1, which makes it difficult to maintain steady solidifications in G1 size furnace, particularly at the end of it. Therefore, G0 ingots grown in G1 DS-furnace are prone to rapid freezing after solid fraction of $g_s = 0.80$. It is expected that the effects of rapid freezing and surface driven fluid dynamics be greatly reduced while working with larger ingots. Therefore, further research is performed on G1 size ingots in Chapter 8. Furthermore, it has to be investigated whether the application of enhanced melt stirring by TMF for G1 ingots results in superior phosphorus evaporation during solidification step, since crystallization time is considerably longer and the ratio of melt surface to its volume is somehow larger. This effect is expected to be pronounced, provided that homogenization time is reduced and TMF is applied only after solidification has started. Moreover, taking into account that phosphorus loss strongly depends on stirring intensity, one can change the strength of TMF during solidification, hence control evaporation and dopant distribution along the entire ingot's length.

7.4. Conclusion

In this chapter, the principal possibility to influence resistivity of phosphorus-doped mc-Si ingots by travelling magnetic field was investigated on G0 ingots grown within 4×G0 setup. It was shown that TMF applied during directional solidification significantly enhances melt stirring and influences phosphorus concentration in silicon ingots. For ingots with duration of melt homogenization stage comparable to that for crystallization, the most pronounced effect is

phosphorus evaporation from the melt surface during homogenization, which changes the dopant concentration in the melt and is significantly stronger than the influence of TMF on segregation mechanism. The effect of TMF on resistivity distribution during crystallization phase becomes significant when the melt stirring during melt homogenization is greatly reduced or excluded. During both homogenization and crystallization phases, the evaporation of phosphorus depends on intensity of melt stirring and enlarges with increasing of TMF strength. An adopted DS recipe with TMF of variable strength applied during the crystallization phase while the melt height decreases is expected to be an effective way to enhance/reduce phosphorus evaporation, hence to control resistivity distribution along phosphorus-doped mc-Si ingots. In order to have a precise control of resistivity distribution, the adopted recipe must take into account the dopant evaporation during homogenization phase. More detailed information about the research on G0 scale can be found in a separate paper [Buc19].

CHAPTER 8

Tailoring of resistivity profiles for G1 mc-Si ingots

The research described in this chapter is focused on the influence of various process parameters on resistivity distribution in phosphorus-doped n-type multicrystalline ingots of G1 size grown by directional solidification. The aim of this study is obtaining mc-Si ingots doped with phosphorus that have resistivity distribution similar to the one for boron-doped ingots. In other words, resistivity variation along the ingot's length must be significantly reduced to approach the industry standard for p-type solar wafers, which is in the range of 1 to 3 Ω·cm. In order to reach the desired resistivity distribution, various methods that effect phosphorus transport in silicon melt were applied. According to the fundamental principles and experimental results described in previous chapters, the distribution of phosphorus in mc-Si ingot is defined by effective segregation coefficient k_{eff} and mass transfer coefficient K. The former is responsible for dopant transport from silicon melt into the ingot and depends on diffusion and convection in liquid phase, while the latter reflects the removal of phosphorus from the melt during crystallization process and depends on complex interactions in the bulk melt, on the melt surface and in the gas above the melt (3.12).

The mass transfer component K_m responsible for the dopant transport in the bulk melt as well as effective segregation coefficient k_{eff} are defined by the pattern and magnitude of the melt flow and can be influenced by stirring with external forces, e.g. TMF. This part of phosphorus transfer cannot be described with a simple empirical formula, but can be successfully simulated by numerical methods

based on convection-diffusion (2.9) and solute conservation equations (3.9). In case the melt mixing is significant enough to ensure homogeneous distribution of phosphorus across the bulk melt, K_m is not the limiting parameter in phosphorous removal. When the melt flow does not provide the uniform dopant distribution, the mass transfer at this stage has a noticeable influence on the total mass transfer coefficient.

In contrast to the mass transfer coefficient in bulk melt K_m, the mass transfer components for the surface boundary layer K_s, evaporation K_e and gas phase K_g can be evaluated for each individual process using analytical relations (3.14), (3.18) and (3.26), respectively. The components of mass transfer coefficient as functions of temperature calculated for typical G1 process are given in Figure 8.1. In order to define the rate-controlling steps of phosphorus evaporation at different temperature conditions, the calculations were performed for a broad temperature range from melting point up to 2500 K and used process parameters typical for G1 ingots (gas pressure and argon flow are set conditions during the growth, melt flow velocity is obtained by numerical simulation). It can be seen that in the range of standard process temperatures close to the silicon melting point K_e is noticeably lower than K_s and K_g. Hence, for uniform dopant distribution in the melt, phosphorus evaporation is the rate-controlling step in dopant transport.

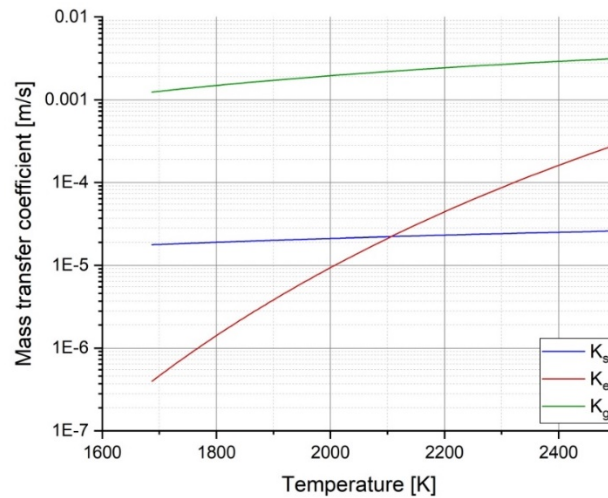

Figure 8.1.: Mass transfer coefficients of phosphorus for surface boundary layer K_s, evaporation K_e and gas phase K_g as functions of temperature calculated for typical G1 process parameters (u_{surf} = 5×10^{-4} m/s, u_{gas} = 6 l/min, P = 600 mbar).

It must be taken into account that the mass transfer coefficient of evaporation is strongly dependent on the chamber pressure P. The calculated function for different process temperatures is shown in Figure 8.2. It can be seen that K_e greatly increases with the reduction of the chamber pressure. Hence, conducting the growth

process at low pressures can significantly enhance phosphorus evaporation. When the chamber pressure is low enough, K_e might reach the value comparable with K_s, thus transfer in the surface boundary layer will have a noticeable influence on total mass transfer coefficient (3.12).

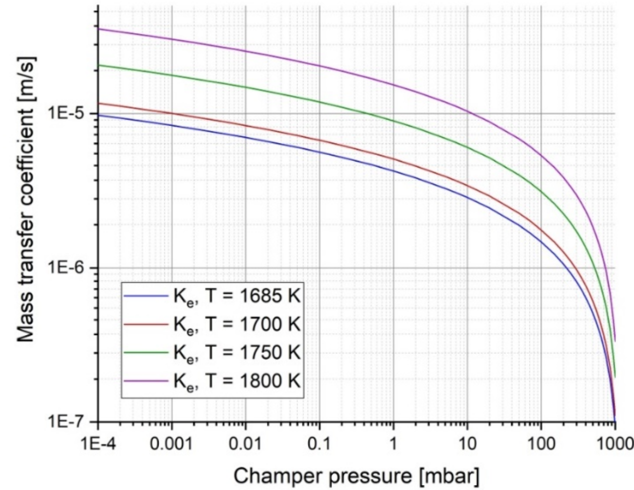

Figure 8.2.: Mass transfer coefficient of phosphorus evaporation as a function of pressure for different process temperatures.

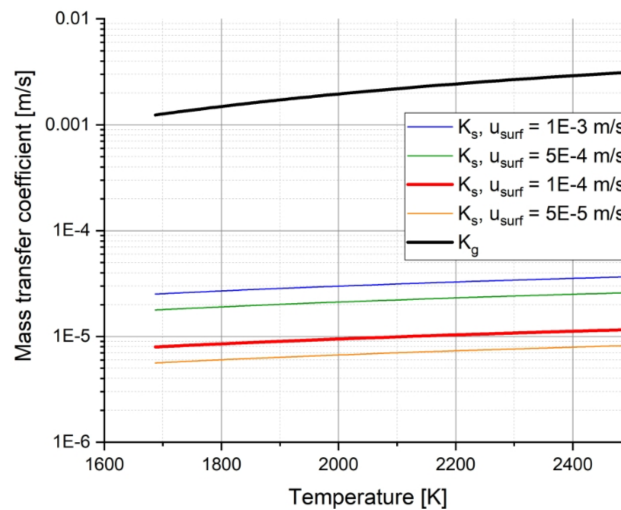

Figure 8.3.: Mass transfer coefficient of phosphorus in the gas phase and in the surface boundary layer as a function of temperature for different surface velocities of the melt.

One of the main parameters that affect dopant transfer in the surface boundary layer is surface velocity of the melt (3.14). K_s for different surface velocities assumed from numerical evaluation of typical DS process is depicted in Figure 8.3. It can be seen than phosphorus transfer increases as the melt velocity grows. However, even for high rates of u_{surf} and elevated temperatures, K_s is still significantly lower than

K_g, thus transport in the gas phase does not influence the total phosphorus mass transfer.

Taking into account all relations between process parameters and dopant transfer, the most promising candidates to influence phosphorus transport during directional solidification are chamber pressure and melt convection induced by external force fields. Since double-frequency travel magnetic field has already proven to be an effective method for enhancing phosphorus evaporation in the research described in Chapter 7, particular attention was given to this tool. As resistivity variation of phosphorus-doped ingots is almost twice larger than that for boron-doped ones (Figure 3.3), the most reliable approach is to focus on two ingot areas with critical resistivity values. Namely, to reduce resistivity at the bottom of the ingot by suppression of phosphorus evaporation in the beginning of crystallisation, and to increase resistivity at the top of the ingot by enhancing of phosphorus evaporation in the end of crystallization.

The parameter study was conducted on G1 multicrystalline ingots with dimensions of 22×22×12 cm^3 and weight of 14 kg, and consisted of 8 experimental growth processes with different parameters of TMF, purging gas flow and chamber pressure. In order to obtain comparable results, all ingots were doped with the same quantity of phosphorus to provide the concentration in ingots charge $C_0 = 4.5\times10^{-15}$ cm^{-3}, which according to Gulliver-Scheil equation (2.10) must result in resistivity range 3.3 – 0.2 Ω·cm along the ingot's length. Such concentration was chosen in order to meet the requirements for resistivity specification 3.0 – 1.0 Ω·cm that is typical for PV industry. Although the aim of the conducted study was resistivity homogenization, particular attention was also given to the quality of the grown ingots. Since the performance of solar cells is defined by the complex properties of silicon wafers, the growth procedure must provide mc-Si material of appropriate quality. Therefore, the complex characterisation including minority carrier lifetime, impurity concentration, spatial resistivity distribution, crystalline structure etc. was conducted for all ingots.

At the first stage of the parameter study, a reference G1 ingot D0 was grown using the power input recipe, which was developed in the set of preliminary experiments and implied a growth rate in the range of 1.0 – 1.2 cm/h (Figure 8.4). A typical temperature profile for the utilized G1 recipe is given in Figure 6.6. In order to minimize phosphorus evaporation at the beginning of crystallization, the melt homogenization phase was set to 30 minutes, which is significantly shorter than 12 h duration of crystallization phase. The conditions of the growth process were maximally close to the standard ones for PV industry, which for a G1 size system means ambient pressure of 600 mbar, argon flow of 6.0 l/min and no TMF applied during solidification. With the aim of visualisation of growth progression 5 TMF markers with total effective current of $I_{eff} = 40$ A were applied at fixed process times.

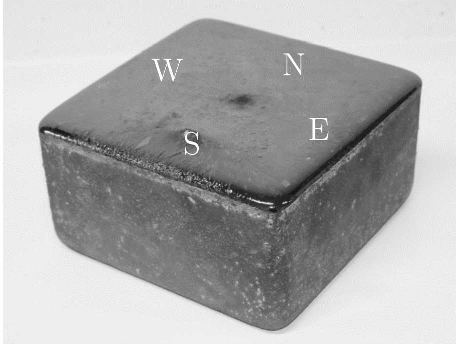

Figure 8.4.: Reference G1 ingot D0 of 22×22×12 cm³ size and 14 kg weight and cardinal marking.

7 subsequent G1 ingots experienced various alterations of process parameters with the aim of improvement of resistivity profile. In order to minimise the complex influence of different factors on dopant distribution, the parameter study was conducted according to a progressive optimisation strategy, which implied the sequence of comparative experiments where only one process parameter was altered at a time. The process parameters for each experiment are given in every respective chapter. Additionally, a summarized list of growth experiments and the detailed process conditions are presented in Table 10.3. in Appendix.

8.1. TMF at early stages of crystallisation

According to the results obtained for G0 ingots in Chapter 7, travelling magnetic field applied during crystallization of mc-Si material have a noticeable effect on resistivity distribution. In order to evaluate this impact in larger dimensions, an ingot D1 of G1 size was grown under the influence of two-component TMF with moderate intensity and constant magnitude, while keeping all other process conditions identical to the reference ingot. The parameters of TMF used in the experiment were defined in previous experiments [Kie18]. All process parameters are given in Table 8.1. Temperature and TMF intensity profiles are shown in Figure 8.5. In order to visualise the shape of solid-liquid interface and growth progression, 5 TMF markers with total effective current of $I_{eff} = 80$ A were applied at the same process times as in the reference ingot D0.

Ingot		D0	D1
Travelling magnetic field	Start I_{eff}, [A]	0	40
	Change I_{eff}, [A]	–	–
	Ramp at solid fraction	–	–
	I_1/I_2	–	10
	f_1 [Hz]	–	20
	f_2 [Hz]	–	200
	ϕ_1	–	+90°
	ϕ_2	–	–90°
Pressure	Start P, [mbar]	600	600
	Change P, [mbar]	–	–
	Ramp at solid fraction	–	–
Gas flow	Start u_{gas}, [l/min]	6.0	6.0
	Change u_{gas}, [l/min]	–	–
	Ramp at solid fraction	–	–

Table 8.1.: Process conditions for ingots D0 and D1.

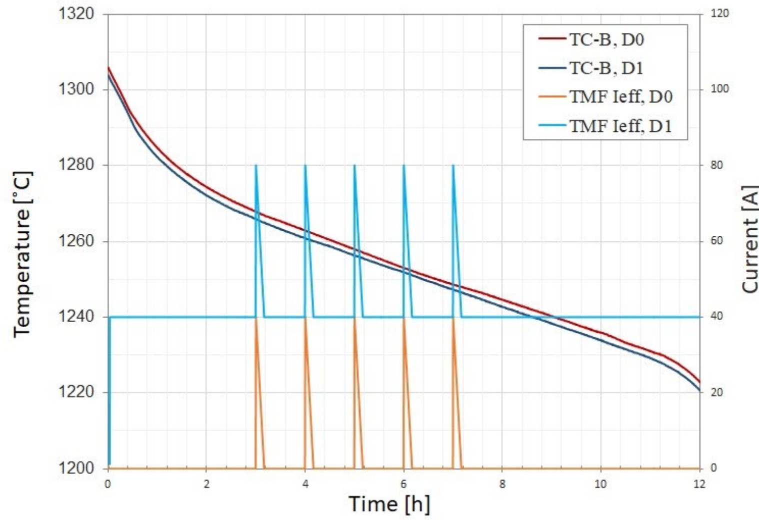

Figure 8.5.: Temperature and TMF intensity profiles used for crystallisation of D0 and D1 ingots.

The process time between complete melting and the end of crystallization of D1 ingot indicated by thermocouples and pyrometer was identical to the one for D0 ingot; hence, the average growth rate of two ingots was equal. The LPS images measured on longitudinal central cuts are given in Figure 8.6. They show similar distances of 1.0 – 1.2 cm between all TMF markers along the ingot's length for both ingots. Since the time between neighbouring markers was set to 1 hour, it can be concluded that both ingots had stable growth rate of 1.0 – 1.2 cm/h during the entire crystallization process. However, the shape of solid-liquid interface is

noticeably different for these two processes. While ingot D0 reveals a more convex growth front, TMF with total effective current of I_{eff} = 40 A applied during D1 growth resulted in a flatter interface, which is favourable for vertically prolonged columnar grains and relaxation of stresses, and slightly concave areas near the crucible walls. This shaping is the result of the applied second frequency and the influence of the acting Lorentz forces on the melt flow. It is also worth noting that both LPS images are slightly tilted to the east (right side). This fact confirms that G1 hot zone is not perfectly symmetric and the west side is somehow colder than the east side, thus it crystalizes earlier. This peculiarity must be taken into account while analysing material properties, which means that only parameters measured at equal positions within an ingot should be compared with each other.

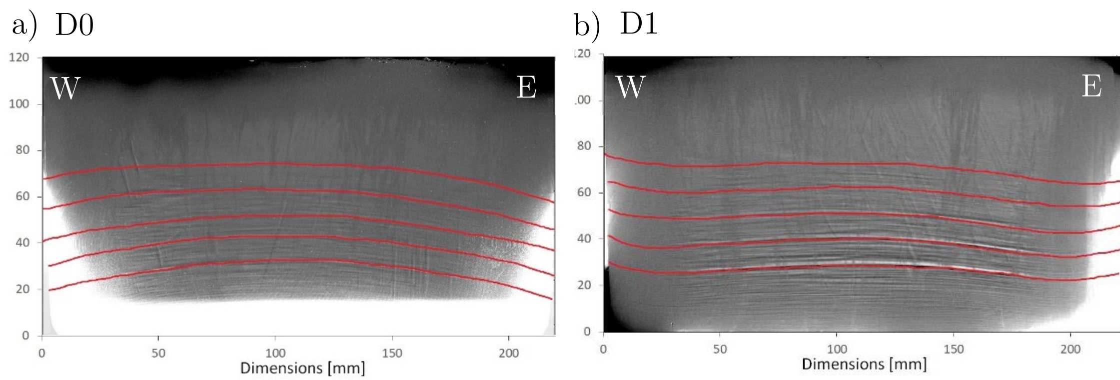

Figure 8.6.: LPS images of D0 (a) and D1 (b) ingots. TMF markers are indicated with red curves.

Resistivity maps measured on longitudinal central cuts are shown in Figure 8.7. Resistivity isolines indicate typical segregation behaviour along the entire solid-liquid interface. Similar to LPS images they also show asymmetric properties with a slight tilt to the east.

The maps show that D0 ingot has noticeably higher resistivity in the lower part than that for D1, while the values in the top part are similar for both ingots. A detailed comparison can be made using the data measured along the same vertical line. The distributions of resistivity along the central and side vertical lines of D0 and D1 ingots are given in Figure 8.8. The side lines are located at a distance of 1 cm from the respective edges. Systematic measurement error of the measurement is less than 2%. It can be seen that D1 ingot have resistivity similar to Scheil distribution, while D0 exhibit higher values in the first half of the ingot. Surprisingly, the lower resistivity for G1 ingot grown under the influence of two-component TMF with I_{eff} = 40 A is in contradiction to the results obtained for G0 ingots grown under the same conditions (Figure 7.9). Hence, it cannot be explained only by simple theoretical consideration of more intensive evaporation rate in the presence of external fields.

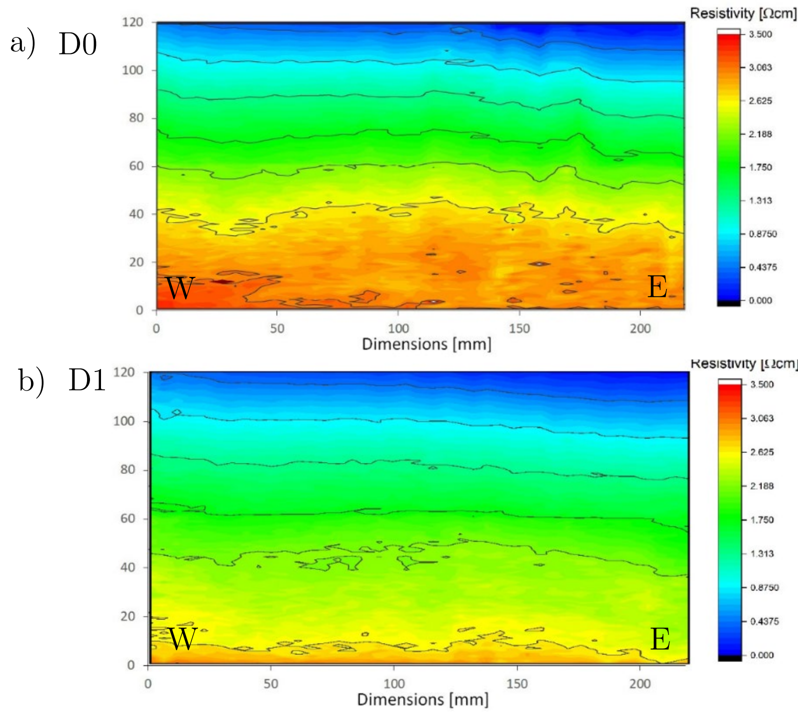

Figure 8.7.: Resistivity maps of D0 (a) and D1 (b) ingots.

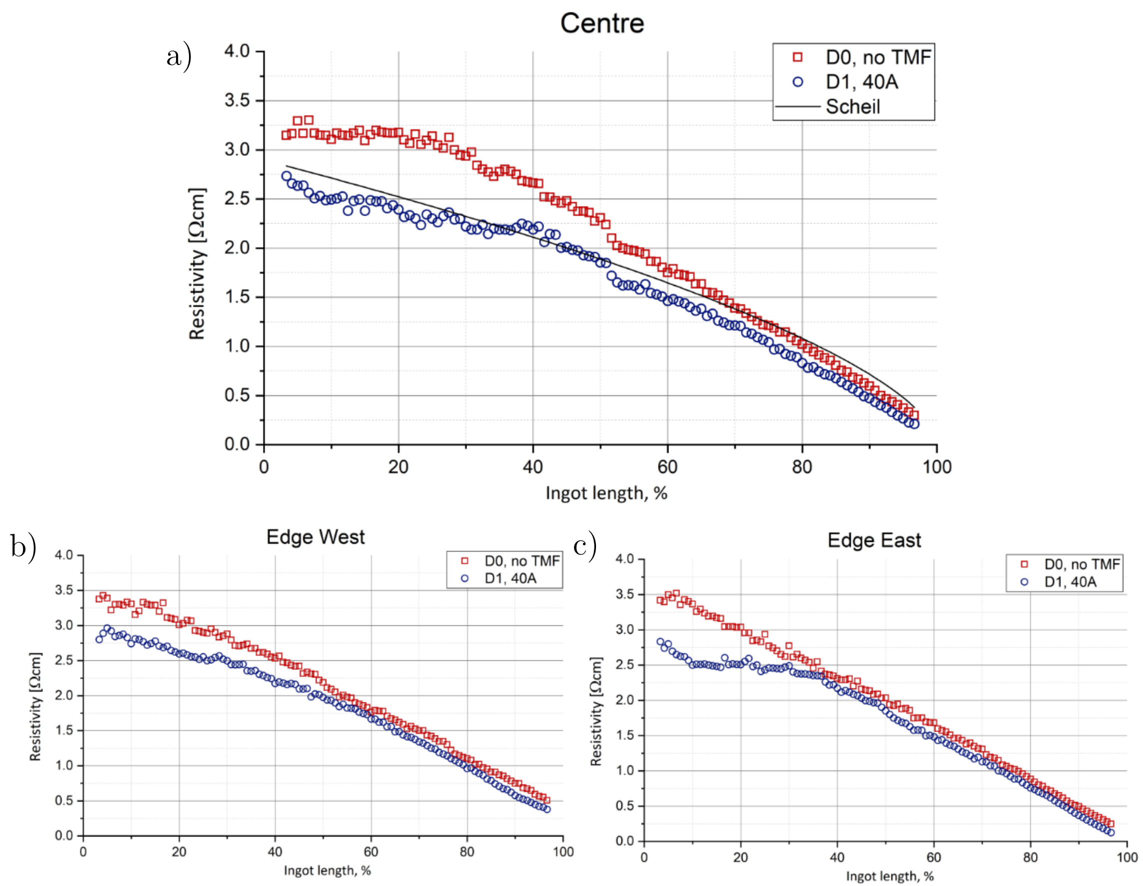

Figure 8.8.: Resistivity distribution along the vertical lines for D0 and D1 ingots: a) central line, b) west edge line, c) east edge line.

In order to study the mechanisms that take place in the melt under the given growth conditions, the mass transport for the investigated growth parameters was evaluated by numerical simulation [Dad19]. The model considered both phosphorus segregation and evaporation during the growth process. However, it did not take into consideration the influence of temperature on mass transfer coefficient. The simulation was performed for the growth rate of υ_{gr} = 1.2 cm/h, phosphorus diffusion coefficient $D = 4.0\times10^{-8}$ m^2/s and phosphorus mass transfer coefficient $K = 1.0\times10^{-6}$ m/s.

The simulation showed that the applied two-component TMF with I_{eff} = 40 A significantly changes the flow pattern of the melt during the first stages of solidification process when the melt height is large. It eliminates the double-torus structure of the flow typical for natural convection and increases the melt velocity at the solid-liquid interface (Figure 8.9). As a result, the TMF of the given configuration increases phosphorus evaporation from the melt surface, but at the same time homogenizes dopant concentration at the solid-liquid interface, thus results in more uniform resistivity distribution in the first half of the ingot. In other words, the applied configuration of the travelling magnetic field affects both segregation and evaporation through mass transfer and effective segregation coefficients. The resulted resistivity distribution for both cases is given in Figure 8.10. The obtained data show similar trend to the ones observed in experiments, hence the simulated model describes the process acceptably well. It can be seen that simulated resistivity profiles are somehow steeper than those for experimentally grown ingots are. Since the slope of the curves depends on the evaporation rate, it can be concluded that the real mass transfer coefficient of phosphorus for the given system is smaller than that assumed in the simulation.

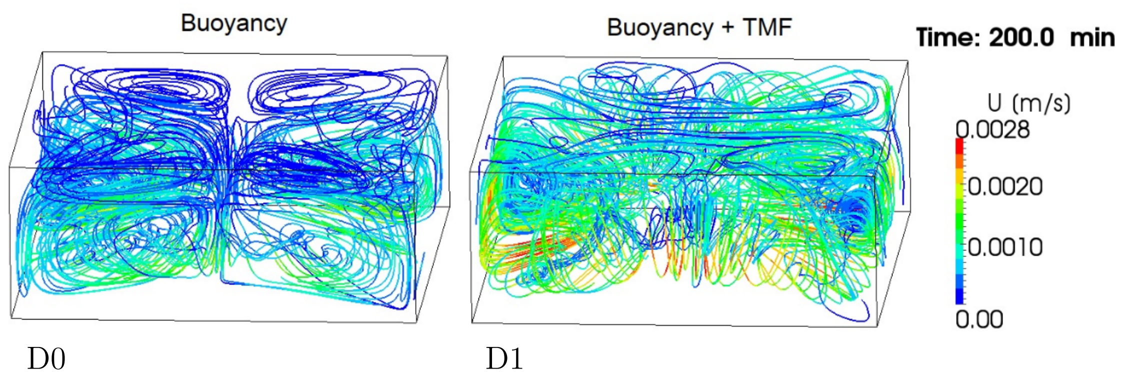

Figure 8.9.: Melt flow after 200 min of solidification for D0 and D1 ingots obtained by numerical simulation.

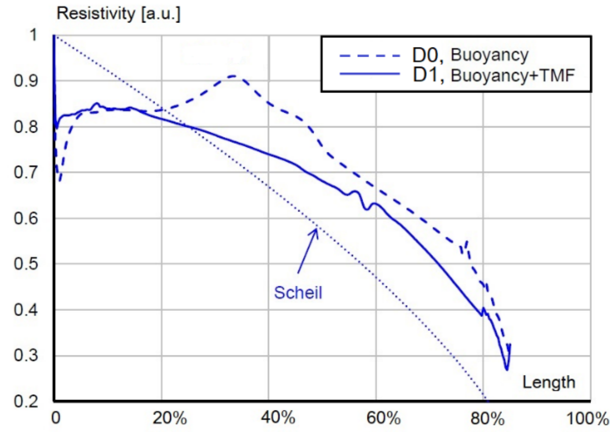

Figure 8.10.: Simulated resistivity distribution for G1 ingots grown under process conditions of D0 and D1.

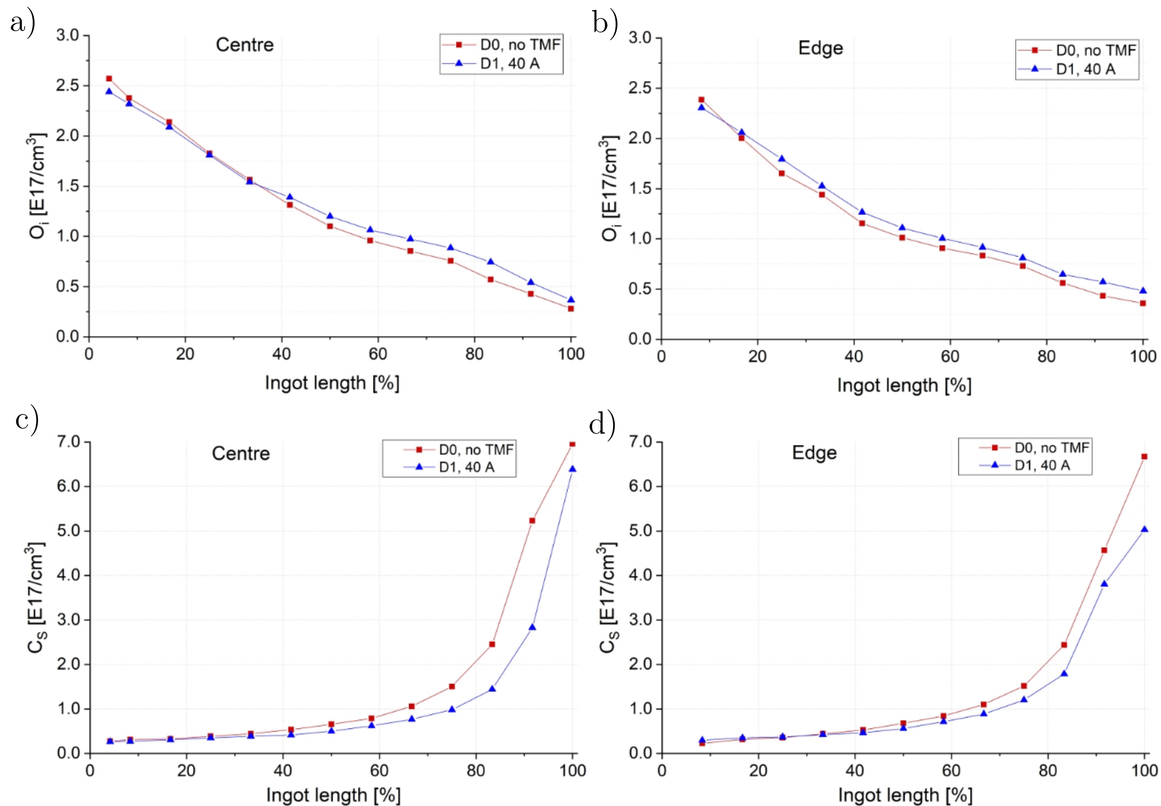

Figure 8.11.: Distribution of O_i and C_s along the vertical lines for D0 and D1 ingots: a) O_i along the central line, b) O_i along the edge line, c) C_s along the central line, d) C_s along the edge line.

The influence of the applied process parameters on the material quality were also evaluated. Vertical cuts of the experimental and reference ingots were measured by FTIR along the central and the east side lines. The measured data are shown in Figure 8.11. The intensified stirring induced by TMF concludes in slightly higher interstitial oxygen concentration in D1 ingot. It is assumed that

increased velocity of the melt flow leads to more uniform distribution of dissolved oxygen in the silicon melt, thus to the reduced oxygen gradient in the vicinity of crucible walls, which in turn enhances further oxygen diffusion from the crucible to the melt. However, this enlargement is not critical and lays within the typical process-to-process fluctuations. In contrast to oxygen, substitutional carbon is advantageously lower for D1 ingot. This phenomenon can be explained by improved mixing at the solid-liquid interface, which reduces the diffusion boundary layer, hence leads to the reduction of carbon incorporated into the ingot.

Another important characteristic of mc-Si material is charge carrier lifetime, since it defines the performance of solar cells. The results of MDP measurements conducted on the longitudinal cuts are given in Figure 8.12. The average lifetime was defined for a central area of the same size indicated by a dotted rectangle that excludes the typical low-quality red zone at the rim. Both D0 and D1 ingots showed identical level of charge carrier lifetime and the size of the red zone. Therefore, it can be concluded that the alteration of resistivity, oxygen and carbon distribution induced by the applied TMF is not supposed to affect the performance of mc-Si material in solar cells.

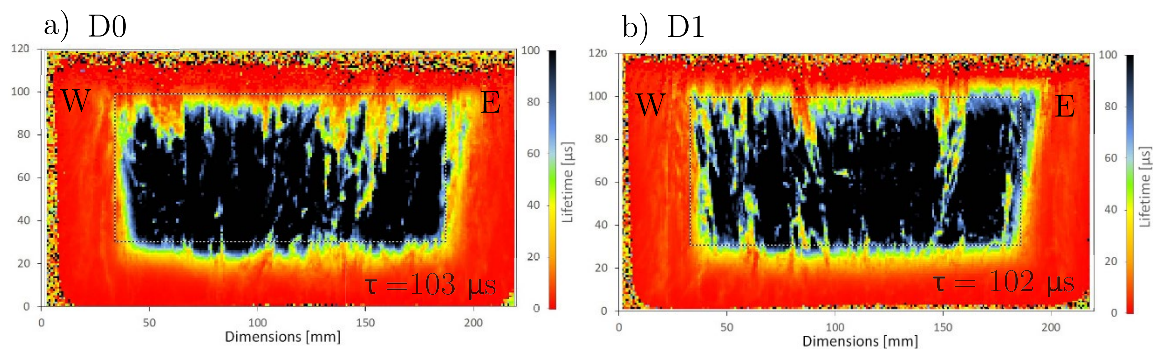

Figure 8.12.: MDP images of D0 (a) and D1 (b) ingots. The average lifetime is calculated for the area indicated with a dotted rectangle.

In summary, two-component traveling magnetic field with total effective current of I_{eff} = 40 A applied during the growth of phosphorus-doped G1 mc-Si ingots noticeably reduces resistivity at early stages of crystallization, which fulfils one of the requirements for resistivity homogenization. An additional advantage of the chosen approach is a more beneficial shape of solid-liquid interface. At the same time, the applied TMF insignificantly increases interstitial oxygen concentration and decreases substitutional carbon concentration, while not affecting the average carrier lifetime and the size of the red zone at the rim.

8.2. Intensification of TMF at later stages of crystallisation

Although travelling magnetic field of moderate intensity results in flatter resistivity distribution in the first half of G1 ingots, it does not have a distinguishable influence on phosphorus concentration at the end of the ingot. Taking into account the findings of the research conducted at G0 scale, it is expected that evaporation of phosphorus will intensify with the increase of TMF strength. As the next stage of the research, the growth conditions of D1 ingot were supplemented with rapid enlargement of TMF current to the double value at the half of the ingot's height, which corresponds to the enlargement of Lorentz force by 4 times. The adopted recipe was used for crystallisation of experimental ingot D2. The process parameters used during the growth are presented in Table 8.2. Temperature and TMF intensity profiles are shown in Figure 8.13.

Ingot		D1	D2
Travelling magnetic field	Start I_{eff}, [A]	40	40
	Change I_{eff}, [A]	–	80
	Ramp at solid fraction	–	0.33
	I_1/I_2	10	10
	f_1 [Hz]	20	20
	f_2 [Hz]	200	200
	ϕ_1	+90°	+90°
	ϕ_2	–90°	–90°
Pressure	Start P, [mbar]	600	600
	Change P, [mbar]	–	–
	Ramp at solid fraction	–	–
Gas flow	Start u_{gas}, [l/min]	6.0	6.0
	Change u_{gas}, [l/min]	–	–
	Ramp at solid fraction	–	–

Table 8.2.: Process conditions for ingots D1 and D2.

Similar to the previous growth experiments, for the purpose of visualisation of solid-liquid interface, 5 TMF markers with total effective current of $I_{eff} = 120$ A were applied during the growth of D2 at the same process times as in D0 and D1 ingots. The temperature profiles and the duration of crystallization were similar to those for previous experiments; hence, the average growth rate of D1 and D2 ingots was identical. The LPS images measured on central vertical cuts of D1 and D2

ingots are shown in Figure 8.14. Both images show similar distances between all TMF markers, which are 1.0 – 1.2 cm, hence indicate uniform growth rate of 1.0 – 1.2 cm/h during the entire crystallization process. Although the shapes of solid-liquid interface look alike, it can be seen that the tilt to the east side for D2 ingot becomes smaller at later process stages. It is supposed that the melt mixing induced by stronger TMF applied during the second half of solidification is more intense, thus the temperature along the solid-liquid interface is more uniform, which flattens the growth front.

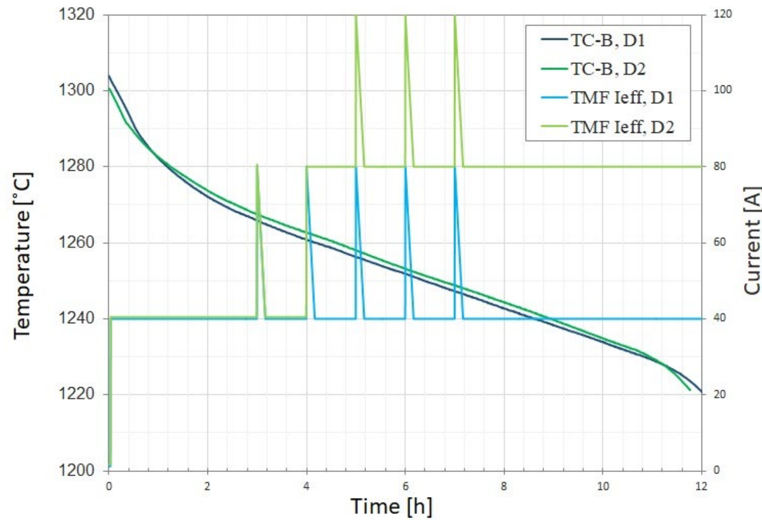

Figure 8.13.: Temperature and TMF intensity profiles used for crystallisation of D1 and D2 ingots.

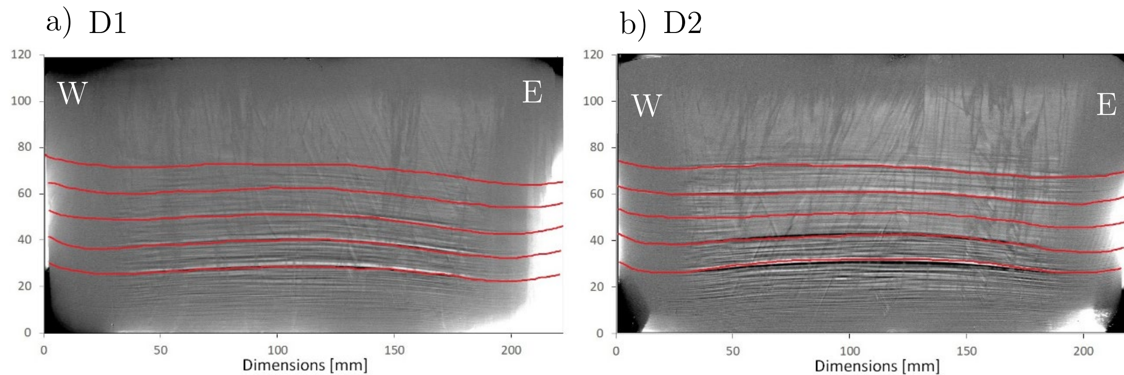

Figure 8.14.: LPS images of D1 (a) and D2 (b) ingots. TMF markers are indicated with red curves.

Resistivity distributions measured along the central and side vertical lines of D1 and D2 ingots are depicted in Figure 8.15. Since the process conditions for both cases are identical up to solid fraction of $g_s = 0.33$, resistivity distribution in this area was expected to be similar for both ingots, which is confirmed by the measured

data. In the second half of the plot where the intensity of TMF for D2 ingot was enhanced, one can observe the expected gradual increase of resistivity. The effect is bigger than the measurement error. The behaviour of resistivity for the central and side lines is similar, which together with LPS images proves that the growth front was sufficiently flat and dopants were uniformly distributed along the solid-liquid interface.

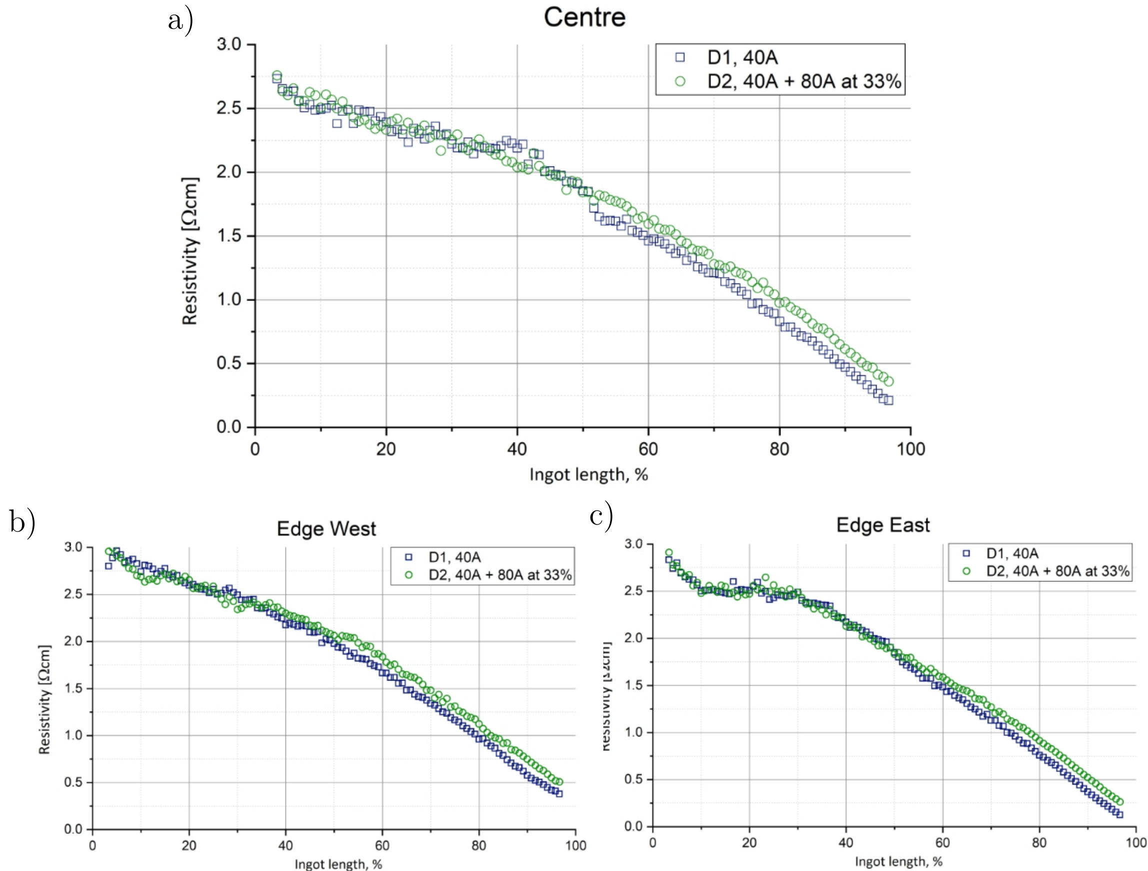

Figure 8.15.: Resistivity distribution along the vertical lines for D1 and D2 ingots: a) central line, b) west edge line, c) east edge line.

The increase of resistivity in the second half of D2 ingot can be explained with intensified phosphorus removal induced by enhanced melt stirring, which was also observed in G0 experiments. Numerical simulation performed for solid fraction of $g_s = 0.50$ shows that the increase of the total effective current I_{eff} of double frequency TMF from 40 A to 80 A changes the pattern and increases the magnitude of the melt flow (Figure 8.16). In such a way, the change of TMF parameters has an influence on the phosphorus mass transfer coefficient in the bulk melt K_m. It also has to be kept in mind that the changes in the melt flow lead to the alteration of the melt surface temperature, thus also effect mass transfer coefficient of phosphorus evaporation K_e. It also has to be mentioned that the performed numerical simulation describes G1 crystallisation process only in general and does

not take into account all process features (e.g. the shape of solid-liquid interface does not fully correspond to the measured one in its central part). Therefore, the data obtained by numerical modelling can only be used for rough estimation of process parameters, not as a precise guidance.

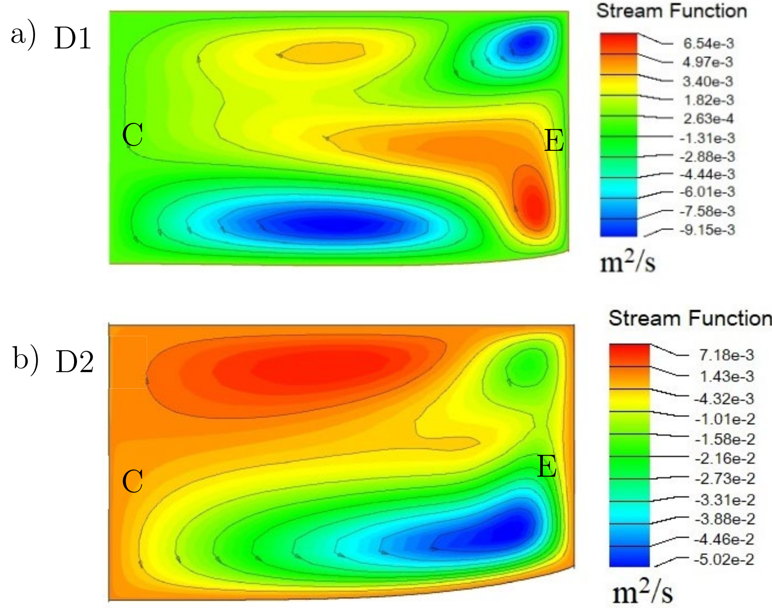

Figure 8.16.: Melt flow after 6 hours of solidification for D1 (a) and D2 (b) ingots obtained by numerical simulation.

In order to evaluate the influence of the investigated process conditions on dopant transport, the detailed analysis of phosphorus distribution along the ingot's length was performed. The phosphorus concentration profiles for D1 and D2 ingots shown in Figure 8.17. were built using the measured resistivity data from Figure 8.15. and standardized relations for semiconductor silicon [Thu80a]. A segregation model for dopant distribution in the second half of D2 ingot was built through OLS curve fitting. The model is described by the modified Gulliver-Scheil equation (3.11)

$$C_s(g_s) = k_{eff}C_0(1-g_s)^{k_{eff}+\frac{K}{v_{gr}}-1} \tag{3.11}$$

using resistivity distribution of D1 ingot as a baseline and the growth rate v_{gr} = 1.0 cm/h. The fitting curve is in a good agreement with the experimental data for total mass transfer coefficient of phosphorus $K = 3.31\times10^{-7}$ m/s. The obtained value lies in the range of theoretically calculated mass transfer coefficient of evaporation (Figure 8.1), which means that both K_m and K_e coefficients are rate-defining parameters for the considered DS system.

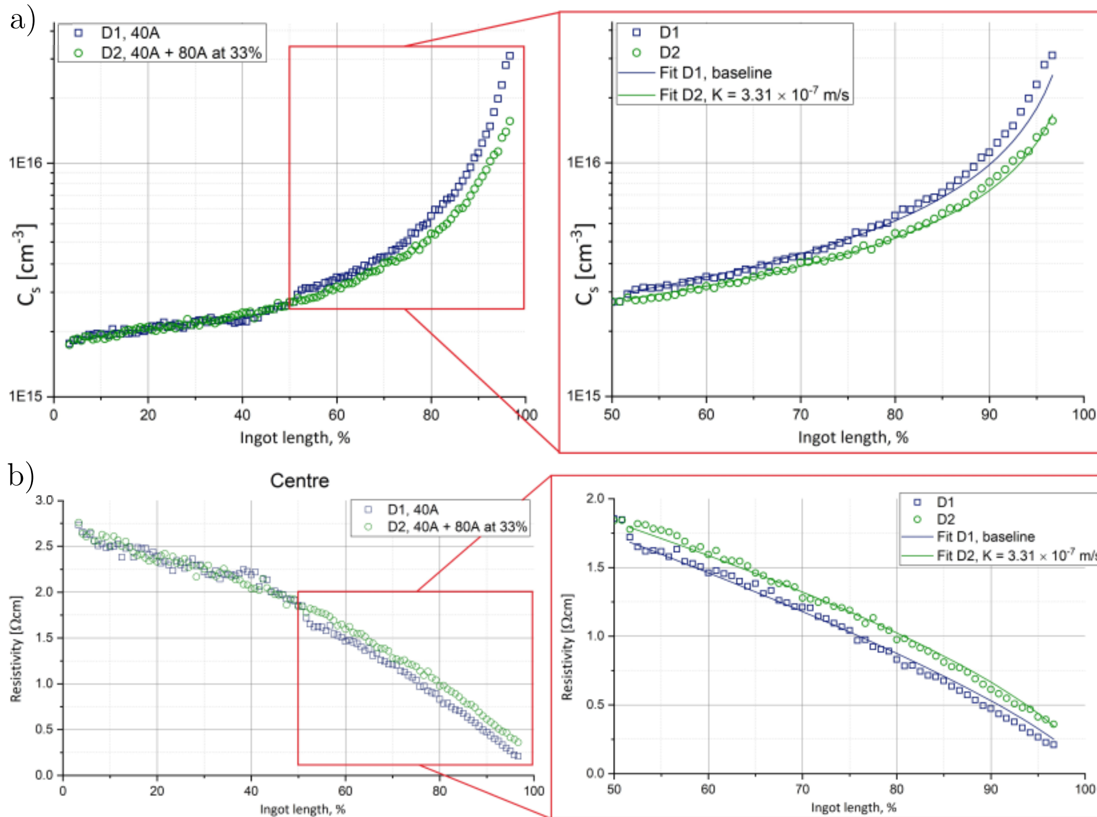

Figure 8.17.: Distribution of phosphorus concentration (a) and resistivity (b) along the ingot's length for D1 and D2 ingots. The discrete points correspond to the data derived from measured resistivity (Figure 8.15). The solid curves are numerical fitting based on modified Gulliver-Scheil equation (3.11).

On the one hand, it can be expected that TMF of higher intensity will enlarge the phosphorus mass transfer coefficient, thus increase the resistivity at the end of crystallisation further. However, on the other hand, too intensive melt mixing can disturb the stable growth process by provoking turbulent melt flow and structure breakage. Due to the differences in thermal properties, the upper limit of TMF intensity can vary from one growth equipment to another. The conditions for turbulent melt flow in the used G1 equipment were not investigated yet. Therefore, further increase in TMF current above 80 A was not performed within this research work.

The effect of the applied TMF on oxygen and carbon distribution was also investigated. The data measured by FTIR are presented in Figure 8.18. Similar to the results obtained in the previous section, more intense melt stirring induced by TMF of higher effective current applied to G1 DS process at solid fraction of $g_s =$ 0.33 concludes in slightly higher interstitial oxygen and lower substitutional carbon concentrations at the end of D2 ingot than those observed for D1 ingot, which confirms that melt mixing is tightly connected with oxygen diffusion from crucible and homogenization of spices at the solid-liquid interface.

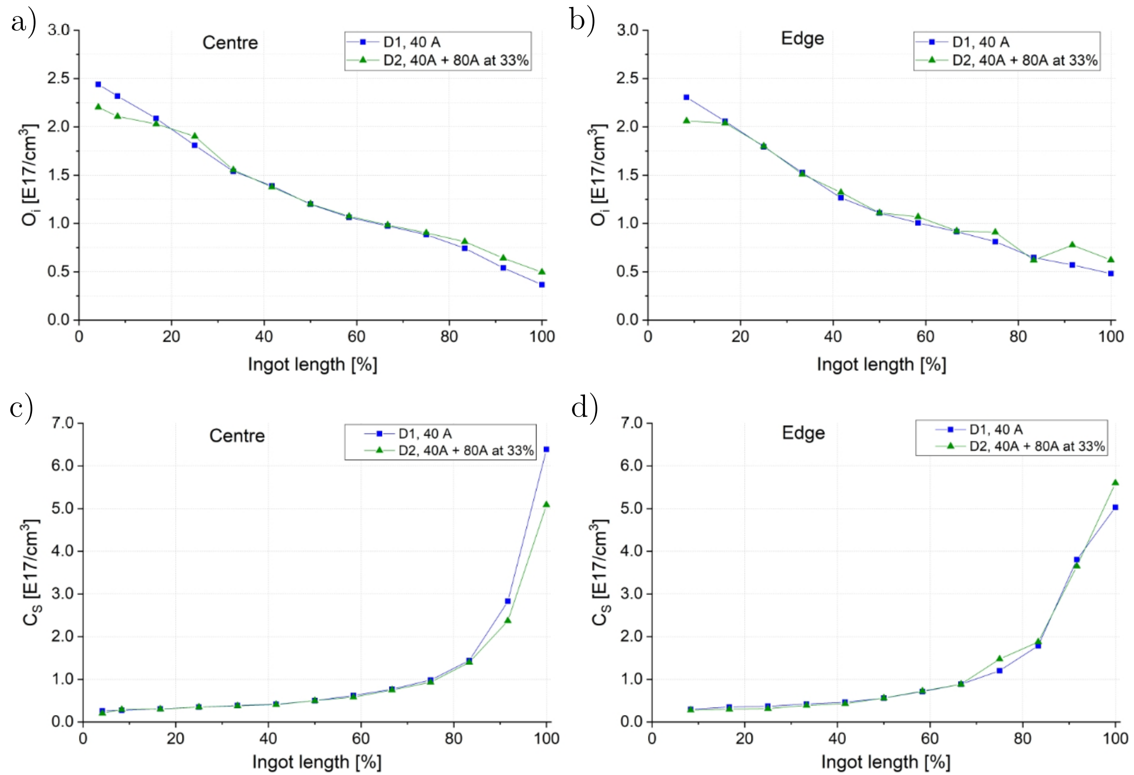

Figure 8.18.: Distribution of O_i and C_s along the vertical lines for D1 and D2 ingots: a) O_i along the central line, b) O_i along the edge line, c) C_s along the central line, d) C_s along the edge line.

The MDP images given in Figure 8.19. show the same level of the average charge carrier lifetime as well as the identical size of the red zone for D1 and D2 ingots, which indicates that the increase of the effective current for double-frequency TMF from 40 A to 80 A does not yet have a deteriorating influence on the quality of phosphorus-doped G1 mc-Si ingots.

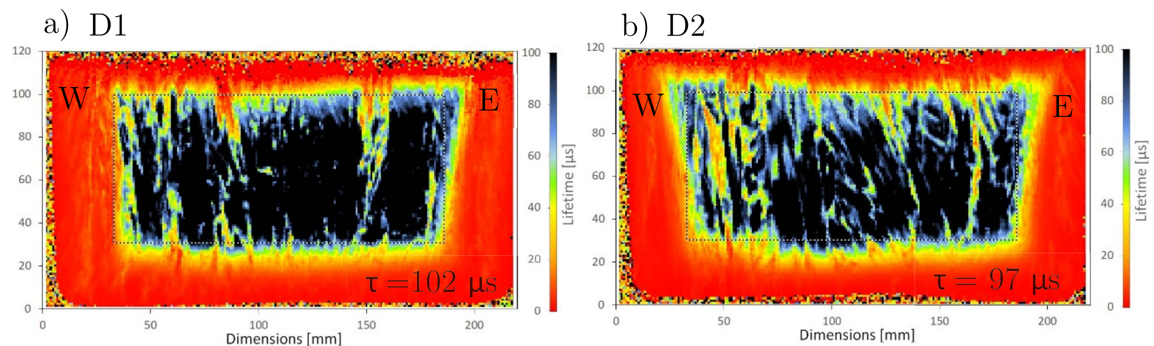

Figure 8.19.: MDP images of D1 (a) and D2 (b) ingots. The average lifetime is calculated for the area indicated with a dotted rectangle.

The obtained data show that two-component traveling magnetic field with total effective current of $I_{eff} = 80$ A applied to phosphorus-doped G1 mc-Si ingots at solid fraction of $g_s = 0.33$ meets the requirements for resistivity homogenization by increasing resistivity at late stages of crystallization. The chosen process parameters flatten solid-liquid interface, which is favourable for the stable grain growth. Similarly to the TMF of smaller intensity, the applied TMF results in insignificantly higher oxygen and lower carbon concentration, and has no influence on the magnitude and distribution of carrier lifetime.

8.3. Gas flow

The next stage of the study was focused on evaluation of phosphorus transport in the gas phase. For this purpose, two experimental G1 ingots D3 and D4 were grown using an elevated argon flow above the melt. In order to eliminate the superposition of different transfer mechanisms, the recipes of the experimental ingots were based on the reference ingot D0, implying using no melt mixing with TMF during the entire growth process. The argon flow for the experimental ingots was increased at different stages of the process up to 8.0 l/min (D3) and 9.0 l/min (D4) compared to 6.0 l/min used for the reference ingot. The process parameters used during the growth are presented in Table 8.3. Temperature and gas flow profiles are given in Figure 8.20.

Ingot		**D0**	**D3**	**D4**
Travelling magnetic field	Start I_{eff}, [A]	0	0	0
	Change I_{eff}, [A]	–	–	–
	Ramp at solid fraction	–	–	–
	I_1/I_2	–	–	–
	f_1 [Hz]	–	–	–
	f_2 [Hz]	–	–	–
	ϕ_1	–	–	–
	ϕ_2	–	–	–
Pressure	Start P, [mbar]	600	600	600
	Change P, [mbar]	–	–	–
	Ramp at solid fraction	–	–	–
Gas flow	Start u_{gas}, [l/min]	6.0	6.0	6.0
	Change u_{gas}, [l/min]	–	8.0	9.0
	Ramp at solid fraction	–	0.58→1.00	0.50→0.58

Table 8.3.: Process conditions for ingots D0, D3 and D4.

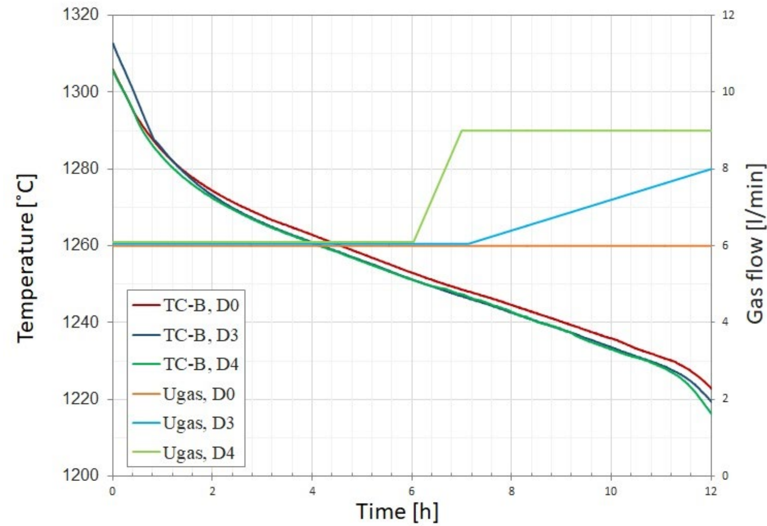

Figure 8.20.: Temperature and gas flow profiles used for crystallisation of D0, D3 and D4 ingots.

Resistivity distribution measured along the central line of respective vertical cuts for D0, D3 and D4 ingots are shown in Figure 8.21. The experimental ingots experience insignificant increase of resistivity in their second half. However, the magnitude of this increase is in the range of the measurement error, therefore it cannot be considered as relevant. This finding is in correspondence with theoretical calculation (Figure 8.1) stating that phosphorus transport in the gas phase is not a defining stage in dopant transfer during directional solidification process.

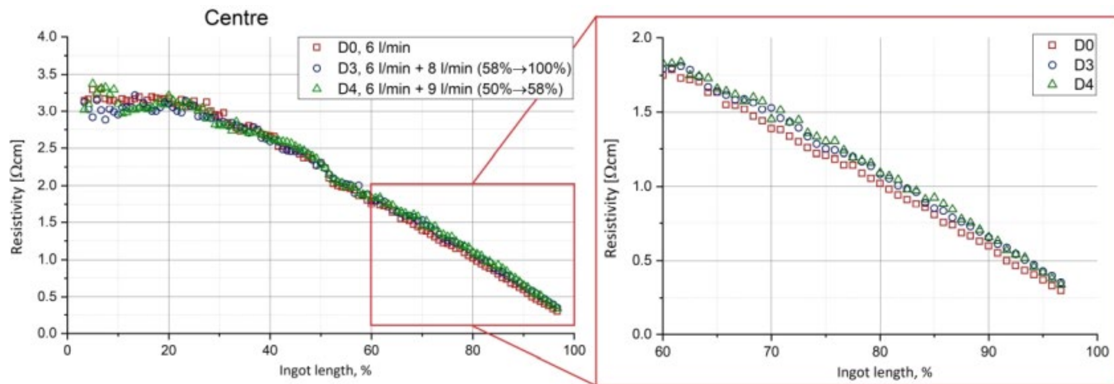

Figure 8.21.: Resistivity distribution along the central vertical line for D0, D3 and D4 ingots.

The obtained results show that the intensification of purging gas flow during directional solidification has no noticeable impact on phosphorus transport; hence, this parameter is not a suitable candidate for influencing resistivity distribution in phosphorus-doped G1 ingots.

8.4. Chamber pressure

According to theoretical consideration at the beginning of the chapter, evaporation from the melt surface is the rate-defining step in phosphorus transfer during directional solidification of G1 ingots (Figure 8.1). Since mass transfer coefficient of phosphorus evaporation is strongly dependent on chamber pressure (Figure 8.2.), it is one of the most promising parameters to influence resistivity distribution of n-type mc-Si ingots.

The growth conditions of D2 ingot were supplemented with gradual reduction of chamber pressure in the second half of crystallization process. Two experimental G1 ingots D5 and D6 were grown using the adopted recipe with the decrease of typical process pressure from 600 mbar to 200 mbar (D5) and 50 mbar (D6) at different process stages. The process parameters used during the growth are presented in Table 8.4. Temperature, chamber pressure and TMF intensity profiles used in the experiment are given in Figure 8.22. 5 TMF markers with total effective current of I_{eff} = 110 A were applied during the growth of D5 and D6 at the same process times as for D2.

Ingot		**D2**	**D5**	**D6**
Travelling magnetic field	Start I_{eff}, [A]	40	40	40
	Change I_{eff}, [A]	80	80	80
	Ramp at solid fraction	0.33	0.33	0.33
	I_1/I_2	10	10	10
	f_1 [Hz]	20	20	20
	f_2 [Hz]	200	200	200
	ϕ_1	+90°	+90°	+90°
	ϕ_2	–90°	–90°	–90°
Pressure	Start P, [mbar]	600	600	600
	Change P, [mbar]	–	200	50
	Ramp at solid fraction	–	0.50→0.58	0.33→0.50
Gas flow	Start u_{gas}, [l/min]	6.0	6.0	6.0
	Change u_{gas}, [l/min]	–	–	–
	Ramp at solid fraction	–	–	–

Table 8.4.: Process conditions for ingots D2, D5 and D6.

The course of the growing process for D5 ingot was close to typical and lasted 12.5 hours, which was 30 minutes longer than those in previous experiments and can be considered as minor discrepancy. In contrast to D5, D6 ingot experienced noticeably smaller cooling rate after the reduction of pressure down to 50 mbar,

although the power input parameters were equal for all recipes. The cooling rate for D6 ingot evaluated from the slope of temperature profile was found to abruptly drop as the chamber pressure was reduced; thereafter it started slowly increasing up to the previous level. Eventually, the solidification time for the second half of D6 ingot was twice as large as that for the first half, making up the entire process duration to be 18 hours. Thus, the average cooling rate of the second half of D6 ingot was half the value than that for D2 ingot.

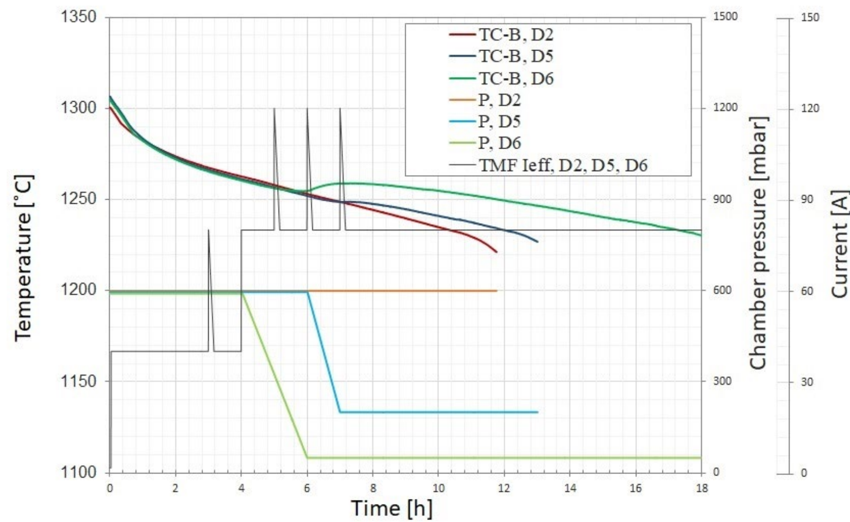

Figure 8.22.: Temperature, chamber pressure and TMF intensity profiles used for crystallisation of D2, D5 and D6 ingots.

The LPS images measured on central vertical cuts of D5 and D6 ingots shown in Figure 8.23. confirm the observation of the altered process time. The time between neighbouring markers was set to 1 hour. The positions of first four TMF markers indicated with red curves are in the range of 1.0 – 1.2 cm for all three processes D2, D5 and D6, which proves that the growth rate in the first half of these ingots is identical and equal to 1.0 – 1.2 cm/cm. However, while the distance between last two markers for D2 and D5 ingots stays in the range of 1.0 cm, the one for D6 is reduced down to 0.3 – 0.4 cm, indicating the average growth rate in this area to be 0.3 – 0.4 cm/h. Since there were no TMF markers made at the late process stages, it is impossible to clearly define the alteration of the growth rate thereat.

Summing up the findings from temperature profile, solidification time and LPS image, it can be concluded that the growth rate for the second half of D6 ingot cannot be considered as constant. After the reduction of chamber pressure down to 50 mbar, the growth rate rapidly went down following by gradual return to the previous level, making up the average growth rate for the second half of the ingot to be 0.5 cm/h. The variation in the growth rate with changes of process pressure can be explained with alteration in thermal conductivity of the gas ambient. The drop in chamber pressure abruptly changes the heat transfer in DS system, thus

leads to rapid alteration in the growth rate. From the resulting temperature profiles, it is not possible to determine precisely the alteration in the growth rate at each process stage after the reduction of chamber pressure. However, one could expect that growth conditions reach their equilibrium point over time and the growth rate finally returns to its original value. It is supposed that the same effect also takes place for D5 ingot, but since the reduction of pressure from 600 bar down to 200 mbar is not as significant as to 50 mbar, the difference in the growth rate is too small and results only in 30 minutes of solidification time extension.

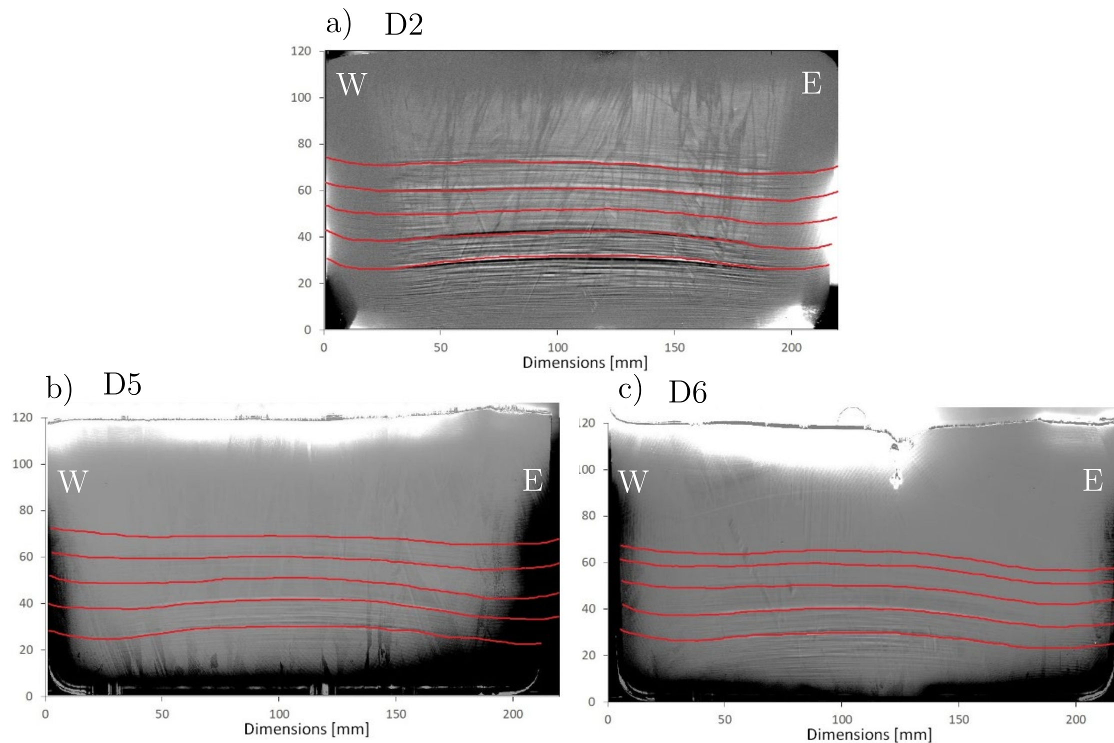

Figure 8.23.: LPS images of D2 (a), D5 (b) and D6 (c) ingots. TMF markers are indicated with red curves.

Another peculiarity observed for the processes conducted under low pressure is transformation of crucible coating condition. During melting and crystallization stages, silicon melt interacts with Si_3N_4 coating, which results in coating infiltration occurring at the triple interface [Cam17]. Infiltration process is dependent on partial pressures of system components [Dre10, Hug14]. Thus, changes in ambient conditions might affect the intensity of infiltration and endurance of crucible coating. The appearance of the crucible walls and ingot surface after the growth is shown in Figure 8.24. For the process conducted under the pressure of 600 mbar, coating infiltration is found to be insignificant, thus crucible walls are clean and covered only with Si_3N_4, which partially peeled off. White flakes seen on the top of completely solidified ingot D2 in Figure 8.24.a) indicate that peeling happens during the cooling phase. When the pressure is reduced, the coating infiltration intensifies, which results in a distinguishable silicon layer on the crucible walls above the

meniscus line. It can be seen that 50 mbar pressure (D6) leads to more intensive infiltration than that for 200 mbar pressure (D5).

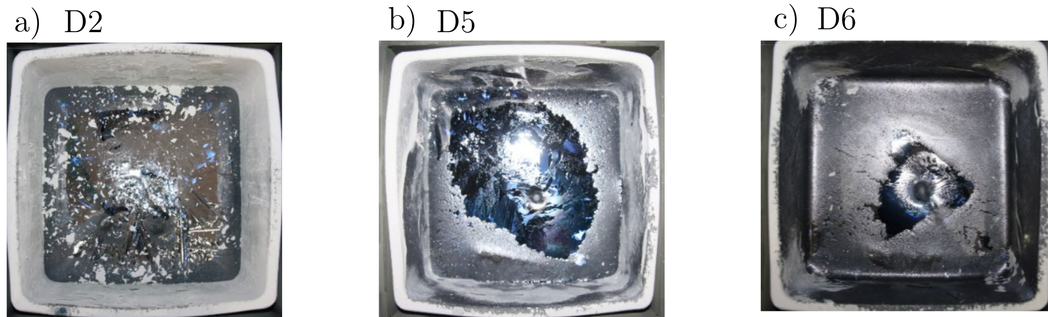

Figure 8.24.: Crucible and ingot surface after crystallization of D2 (a), D5 (b) and D6 (c) ingots.

In addition, the intensified infiltration changes the wettability of crucible coating by silicon [Hug14, Bry10], thus leads to adhesion of silicon to the crucible walls at the end of the growth process, which results in a slightly concave ingot surface in contrast to the convex one when no infiltration takes place (Figure 8.25). Nevertheless, Si_3N_4 crucible coating used in the conducted experiments was strong enough to withstand the pressure as low as 50 mbar, so that no ingot cracking and no significant sticking between the crucible and ingot was observed.

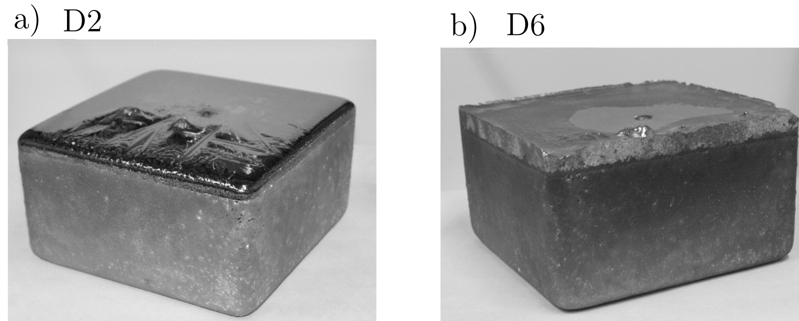

Figure 8.25.: G1 ingots grown under a) 600 mbar (D2) and b) 50 mbar (D6).

Resistivity distributions measured along the central and side vertical lines of D1 and D2 ingots are given in Figure 2.26. It can be seen that up to solid fraction of $g_S = 0.33$ the measured values are very similar, since the process conditions in this area are identical. In the second half of the ingot where the chamber pressure was reduced, the resistivity for both D5 and D6 ingots is increased. The effect is more pronounced for ingot D6, which utilized lower pressure than D5. As it was expected from theoretical calculations, the reduction of chamber pressure leads to the enlargement of mass transfer coefficient of phosphorus evaporation (Figure 8.2), resulting in greater increase in resistivity for the ingot grown under lower pressure. The increase in resistivity for D6 is sufficient to ensure the target range of 3.0 – 1.0 Ω·cm along the central axis.

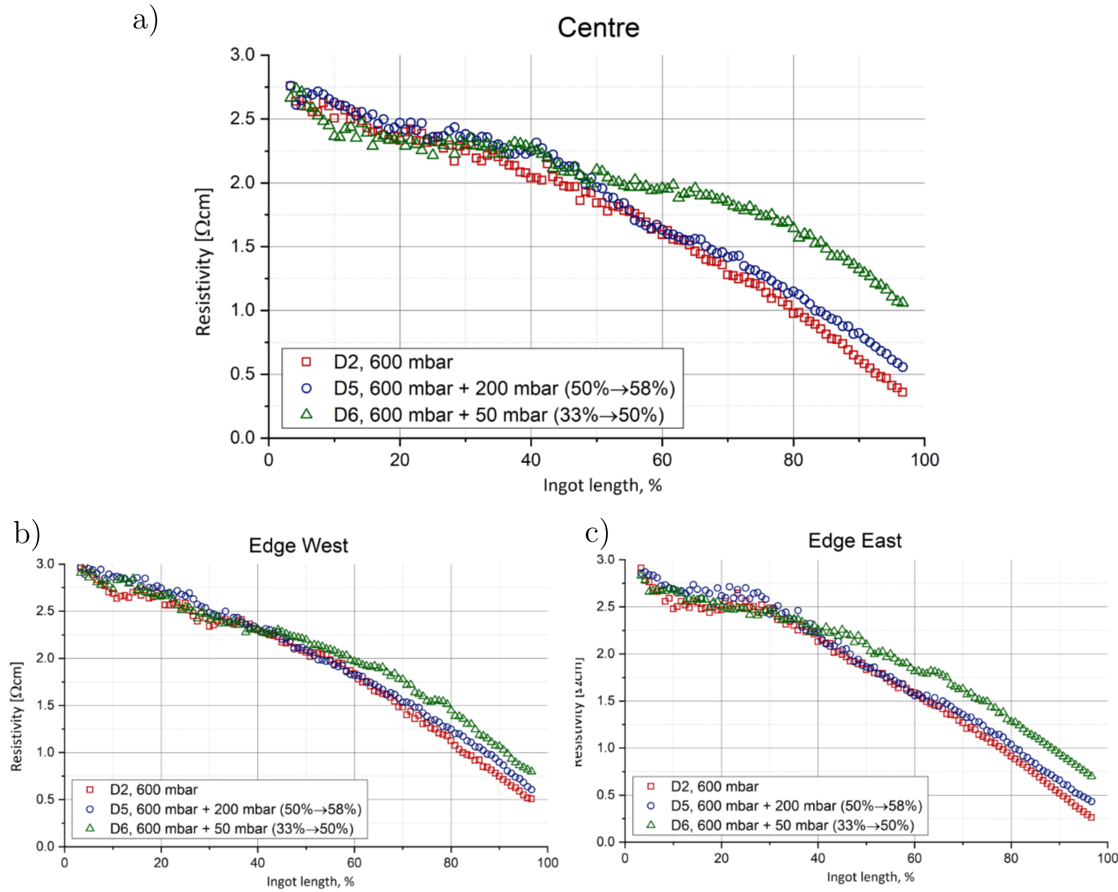

Figure 8.26.: Resistivity distribution along the vertical lines for D2, D5 and D6 ingots: a) central line, b) west edge line, c) east edge line.

To define the relation between chamber pressure and mass transfer coefficient, the phosphorus concentration profiles for the experimental ingots depicted in Figure 8.27. were built using the measured resistivity data from Figure 2.26. and standardized relations for semiconductor silicon [Thu80a]. Similar to the procedure performed in previous sections, a segregation model for dopant distribution in the second half of D5 and D6 ingot was built through OLS curve fitting. The model is described by the modified Gulliver-Scheil equation (3.11) with previously defined growth rate of $v_{gr} = 1.0$ cm/h for D5 and $v_{gr} = 0.5$ cm/h for D6. The fitting curves are in a good agreement with the experimental data for total mass transfer coefficient of phosphorus to be $K = 6.70\times10^{-7}$ m/s for D5 ingot and $K = 8.38\times10^{-7}$ m/s for D6 ingot. The obtained values for total mass transfer coefficient K are plotted in Figure 8.28. It can be seen that they fit the theoretically calculated range for mass transfer coefficient of evaporation K_e Figure 8.2.

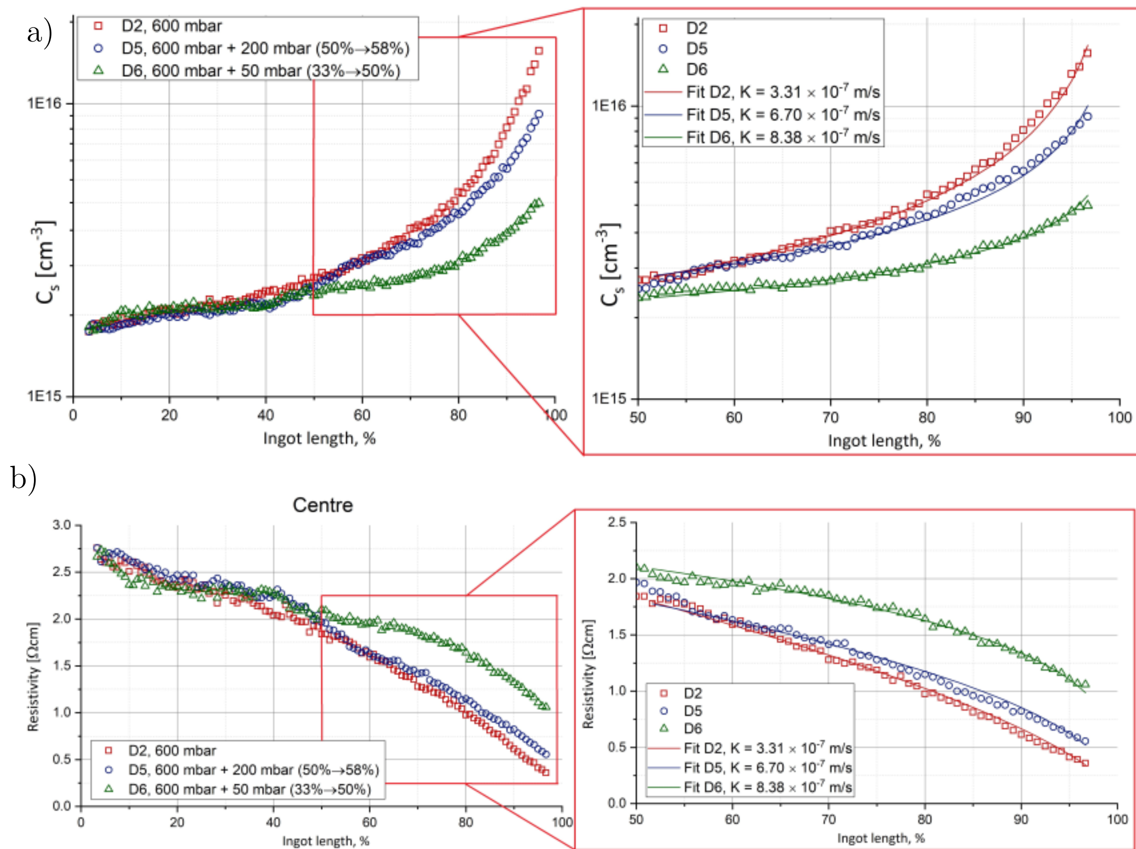

Figure 8.27.: Distribution of phosphorus concentration (a) and resistivity (b) along the ingot's length for D2, D5 and D6 ingots. The discrete points correspond to the data derived from measured resistivity (Figure 2.26). The solid curves are numerical fitting based on modified Gulliver-Scheil equation (3.11).

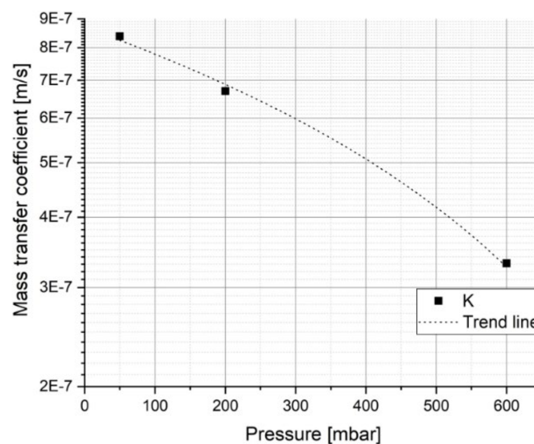

Figure 8.28.: Total mass transfer coefficient of phosphorus obtained from experimental data as a function of pressure.

Since the ingots were grown using two adjustments (intensified melt stirring with TMF and reduced pressure), the resulted phosphorus transport is defined by two mechanisms: transfer in the bulk melt and evaporation from the melt surface. In order to evaluate the impact of each mechanism separately, the ingot D7 was grown using the process conditions of D1 (no increasing of TMF intensity in the second half of the ingot) with pressure profile of D6 (reduction of pressure in the second half of the ingot). The process parameters used during the growth are presented in Table 8.5. Temperature, chamber pressure and TMF intensity profiles used in the experiment are given in for D6 and D7 are shown in Figure 8.29.

Ingot		D6	D7
Travelling magnetic field	Start I_{eff}, [A]	40	40
	Change I_{eff}, [A]	80	–
	Ramp at solid fraction	0.33	–
	I_1/I_2	10	10
	f_1 [Hz]	20	20
	f_2 [Hz]	200	200
	ϕ_1	+90°	+90°
	ϕ_2	–90°	–90°
Pressure	Start P, [mbar]	600	600
	Change P, [mbar]	50	50
	Ramp at solid fraction	0.33→0.50	0.33→0.50
Gas flow	Start u_{gas}, [l/min]	6.0	6.0
	Change u_{gas}, [l/min]	–	–
	Ramp at solid fraction	–	–

Table 8.5.: Process conditions for ingots D6 and D7.

D7 growth process showed similar behaviour as it was observed for D6 with regard to crucible coating infiltration and halved growth rate in the second half of solidification. The resistivity profiles showed slightly lower values towards the top of the ingot than those obtained for D6, which means that the enhanced melt mixing with TMF noticeably increases phosphorus removal even at chamber pressures as low as 50 mbar.

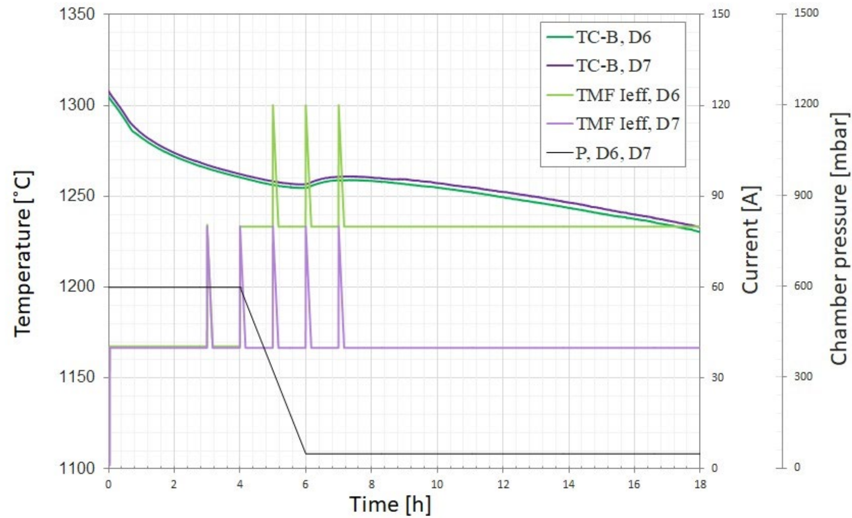

Figure 8.29.: Temperature, chamber pressure and TMF intensity profiles used for crystallisation of D6 and D7 ingots.

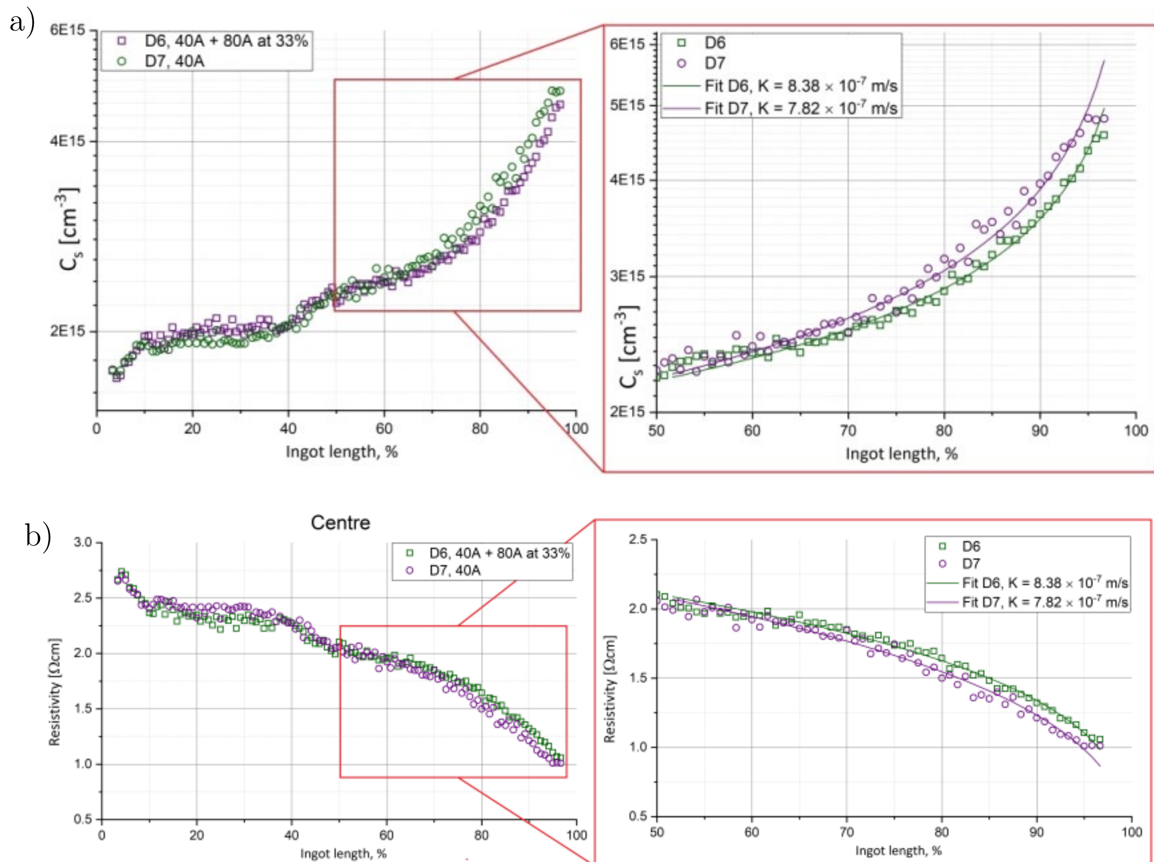

Figure 8.30.: Distribution of phosphorus concentration (a) and resistivity (b) along the ingot's length for D6 and D7 ingots. The discrete points correspond to the data derived from measured resistivity. The solid curves are numerical fitting based on modified Gulliver-Scheil equation (3.11).

The same procedure of the curve fitting to the modified Gulliver-Scheil equation (3.11) was performed for the measured data and results are given in Figure 8.30. Total mass transfer coefficient of phosphorus for D7 process was calculated to be $K = 7.82 \times 10^{-7}$ m/s. In such a way, it can be concluded that although mass transfer coefficient of phosphorus evaporation has stronger influence on dopant transport than mass transfer coefficient in the bulk melt, both these components are rate-controlling parameters. The obtained results show that the optimal process parameters to ensure the narrowest resistivity profile along phosphorus-doped G1 ingots are those used for D6 process.

The effect of chamber pressure variation on oxygen and carbon distribution was evaluated by FTIR measurements. The measured data are given in Figure 8.31. The reduction of chamber pressure results in the rapid increase of interstitial oxygen concentration at the time point when the pressure is changed. In order to explain this phenomenon it is necessary to consider the oxygen transport, which is defined by two main mechanisms – diffusion of oxygen from crucible to silicon melt and evaporation of silicon monoxide from the melt surface [Gao10]. The reduction of ambient pressure has a similar effect on SiO evaporation as it has on phosphorous evaporation, namely, the evaporation intensifies as the ambient pressure decreases. Therefore, one could expect that the concentration of interstitial oxygen would be lower for the ingots grown under reduced pressure. Such an effect was confirmed by Teng et al. considering the results of numerical simulation for multicrystalline ingots grown under reduced chamber pressure [Ten11]. Unfortunately, the reported model assumed that the flux density of oxygen transferred from the crucible to the melt is constant throughout the crystallization process and is not affected by the chamber pressure. However, as it was already shown, the reduction of chamber pressure leads to significant infiltration of Si_3N_4 coating, which in turn results in intensified diffusion of oxygen from the crucible to the silicon melt along the meniscus line. Since the alteration of chamber pressure affects both oxygen diffusion and SiO evaporation, the resulting effect on oxygen distribution is defined by correlation between these mechanisms.

The results presented in Figure 8.31a) and Figure 8.31b) indicate that in the investigated G1 system the effect of chamber pressure on oxygen diffusion is greater than that for silicon monoxide evaporation. Hence, the reduction of chamber pressure leads to increase in interstitial oxygen concentration. The lower the chamber pressure drops, the more pronounced the effect is. However, even at pressure as low as 50 mbar, the interstitial oxygen concentration in the second half of G1 ingots never becomes higher than elevated values at the bottom of the ingot.

In contrast to oxygen, substitutional carbon concentration becomes lower with the reduction of chamber pressure (Figure 8.31c) and Figure 8.31d). Since the main source of carbon is graphite parts of the hot zone and it is introduced to the melt

surface through the gas phase, this effect can be explained with slower spices transport in diluted argon under low pressure [Gao10].

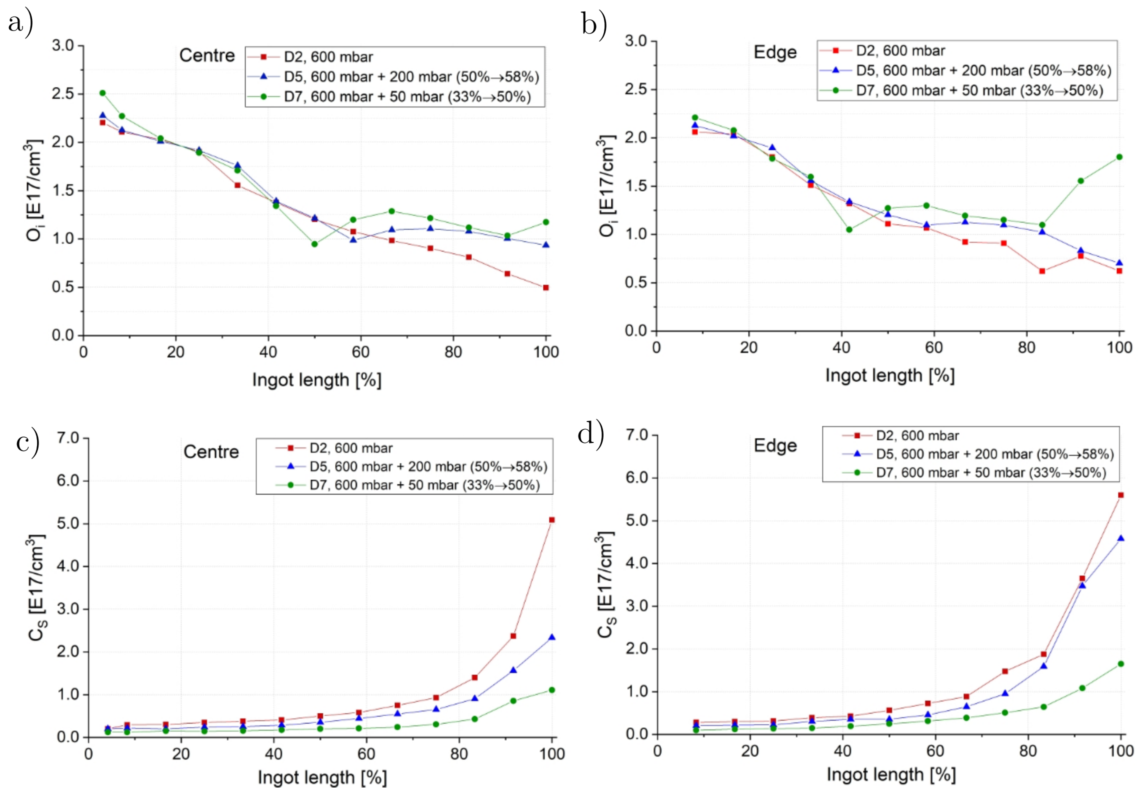

Figure 8.31.: Distribution of O_i and C_s along the vertical lines for D2, D5 and D7 ingots: a) O_i along the central line, b) O_i along the edge line, c) C_s along the central line, d) C_s along the edge line.

The MDP images for D2 and D6 ingots are given in Figure 8.32. Both ingots show the same level of the average charge carrier lifetime. However, the red zone at the sides near the bottom of D6 ingot is about 50% larger than that for D2. This effect can be explained with the reduced growth rate in the second half of D6 ingot. Since the solidification of the upper part of D6 ingot took almost twice longer, the solidified material was subjected to the diffusion of metal impurities from the crucible at elevated temperature for a longer time, which resulted in a larger red zone area [Nae09]. In the future, this problem must be solved by adoption of the power input recipe to thermal conditions at low chamber pressures, so that it will ensure the same growth rate as the one typical for standard pressures.

At the same time, the central area of ingot D6 has more uniform and slightly higher carrier lifetime than that for D2 ingot. This effect cannot be explained solely by higher resistivity of D6 ingot and is supposed to be provoked by crystalline material properties, which are investigated in the following chapter.

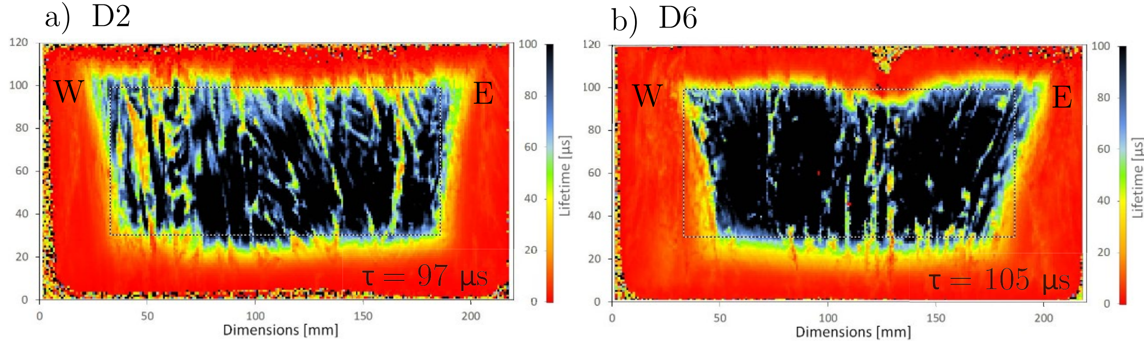

Figure 8.32.: MDP images of D2 (a) and D6 (b) ingots. The average lifetime is calculated for the area indicated with a dotted rectangle.

In summary, the reduction of pressure down to 50 mbar applied to phosphorus-doped G1 mc-Si ingots at solid fraction of $g_s = 0.33$ significantly increases resistivity at late stages of crystallization, which is sufficient to ensure the target range set by PV market. Although such an approach intensifies infiltration of crucible coating, it does not lead to ingot cracking or sticking between crucible and ingot. On the other hand, the applied growth conditions lengthen the crystallization time, which results in the larger red zone at the ingot sides. At the same time, the reduced pressure increases interstitial oxygen concentration and decreases substitutional carbon concentration, while ensuring more uniform and somewhat higher carrier lifetime in the central part of the ingot.

8.5. Material properties

Taking into account all the results obtained during parameter study, it can be concluded that process conditions used for D6 provide the optimal resistivity distribution along the ingot, decreasing the values in the bottom and increasing at the top. These conditions can be considered as an optimized growth recipe for phosphorus-doped G1 mc-Si ingots. In previous chapters, the properties of mc-Si ingots were estimated systematically after every process alteration. In order to evaluate the cumulative effect of all process adjustments on characteristics of multicrystalline material and the potential of the developed recipe for growing mc-Si ingots with the quality suitable for PV application, the parameters of ingot grown under the optimized recipe must be carefully summarized and compared to those for the reference one. Process parameters used during the growth of both ingots are presented in Table 8.6. Temperature, chamber pressure and TMF intensity profiles used in the experiment are given in Figure 8.33.

Ingot		D0	D6
Travelling magnetic field	Start I_{eff}, [A]	0	40
	Change I_{eff}, [A]	–	80
	Ramp at solid fraction	–	0.33
	I_1/I_2	–	10
	f_1 [Hz]	–	20
	f_2 [Hz]	–	200
	ϕ_1	–	+90°
	ϕ_2	–	–90°
Pressure	Start P, [mbar]	600	600
	Change P, [mbar]	–	50
	Ramp at solid fraction	–	0.33→0.50
Gas flow	Start u_{gas}, [l/min]	6.0	6.0
	Change u_{gas}, [l/min]	–	–
	Ramp at solid fraction	–	–

Table 8.6.: Process conditions for ingots D0 and D6.

Resistivity distribution for D0 and D6 ingots is given in Figure 8.34. Process conditions employed in the optimized growth recipe resulted in lower resistivity in the first half of ingot and higher resistivity in the second half, thus in more uniform distribution along the entire mc-Si ingot. Resistivity range for the optimized recipe is 45% narrower than that for the reference, which meets standard PV market requirements of 1.0 – 3.0 Ω·cm.

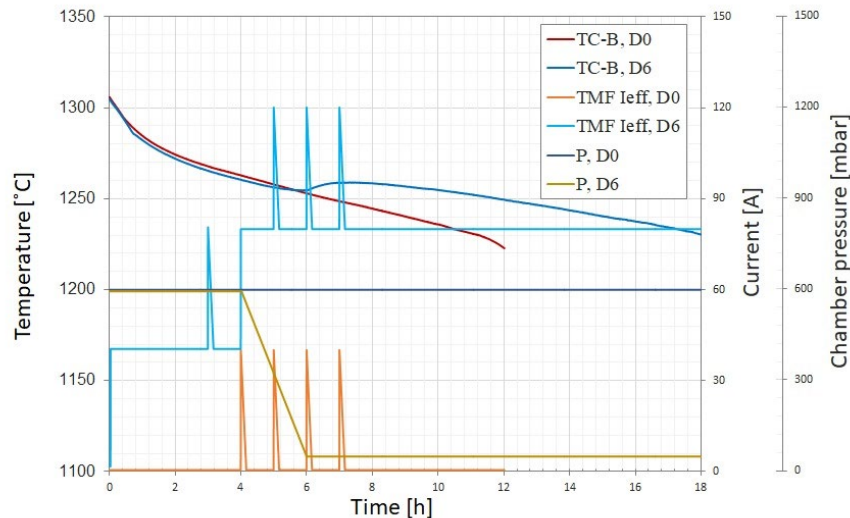

Figure 8.33.: Temperature, chamber pressure and TMF intensity profiles used for crystallisation of D0 and D6 ingots.

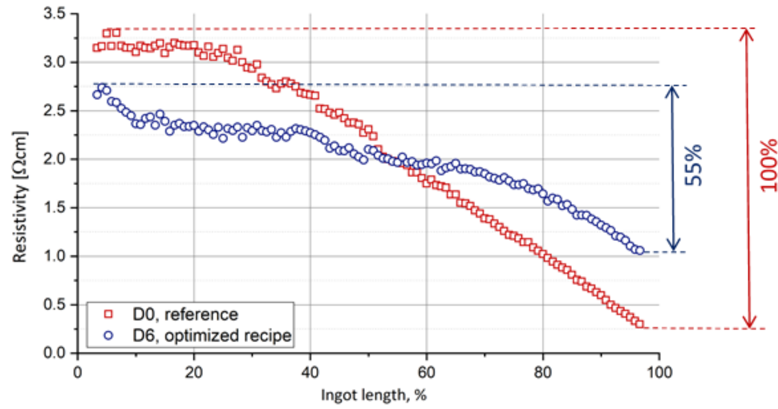

Figure 8.34.: Resistivity distribution along the central axis for phosphorus-doped G1 mc-Si ingots grown using the reference and optimized recipes.

As it was described in Chapter 5, in this research work the concentration of phosphorus in the grown ingots was defined indirectly by calculation from resistivity data. This approach is considered more accurate than direct methods of analytical chemistry, since the concentration of dopant in investigated mc-Si ingots is rather low and in this range of values, the measurement error for FPP method is significantly smaller compared to that for analytical ones. In addition, direct methods imply sophisticated sample preparation and/or utilization of corresponding reference material and calibration procedures, which are defining for the correctness of measurements. However, direct analytical methods can serve as a supplementary source of data for comprehensive analysis. Thereby, with the aim of additional verification of phosphorus distribution, both D0 and D6 ingots where investigated by direct GDMS measurements. The measurements were performed on 5 samples taken from equidistant positions along the central vertical axis. The obtained data are presented in Figure 8.35.

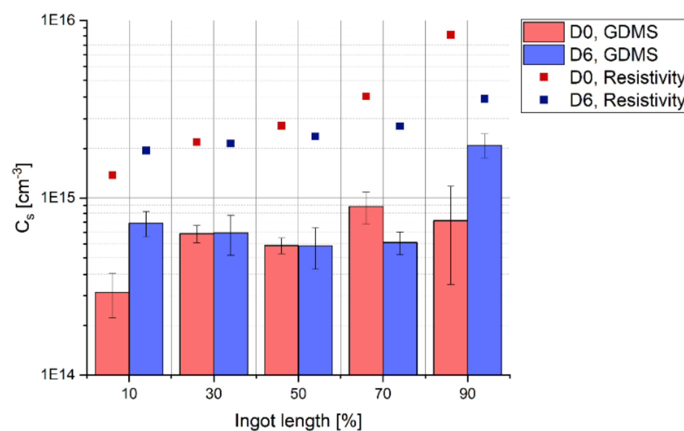

Figure 8.35.: Distribution of phosphorus along the central vertical line of D0 and D6 ingots. Bars correspond to the values measured by GDMS. Solid points show the data derived from measured resistivity.

The absolute values obtained by GDMS show significantly lower level of phosphorus concentration than that derived from resistivity data. However, both types of data follow the same trend of dopant distribution along both ingots. Since resistivity data measured by FPP were additionally confirmed by eddy current and Hall measurements, they are considered to be more reliable than GDMS data. The difference in absolute values obtained by two methods is supposed to be explained by not optimised calibration of GDMS measurements. Nevertheless, the same data trend for both types of measurement confirms successful homogenization of phosphorus concentration in D6 ingot that was grown using the optimized recipe. Significantly higher value measured by GDMS for D6 at solid fraction of $g_s = 0.90$ cannot be considered as the reliable one, since the last-to-freeze material is prone to rapid crystallization and dopant distribution therein is highly non-uniform.

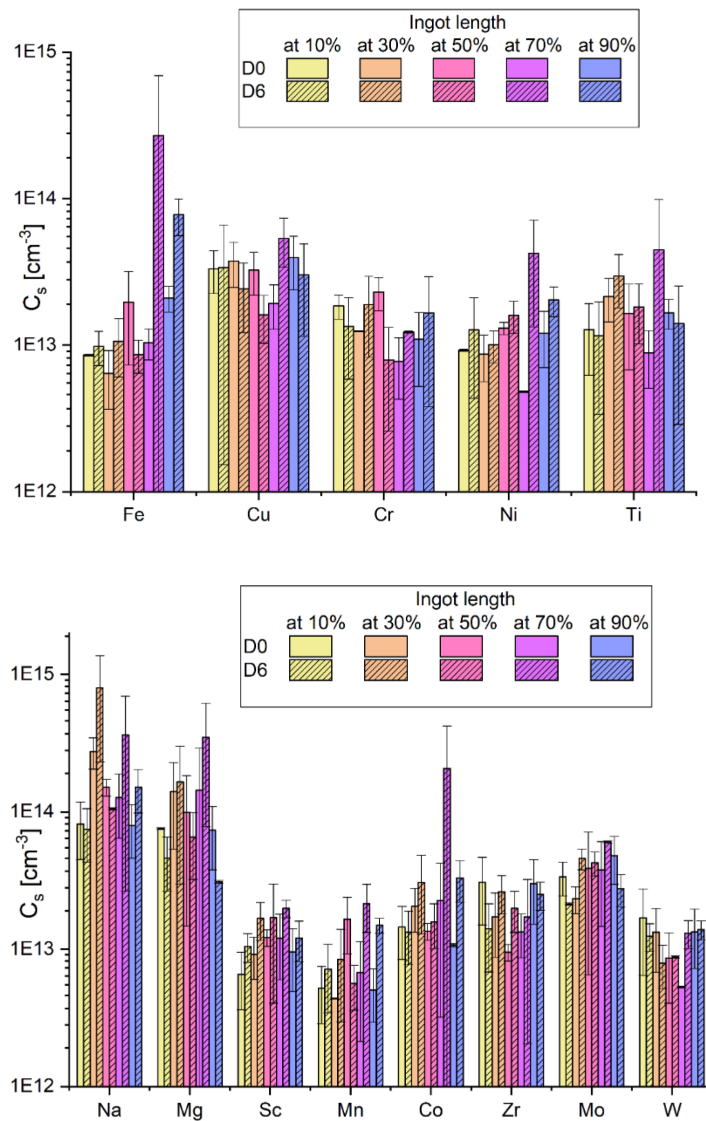

Figure 8.36.: Distribution of metals along the central vertical line of D0 and D6 ingots measured by GDMS.

Together with phosphorous, the above-mentioned samples were also investigated with GDMS with regard to metal contamination. The measured data are given in Figure 8.36. It can be seen that both ingots show almost identical level of contamination within the measurement error. It also has to be mention that the obtained values are in the safe range for PV mc-Si, which does not have a harmful effect on solar cell performance [Col12, Col13]. This assumption is also confirmed by rather high level of charge carrier lifetime measured by MDP (Figure 8.37).

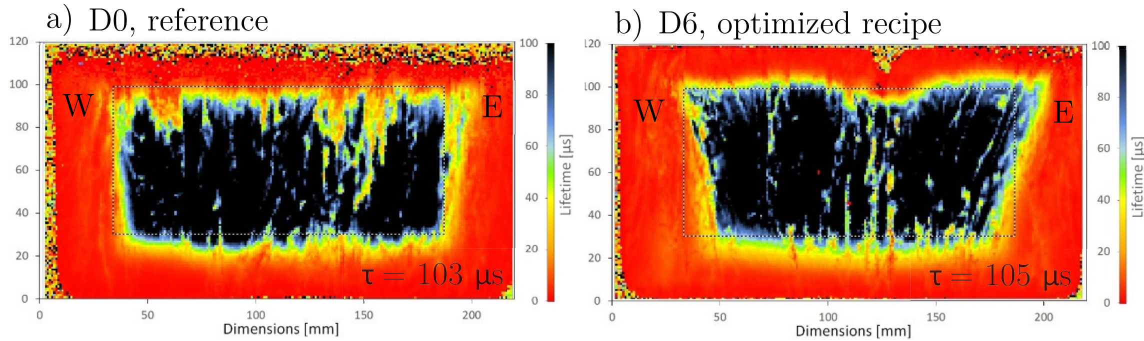

Figure 8.37.: MDP images for phosphorus-doped G1 mc-Si ingots grown using the reference (a) and optimized (b) recipes. The average lifetime is calculated for the area indicated with a dotted rectangle.

MDP images for the ingots grown under the reference and optimized recipes are shown in Figure 8.37. It can be seen that the average carrier lifetime for both ingots are identical, which confirms that the adjustments applied in the optimized recipe do not lead to deterioration in the bulk quality of mc-Si material. However, they result in the enlarged red zone area at the crucible sides near the bottom of the ingot. As it was described in Chapter 8.4, this enlargement is caused by higher contamination with metals diffusing from crucible and its coating into mc-Si ingot due to longer crystallization process. On the other hand, the distribution of minority carrier lifetime across the longitudinal central cut for the optimized growth recipe is more uniform and the local values are slightly higher than that for the reference one, which is supposed to be caused by more homogeneous material properties and less structural defects that lead to recombination of charge carriers.

In order to evaluate recombination active defect structures, both D0 and D6 ingots were investigated with PL method. PL images measured on east halves of longitudinal central cuts for both ingots are given in Figure 8.38. PL images accurately reproduce the grain pattern for both ingots and reveal the same thickness and position of the red zone as that seen in MDP images in Figure 8.37. Besides that, the resulting pictures show no specific artefacts or clusters that could deteriorate the quality of mc-Si material, which indicates no obvious reason for higher local lifetime in D6 ingot. Thus, this phenomenon must be investigated in the future applying in-depth structural studies of the grown mc-Si material.

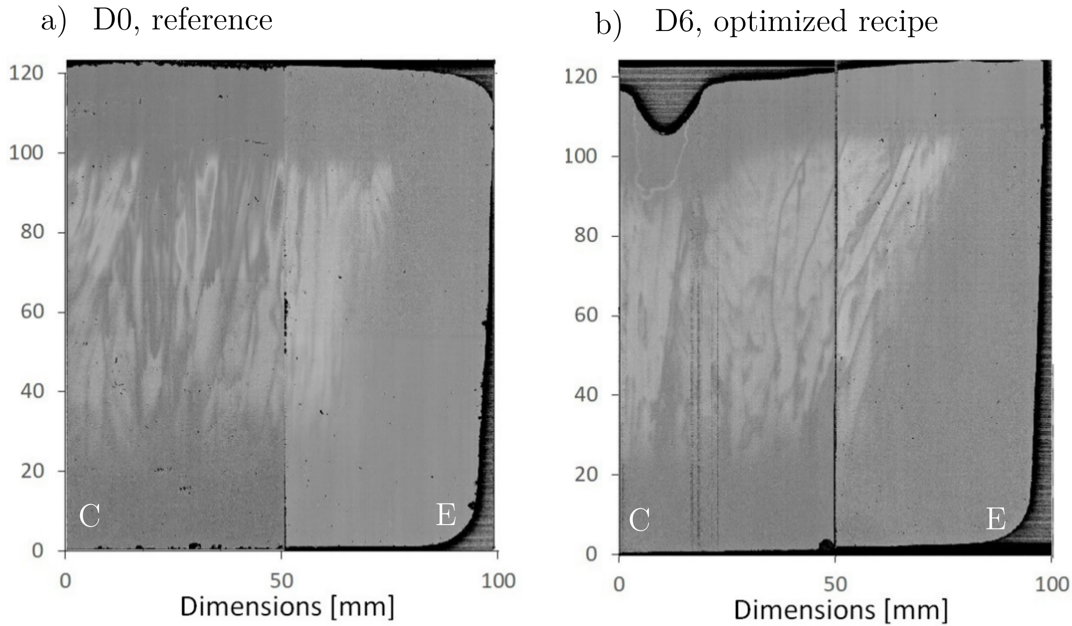

Figure 8.38.: PL images for phosphorus-doped G1 mc-Si ingots grown using the reference (a) and optimized (b) recipes.

Comparative FTIR data for both ingots are presented in Figure 8.39. The adjustments applied for the optimized recipe lead to the significant increase of interstitial oxygen concentration in the second half of G1 ingot. As it was discussed in previous chapters, the reason lies in higher oxygen diffusion from crucible to silicon melt due to strong coating infiltration at low ambient pressure and more intensive melt mixing induced by TMF [Dre10, Hug14]. At the same time, the application of optimized recipe results in effective reduction of substitutional carbon, which is explained with slower back transport of carbon monoxide in diluted argon under low pressure [Gao10].

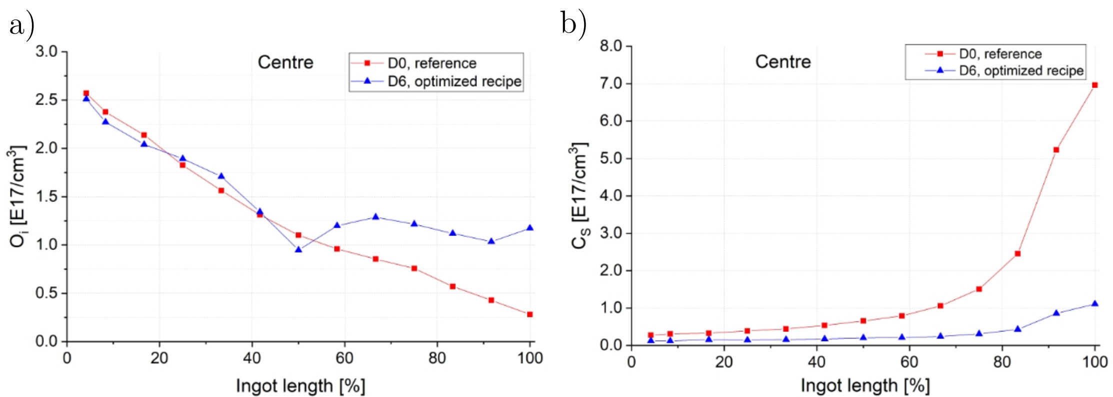

Figure 8.39.: Distribution of O_i (a) and C_s (b) along the central vertical line for phosphorus-doped G1 mc-Si ingots grown using the reference and optimized recipes.

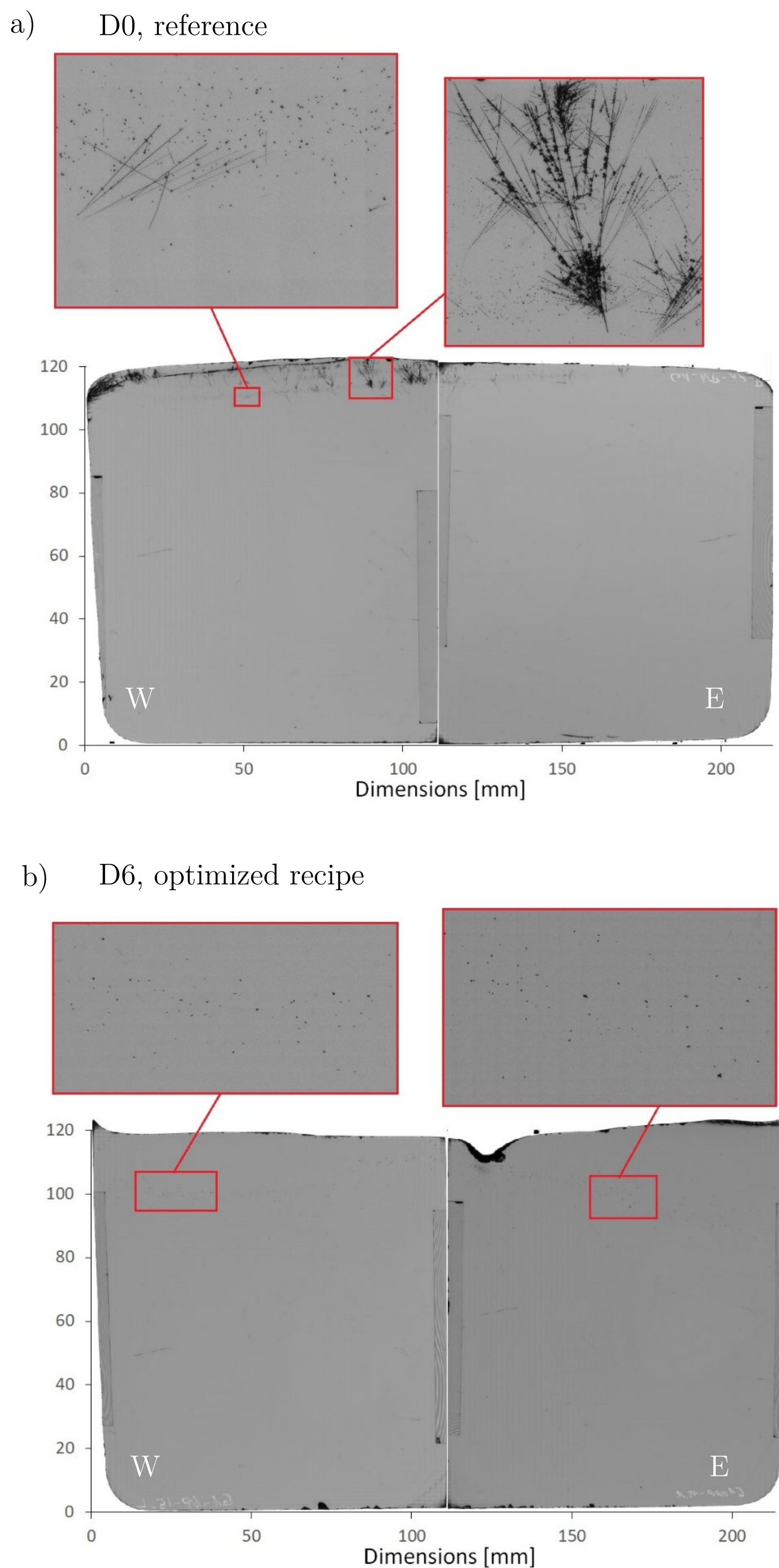

Figure 8.40.: NIR images for phosphorus-doped G1 mc-Si ingots grown using the reference (a) and optimized (b) recipes.

Another parameter important for evaluation of mc-Si material quality is the presence of SiC and Si_3N_4 inclusions in the grown ingots. NIR images for ingots grown using the reference and optimized recipes are given in Figure 8.40. The measured data reveal that D0 ingot contains relatively large inclusions in the very top part. These are supposed to be clusters containing Si_3N_4 filaments and SiC precipitates nucleated therein [Rak05]. Such location of precipitates is favoured over the bulk material, since this part of the ingot in any case is not used for production of solar cells due to its high contamination with metals. In contrast to D0, D6 contains rather small inclusions in the near-top area. Such distribution is unfavourable, since it makes the near-top part of mc-Si ingot inapplicable for PV purpose. In order to explain the changes in distribution of inclusions, one has to consider their origin and transport mechanism. SiC and Si_3N_4 particles are formed in the silicon melt and later incorporated into crystal during as it grows [Moe10]. At moderate growth rates, they are pushed to the liquid phase during early stages of crystal growth, which makes the melt saturated with particles by the end of solidification. Thus, the probability of SiC and Si_3N_4 particles to be captured at solid-liquid interface and incorporated into the crystal is significantly higher at late stages of crystal growth. Therefore, at this time the pattern of the melt flow is highly important, since it is responsible for the mass transport at solid-liquid interface. The growth recipe used for D6 implied enhanced melt mixing induced by TMF, which dramatically changes the structure of melt vortexes (Figure 8.9 and Figure 8.16). These alterations might create unfavourable growth conditions at the final stages of solidification due to inhomogeneous flow velocity near solid-liquid interface and provoke SiC and Si_3N_4 particles to be captured thereat. It is believed that optimization of growth rate and melt convection at the late stages of crystallization might reduce or even eliminate this problem.

8.6. Conclusion

In this chapter, we investigated the influence of travelling magnetic field, ambient pressure and gas flow on resistivity distribution in phosphorus-doped G1 mc-Si ingots. It was shown that double frequency TMF is one of the tools to influence phosphorus distribution in the grown ingots. Weak melt mixing induced by travelling magnetic field with total effective current of $I_{eff} = 40$ A affects both effective segregation coefficient and mass transfer coefficient of phosphorus in the bulk melt. The induced flow pattern results in more uniform dopant distribution at solid-liquid interface during the initial stages of growth, which leads to reduction of ingot resistivity in the first half of mc-Si ingot. At the same time, strong melt mixing induced by travelling magnetic field with total effective current of $I_{eff} =$ 80 A leads to intensified phosphorus evaporation from the melt surface during late

stages of ingot growth through the enlarged mass transfer coefficient of phosphorus in the bulk melt. In such a way, the induced melt flow pattern increases resistivity in the second half of the ingot. Another process parameter, which has a strong influence on phosphorus transport during solidification of mc-Si, is ambient pressure. The reduction of chamber pressure results in significant enlargement of mass transport coefficient of phosphorus evaporation. Chamber pressure as low as 50 mbar is able to significantly increase resistivity in the second half of mc-Si ingot. At the same time, low process pressure leads to intensified infiltration of crucible coating, which results in increased concentration of interstitial oxygen. Therefore, the rigidity of applied coating is greatly important to secure high quality of mc-Si material and stability of the growth process. In addition, the alteration of ambient pressure can significantly change the thermal conductivity of the system, which results in variation in ingots growth rate. Thus, in order to keep stable process conditions, the alteration of this process parameter must be supplemented with modification of power input recipe. In contrast to melt flow and chamber pressure, gas flow is not a defining parameter for dopant transport in DS process; hence, it does not have any noticeable influence on resistivity distribution.

A standard growth recipe was supplemented with combination of varying TMF and pressure profiles. The optimized growth recipe implied application of double frequency TMF with total effective current of $I_{eff} = 40$ A with its subsequent raising up to 80 A together with reduction of chamber pressure from 600 mbar down to 50 mbar at solid fraction of $g_s = 0.33$. A conventional multicrystalline ingot grown using the optimized recipe shows 45% narrower resistivity variation along its length, thus proving that combination of varying TMF and chamber pressure profiles is an effective tool for tailoring resistivity distribution in phosphorus-doped ingots.

CHAPTER 9

Process replication for G1 HPM ingots

In Chapter 8 it was shown that travelling magnetic field and chamber pressure can effectively influence resistivity distribution of phosphorus-doped G1 mc-Si ingots. An optimized growth recipe supplemented with combination of varying TMF and pressure profiles showed impressive results for conventional multicrystalline ingot. In order to verify the applicability of this technique for seeded DS process, the developed approach was replicated for phosphorus-doped HPM ingots.

The study was conducted on two G1 HPM ingots with dimensions of 22×22×14 cm^3 and weight of 16 kg. A 2 cm thick seeding layer consisting of fine silicon chunks was placed on the bottom of every crucible (Figure 6.5) to assure multicrystalline structure of small randomly oriented grains. In order to obtain comparable results with conventional multicrystalline G1 ingots described in Chapter 8, all ingots were doped with the same quantity of phosphorus to provide the concentration in ingots charge $C_0 = 4.5\times10^{-15}$ cm^{-3}. Since the complimentary fine chunks at the bottom serve mainly as a seeding layer and do not noticeably contribute to the amount of the silicon melt, the quantity of phosphorus dopant used in HPM experiments was the same as in conventional multicrystalline G1 ingots.

At the first stage of the study, a reference HPM ingot E0 was grown using a power input recipe, which was developed in the set of preliminary experiments and implied a growth rate in the range of 1.0 – 1.2 cm/h. The conditions of the growth process were maximally close to the standard ones for PV industry, which means chamber pressure of 600 mbar, argon flow of 6.0 l/min and no TMF applied during solidification. In order not to disturb the HPM growth, no TMF markers were applied during the process.

Ingot		E0	E1
Travelling magnetic field	Start I_{eff}, [A]	0	40
	Change I_{eff}, [A]	–	80
	Ramp at solid fraction	–	0.33
	I_1/I_2	–	10
	f_1 [Hz]	–	20
	f_2 [Hz]	–	200
	ϕ_1	–	+90°
	ϕ_2	–	–90°
Pressure	Start P, [mbar]	600	600
	Change P, [mbar]	–	50
	Ramp at solid fraction	–	0.33→0.50
Gas flow	Start u_{gas}, [l/min]	6.0	6.0
	Change u_{gas}, [l/min]	–	–
	Ramp at solid fraction	–	–

Table 9.1.: Process conditions for ingots E0 and E1.

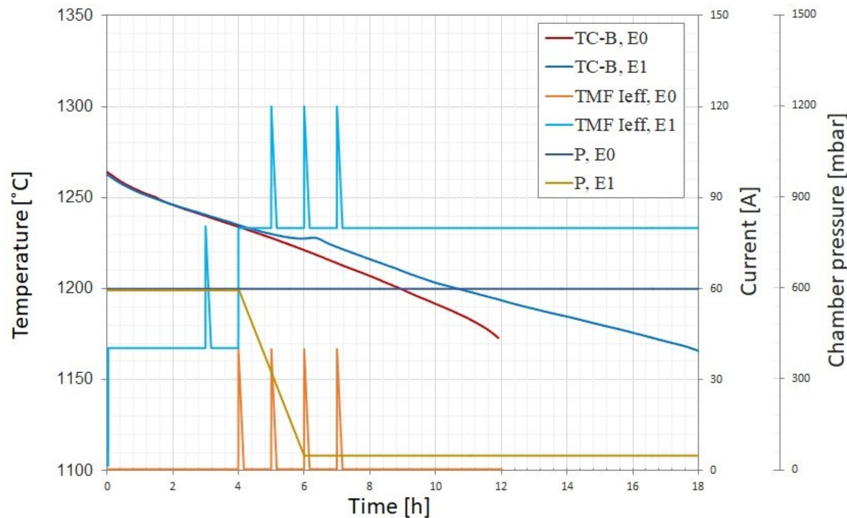

Figure 9.1.: Temperature, chamber pressure and TMF intensity profiles used for crystallisation of E0 and E1 ingots.

The second HPM ingot E1 was grown using the same approach as the one used for conventional multicrystalline ingot D6: reference recipe E0 was supplemented with double frequency TMF of total effective current I_{eff} = 40 A with its subsequent raising up to 80 A together with reduction of chamber pressure from 600 mbar down to 50 mbar at solid fraction of g_s = 0.33. The detailed process conditions are presented in Table 9.1 and Table 10.4. in Appendix. Temperature, chamber pressure and TMF intensity profiles are shown in Figure 9.1.

According to the data received from pyrometer and thermocouples, the duration of complete solidification for E0 ingot after seeding was equal to 12 h. Taking into account 120 mm height of the ingot without the seeding layer, it can be concluded that the average growth rate of E0 ingot was 1.0 cm/h. Similar to the experiments with low pressure during growth of conventional G1 mc-Si ingots conducted in Chapter 8, after the reduction of pressure, the duration of crystallization for E1 ingot increased to the double value compared to that for E0 ingot, even though the power input recipes were equal for both E0 and E1 ingots. Hence, the growth rate during the second half of E1 ingot was equal to 0.5 cm/h, which is twice lower than that for the first half. The entire solidification process for E1 ingot made up 18 hours.

The appearance of the crucible and ingot surface after the growth is shown in Figure 9.2. The crucible after E0 process conducted under the pressure of 600 mbar is clean and the ingot is covered only with Si_3N_4, which partially peels off during the cooling phase, while the crucible after E1 process conducted under the pressure of 50 mar reveals strong infiltration during crystallization. However, similar to D6 ingot, the crucible coating in E1 experiment had enough adhesive strength to withstand the process, thus no ingot cracking or significant sticking between the crucible and ingot was observed.

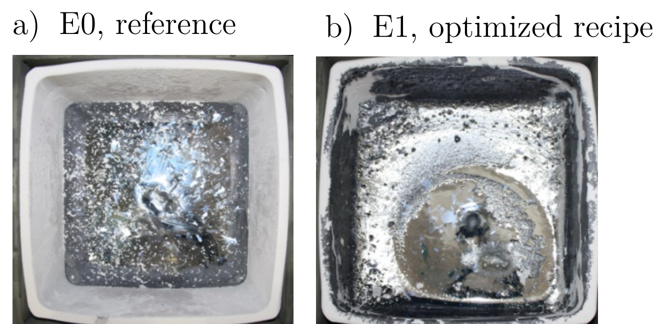

Figure 9.2.: Crucible and ingot surface after crystallization of E0 (a) and E1 (b) ingots.

The picture of central longitudinal cut for ingot E1 grown under optimized HPM recipe in comparison to the respective cut for ingot D6 grown under analogical conventional recipe is presented in Figure 9.3. Small cavities and unmolten chunks at the bottom of E1 indicate that the seeding layer was not entirely molten leaving approximately 1 cm of solid silicon. Hence, when crystal growing started, the nucleation of multicrystalline grains took place thereat. The grain pattern show that HPM ingot consists of elongated columnar crystallites of significantly smaller size than those for conventional multicrystalline ingots grown. Thus, it can be concluded that after successful seeding E1 ingot experienced HPM growth.

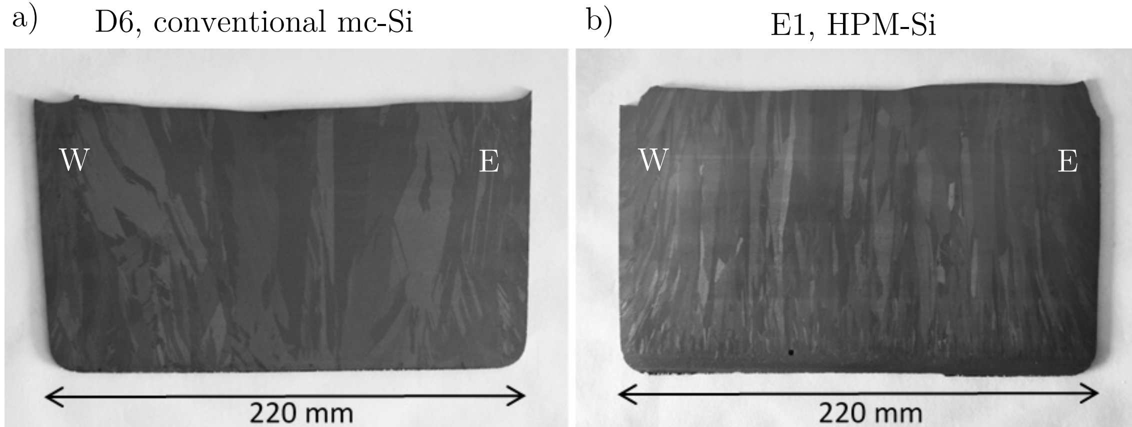

Figure 9.3.: Central vertical cuts of D6 (a) and E1 (b) ingots showing the difference in grain pattern.

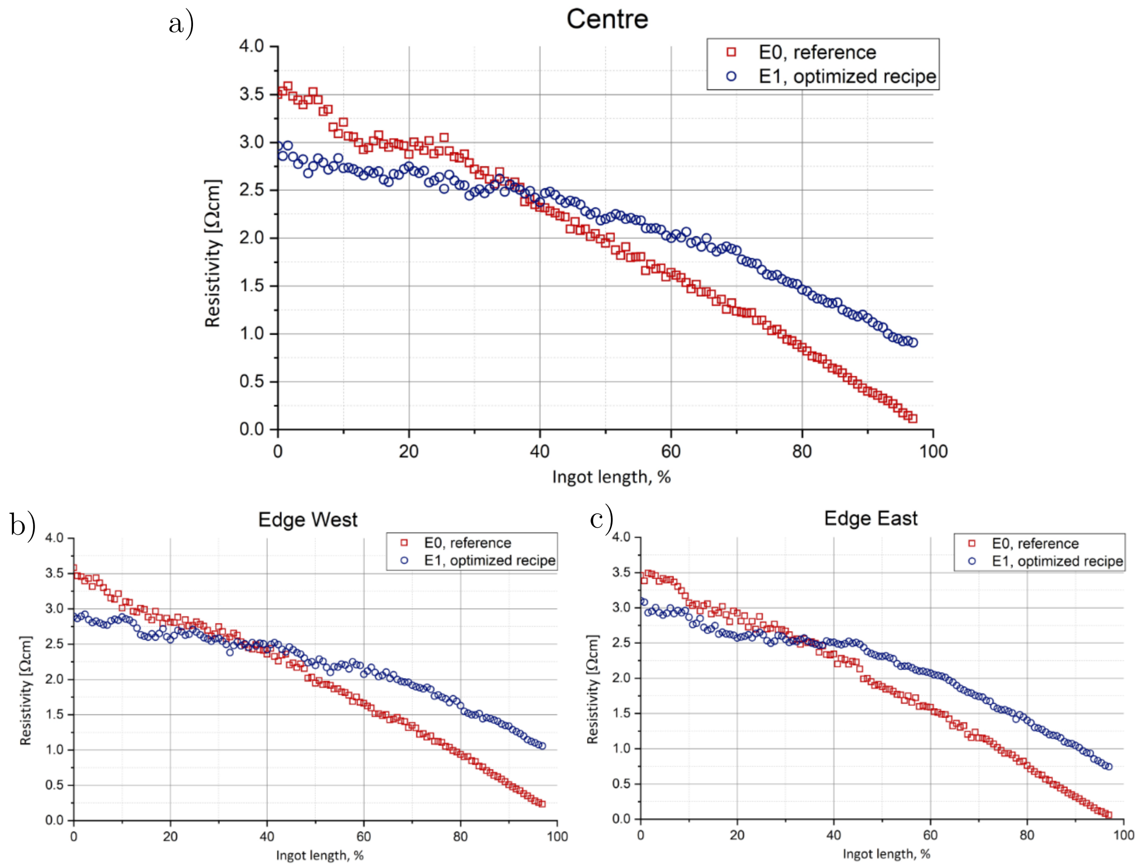

Figure 9.4.: Resistivity distribution along the vertical lines for E0 and E1 ingots: a) central line, b) west edge line, c) east edge line.

Resistivity distributions measured along the central and side vertical lines of E0 and E1 ingots are given in Figure 9.4. The differences in distribution for the central and side lines indicate that the liquid-solid interface is slightly tilted to the east (right side). This fact confirms the previous findings that G1 hot zone is not perfectly symmetric and the west side is somehow colder than the east side, thus it

crystalizes earlier (e.g. Figure 8.14). Similar to the effects observed for conventional mc-Si ingots in set D, the adjusted recipe leads to decreased resistivity in the first half of E1 ingot, which is caused by more uniform dopant distribution at solid-liquid interface induced by TMF with $I_{eff} = 40$ A, and increased resistivity in the second half, which is the result of intensified phosphorus evaporation induced by low pressure and enhanced melt mixing with TMF of $I_{eff} = 80$ A.

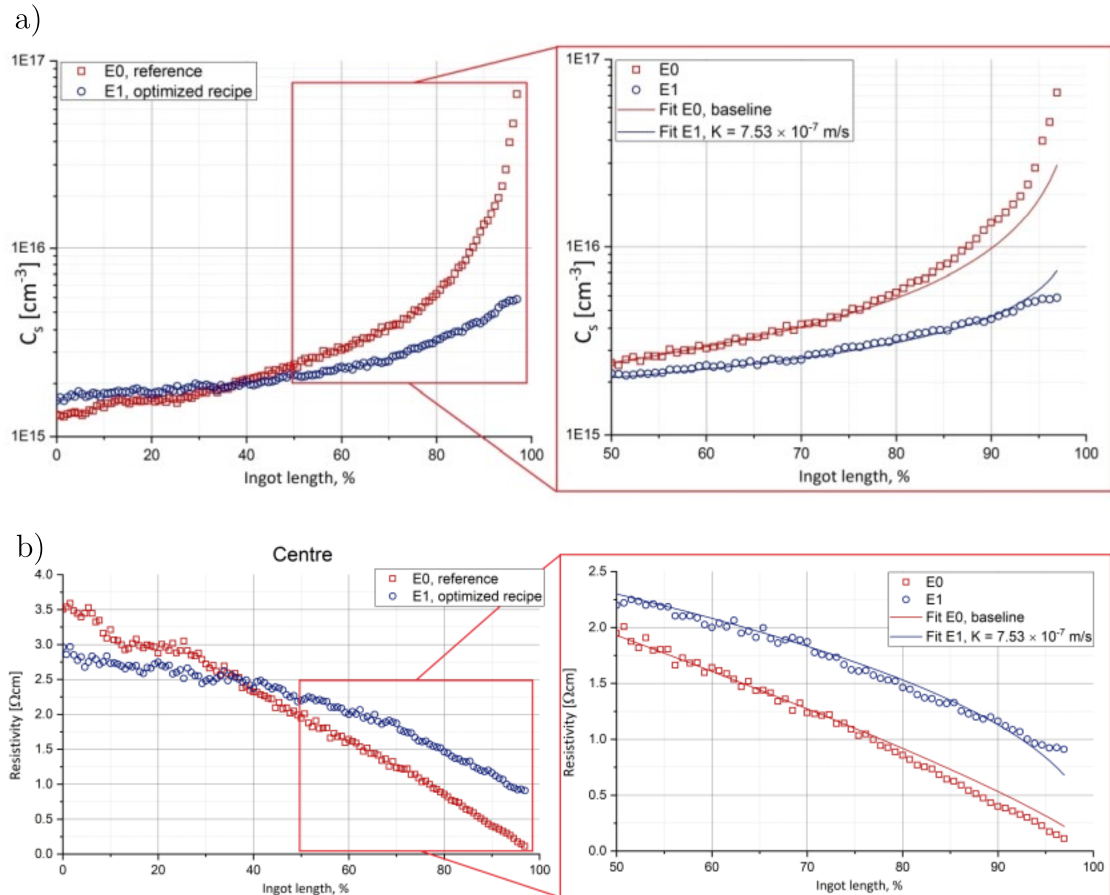

Figure 9.5.: Distribution of phosphorus concentration (a) and resistivity (b) along the ingot's length for E0 and E1 ingots. The discrete points correspond to the data derived from measured resistivity (Figure 9.4). The solid curves are numerical fitting based on modified Gulliver-Scheil equation (3.11).

In order to evaluate numerically the influence of the applied adjustments on dopant transport, the phosphorus concentration profiles for the experimental ingots depicted in Figure 9.5. were built using the measured resistivity data from Figure 9.4. and standardized relations for semiconductor silicon [Thu80a]. Similar to the procedure performed for conventional mc-Si ingots described in Chapter 8, a segregation model for dopant distribution in the second half of E1 ingot was built through OLS curve fitting. The model is described by the modified Gulliver-Scheil equation (3.11):

$$C_s(g_s) = k_{eff} C_0 (1 - g_s)^{k_{eff} + \frac{K}{v_{gr}} - 1} \tag{3.11}$$

using resistivity distribution of E0 ingot as a baseline and previously defined growth rate v_{gr} = 0.5 cm/h. The fitting curve is in a good agreement with the experimental data for total mass transfer coefficient of phosphorus $K = 6.70 \times 10^{-7}$ m/s. The obtained value lies in the range of theoretically calculated mass transfer coefficient of evaporation (Figure 8.1), which confirms the results obtained for conventional mc-Si that both K_m and K_e coefficients are rate-defining parameters for G1 HPM process. The total mass transfer coefficient of phosphorus for HPM ingot is slightly smaller than that for conventional mc-Si. It can be explained with some differences in temperature gradients and melt flow pattern, which are induced by seeding procedure. In such a way the developed approach results in 40% narrower resistivity range than that for the reference ingot, which is very close to standard PV requirements of 3.0 – 1.0 Ω·cm (Figure 9.6).

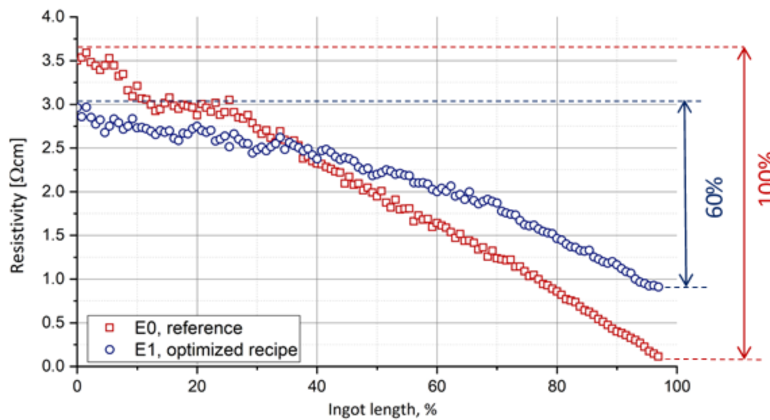

Figure 9.6.: Resistivity distribution along the central axis for phosphorus-doped G1 HPM-Si ingots grown using the reference and optimized recipes.

As a conclusion, it can be stated that the process adjustment developed for conventional G1 mc-Si ingots can be successfully applied for HPM process. The applied approach enables successful nucleation from the seeding layer and does not disturb HPM growth of elongated columnar crystallites. The optimized recipe results in 40% reduction of resistivity variation along the HPM ingot. However, it is advisable to perform fine tuning of the developed recipe in order to optimize it specifically for seeded DS process.

CHAPTER 10

Summary and Outlook

10.1. Summary

This research investigates phosphorus-doped directionally solidified silicon ingots grown under different process conditions. Owing to relatively simple and inexpensive technique, multicrystalline silicon produced by directional solidification is the most widespread substrate material for photovoltaic application. Although nowadays most crystalline solar cells utilize p-type wafers, newly developed concepts for high-efficiency solar cells are based on n-type material and are considered to be the future PV standard. Although n-type crystalline silicon exhibits superior quality over the p-type one, it has a non-uniform axial resistivity profile due to the low segregation coefficient of phosphorus in silicon melt, which brings additional difficulties for solar cell manufacturers. Therefore, the main part of this research was dedicated to homogenization of resistivity along phosphorus-doped mc-Si ingots.

Fundamental analytical study, conducted in this work considered the following mass transport mechanisms during DS process:

- solid-liquid interface: incorporation of phosphorus into the solid phase,
- bulk melt: phosphorus transport from the melt volume to the boundary layer at the melt surface,
- boundary layer: phosphorus transport through the boundary layer at the melt surface,
- melt surface: evaporation of phosphorus into the gas phase,

- gas chamber: evacuation of gaseous phosphorus from the system by purging argon flow.

The theoretical calculations showed that melt mixing is the influencing factor for dopant transport during ingot crystallization. In the case of incomplete melt mixing, dopant transport is defined by the melt flow pattern at different stages of solidification. In case the melt mixing ensures homogeneous distribution of phosphorus across the melt, phosphorus evaporation becomes the rate-controlling step in dopant transport, which is strongly dependent on the chamber pressure. Thus, in typical DS process the defining mechanisms for resistivity distributions are melt mixing and evaporation of phosphorus from the free melt surface. Mass transport above the melt surface was found not to affect the total phosphorus mass transfer for typical G1 ingots. However, it might be rate-defining in DS systems with insufficient gas flow above the melt.

Based on this analytical study of mass transport mechanisms, three process parameters, which have the most significant influence on phosphorus distribution in multicrystalline ingots, were chosen to be investigated experimentally: melt mixing, chamber pressure and gas flow above the melt. The experimental study was conducted in directional solidification furnace of G1 size equipped with KRIST*MAG*® heater-magnet module, which can produce heat and magnetic fields at the same time. Since travelling magnetic field is known to be the effective method to affect the flow of semiconductor melts, particular attention was given to this tool. The effect of the chosen process parameters on phosphorus transport was studied through the analysis of resistivity distribution in the grown ingots and supported by numerical modelling. In addition, the changes in process conditions were also evaluated with regard to their influence on other important material properties, e.g. concentrations and distribution of impurities, charge carrier lifetime etc.

In order to assess the effect of TMF on resistivity distribution, the first stage of experiments was performed in a specially developed 4×G0 setup that enables simultaneous growth of four ingots of G0 size in similar conditions. It was found that enhanced melt mixing induced by TMF intensifies evaporation of phosphorus from the free melt surface. This effect takes place during melt homogenization phase as well as during solidification process and increases with the strength of the field.

In the second stage of experiments, a detailed parameter study was conducted in a G1 setup, which provides solidification of G1 size mc-Si ingots in conditions similar to those used in PV industry. A systematic study was performed on conventional multicrystalline material and later the resulting findings were replicated for HPM material. During the detailed study for G1 ingots it was discovered that weak TMF (I_{eff} = 40 A) applied during DS process provokes more uniform dopant distribution at the initial stages of crystallization resulting in reduced ingot resistivity. Afterwards it was shown that strong TMF (I_{eff} = 80 A)

applied at the late stages of crystallization has more pronounced effect on phosphorus evaporation that leads to the desired increase of resistivity towards the ingots end.

Enhanced melt mixing induced by TMF insignificantly increases interstitial oxygen concentration due to more intensive dissolution of crucible coating. In addition, it was experimentally confirmed that two-component travelling magnetic field with frequencies $f_1 = 20$ Hz and $f_2 = 200$ Hz applied during solidification of G1 mc-Si ingots flattens solid-liquid interface, which is favorable for the stable growth of elongated crystal grains.

The chamber pressure was shown to have the most significant influence on phosphorus transport among all process parameters considered in the study. The reduction of ambient pressure during the solidification process leads to significantly intensified phosphorus evaporation from the free melt surface thus increases resistivity of the solidified ingot towards its end. At the same time, low chamber pressure provokes infiltration of crucible coating, which increases the probability of sticking between crucible and ingot as well as ingot cracking. In addition, coating infiltration results is significant increase of interstitial oxygen concentration. However, this effect does not lead to crucial deterioration of material quality since the reduction of chamber pressure is performed in the middle of DS process and the increased oxygen level at this stage is still approximately twice lower than that in the bottommost part of the ingot. Advantageously, the reduction of ambient pressure suppresses species transport in the furnace atmosphere, which results in significantly smaller concentration of substitutional carbon in the grown ingots. Another expected effect observed during experiments with low pressure is the decrease in thermal conductivity of the gas ambient that affects the ingots growth rate. A decreased growth rate leads to the enlargement of the red zone of charge carrier lifetime.

During the preliminary tests conducted in 4×G0 setup it was found that phosphorus evaporation strongly depends on the relative position of the crucible and the gas inlet. However, the results of experiments carried out on G1 scale showed that in typical DS process of larger size the purging gas flow is sufficient to remove the evaporated dopant from the melt surface and its variation has no noticeable influence on phosphorus transport, which confirms the previously conducted theoretical calculations.

The findings obtained during the study were used for the adjustment of typical G1 growth recipe. The optimized recipe implied the application of weak two-component TMF with total effective current of $I_{eff} = 40$ A with its subsequent strengthening up to $I_{eff} = 80$ A together with the reduction of chamber pressure from 600 mbar down to 50 mbar at solid fraction of $g_s = 0.33$. Conventional G1 mc-Si ingots grown using this recipe showed more uniform resistivity distribution than those grown using a typical one. Resistivity variation was reduced to 55% and

met the target range of 3.0 – 1.0 Ω·cm set by market specification. Numerical fitting performed for the experimental results were in alignment with theoretical calculations of phosphorus transport parameters.

The developed recipe was successfully replicated for DS seeded growth. It was experimentally confirmed that the application of travelling magnetic fields and the reduction of chamber pressure in the chosen range do not disturb the seeded growth. HPM ingot of G1 size also showed more uniform resistivity distribution along the ingot's length, even though the effect was somehow smaller and concluded in reduction of the variation to 60%.

10.2. Outlook

Following the results presented in this thesis, there are still several topics for future research. One of the most important directions is further adjustment of the developed recipe. Since the ingots grown under low pressure exhibit minor deterioration in quality induced by the reduced growth rate, it is important to adjust the power input recipe to the optimal temperature gradients that will ensure a constant growth rate throughout the entire process. A particular interest must be given to HPM process, since its requirements for optimal process conditions slightly differ from those for conventional mc-Si ingots due to seeding procedure. Another important topic for investigation is strengthening of crucible coating in order to avoid its infiltration under low pressures. Furthermore, it will be interesting to supplement already conducted research with more fundamental numerical simulation that takes into account the dependence of mass transfer coefficient on melt surface temperature and chamber pressure. Such simulation will allow finding the most optimal parameters of TMF and chamber pressure for fine-tuning of the developed growth recipe. Finally, the developed adjustments must be replicated for larger ingots of industrial size.

Appendix

Property	
Melting point	1414°C
Density (solid at 25°C)	2329 kg/m^3
Density (liquid at 1420°C)	2530 kg/m^3
Latent heat of fusion	4.6×10^{-9} J/m^3
Thermal conductivity (solid at 1410°C)	22 W/m·K
Thermal conductivity (liquid at 1420°C)	67 W/m·K
Thermal expansion coefficient (at 25°C)	2.6×10^{-6} K^{-1} [Oka84]
Thermal expansion coefficient (at 400°C)	4.0×10^{-6} K^{-1} [Oka84]
Band gap	1.12 eV
Electrical conductivity (solid at 1410°C)	5.0×10^4 Ω^{-1}m^{-1}
Electrical conductivity (liquid at 1420°C)	1.2×10^6 Ω^{-1}m^{-1}
Relative magnetic permeability	0.99837

Table 10.1.: Physical properties of silicon [Hul99].

Ingot	Position within 4×G0 setup	C_0, concentration of phosphorus in ingot charge, [cm^{-3}]	Travelling magnetic field												Pressure, mbar	Gas flow, l/min
			Start I_{eff}, [A]	1st change I_{eff}, [A]	1st ramp at process time, h	2nd change I_{eff}, [A]	2nd ramp at process time, h	3rd change I_{eff}, [A]	3rd ramp at process time, h	I_1/I_2	f_1 [Hz]	f_2 [Hz]	ϕ_1	ϕ_2		
A1/1	-/1	5.5×10^{15}	40	–	–	–	–	–	–	10	20	200	+90°	–90°	600	6.0
A1/2	-/2	5.5×10^{15}	40	–	–	–	–	–	–	10	20	200	+90°	–90°	600	6.0
A1/3	-/3	5.5×10^{15}	40	–	–	–	–	–	–	10	20	200	+90°	–90°	600	6.0
A1/4	-/4	5.5×10^{15}	40	–	–	–	–	–	–	10	20	200	+90°	–90°	600	6.0
B0/1	-/1	5.5×10^{15}	0	–	–	–	–	–	–	–	–	–	–	–	600	6.0
B0/2	-/2	1.0×10^{16}	0	–	–	–	–	–	–	–	–	–	–	–	600	6.0
B0/3	-/3	2.5×10^{16}	0	–	–	–	–	–	–	–	–	–	–	–	600	6.0
B0/4	-/4	6.0×10^{16}	0	–	–	–	–	–	–	–	–	–	–	–	600	6.0
B1/1	-/1	5.5×10^{15}	40	–	–	–	–	–	–	10	20	200	+90°	–90°	600	6.0
B1/2	-/2	1.0×10^{16}	40	–	–	–	–	–	–	10	20	200	+90°	–90°	600	6.0
B1/3	-/3	2.5×10^{16}	40	–	–	–	–	–	–	10	20	200	+90°	–90°	600	6.0
B1/4	-/4	6.0×10^{16}	40	–	–	–	–	–	–	10	20	200	+90°	–90°	600	6.0

Ingot	Position within 4×G0 setup	C_0, concentration of phosphorus in ingot charge, [cm^{-3}]	Travelling magnetic field												Pressure, mbar	Gas flow, l/min
			Start I_{eff}, [A]	1st change I_{eff}, [A]	1st ramp at process time, h	2nd change I_{eff}, [A]	2nd ramp at process time, h	3rd change I_{eff}, [A]	3rd ramp at process time, h	I_1/I_2	f_1 [Hz]	f_2 [Hz]	ϕ_1	ϕ_2		
B2/1	-/1	5.5×10^{15}	70	–	–	–	–	–	–	10	20	200	+90°	–90°	600	6.0
B2/2	-/2	1.0×10^{16}	70	–	–	–	–	–	–	10	20	200	+90°	–90°	600	6.0
B2/3	-/3	2.5×10^{16}	70	–	–	–	–	–	–	10	20	200	+90°	–90°	600	6.0
B2/4	-/4	6.0×10^{16}	70	–	–	–	–	–	–	10	20	200	+90°	–90°	600	6.0
C1/1	-/1	5.5×10^{15}	0	40	3	–	–	–	–	10	20	200	+90°	–90°	600	6.0
C2/1	-/1	5.5×10^{15}	0	40	3	100	6→12	–	–	10	20	200	+90°	–90°	600	6.0
C3/1	-/1	5.5×10^{15}	0	40	3	80	6	100	6→12	10	20	200	+90°	–90°	600	6.0
C4/1	-/1	5.5×10^{15}	0	100	6→12	–	–	–	–	10	20	200	+90°	–90°	600	6.0
C5/1	-/1	5.5×10^{15}	0	100	6→8	–	–	–	–	10	20	200	+90°	–90°	600	6.0

Table 10.2.: Process conditions for G0 ingots.

Ingot	C_0, concentration of phosphorus in ingot charge, [cm^{-3}]	Travelling magnetic field								Pressure			Gas flow		
		Start I_{eff}, [A]	Change I_{eff}, [A]	Ramp at solid fraction	I_1/I_2	f_1 [Hz]	f_2 [Hz]	ϕ_1	ϕ_2	Start P, [mbar]	Change P, [mbar]	Ramp at solid fraction	Start u_{gas}, [l/min]	Change u_{gas}, [l/min]	Ramp at solid fraction
D0	4.5×10^{15}	0	–	–	–	–	–	–	–	600	–	–	6.0	–	–
D1	4.5×10^{15}	40	–	–	10	20	200	+90°	–90°	600	–	–	6.0	–	–
D2	4.5×10^{15}	40	80	0.33	10	20	200	+90°	–90°	600	–	–	6.0	–	–
D3	4.5×10^{15}	0	–	–	–	–	–	–	–	600	–	–	6.0	8.0	0.58→1.00
D4	4.5×10^{15}	0	–	–	–	–	–	–	–	600	–	–	6.0	9.0	0.50→0.58
D5	4.5×10^{15}	40	80	0.33	10	20	200	+90°	–90°	600	200	0.50→0.58	6.0	–	–
D6	4.5×10^{15}	40	80	0.33	10	20	200	+90°	–90°	600	50	0.33→0.50	6.0	–	–
D7	4.5×10^{15}	40	–	–	10	20	200	+90°	–90°	600	50	0.33→0.50	6.0	–	–

Table 10.3.: Process conditions for conventional G1 ingots.

Ingot	C_0, concentration of phosphorus in ingot charge, [cm^{-3}]	Travelling magnetic field								Pressure			Gas flow		
		Start I_{eff}, [A]	Change I_{eff}, [A]	Ramp at solid fraction	I_1/I_2	f_1 [Hz]	f_2 [Hz]	ϕ_1	ϕ_2	Start P, [mbar]	Change P, [mbar]	Ramp at solid fraction	Start u_{gas}, [l/min]	Change u_{gas}, [l/min]	Ramp at solid fraction
E0	4.5×10^{15}	0	–	–	–	–	–	–	–	600	–	–	6.0	–	–
E1	4.5×10^{15}	40	80	0.33	10	20	200	+90°	–90°	600	50	0.33→0.50	6.0	–	–

Table 10.4.: Process conditions for HPM G1 ingots.

Bibliography

[Ais15] B. Aïssa, M. M. Kivambe, M. I. Hossain, O. E. Daif, A. A. Abdallah, F. Ali and N. Tabet. Emerging frontiers of N-Type silicon material for photovoltaic applications: The impurity-defect interactions. Frontiers in Nanoscience and Nanotechnology 1, 1-12 (2015).

[Alb13] M. Albaric, C. Audoin, S. Rousseau, S. Caron, E. Pihan, D. Pelletier, JP. Garandet, A. Jouini. Convection in the silicon melt: effect of segregation. Proc. of the 28th European Photovoltaic Solar Energy Conference and Exhibition, Paris, France, 1456-1459 (2013).

[All13] T. B. Allen. Silicon article, US patent 1073560A, 1913.

[Amm05] W. von Ammon, Yu. Gelfgat, L. Gorbunov, A. Mühlbauer, A. Muiznieks, Y. Makarov, J. Virbulis, G. Müller. Application of magnetic fields in industrial growth of silicon single crystals. Proc. of the 15th Riga and 6th PAMIR conference on fundamental and applied MHD, 41-54 (2005).

[Ans93] A. Anselmo, V. Prasad, J. Koziol and K. P. Gupta. Numerical and experimental study of a solid pellet feed continuous Czochralski growth process for silicon single crystals. Journal of Crystal Growth 131, 247-264 (1993).

[Ara06] K. Arafune, T. Sasaki, F. Wakabayashi, Y. Terada, Y. Ohshita, M. Yamaguchi. Study on defects and impurities in cast-grown polycrystalline silicon substrates for solar cells. Physica B 376-377, 236-239 (2006).

[Aut78] B. Authier. Poly-crystalline silicon with columnar structure. Advances in Solid State Physics 18, 1-17 (1978).

[Bau07] J. Bauer, O. Breitenstein, and J.-P. Rakotoniaina. Electronic activity of SiC precipitates in multicrystalline solar silicon. Physica Status Solidi (a) 204, 2190-2195 (2007).

[Bel10] M. P. Bellmann, E. A. Meese, L. Arnberg. Impurity segregation in directional solidified multi-crystalline silicon. Journal of Crystal Growth 312, 3091-3095 (2010).

[Bel11] M. P. Bellmann, E. A. Meese, L. Arnberg. Effect of accelerated crucible rotation on the segregation of impurities in vertical Bridgman growth of multi-crystalline silicon. Journal of Crystal Growth 318, 239-143 (2011).

[Bel13a] M. P. Bellmann, H. Dalaker, M. Syvertsen, S. Gouttebroze, M. M'Hamdi. Optimization of silicon crystallization in a Bridgman growth furnace by numerical modelling. Journal of Crystal Growth 362, 38-41 (2013).

[Bel13b] M. P. Bellmann, M. M'Hamdi. Effect of flow pattern on the segregation of impurities in vertical Bridgman growth of multi-crystalline silicon. Journal of Crystal Growth 362, 93-98 (2013).

[Bel14] M. P. Bellmann, D. Lindholm, M. M'Hamdi. A novel method for gas flow and impurity control in directional solidification of multi-crystalline silicon. Journal of Crystal Growth 399, 33-38 (2014).

[Ben17] J. Benick, A. Richter, R. Müller, H. Hauser, F. Feldmann, P. Krenckel, S. Riepe, F. Schindler, M. C. Schubert, M. Hermle, A. W. Bett, and S. W. Glunz. High-Efficiency n-Type HP mc Silicon Solar Cells. IEEE Journal of Photovoltaics 7, 1171-1175 (2017).

[Bly97] J. M. Bly, M. L. Kaforey, D. H. Matthiesen, A. Chait. Interface shape and growth rate analysis of Se/GaAs bulk crystals grown in the NASA crystal growth furnace (CGF). Journal of Crystal Growth 174, 220-225 (1997).

[Bri25] P. W. Bridgman. Certain physical properties of single crystals of tungsten, antimony, bismuth, tellurium, cadmium, zinc, and tin. Proc. of the American Academy of Arts and Science 60, 305-383 (1925).

[Bry10] I. Brynjulfsen, A. Bakken, M. Tangstad, L. Arnberg. Influence of oxidation on the wetting behavior of liquid silicon on Si_3N_4-coated substrates. Journal of Crystal Growth 312, 2404-2410 (2010).

[Buc11] I. Buchovska, T. Vlasenko, S. Beringov. Roadmap to crystalline wafers for improved solar cells application. Presented at 5th Photovoltaic Fab Managers Forum, Berlin, Germany (2011).

[Buc12] I. Buchovska, O. Liaskovskiy, S. Yatsuk, T. Vlasenko, S. Beringov. Proc. of the 6th International Workshop on Crystalline Silicon for Solar Cells, Aix les Bains, France (2012).

[Buc17] I. Buchovska, O. Liaskovskiy, T. Vlasenko, S. Beringov, F. M. Kiessling. Different nucleation approaches for production of high-performance multi-crystalline silicon ingots and solar cells. Solar Energy Material and Solar Cells 159, 128–135 (2017).

[Buc19] I. Buchovska, N. Dropka, S. Kayser, F. M. Kiessling. The influence of travelling magnetic field on phosphorus distribution in n-type multi-crystalline silicon. Journal of Crystal Growth 507, 299-306 (2019).

[Buc20] I. Buchovska, A. Lüdge, W. Lüdge, and F. M. Kiessling. Characterization of Mono-Crystalline and Multi-Crystalline Silicon by the Extended Lateral Photovoltage Scanning and Scanning Photoluminescence. ECS Journal of Solid State Science and Technology 9, 086001 (2020).

[Bue08] F. Buellesfeld, U. Sahr, W. Miller, P. Rudolph, U. Rehse, N. Dropka. Verfahren zum Erstarren einer Nichtmetall-Schmelze, patent DE102008059521B4, 2008.

[Buo06a] T. Buonassisi, A. A. Istratov, M. D. Pickett, J-P. Rakotoniaina, O. Breitenstein, M. A. Marcus, S. M. Heald, E. R. Weber. Transition metals in photovoltaic-grade ingot-cast multicrystalline silicon: Assessing the role of impurities in silicon nitride crucible lining material. Journal of Crystal Growth 287, 402-407 (2006).

[Buo06b] T. Buonassisi, A. A. Istratov, M. D. Pickett, M. A. Marcus, T. F. Ciszek, and E. R. Weber. Metal precipitation at grain boundaries in silicon: Dependence on grain boundary character and dislocation decoration. Applied Physics Letters 89, 042102 (2006).

[Bur53] J. A. Burton, R. C. Prim, and W. P. Slichter. The Distribution of Solute in Crystals Grown from the Melt. Part I. Theoretical. The Journal of Chemical Physics 21, 1987 (1953).

[Bus13] R. J. Bushby, S. M. Kelly, M. O'Neill, editors. *Liquid Crystalline Semiconductors: material, properties and applications*, Springer Series in Material Science, v. 169 (Springer, Dordrecht, the Netherlands, 2013).

[Cab15] M. Cablea. *Numerical and experimental studies of magnetic field effects on solidification of metallurgical silicon for photovoltaic applications*. PhD thesis, Université de Grenoble, 2015.

[Cam17] D. Camel, B. Drevet, V. Brizé, F. Disdier, E. Cierniak, N. Eustathopoulos. The crucible/silicon interface in directional solidification of photovoltaic silicon. Acta Materialia 129, 415-427 (2017).

[Cam86] D. Camel, J. J. Favier. Scaling analysis and segregation of convective solute transport in Bridgman crystal growth from the doped melt. Journal of Crystal Growth 47, 1001-1014 (1986).

[Cap10] P. Capper, P. Rudolph, editors. *Crystal Growth Technology: Semiconductors and Dielectrics* (Wiley-VCH, Weinheim, Germany, 2010).

[Cau67] D. M. Caughey, R. E. Thomas. Carrier mobilities in silicon empirically related to doping and field. Proc. of 3rd IEEE Conference 55, 2192-2193 (1967).

[Cen15] Y. A. Cengel, A. J. Ghajar. *Heat and Mass Transfer: Fundamentals & Applications, 5th edition* (McGraw-Hill Education, New York, US-NY, 2015).

[Che05] J. Chen, T. Sekiguchi, R. Xie, P. Ahmet, T. Chikyo, D. Yang, S. Ito, F. Yin. Electron-beam-induced current study of small-angle grain boundaries in multicrystalline silicon. Scripta Materialia 52, 1211-1215 (2005).

[Che08] X. J. Chen, S. Nakano, L. J. Liu, K. Kakimoto. Study on thermal stress in a silicon ingot during a unidirectional solidification process. Journal of Crystal Growth 310, 4330-4335 (2008).

[Che10] X. Chen, S. Nakano, K. Kakimoto. Three-dimensional global analysis of thermal stress and dislocations in a silicon ingot during a unidirectional solidification process with a square crucible. Journal of Crystal Growth 312, 3261-3266 (2010).

[Che12] J. Chen, A. J. Deshpande, G. Shi, L. Wen, M. Seacrist, J. Kearns. Key issues in crystalline silicon manufacturing technology for photovoltaics. In: China PV Technology International Conference CPTIC, Shanghai, France (2012).

[Che66] H. A. Chedzey, D. T. J. Hurle. Avoidance of growth-striae in semiconductor and metal crystals grown by zone-melting techniques. Nature 210, 933-934 (1966).

[Chu11] S. K. Chunduri. Preparing for bigger loads. Photon International 06, 236-259 (2011).

[Coc11] J. Cochard. *Constitutive modelling of Solar-grade silicon materials*. PhD thesis, Norwegian University of Science and Technology, 2011.

[Col11] G. Coletti, P. C. P. Bronsveld, G. Hahn, W. Warta, D. Macdonald, B. Ceccaroli, K. Wambach, N. L. Quang, and J. M. Fernandez. Impact of Metal Contamination in Silicon Solar Cells. Advanced Functional Materials 21, 879-890 (2011).

[Col12] G. Coletti, D. Macdonald and D. Yang. Role of Impurities in Solar Silicon. In S. Pizzini, editor, *Advanced Silicon Materials for Photovoltaic Applications*, chapter 3, 79-125 (John Wiley & Sons, Chichester, UK, 2012).

[Col13] G. Coletti. Sensitivity of state-of-the-art and high efficiency crystalline silicon solar cells to metal impurities. Progress in Photovoltaics: Research and Applications 21, 1163-1170 (2013).

[Col34] S. S. Cole. The conversion of quartz into cristobalite below 100°C, and some properties of the cristobalite formed. Proc. of Annual Meeting, American Ceramic Society, Cincinnati, Ohio, USA, 149-154 (1934).

[Cue04] A. Cuevas, D. Macdonald. Measuring and interpreting the lifetime of silicon wafers. Solar Energy 76, 255-262 (2004).

[Cun08] D. W. Cunningham, A. Parr, J. Posbic, B. Poulin. Performance comparison between BP Solar Mono^{2TM} and traditional multicrystalline modules. Proc. of the 23rd European Photovoltaic Solar Energy Conference and Exhibition, Valencia, Spain, 2829-2833 (2008).

[Dad12] K. Dadzis. *Modeling of directional solidification of multicrystalline silicon in a traveling magnetic field*. PhD thesis, Technischen Universität Bergakademie Freiberg, 2012.

[Dad13a] K. Dadzis, D. Vizman, J. Friedrich. Unsteady coupled 3D calculations of melt flow, interface shape, and species transport for directional solidification of silicon in a traveling magnetic field. Journal of Crystal Growth 367, 77-87 (2013).

[Dad13b] K. Dadzis, K. Niemietz, O. Pätzold, U. Wunderwald, J. Friedrich. Non-isothermal model experiments and numerical simulations for directional solidification of multicrystalline silicon in a traveling magnetic field. Journal of Crystal Growth 372, 145-156 (2013).

[Dad19] K. Dadzis, I. Buchovska, F. M. Kiessling. 3D numerical simulation of melt flow and dopant transport in directional solidification of silicon. DGKK-Arbeitskreis Massive Halbleiter, Berlin, Germany (2019).

[Deg12] J. Degoulange, C. Martin, L. Arnberg, C. Ndzogha, E. Pihan, S. Dubois. Ready to Use SOLAR® Crucible: Impact on Multicrystalline Ingot Properties and Cell Performance. Proc. of the 6th International Workshop on Crystalline Silicon for Solar Cells, 1261 (2012).

[Dol97] P. Dold, K. W. Benz. Modification of Fluid Flow and Heat Transport in Vertical Bridgman Configurations by Rotating Magnetic Fields. Crystal Research Technology 32, 51–60 (1997).

[Dor81] J. M. Dorkel, Ph. Leturcq. Carrier mobilities in silicon semi-empirically related to temperature, doping and injection level. Solid-State Electronics 24, 821-825 (1981).

[Dre10] B. Drevet, O. Pajani, N. Eustathopoulos. Wetting, infiltration and sticking phenomena in Si_3N_4 releasing coatings in the growth of photovoltaic silicon. Solar Energy Materials and Solar Cells 94, 425-431 (2010).

[Dro10] N. Dropka, W. Miller, R. Menzel, U. Rehse. Numerical study on transport phenomena in a directional solidification process in the presence of travelling magnetic fields. Journal of Crystal Growth 312, 1407-1410 (2010).

[Dro11] N. Dropka, W. Miller, U. Rehse, P. Rudolph, F. Büllesfeld, U. Sahr, O. Klein, D. Reinhardt. Numerical study on improved mixing in silicon melts by double-frequency TMF. Journal of Crystal Growth 318, 275-279 (2011).

[Dro12] N. Dropka, C. Frank-Rotsch, W. Miller, P. Rudolph. Influence of travelling magnetic fields on S–L interface shapes of materials with different electrical conductivities. Journal of Crystal Growth 338, 208-213 (2012).

[Dro13] N. Dropka, C. Frank-Rotsch, P. Rudolph. Comparison of stirring efficiency of various non-steady magnetic fields during unidirectional solidification of large silicon melts. Journal of Crystal Growth 365, 64-72 (2013).

[Du07] G. P. Du, L. Zhoua, P. Rossetto, Y. P. Wan. Hard inclusions and their detrimental effects on the wire sawing process of multicrystalline silicon. Solar Energy Materials and Solar Cells 91, 1743–1748 (2007).

[Dum12] S. Dumitrica, D. Vizman, J.-P. Garandet, A. Popescu. Numerical studies on a type of mechanical stirring in directional solidification method of multicrystalline silicon for photovoltaic applications. Journal of Crystal Growth 360, 76-80 (2012).

[Eks15] K. E. Ekstrøm, G. Stokkan, R. Søndenå, H. Dalaker, T. Lehmann, L. Arnberg, and M. Di Sabatino. Structure and dislocation development in mono-like silicon. Physica Status Solidi (a) 212, 2278-2288 (1979).

[End02] A. L. Endrös. Mono- and tri-crystalline Si for PV application. Solar Energy Materials & Solar Cells 72, 109-124 (2002).

[End79] Y. Endo, Y. Yatsurugi, Y. Terai and T. Nozaki. Equilibrium of Carbon and Oxygen in Silicon with Carbon Monoxide in Ambient Atmosphere. Journal of Electrochemical Society 126, 1422–1425 (1979).

[Eng92] T. A. Engh, C. J. Simensen, O. Wijk. Principles of metal refining. (Oxford University Press, Oxford, UK, 1992).

[EPI20] European Photovoltaic Industry Association. *EPIA report, Global Market Outlook for Solar Power 2020-2024* (2020).

[Erv13] T. Ervik. *Dislocations in directionally solidified crystalline silicon*. PhD thesis, Norwegian University of Science and Technology, 2013.

[Erv14] T. Ervik, G. Stokkan, T. Buonassisi, O. Mjos, O. Lohne. Dislocation formation in seeds for quasi-monocrystalline silicon for solar cells. Acta Materialia 67, 199-206 (2014).

[Fic01] B. Fickett, G. Mihalik. Multiple batch recharging for industrial CZ silicon growth. Journal of Crystal Growth 225, 580-585 (2001).

[Fis76] H. Fischer and W. Pschunder. Low-Cost Solar Cells Based on Large-Area Unconventional Silicon. Proc. of 12th IEEE Photovoltaic Specialists Conference, New York, NY, USA, 86-92 (1976).

[Fis99] B. Fischer, J. Friedrich, C. Kupfer, D. Vizman, G. Müller. Experimental and Numerical Analysis of the Influence of a Rotating Magnetic Field on Convection in Rayleigh-Bénard Configurations, in A. Alemany, P. Marty, J. P. Thibault, editors, *Transfer Phenomena in Magnetohydrodynamic and Electroconducting Flows*, 279-294 (Kluwer Academic Publishers, Dordrecht, the Netherlands, 1999).

[Fle74] M. C. Flemings. *Solidification Processing* (McGraw-Hill, New York, US-NY, 1974).

[For13] M. Forster, B. Dehestru, A. Thomas, E. Fourmond, R. Einhaus, A. Cuevas, M. Lemiti. Compensation engineering for uniform n-type silicon ingots. Solar Energy Materials and Solar Cells 111, 146–152 (2013).

[Fra00] D. Franke. *Numerische Simulation der Versetzungsmultiplikation in multikristallinem Silicium aus der gerichteten Blockkristallisation*. PhD thesis, Technische Hochschule Aachen, 2000.

[Fra07] Ch. Frank-Rotsch, P. Rudolph, O. Klein, B. Nacke, R.-P. Lange. Vorrichtung und Verfahren zur Herstellung von Kristallen aus elektrisch leitenden Schmelzen, patent DE102007028548B4, 2007.

[Fra20] Ch. Frank-Rotsch, N. Dropka, F. M. Kiessling, and P. Rudolph. Semiconductor Crystal Growth under the Influence of Magnetic Fields. Crystal Research and Technology 55, 1900115 (2020).

[Fra50] F. C. Frank and W. T. Read. Multiplication Process for Slow Moving Dislocations. Physical Review 79, 722-723 (1950).

[Frie07] J. Friedrich. Control of melt convection in VGF and CZ crystal growth configurations by using magnetic fields. In S. Dost, Y. Okano, editors, *Crystal Growth under Applied Fields*, 31-59 (Transworld Research Network, Kerala, India, 2007).

[Fuj06a] K. Fujiwara, W. Pan, N. Usami, K. Sawada, M. Tokairin, Y. Nose, A. Nomura, T. Shishido, K. Nakajima. Growth of structure-controlled polycrystalline silicon ingots for solar cells by casting. Acta Materialia 54, 3191-3197 (2006).

[Fuj06b] K. Fujiwara, W. Pan, K. Sawada, M. Tokairin, N. Usami, Y. Nose, A. Nomura, T. Shishido, K. Nakajima. Directional growth method to obtain high quality polycrystalline silicon from its melt. Journal of Crystal Growth 292, 282-285 (2006).

[Fuj70] K. Fujimori and T. Ayusawa. Vorrichtung zum Züchten von Einkristallen aus Schmelzen, patent DE000002107646A, 1970.

[Gao10] B. Gao, X. J. Chen, S. Nakano, K. Kakimoto. Crystal growth of high-purity multicrystalline silicon using a unidirectional solidification furnace for solar cells. Journal of Crystal Growth 312, 1572-1576 (2010).

[Gao11] B. Gao, S. Nakano, K. Kakimoto. Influence of reaction between silica crucible and graphite susceptor on impurities of multicrystalline silicon in a unidirectional solidification furnace. Journal of Crystal Growth 314, 239-245 (2011).

[Gao12] B. Gao, S. Nakano, and K. Kakimoto. Influence of Back-Diffusion of Iron Impurity on Lifetime Distribution near the Seed-Crystal Interface in Seed Cast-Grown Monocrystalline Silicon by Numerical Modeling. Crystal Growth and Design 12, 522-525 (2012).

[Gao13] B. Gao, S. Nakano, and K. Kakimoto. Reduction of Oxygen Impurity in Multicrystalline Silicon Production. International Journal of Photoenergy 2013, 1-6 (2013).

[Gar12] J. P. Garandet, N. Kaupp, D. Pelletier. The effect of lid driven convective transport on lateral solute segregation in the vicinity of a crucible wall. Journal of Crystal Growth 361, 195-200 (2012).

[Gar90] J. P. Garandet, T. Duffar, J. J. Favier. On the scaling analysis of the solute boundary layer in idealized growth configurations. Journal of Crystal Growth 106, 437-444 (1990).

[Gas17] G. M. M. Gaspar, A. Autruffe and J. M. Pó. Silicon Growth Technologies for PV Applications. In V. I. Talanin, editor, *New Research on Silicon. Structure, Properties, Technology*, chapter 9, 1484-411 (InTech, Rijeka, Croatia, 2017).

[Gey05] B. Geyer, G. Schwichtenberg, A. Müller. Increased wafer yield in silicon ingots by the application of high purity silicon nitride-coating and high purity crucibles. Proc. 31st IEEE Photovoltaic Specialists Conference in IEEE Journal of Photovoltaics, 1059-1061 (2005).

[Gla14] A. Glacki. *VGF growth of 4" GaAs single crystals with traveling magnetic fields.* PhD thesis, Humboldt-Universität zu Berlin, 2014.

[Gli11] M. E. Glicksman. *Principles of Solidification: An Introduction to Modern Casting and Crystal Growth Concepts* (Springer, New York, US-NY, 2011).

[Glu01] S. W. Glunz, S. Rein, J. Y. Lee, and W. Warta. Minority carrier lifetime degradation in boron-doped Czochralski silicon. Journal of Applied Physics 90, 2397-2404 (2001).

[Gra04] I. Grants, G. Gerbeth. Stability of melt flow due to a traveling magnetic field in a closed ampoule. Journal of Crystal Growth 269, 630-638 (2004).

[Gra08] I. Grants, G. Gerbeth. Use of a traveling magnetic field in VGF growth: Flow reversal and resulting dopant distribution. Journal of Crystal Growth 310, 3699-3705 (2008).

[Gra09] I. Grants, A. Klyukin, G. Gerbeth. Instability of the melt flow in VGF growth with a traveling magnetic field. Journal of Crystal Growth 311, 4255-4264 (2009).

[Gul22] G. H. Gulliver. *Metallic Alloys: Their Structure and Constitution, 5th edition* (Charles Griffin & Co, London, UK, 1922).

[Hag90] D. J. Hagemaier. *Fundamentals of Eddy Current Testing* (Amer Society of Nondestructive, Columbus, US-OH, 1990).

[Har82] R. Harris and W. G. Davenport. Vacuum Distillation of Liquid Metals. Part I. Theory and Experimental Study. Metallurgical Transactions B. 13B, 581-588 (1982).

[Hsi14] C. C. Hsieh, A. Lan, C. Hsu, C. W. Lan. Improvement of multi-crystalline silicon ingot growth by using diffusion barriers. Journal of Crystal Growth 311, 4255-4264 (2009).

[Hu15] D. Hu, S. Yuan, L. He, H. Chen, Y. Wan, X. Yu, D. Yang. Higher quality mono-like cast silicon with induced grain boundaries. Solar Energy Materials and Solar Cells 140, 121-125 (2015).

[Hug11] C. Huguet, V. Brizé, S. Bailly, H. Lignier, E. Flahaut, D. Drevet, D. Camel, N. Eustathopoulos. Releasing coatings for PV-Si processing by liquid routs: Comparison between the conventional and a high-purity coating. Proc. 26th European Photovoltaic Solar Energy Conference, Hamburg, Germany, 914-919 (2011).

[Hug14] C. Huguet, C. Dechamp, R. Voytovych, B. Drevet, D. Camel, N. Eustathopoulos. Initial stages of silicon–crucible interactions in crystallisation of solar grade silicon: Kinetics of coating infiltration. Acta Materialia 76, 151-167 (2011).

[Hul99] R. Hull, editor. *Properties of Crystalline Silicon* (INSPEC, the Institution of Electrical Engineers, London, UK, 1999).

[Inc90] F. P. Incropera, D. P DeWitt. *Introduction to heat transfer, 2nd edition* (Willey, New York, US-NY, 1990).

[ITR20] International Technology Roadmap for Photovoltaics (ITRPV) 2019 Results, Eleventh Edition (2020). Stage: 28.04.2020. https://itrpv.vdma.org/viewer/-/v2article/render/48393879

[Jay14] F. Jay, D. Muñoz, T. Desrues, E. Pihan, V. Amaral de Oliveira, N. Enjalbert, A. Jouini. Advanced process for n-type mono-like silicon a-Si:H/c-Si heterojunction solar cells with 21.5% efficiency. Solar Energy Materials and Solar Cells 130, 690-695 (2014).

[Jia14] D. Jiang, S. Ren, S. Shi, W. Dong, J. Qiu, Y. Tan, and J. Li. Phosphorus Removal from Silicon by Vacuum Refining and Directional Solidification. Journal of Electronic Materials 43, 314-319 (2014).

[Joh12] M. D. Johnston, L. T. Khajavi, M. Li, S. Sokhanvaran, and M. Barati. High-Temperature Refining of Metallurgical-Grade silicon: A Review. Journal of the Minerals, Metals & Materials Society 64, 935-945 (2012).

[Jou13] A. Jouini, F. Jay, V. Amaral, E. Pihan, Y. Veschetti. Proc. of the 7th International Workshop on Crystalline Silicon for Solar Cells, Fukuoka, Japan (2013).

[Kak15] K. Kakimoto and B. Gao. Fluid dynamics: Modeling and analysys. In T. Nashinaga, editor, *Handbook of Crystal Growth 1b, 2nd edition*, chapter 21, 845-870 (Elsevier, Amsterdam, the Netherlands, 2015).

[Kar18] S. M. Karabanov, D. V. Suvorov, D. Yu. Tarabrin, E. V. Slivkin, A. E. Serebryakov, V. V. Klimakov, A. S. Karabanov, and O. A. Belyakov. Mathematical modeling of vacuum refining of silicon melt under the conditions of electromagnetic stirring. AIP Conference Proceedings 1999, 020012 (2018).

[Key04] B. M. Keyes, L. M. Gedvilas, R. Bhattacharya, Y. Xu, X. Li, and Q. Wang. The FTIR Laboratory in Support of the PV Program Proc. of DOE Solar Energy Technologies Program Review Meeting, Denver, Colorado, USA (2004).

[Kie11a] F. M. Kiessling. New developments of solar silicon growth. Proc. of Freiberger Siliziumtage, Freiberg, Germany (2011).

[Kie11b] F. M. Kiessling, N. Dropka, Ch. Frank-Rotsch, U. Juda, A. Lüdge, M. Müller, M. Naumann, P. Rudolph. Directional solidification of solar-grade silicon in travelling magnetic fields. Proc. of German Polish Conference on Crystal Growth, Frankfurt (Oder)/Slubice, Germany/ Poland (2011).

[Kie12a] F. M. Kiessling, F. Büllesfeld, N. Dropka, Ch. Frank-Rotsch, M. Müller, P. Rudolph. Characterization of mc-Si directionally solidified in travelling magnetic fields. Journal of Crystal Growth 360, 81-86 (2012).

[Kie12b] F. M. Kiessling, Ch. Frank-Rotsch, N. Dropka, P. Rudolph. Verfahren zur gerichteten Kristallisation von Ingots, patent DE102011076860A1, 2012.

[Kie18] F. M. Kiessling, T. K. Ervik, A.-K. Søiland, and B. R. Henriksen. Coating Roughness Effects on the Defect Structure of mc-Si and its Comparison to High-Performance mc-Si. Crystal Research and Technology 53, 1700272 (2013).

[Kim82] K. M. Kim. Suppression of Thermal Convection by Transverse Magnetic Field. Journal of The Electrochemical Society 129, 427-429 (1982).

[Kla92] D. B. M. Klaassen. A unified mobility model for device simulation – I. Model equations and concentration dependence. Solid-State Electronics 35, 953-959 (1992).

[Kod63] H. Kodera. Diffusion Coefficient of Impurities in Silicon Melt. Japanese Journal of Applied Physics 2, 212-218 (1963).

[Kre17] P. Krenckel, S. Riepe, F. Schindler, T. Strauch. Feeding of liquid silicon for high performance multicrystalline silicon with increased ingot height and homogenized resistivity. Journal of Crystal Growth 463, 145-150 (2017).

[Kud13] Ch. Kudla A. T. Blumenau, F. Büllesfeld, N. Dropka, Ch. Frank-Rotsch, F. Kiessling, O. Klein, P. Lange, W. Miller, U. Rehse, U. Sahr, M. Schellhorn, G. Weidemann, M. Ziem, G. Bethin, R. Fornari, M. Müller, J. Sprekels, V. Trautmann, P. Rudolph. Crystallization of 640 kg mc-silicon ingots under traveling magnetic field by using a heater magnet module. Journal of Crystal Growth 365, 54-58 (2013).

[Kva09] R. Kvande, L. Arnberg, C. Martin. Influence of crucible and coating quality on the properties of multicrystalline silicon for solar cells. Journal of Crystal Growth 311, 765-768 (2009).

[Kwa12] W. Kwapil, A. Zuschlag, I. Reis, I. Schwirtlich, S. Meyer, R. Zierer, R. Krain, F. M. Kießling, M. Schumann, C. Schmid, S. Riepe. Influence of crucible and coating on the contamination of directionally solidified silicon: First results of the German research network "SolarWins". Proc. 27th European Photovoltaic Solar Energy Conference and Exhibition, Frankfurt, Germany, 627-635 (2012).

[Lan07a] P. Lange, D. Jockel, M. Ziem, P. Rudolph, F. Kiessling, Ch. Frank-Rotsch, M. Czupalla, B. Nacke, H. Kasjanow. Vorrichtung zur Herstellung von Kristallen aus elektrisch leitenden Schmelzen, patent DE102007028547B4, 2007.

[Lan07b] R. Lantzsch, V. Galindo, I. Grants, C. Zhang, O. Patzold, G. Gerbeth, M. Stelter. Experimental and numerical results on the fluid flow driven by a traveling magnetic field. Journal of Crystal Growth 305, 249-256 (2007).

[Lan12a] C. W. Lan, W. C. Lan, T. F. Lee, A. Yu, Y. M. Yang, W. C. Hsu, B. Hsu, A. Yang. Grain control in directional solidification of photovoltaic silicon. Journal of Crystal Growth 360, 68-75 (2012).

[Lan12b] C. W. Lan, W. C. Lan, A. Yu, Y. M. Yang, W. C. Hsu, B. Hsu and A. Yang. Proc. of the 6th International Workshop on Crystalline Silicon for Solar Cells, Aix les Bains, France (2012).

[Lan12c] C. W. Lan, M. Yang, A. Yu, B. Hsu, A. Yang. Proc. of the 27th European Photovoltaic Solar Energy Conference and Exhibition, Frankfurt, Germany, 1456-1459 (2012).

[Lan12d] P. Lange, D. Jockel, M. Ziem, P. Rudolph, F. Kiessling, Ch. Frank-Rotsch, M. Czupalla, B. Nacke, H. Kasjanow. Device for producing crystals from electroconducting melts, patent EP2162570B1, 2012.

[Lan13] C. W. Lan, Y. M. Yang, A. Yu, B. Hsu, W. C. Hsu, A. Yang. Proc. of the 7th International Workshop on Crystalline Silicon for Solar Cells, Fukuoka, Japan (2013).

[Lan15] C. W. Lan, C. Hsu, K. Nakajima. Multicrystalline silicon crystal growth for photovoltaic applications. In T. Nashinaga, editor, *Handbook of Crystal Growth 2a, 2nd edition*, chapter 10, 373-411 (Elsevier, Amsterdam, the Netherlands, 2015).

[Lan16] C. W. Lan, C. F. Yang, A. Lan, M. Yang, A. Yu, H. P. Hsu, B. Hsu and C. Hsu. Engineering silicon crystal for photovoltaics. CrystEngComm 18, 1474-1485 (2016).

[Lan95] C. W. Lan, C. C. Ting. Numerical investigation on the batch characteristics of liquid encapsulated vertical Bridgman crystal growth. Journal of Crystal Growth 149, 175-186 (1995).

[Leh16] T. Lehmann, I. Kupka, M. Trempa, M. Beier, C. Reimann, D. Oriwol, F. Kropfgans, L. Sylla, J. Friedrich. Influence of extraordinary long ingot heights on the wafer quality of high performance multi-crystalline silicon for PV application. Proc. of the 18th International Conference on Crystal Growth and Epitaxy, Nagoya, Japan (2016).

[Li11] T. F. Li, K. M. Yeh, W. C. Hsu, C. W. Lan, High-quality multi-crystalline silicon (mc-Si) grown by directional solidification using notched crucibles. Journal of Crystal Growth 318, 219-223 (2011).

[Li13] J. Li, R. R. Prakash, K. Jiptner, J. Chen, Y. Miyamura, H. Harada, K. Kakimoto, A. Ogura, T. Sekiguchi. Butterfly-shaped distribution of SiNx precipitates in multi-crystalline Si for solar cells. Journal of Crystal Growth 377, 37-42 (2013).

[Li18] P. Li, Z. Wang, Sh. Shi, Sh. Ren, D. Jiang, J. Li, H. M. Noor ul Huda Khan Asghar, and Y. Tan. Distribution of Phosphorus in n-Type Multicrystalline Silicon Produced by Directional Solidification. IEEE Journal of Photovoltaics 8, 1486-1493 (2018).

[Liu06] L. Liu, S. Nakano, K. Kakimoto. Dynamic simulation of temperature and iron distributions in a casting process for crystalline silicon solar cells with a global model. Journal of Crystal Growth 292, 515-518 (2006).

[Liu17] L. Liu, W. Ma, X. Qi, Z. Li, Y. Zhang. Global simulation of coupled oxygen and carbon transport in an industrial directional solidification furnace for crystalline silicon ingots: Effect of crucible cover coating. International Journal of Heat and Mass Transfer 108, 2355-2364 (2017).

[Lop12] S. I. Lopatin, V. L. Stolyarova, V. G. Sevast'yanov, P. Ya. Nosatenko, V. V. Gorskii, D. V. Sevast'yanov, N. T. Kuznetsov. Determination of the Saturation Vapor Pressure of Silicon by Knudsen Cell Mass Spectrometry. Russian Journal of Inorganic Chemistry 57, 219-225 (2012).

[Lue97] A. Lüdge and H. Riemann. Doping Inhomogeneities in Silicon Crystals Detected by the Lateral Photovoltage Scanning (LPS) Method. Institute of Physics Conference Series 160, 145-148 (1997).

[Lyu04] T. P. Lyubimova, A. Croell, P. Dold, O. Khlybov, I. S. Fayzrakhmanova. Time-dependent magnetic field influence on GaAs crystal growth by vertical Bridgman method. Journal of Crystal Growth 266, 404-410 (2004).

[Mac04] D. Macdonald, and L. J. Geerligs. Recombination activity of interstitial iron and other transition metal point defects in p- and n-type crystalline silicon. Applied Physics Letters 85, 4061-4063 (2004).

[Mac60] E. S. Machlin. Kinetics of Vacuum Induction Refining Theory. Transactions TMS-AIME 218, 314-326 (1960).

[Mar03] T. Markvart and L. Castañer, editors. *Practical Handbook of Photovoltaics. Fundamentals and Applications, 1st edition* (Elsevier Advanced Technology, Oxford, UK, 2003).

[Mar08] C. Martin, C. Ndzogha, G. Rancoule, J. Grygowski. Development of various crucible coating concepts for crystallization of multi crystalline silicon, ingots. Proc. 23th European Photovoltaic Solar Energy Conference and Exhibition, Valencia Spain, 1084-1089 (2008).

[Mic13] B. Michl, J. Benick, A. Richter, M. Bivour, J. Yong, R. Steeman, M. C. Schubert, S. W. Glunz. Excellent Average Diffusion Lengths of 600 µm of N-Type Multicrystalline Silicon Wafers after the Full Solar Cell Process including Boron Diffusion. Energy Procedia 33, 41-49 (2013).

[Mih08] V. D. Mihailetchi, G. Coletti, Y. Komatsu, L. J. Geerligs, R. Kvande, L. Arnberg, K. Wambach, C. Knopf, R. Kopecek, A. W. Weeber. Large area and screen printed n-type silicon solar cells with efficiency exceeding 18%. Proc. 23rd European Photovoltaic Solar Energy Conference and Exhibition, Valencia, Spain, 1036-1039 (2008).

[Mik96] T. Miki, K. Morita, and N. Sano. Thermodynamics of Phosphorus in Molten Silicon. Metallurgical and Materials Transactions B 27, 937-941 (1996).

[Mit06] A. Mitric, T. Duffar, C. Diazguerra, V. Corregidor, L. Alves, C. Garnier, G. Vian. Growth of $Ga_{(1-x)}In_xSb$ alloys by Vertical Bridgman technique under alternating magnetic field. Journal of Crystal Growth 287, 224-229 (2006).

[Moe05] H. J. Möller, C. Funke, M. Rinio, S. Scholz. Multicrystalline silicon for solar cells. Thin Solid Films 487, 179-187 (2005).

[Moe10] H. J. Möller, C. Funke, J. Bauer, S. Köstner, H. Straube, O. Breitenstein. Growth of Silicon Carbide Filaments in Multicrystalline Silicon for Solar Cells. Solid State Phenomena 35-40, 156-158 (2010).

[Mue03] A. Mühe, B. Altekrüger, A. Vonhoff. Kristallzüchtungsanlage, patent DE000010349339A1, 2003.

[Muk00] K. Mukai and Zh. Yuan. Measurement of the Density of Molten Silicon by a Modified Sessile Drop Method. Material Transactions, JIM 41, 323-330 (2000).

[Nae09] T. Naerland, L. Arnberg and A. Holt. Origin of the Low Carrier Lifetime Edge Zone in Multicrystalline PV Silicon. Progress in Photovoltaics: Research and Applications 17, 289-296 (2009).

[Nak11] S. Nakano, X. J. Chen, B. Gao, K. Kakimoto. Numerical analysis of cooling rate dependence on dislocation density in multicrystalline silicon for solar cells. Journal of Crystal Growth 318, 280-282 (2011).

[Nak12] K. Nakajima, R. Murai, K. Morishita, K. Kutsukake, N. Usami. Growth of multicrystalline Si ingots using noncontact crucible method for reduction of stress. Journal of Crystal Growth 344, 6-11 (2012).

[Nak13] S. Nakano, B. Gao, K. Kakimoto. Relationship between oxygen impurity distribution in multicrystalline solar cell silicon and the use of top and side heaters during manufacture. Journal of Crystal Growth 375, 62-66 (2013).

[Nar10] M. Narayanan, T. Ciszek. Silicon Solar Cells: Materials, Devices, and Manufacturing. In G. Dhanaraj, K. Byrappa, V. Prasad, M. Dudley, editors, *Springer Handbook of Crystal Growth*, chapter 51, 1701-1718 (Springer-Verlag, Berlin, Germany, 2010).

[Nie11] K. Niemietz, V. Galindo, O. Pätzold, G. Gerbeth, M. Stelter. Flow modelling with relevance to vertical gradient freeze crystal growth under the influence of a travelling magnetic field. Journal of Crystal Growth 318, 150–155 (2011).

[Noz70] T. Nozaki, Y. Yatsurugi and N. Akiyama. Concentration and Behavior of Carbon in Semiconductor Silicon. Journal of Electrochemical Society 117, 1566–155 (1970).

[NRE20] NREL Photovoltaic Research, Efficiency Chart and Explanatory Notes. Stage: 01.10.2020. https://www.nrel.gov/pv/cell-efficiency.html

[Oka84] Y. Okada and Y. Tokumaru. Precise determination of lattice parameter and thermal expansion coefficient of silicon between 300 and 1500 K. Journal of Applied Physics 56, 314-320 (1984).

[Ols08] E. Olsen and E. J. Øvrelid. Silicon Nitride Coating and Crucible – Effects of Using Upgraded Materials in the Casting of Multicrystalline Silicon Ingots. Progress in Photovoltaics: Research and Applications 16, 93-100 (2008).

[Osb10] M. Osborne. Cost reduction and productivity improvement strategies for multicrystalline wafering processes. Photovoltaics International 08, 52-59 (2010).

[Ost15] A. G. Ostrogorsky, M. E. Glicksman. Segregation and component distribution. In T. Nashinaga, editor, *Handbook of Crystal Growth 2b, 2nd edition*, chapter 25, 995-1047 (Elsevier, Amsterdam, the Netherlands, 2015).

[Ost92] A. Ostrogorsky, G. Müller. A model of effective segregation coefficient, accounting for convection in the solute layer at the growth interface. Journal of Crystal Growth 121, 587-598 (1992).

[Ozb86] E. Ozberk and R. I. L. Guthrie. A Kinetic Model for the Vacuum Refining of Inductively Stirred Copper Melts. Metallurgical Transactions B. 17B, 87-103 (1986).

[Pau58] L. J. van der Pauw. A Method of Measuring Specific Resistivity and Hall Effect of Discs of Arbitrary Shapes. Philips Research Reports 13, 1-9 (1958).

[Phi20] S. Philipps and W. Warmuth. Photovoltaic Report. Stage 16.09.2020. https://www.ise.fraunhofer.de/en/publications/studies/photovoltaics-report.html.

[Pic20] K. Pickerel. Canadian Solar now also holds world-record efficiency for n-type P5 solar cell. Stage: 06.03.2020. https://www.solarpowerworldonline.com/2020/03/canadian-solar-now-also-holds-world-record-efficiency-for-n-type-p5-solar-cell.

[Pie96] R. F. Pierret. *Semiconductor Device Fundamentals* (Addison-Wesley Inc., Reading, US-MA, 1996).

[Por17] M. Porrini, R. Scala, V.V. Voronkov, Behavior of volatile dopants (P, Sb) in Czochralski silicon growth, Journal of Crystal Growth 460, 13-15 (2017).

[Pow12] D. M. Powell, M. T. Winkler, H. J. Choi, C. B. Simmons, D. B. Needleman and T. Buonassisi. Crystalline silicon photovoltaics: a cost analysis framework for determining technology pathways to reach baseload electricity cost. Energy & Environmental Science 5, 5874-5883 (2012).

[Pri07] J. Priede, G. Gerbeth. Matched asymptotic solution for the solute boundary layer in a converging axisymmetric stagnation point flow. International Journal of Heat and Mass Transfer 50, 216-225 (2007).

[PVE20] PVEducation. General properties of silicon. Stage 28.07.2020. https://www.pveducation.org/pvcdrom/materials/general-properties-of-silicon.

[Qua17] C. D. Quarles Jr., J. Castro and R. K. Marcus. Glow Discharge Mass Spectrometry. In J. C. Lindon, G. E. Tranter, D. W. Koppenaal, editors, *Encyclopaedia of Spectroscopy and Spectrometry, 3rd edition*, 30-36 (Elsevier, Oxford, UK, 2017).

[Rab10] J. Rabier, L. Pizzagalli, J. L. Demenet. Dislocations in Silicon at High Stress. Dislocations in Solids 16, 47-108 (2010).

[Rak05] J. P. Rakotoniaina, O. Breitenstein, M. Werner, M. Hejjo Al-Rifai, T. Buonassisi, M. D. Pickett, M. Ghosh, A. Müller, N. Le Quang. Distribution and formation of silicon carbide and silicon nitride precipitates in block-cast multicrystalline silicon. Proc. 20th European Photovoltaic Solar Energy Conference and Exhibition, Barcelona, Spain, 773-776 (2005).

[Ram27] H. C. Ramsperger and E. H. Melvin. The Preparation of Large Single Crystals. Journal of the Optical Society of America 15, 359-363 (1927).

[Reh13] A. ur Rehman and S. H. Lee. Advancements in n-Type Base Crystalline Silicon Solar Cells and Their Emergence in the Photovoltaic Industry. The Scientific World Journal 2013, 1-13 (2013).

[Rei10] C. Reimann, M. Trempa, T. Jung, J. Friedrich, G. Müller. Modeling of incorporation of O, N, C and formation of related precipitates during directional solidification of silicon under consideration of variable processing parameters. Journal of Crystal Growth 312, 878-885 (2010).

[Ren15] Sh. Ren, P. Li, D. Jiang, Sh. Shi, J. Li, Sh. Wen, Y. Tan. Removal of Cu, Mn and Na in multicrystalline silicon by directional solidification under low vacuum condition. Vacuum 115, 108-112 (2015).

[Ric17a] S. Richter, J. Bauer, and O. Breitenstein. Growth of carbon and nitrogen containing precipitates in crystalline solar silicon and their influence on solar cells. Physica Status Solidi (RRL) 2, 1-17 (2017).

[Ric17b] A. Richter, J. Benick, F. Feldmann, A. Fell, M. Hermle, S. W. Glunz. n-Type Si solar cells with passivating electron contact: Identifying sources for efficiency limitations by wafer thickness and resistivity variation. Solar Energy Materials and Solar Cells 173, 96-105 (2017).

[Roh17] A. Rohatgi, B. Rounsaville, Y. W. Ok, A. M. Tam, F. Zimbardi, A. D. Upadhyaya, Y. Tao, K. Madani, A. Richter, J. Benick, and M. Hermle. Fabrication and Modeling of High-Efficiency Front Junction N-Type Silicon Solar Cells With Tunnel Oxide Passivating Back Contact. IEEE Journal of Photovoltaics 7, 1236-1243 (2017).

[Rud08] P. Rudolph. Travelling magnetic fields applied to bulk crystal growth from the melt: The step from basic research to industrial scale. Journal of Crystal Growth 310, 1298-1306 (2008).

[Rud09] P. Rudolph and K. Kakimoto. Crystal Growth from the Melt under External Force Fields. Materials Research Society Bulletin 34, 251-258 (2009).

[Ryn11] B. Ryningen, G. Stokkan, M. Kivambe, T. Ervik, O. Lohne. Growth of dislocation clusters during directional solidification of multicrystalline silicon ingots. Acta Materialia 59, 7703-7710 (2011).

[Sab14] M. Di Sabatino. Detection limits for glow discharge mass spectrometry (GDMS) analyses of impurities in solar cell silicon. Measurement 50, 135-140 (2014).

[Saf12] J. Safarian and M. Tangstad. Vacuum Refining of Molten Silicon. Metallurgical and Materials Transactions B 43, 1427-1445 (2012).

[San12] F. Santara, Y. Delannoy, A. Autruffe. Electromagnetic stirring and retention to improve segregation in silicon for photovoltaics. Journal of Crystal Growth 340, 41-46 (2012).

[Sat03] Y. Sato, Y. Kameda, T. Nagasawa, T. Sakamoto, Sh. Moriguchi, T. Yamamura, Y. Waseda. Viscosity of molten silicon and the factors affecting measurement. Journal of Crystal Growth 249, 404-415 (2003).

[Sch00] H. J. Scheel. Historical aspects of crystal growth technology. Journal of Crystal Growth 211, 1-12 (2000).

[Sch03] J. Schmidt. Light-Induced Degradation in Crystalline Silicon Solar Cells. Solid State Phenomena 95-96, 187-196 (2004).

[Sch04] P. Schwesig, M. Hainke, J. Friedrich, G. Müller. Comparative numerical study of the effects of rotating and travelling magnetic fields on the interface shape and thermal stress in the VGF growth of InP crystals. Journal of Crystal Growth 266, 224-228 (2004).

[Sch06] D. K. Schroder. *Semiconductor Material and Device Characterization, 3rd edition* (John Wiley & Sons, Hoboken, US-NJ, 2006).

[Sch10] N. Schüler, T. Hahn, K. Dornich, J. R. Niklas, B. Gründig-Wendrock. Theoretical and experimental comparison of contactless lifetime measurement methods for thick silicon samples. Solar Energy Materials and Solar Cells 94, 1076-1080 (2010).

[Sch12] E. Schmid, S. Würzner, C. Funke, V. Galindo, O. Pätzold, M. Stelter. The effect of the growth rate on the microstructure of multi-crystalline silicon. Journal of Crystal Growth 359, 77-82 (2012).

[Sch14] F. Schindler, B. Michl, J. Schön, W. Kwapil, W. Warta, M. C. Schubert. Solar Cell Efficiency Losses Due to Impurities From the Crucible in Multicrystalline Silicon. IEEE Journal of Photovoltaics 4, 122-129 (2014).

[Sch42] E. Scheil. Bemerkungen zur Schichtkristallbildung. Zeitschrift für Metallkunde 34, 70-72 (1942).

[Shi17] S. Shi, P. Li, J. Meng, D. Jiang, Y. Tan and H. M. N. U. H. K. Asghar. Kinetics of volatile impurities removal from silicon by electron beam melting for photovoltaic applications. Physical Chemistry Chemical Physics 41, 28424-28433 (2017).

[Sol15] Ch. S. Solanki. *Solar Photovoltaics: Fundamentals, Technologies and Application, 3rd edition* (PHI Learning Pvt. Ltd., Dehli, India 2015).

[Ste04] C. Stelian, Y. Delannoy, Y. Fautrelle, Th. Duffar. Solute segregation in directional solidification of GaInSb concentrated alloys under alternating magnetic fields Journal of Crystal Growth 266, 207-215 (2004).

[Sto06] N. G. Stoddard. BP Corporation North America Inc, WO patent 084936, 2007.

[Sto08] N. Stoddard, B. Wu, I. Witting, M. Wagener, Y. Park, G. Rozgonyi, R. Clark. Casting Single Crystal Silicon: Novel Defect Profiles from BP Solar's Mono^{2} ™ wafers. Solid State Phenomena 131-133, 1-8 (2008).

[Sto10] G. Stokkan. Relationship between dislocation density and nucleation of multicrystalline silicon. Acta Materialia 58, 3223–3229 (2010).

[Sto25] F. Stöber. Künstliche Darstellung großer, fehlerfreier Kristalle. Zeitschrift für Kristallographie 61, 299-314 (1925).

[Sto36] D. C. Stockbarger. The Production of Large Single Crystals of Lithium Fluoride. Review of Scientific Instruments 7, 133-136 (1936).

[Tak10] I. Takahashi, N. Usami, K. Kutsukake, G. Stokkan, K. Morishita, K. Nakajima. Generation mechanism of dislocations during directional solidification of multicrystalline silicon using artificially designed seed. Journal of Crystal Growth 312, 897-901 (2010).

[Tam14] G. Tammann. *Lehrbuch der Metallographie: Chemie und Physik der Metalle und ihrer Legierungen* (Leopold Voss, Leipzig, Germany, 1914).

[Ten10] Y-Y. Teng, J-C. Chen, C-W. Lu, C-Y. Chen. The carbon distribution in multicrystalline silicon ingots grown using the directional solidification process. Journal of Crystal Growth 312, 1282-1290 (2010).

[Ten11] Y-Y. Teng, J-C. Chen, C-W. Lu, H-I. Chen, C. Hsu, C-Y. Chen. Effects of the furnace pressure on oxygen and silicon oxide distributions during the growth of multicrystalline silicon ingots by the directional solidification process. Journal of Crystal Growth 318, 224-229 (2011).

[Ten14] Y-Y. Teng, J-C. Chen, B-S. Huang, C-H. Chang. Numerical simulation of impurity transport under the effect of a gas flow guidance device during the growth of multicrystalline silicon ingots by the directional solidification process. Journal of Crystal Growth 385, 1-8 (2014).

[The52] T. B. Allen. Method of processing semiconductive materials, US patent 3060123, 1952.

[Thu80a] W. R. Thurber, R. L. Mattis, Y. M. Liu, and J. J. Filliben. Resistivity-Dopant Density Relationship for Phosphorus-Doped Silicon. Journal of the Electrochemical Society 127, 1807-1812 (1980).

[Thu80b] W. R. Thurber, R. L. Mattis, Y. M. Liu, and J. J. Filliben. Resistivity-Dopant Density Relationship for Boron-Doped Silicon. Journal of the Electrochemical Society 127, 2291-2294 (1980).

[Thu81] W. R. Thurber, R. L. Mattis, Y. M. Liu, and J. J. Filliben. The Relationship Between Resistivity and Dopant Density for Phosphorus- and Boron-Doped silicon. National Bureau of Standards Special Publication 400-64 (1981).

[Til53] W. A. Tiller, K. A. Jackson, J. W. Rutter, B. Chalmers. The redistribution of solute atoms during the solidification of metals. Acta Metallurgica 1, 428–437 (1953).

[Top14] Topsil. PV-FZ™ Silicon wafers for high efficiency solar cells. Stage: 01.01.2014.
http://www.topsil.com/media/56383/pv_fz_application_note_january_2014.pdf.

[Tre10] M. Trempa, C. Reimann, J. Friedrich, G. Müller. The influence of growth rate on the formation and avoidance of C and N related precipitates during directional solidification of multicrystalline silicon. Journal of Crystal Growth 312, 1517-1524 (2010).

[Tre12] M. Trempa, C. Reimann, J. Friedrich, G. Müller, D. Oriwol. Mono-crystalline growth in directional solidification of silicon with different orientation and splitting of seed crystals. Journal of Crystal Growth 351, 131-140 (2012).

[Tre15] M. Trempa, C. Reimann, J. Friedrich, G. Müller, L. Sylla, A. Krause, T. Richter. Investigation of iron contamination of seed crystals and its impact on lifetime distribution in Quasimono silicon ingots. Journal of Crystal Growth 429, 56-62 (2015).

[Tre20] M. Trempa, F. Sturm, C. Kranert, S. Schwanke, C. Reimann, J. Friedrich, C. Schenk. Impact of different SiO_2 diffusion barrier layers on lifetime distribution in multi-crystalline silicon ingots. Journal of Crystal Growth 532, 125378 (2020).

[Tru12] T. Trupke, B. Mitchell, J. W. Weber, W. McMillan, R.A. Bardos and R. Kroeze. Photoluminescence Imaging for Photovoltaic Applications. Energy Procedia 15, 135-146 (2012).

[Tru60] F. A. Trumbore. Solid solubilities of impurity elements in germanium and silicon. Bell System Technical Journal 39, 205-233 (1960).

[Tsa91] C. T. Tsai. On the finite element modeling of dislocation dynamics during semiconductor crystal growth. Journal of Crystal Growth 113, 499-507 (1991).

[Ubb12] B. Ubbenjans. *Einsatz von Vibratoren und Ultraschall in der Züchtung von Halbleiterkristallen für die Photovoltaikindustrie*. PhD thesis, Wilhelm Leibniz Universität Hannover, 2012.

[Usa10] N Usami, R. Yokoyama, I. Takahashi, K. Kutsukake, K. Fujiwara, and K. Nakajima. Relationship between grain boundary structures in Si multicrystals and generation of dislocations during crystal growth. Journal of Applied Physics 107, 013511 (2010).

[Uwa15] M. Uwaha. Growth Kinetics: Basics of crystal growth mechanisms. In T. Nashinaga, editor, *Handbook of Crystal Growth 1a, 2nd edition*, chapter 8, 359-400 (Elsevier, Amsterdam, the Netherlands, 2015).

[Val01] F. Vallino, J-Ph. Château, A. Jacques, A. George. Dislocation multiplication during the very first stages of plastic deformation in silicon observed by X-ray topography. Materials Science and Engineering: A 319-321, 152-155 (2001).

[Vie74] D. Viechnicki, F. Schmid. Crystal growth using the heat exchanger method (HEM). Journal of Crystal Growth 26, 162-164 (1974).

[Viz07] D. Vizman, J. Friedrich, G. Mueller. 3D time-dependent numerical study of the influence of the melt flow on the interface shape in a silicon ingot casting process. Journal of Crystal Growth 303, 231-235 (2007).

[Viz13] D. Vizman, K. Dadiz, J. Friedrich. Numerical parameter studies of 3D melt flow and interface shape for directional solidification of silicon in a traveling magnetic field. Journal of Crystal Growth 381, 169-178 (2013).

[Viz15] D. Vizman. Flow control by magnetic fields during crystal growth from melt. In T. Nashinaga, editor, *Handbook of Crystal Growth 2b, 2nd edition*, chapter 23, 909-950 (Elsevier, Amsterdam, the Netherlands, 2015).

[Wan06] X. Wang, N. Ma, D. F. Bliss, G. W. Iseler. Solute segregation during modified vertical gradient freezing of alloyed compound semiconductor crystals with magnetic and electric fields. International Journal of Heat and Mass Transfer 49, 3429-3438 (2006).

[Wan09] H. Y. Wang, N. Usami, K. Fujiwara, K. Kutsukake, K. Nakajima. Microstructures of Si multicrystals and their impact on minority carrier diffusion length. Acta Materialia 57, 3268-3278 (2009).

[Wan11] Q. Wang, W. Dong, Y. Tan, D, Jiang, C. Zhang, and X. Peng. Impurities evaporation from metallurgical silicon electron beam melting process. Rare Metals 30, 274–277 (2011).

[Wei07] K. Wei, W. Ma, Y. Dai, B. Yang, D. Liu and J. Wang. Vacuum distillation refining of metallurgical grade silicon (I) – Thermodynamics on removal of phosphorus from metallurgical grade silicon. Transactions of Nonferrous Metal Society of China 17, 1022-1025 (2007).

[Wil78] L. O. Wilson. On interpreting a quantity in the Burton, Prim and Slichter equation as a diffusion boundary layer thickness. Journal of Crystal Growth 44, 247-250 (1978).

[Wru79] D. Wruck and P. Gaworzewski. Electrical and Infrared Spectroscopic Investigations of Oxygen-Related Donors in Silicon. Physica Status Solidi (a) 56, 557-564 (1979).

[Wu16] Y. C. Wu, A. Lan, C. F. Yang, C. W. Hsu, C. M. Lu, A. Yang, and C. W. Lan. Effect of Seed Arrangements on the Quality of n-Type Monolike Silicon Grown by Directional Solidification. Crystal Growth and Design 16, 6641-6647 (2016).

[Wue10] S. Würzner, R. Helbig, C. Funke, and H. J. Möller. The relationship between microstructure and dislocation density distribution in multicrystalline silicon. Journal of Applied Physics 108, 083516 (2010).

[Xi07] J. Xi, J. Tang, H. Deng, D. Yang, D. Que. A model for distribution of oxygen in multicrystalline silicon ingot grown by directional solidification. Solar Energy Materials and Solar Cells 91, 1688-1691 (2007).

[Xu15] H. Xu. Characterization of n-type mono-crystalline silicon ingots produced by continuous Czochralski (Cz) Technology. Energy Procedia 77, 658-664 (2015).

[Xu16] H. Xu, X. Tian. Minority carrier lifetime of n-type mono-crystalline silicon produced by continuous Czochralski technology and its effect on hetero-junction solar cells. Energy Procedia 92, 708-714 (2016).

[Yan13] Y. M. Yang, A. Yu, B. Hsu, W. C. Hsu, A. Yang, C. W. Lan. Development of high-performance multicrystalline silicon for photovoltaic industry. Progress in Photovoltaics 23, 340-351 (2013).

[Yan80] K. Yang, G. H. Schwuttke, T. F. Ciszek. Structural and electrical characterization of crystallographic defects in silicon ribbons. Journal of Crystal Growth 50, 301-310 (1980).

[Yat73] Y. Yatsurugi, N. Akiyama, Y. Endo, and T. Nozaki. Concentration, Solubility, and Equilibrium Distribution Coefficient of Nitrogen and Oxygen in Semiconductor Silicon. Journal of Electrochemical Society 120, 975–979 (1973).

[Yeh10] K. M. Yeh, C. K. Hseih, W. C. Hsu and C. W. Lan. High-quality multi crystalline silicon growth for solar cells by grain-controlled directional solidification. Progress in Photovoltaics: Research and Application 18, 265-271 (2010).

[Yu18] Q. Yu, L. Liu, Z Li, Y. Shao. Parameter study of traveling magnetic field for control of melt convection in directional solidification of crystalline silicon ingots. International Journal of Heat and Fluid Flow 71, 55-67 (2018).

[Zha10] E. V. Zharikov. Advanced Technologies of Crystal Growth from Melt Using Vibrational Influence. In P. Capper, P. Rudolf, editors, *Crystal Growth Technology: Semiconductors and Dielectrics*, chapter 3, 41-64 (Wiley-VCH, Weinheim, Germany, 2010).

[Zha17] C. Zhang, K. Wei, D. Zheng, W. Ma, Y. Dai. Phosphorus removal from upgraded metallurgical-grade silicon by vacuum directional solidification. Vacuum 146, 159-163 (2017).

[Zhe10] S-Sh. Zheng, W-H. Chen, J. Cai, J-T Li, Ch. Chen, and X-T. Luo. Mass Transfer of Phosphorus in Silicon Melts Under Vacuum Induction Refining. Metallurgical and Materials Transactions B 41, 1268-1273 (2010).

[Zhe11] S-Sh. Zheng, T. A. Engh, M. Tangstad, and X-T. Luo. Numerical Simulation of Phosphorus Removal from Silicon by Induction Vacuum Refining. Metallurgical and Materials Transactions A 42, 2214-2225 (2011).

[Zhe16] D. Zheng, K. Wei, W. Ma, Z. Sheng, Y. Dai. A mathematical model for distribution of calcium in silicon by vacuum directional solidification. Journal of Mining and Metallurgy B 2, 157-162 (2016).

[Zho14] G. Zhong, Q. Yu, X. Huang, L. Liu. Influencing factors on the formation of the low minority carrier lifetime zone at the bottom of seed-assisted cast ingots. Journal of Crystal Growth 402, 65-70 (2014).

[Zie07] M. Ziem, P. Rudolph and P. Lange. Vorrichtung zur Herstellung von Kristallen aus elektrisch leitfähigen Schmelzen, patent DE102007020239B4, 2007.

List of Figures

1.1 Evolution of the worldwide installed PV capacity. 2
1.2 Solar cells efficiency chart. 3
2.1 Sketch of the temperature profiles (left) for different time steps ($t_1 < t_2 < t_3 < t_4$) with positions (x_1, x_2, x_3, and x_4) of the solid-liquid interface (at temperature of melting point $T < T_m$) during directional solidification of silicon melt placed in a crucible (right) 8
2.2 Sketch of a lab-scale directional solidification furnace 10
2.3 Typical minority carrier lifetime map of a central vertical cut from Gen5 mc-Si ingot. 14
2.4 Sketch of natural melt flow during directional solidification of silicon. 16
2.5 Incorporation of oxygen and carbon into a mc-Si ingot during DS. . 19
2.6 Solute distribution in the melt and in the crystal: 1) perfect mixing; 2) pure diffusion; 3) convecto-diffusive case. 25
2.7 Crucible loading for nucleation of different types of crystalline material: a) conventional mc-Si; b) high-performance mc-Si; c) quasi-mono c-Si. 31
2.8 Grain structure of different types of crystalline material in vertical and horizontal cross-section: a) conventional mc-Si; b) high-performance mc-Si; c) quasi-mono c-Si. 32
3.1 Sketch of silicon crystal lattice with incorporated dopants: a) n-type, b) p-type. 34
3.2 The relationship between resistivity and dopant concentration for crystalline silicon doped with boron and phosphorus [PVE20] 36
3.3 Resistivity distribution along the ingot's length for multicrystalline silicon doped with boron and phosphorus. 37
3.4 The vapour pressure of pure substances with temperature [Saf12] . . 38
3.5 Schematic diagram of phosphorus transport during directional solidification process. 41
3.6 Schematic model of phosphorus removal from the silicon melt during directional solidification process. 42
4.1 The arrangement of the electro-magnetic coils for the generation of different types of nonsteady magnetic fields. 51

4.2 The shape of solid-liquid interface and flow patterns for directional solidification under the influence of TMF with various orientations. 53
4.3 Sketch of a TMF coil system with three axially arranged coils. 55
5.1 a) Conventional DS furnace with additional external coils for TMF generation; b) DS furnace equipped with KRIST*MAG*® heater-magnet module. 60
5.2 a) Image of KRIST*MAG*® G1 size DS furnace; b) Layout of KRIST*MAG*® DS setup. 62
5.3 Sketch of four-point probe setup. 65
5.4 The principal of MDP measurement: a) energy scheme of the measurement; b) measurement signal. 66
6.1 a) Simplified layout of G1 KRIST*MAG*® hot zone with G1 setup and cardinal marking. b) Scheme of G1 setup inside G1 hot zone, side view. c) Picture of top H1-H3 and side heaters of G1 KRIST*MAG*® hot zone, bottom view. 72
6.2 a) G1 set up, side view; b) SiC cover, top view. 73
6.3 a) Simplified layout of G1 KRIST*MAG*® hot zone with 4×G0 setup and cardinal marking. b) Scheme of the 4×G0 setup inside the G1 hot zone, side view. c) Picture of the 4×G0 setup, side view. 74
6.4 a) G1 crucible with 14 kg of polysilicon feedstock; b) 4×G0 setup with four G0 crucibles each filled with 0.9 kg of polysilicon feedstock. 77
6.5 Seeding layer of fine polysilicon chunks placed on the bottom of G1 crucible for the growth of an HPM ingot. 78
6.6 Typical temperature profile of G1 DS process measured by the upper thermocouple TC-1 and the lower thermocouple TC-B, supplemented by pyrometer Pyro observing the melt surface. a) Heating; b) melting; c) homogenization; d) solidification; e) cooling. 79
6.7 Lorentz force density distribution for the double-frequency TMF consisting of two components with opposite directions. 83
6.8 a) Cutting scheme and b) measurement pattern for G1 ingots. . . . 85
6.9 a) Cutting scheme and b) measurement pattern for G0 ingots . . . 86
7.1 a) G0 ingot of 80×80×60 mm^3 size. (b) 4 G0 ingots grown in 4×G0 setup. 87
7.2 a) Four ingot positions within the 4×G0 setup. b) Temperature distribution within 4×G0 setup in the end of the melting phase obtained by 3D numerical simulation. 89
7.3 LPS images for G0 ingots grown in different positions within 4×G0 setup in A1 set: a) A1/1, b) A1/2, c) A1/3, d) A1/4. 90

7.4 Resistivity distribution along the central vertical axis of G0 ingots grown in different positions within 4×G0 setup in A1 set. 91
7.5 Typical temperature profile of DS process conducted in 4×G0 setup measured by the lower thermocouple TC-B. 92
7.6 TMF intensity profiles used in the experimental sets of Group B. . . 93
7.7 Typical results of 3D numerical simulation for TMF driven flow in silicon melt at the end for the melting phase for G0 ingot B1/2: (a) temperature, (b) Lorentz force density streamlines induced by TMF, (c) velocity streamlines for summarized melt flow driven by natural convection and TMF. 94
7.8 Lorentz force density streamlines induced by TMF obtained by 3D numerical simulation for (a) B1 and (b) B2 sets. 94
7.9 Resistivity distribution along the central vertical axis of the ingots grown in different positions within 4×G0 setup in three experimental sets (B0, B1, B2): a) -/1, b) -/2, c) -/3, d) -/4. 95
7.10 Distribution of phosphorus concentration along the ingot's length for ingots grown in different positions within 4×G0 setup in three experimental sets (B0, B1, B2): a) -/1, b) -/2, c) -/3, d) -/4. 97
7.11 Distribution of O_i and C_s along the central vertical line for ingots grown in positions -/1 and -/2 in experimental sets of Group B: a) O_i for -/1, b) O_i for -/2, c) C_s for -/1, d) C_s for -/2. 99
7.12 TMF intensity profiles used in the experimental sets of Group C. . . 100
7.13 Resistivity distribution along the central vertical axis of G0 ingots grown in position -/1 within 4×G0 setup in the experimental sets of Group C. 101
8.1 Mass transfer coefficients of phosphorus for surface boundary layer K_s, evaporation K_e and gas phase K_g as functions of temperature calculated for typical G1 process parameters (u_{surf} = 5×10^{-4} m/s, u_{gas} = 6 l/min, P = 600 mbar). 106
8.2 Mass transfer coefficient of phosphorus evaporation as a function of pressure for different process temperatures. 107
8.3 Mass transfer coefficient of phosphorus in the gas phase and in the surface boundary layer as a function of temperature for different surface velocities of the melt. 107
8.4 Reference G1 ingot D0 of 22×22×12 cm^3 size and 14 kg weight and cardinal marking. 109
8.5 Temperature and TMF intensity profiles used for crystallisation of D0 and D1 ingots. 110
8.6 LPS images of D0 (a) and D1 (b) ingots. 111
8.7 Resistivity maps of D0 (a) and D1 (b) ingots. 112

8.8 Resistivity distribution along the vertical lines for D0 and D1 ingots: a) central line, b) west edge line, c) east edge line. 112
8.9 Melt flow after 200 min of solidification for D0 and D1 ingots obtained by numerical simulation. 113
8.10 Simulated resistivity distribution for G1 ingots grown under process conditions of D0 and D1. 114
8.11 Distribution of O_i and C_s along the vertical lines for D0 and D1 ingots: a) O_i along the central line, b) O_i along the edge line, c) C_s along the central line, d) C_s along the edge line. 114
8.12 MDP images of D0 (a) and D1 (b) ingots. 115
8.13 Temperature and TMF intensity profiles used for crystallisation of D1 and D2 ingots. 117
8.14 LPS images of D1 (a) and D2 (b) ingots. 117
8.15 Resistivity distribution along the vertical lines for D1 and D2 ingots: a) central line, b) west edge line, c) east edge line. 118
8.16 Melt flow after 6 hours of solidification for D1 (a) and D2 (b) ingots obtained by numerical simulation. 119
8.17 Distribution of phosphorus concentration (a) and resistivity (b) along the ingot's length for D1 and D2 ingots. 120
8.18 Distribution of O_i and C_s along the vertical lines for D1 and D2 ingots: a) O_i along the central line, b) O_i along the edge line, c) C_s along the central line, d) C_s along the edge line. 121
8.19 MDP images of D1 (a) and D2 (b) ingots. 121
8.20 Temperature and gas flow profiles used for crystallisation of D0, D3 and D4 ingots. 123
8.21 Resistivity distribution along the central vertical line for D0, D3 and D4 ingots. 123
8.22 Temperature, chamber pressure and TMF intensity profiles used for crystallisation of D2, D5 and D6 ingots. 125
8.23 LPS images of D2 (a), D5 (b) and D6 (c) ingots. 126
8.24 Crucible and ingot surface after crystallization of D2 (a), D5 (b) and D6 (c) ingots. 127
8.25 G1 ingots grown under a) 600 mbar (D2) and b) 50 mbar (D6). . . . 127
8.26 Resistivity distribution along the vertical lines for D2, D5 and D6 ingots: a) central line, b) west edge line, c) east edge line. 128
8.27 Distribution of phosphorus concentration (a) and resistivity (b) along the ingot's length for D2, D5 and D6 ingots. 129
8.28 Total mass transfer coefficient of phosphorus obtained from experimental data as a function of pressure. 129
8.29 Temperature, chamber pressure and TMF intensity profiles used for crystallisation of D6 and D7 ingots. 131

8.30 Distribution of phosphorus concentration (a) and resistivity (b) along the ingot's length for D6 and D7 ingots. 131
8.31 Distribution of O_i and C_s along the vertical lines for D2, D5 and D7 ingots: a) O_i along the central line, b) O_i along the edge line, c) C_s along the central line, d) C_s along the edge line. 133
8.32 MDP images of D2 (a) and D6 (b) ingots. 134
8.33 Temperature, chamber pressure and TMF intensity profiles used for crystallisation of D0 and D6 ingots. 135
8.34 Resistivity distribution along the central axis for phosphorus-doped G1 mc-Si ingots grown using the reference and optimized recipes. . . 136
8.35 Distribution of phosphorus along the central vertical line of D0 and D6 ingots. 136
8.36 Distribution of metals along the central vertical line of D0 and D6 ingots measured by GDMS. 137
8.37 MDP images for phosphorus-doped G1 mc-Si ingots grown using the reference (a) and optimized (b) recipes. 138
8.38 PL images for phosphorus-doped G1 mc-Si ingots grown using the reference (a) and optimized (b) recipes. 139
8.39 Distribution of O_i (a) and C_s (b) along the central vertical line for phosphorus-doped G1 mc-Si ingots grown using the reference and optimized recipes. 139
8.40 NIR images for phosphorus-doped G1 mc-Si ingots grown using the reference (a) and optimized (b) recipes. 140
9.1 Temperature, chamber pressure and TMF intensity profiles used for crystallisation of E0 and E1 ingots. 144
9.2 Crucible and ingot surface after crystallization of E0 (a) and E1 (b) ingots. 145
9.3 Central vertical cuts of D6 (a) and E1 (b) ingots showing the difference in grain pattern. 146
9.4 Resistivity distribution along the vertical lines for E0 and E1 ingots: a) central line, b) west edge line, c) east edge line. 146
9.5 Distribution of phosphorus concentration (a) and resistivity (b) along the ingot's length for E0 and E1 ingots. 147
9.6 Resistivity distribution along the central axis for phosphorus-doped G1 HPM-Si ingots grown using the reference and optimized recipes. 148

List of Tables

2.1 Concentration of impurities in crucible, Si_3N_4 and SoG silicon [Col12, Deg12, Lan15, Ols08]. . . . 13
2.2 Segregation coefficient, diffusivity and solubility for typical impurities in silicon. . . . 27
7.1 Phosphorus concentrations used in crucible charges for ingots in Group A. . . . 89
7.2 Phosphorus concentrations used in crucible charges for ingots in Group B. . . . 92
7.3 TMF parameters used during growth process in the experimental sets of Group B. . . . 93
7.4 Concentration of phosphorus left in the melt after homogenization calculated from experimental data for ingots in Group B. . . . 98
8.1 Process conditions for ingots D0 and D1. . . . 110
8.2 Process conditions for ingots D1 and D2. . . . 116
8.3 Process conditions for ingots D0, D3 and D4. . . . 122
8.4 Process conditions for ingots D2, D5 and D6. . . . 124
8.5 Process conditions for ingots D6 and D7. . . . 130
8.6 Process conditions for ingots D0 and D6. . . . 135
9.1 Process conditions for ingots E0 and E1. . . . 144
10.1 Physical and chemical properties of silicon [Hul99]. . . . 153
10.2 Process conditions for G0 ingots. . . . 155
10.3 Process conditions for conventional G1 ingots. . . . 156
10.4 Process conditions for HPM G1 ingots. . . . 157

Publications and Contributions

Peer reviewed publications

- I. Buchovska, A. Lüdge, W. Lüdge and F. M. Kiessling. Characterization of mono-crystalline and multi-crystalline silicon by the extended Lateral Photovoltage Scanning and Scanning Photoluminescence. ECS Journal of Solid State Science and Technology 9, 086001 (2020).
- I. Buchovska, N. Dropka, S. Kayser and F. M. Kiessling. The influence of travelling magnetic field on phosphorus distribution in n-type multi-crystalline silicon. Journal of Crystal Growth 507, 299-306 (2019).
- I. Buchovska, O. Liaskovskiy, T. Vlasenko, S. Beringov and F. M. Kiessling. Different nucleation approaches for production of high-performance multi-crystalline silicon ingots and solar cells. Solar Energy Material and Solar Cells 159, 128–135 (2017).
- H. J. Rost, I. Buchovska, K. Dadzis, U. Juda, M. Renner and R. Menzel. Thermally stimulated dislocation generation in silicon crystals grown by the Float- Zone method. Journal of Crystal Growth 552, 125842 (2020).
- N. Dropka, I. Buchovska, F. M. Kiessling and U. Degenhardt. Influence of impurities from SiC and TiC crucible cover on directionally solidified silicon. Journal of Crystal Growth 542, 125692 (2020).
- N. Dropka, I. Buchovska, I. Herrmann-Geppert, D. Klimm, F. M. Kiessling and U. Degenhardt. Towards graphite-free hot zone for directional solidification of silicon. Journal of Crystal Growth 492, 299-306 (2018).

Conference proceedings

- I. Buchovska, N. Dropka, M. Pietsch and F. M. Kiessling. Parameter study on n-type multicrystalline ingots with tailored resistivity profiles. Proc. of Deutsche Kristallzüchtungstagung, Munic, Germany (2020).
- F. M. Kiessling, I. Buchovska, G. McGee, M. Kinley-Hanlon, I. Martin, P. Murray, R. Schnabel, J. Steinlechner and S. Tait. Investigation of directionally

solidified quasi-mono silicon for future gravitation-wave detector test-mass mirrors. Proc. of Deutsche Kristallzüchtungstagung, Munic, Germany (2020).

- I. Buchovska, N. Dropka and F. M. Kiessling. Adjustment of resistivity for phosphorus doped n-type multicrystalline silicon. Proc. of the 3rd German Polish Conference on Crystal Growth, Poznan, Poland (2019).
- I. Buchovska, N. Dropka, S. Kayser and F. M. Kiessling. The influence of travelling magnetic field on phosphorus distribution in n-type multi-crystalline silicon. Proc. of the 10th International Workshop on Crystalline Silicon for Solar Cells, Sendai, Japan (2018).
- I. Buchovska, N. Dropka, S. Kayser and F. M. Kiessling. Segregation effects during growth of n-type multicrystalline silicon using travelling magnetic fields. Proc. of the 18th International Conference on Crystal Growth and Epitaxy, Nagoya, Japan (2016).
- I. Buchovska, O. Liaskovskiy, T. Vlasenko, S. Beringov and F. M. Kiessling. High-performance silicon multicrystalline ingots and wafers produced from different feedstock and with different seeding approach. Proc. of the 8th International Workshop on Crystalline Silicon for Solar Cells, Bamberg, Germany (2015).

Conference contributions

- I. Buchovska, N. Dropka, K. Dadzis and F. M. Kiessling. Homogenization of resistivity for n-type multicrystaline silicon. DGKK Workshop on Production and Characterization of Bulk Semiconductor Crystals in Berlin/Germany, October 2019.
- I. Buchovska, N. Dropka, S. Kayser and F. M. Kiessling. The effect of asymmetric growth conditions on phosphorus distribution in n-type multicrystalline silicon. DGKK Workshop on Production and Characterization of Bulk Semiconductor Crystals in Freiberg/Germany, October 2017.
- I. Buchovska, N. Dropka, S. Kayser and F. M. Kiessling. The influence of travelling magnetic field on phosphorus distribution in n-type multi-crystalline silicon. DGKK Workshop on Bulk Semiconductor Crystals in Erlangen/Germany, October 2016.
- I. Buchovska, O. Liaskovskiy, T. Vlasenko, S. Beringov and F. M. Kiessling. Different assisted nucleation methods for production of high performance multi-crystalline silicon ingots. DGKK Workshop on Bulk Semiconductor Crystals in Berlin/Germany, October 2015.

Awards

- DGKK Award for the best poster presented at the Conference on Crystal Growth (DKT 2020) and 50th Anniversary of the German Association of Crystal Growth.
  I. Buchovska, N. Dropka, K. Dadzis and F. M. Kiessling. Homogenization of resistivity for n-type multicrystaline silicon.

Acknowledgments

First and foremost, I want to express my deepest gratitude to Dr. Frank Kiessling for his incredible support during my research, his excellent leadership, wiliness to share his expertise in directional solidification, his priceless help in conducting experiments and fruitful discussions with regards to this thesis. This project would not have been possible without him.

I am thankful to Dr. Natasha Dropka and Dr. Kaspars Dadzis for their excellent support of my experimental work with numerical simulations and their helpful suggestions. I am indebted to Prof. Thomas Schröder for giving me the opportunity to perform this study and for his ongoing interest in my research.

I would like to thank Prof. Marisa Sabatino for exceptionally helpful comments, inspiring discussions, invaluable support in material characterization and her willingness to review this thesis.

I am extremely grateful to Dr. Anke Lüdge and Stefan Kayser for their guidance and assistance in performing LPS, PL and FPP measurements. Furthermore, I would like to thank Dr. Torunn Ervik for sharing her experience in PV crystal growth, valuable discussions and encouragement during my first days at IKZ.

I also want to express my appreciation to the following colleagues at IKZ: Thomas Wurche, Manuela Immimg-Friedland, Viola Lange and Katrin Berger for crystal processing and sample preparation and Mike Pietsch for FTIR measurements. I want to thank Gagan Paudel from the Department of Material Science and Engineering at NTNU for GDMS measurements and his exceptional attention to their quality.

I am thankful to Ralf-Peter Lange, Mario Ziem, Uwe Kupfer, Bernd Spotowitz, Kevin Reinhold, Jörg Fischer, Friedemann Münter, and Jens Klose for their contributions to the growth equipment, technical support and prompt responses to both routine and special requests. Thanks also to my roommates Dr. Robert Menzel and Angelina Nikiforova for exceptionally pleasant working atmosphere.

My special thanks goes to my first mentor Timur Vlasenko. He was the person who made me fall in love with photovoltaics and who supported me during my entire professional journey.

Last but not least, I want to thank my friends and family for their help and unconditioned love. I am very cordially grateful to my boyfriend for encouraging

me to stay on this path and never-ending inspiration. Moreover, especially to my beloved sister for her all-embracing support in all my endeavours, for believing in me and being my best friend and reliance throughout life.

Selbständigkeitserklärung

Ich erkläre, dass ich die Dissertation selbständig und nur unter Verwendung der von mir gemäß § 7 Abs. 3 der Promotionsordnung der Mathematisch-Naturwissenschaftlichen Fakultät, veröffentlicht im Amtlichen Mitteilungsblatt der Humboldt-Universität zu Berlin Nr. 42/2018 am 11.07.2018 angegebenen Hilfsmittel angefertigt habe.

Des Weiteren bestätige ich hiermit, dass ich mich an keiner anderen Universität um einen Doktorgrad beworben habe und keinen entsprechenden Doktorgrad besitze. Ich habe Kenntnis über die dem Verfahren zugrunde liegende Promotionsordnung der Mathematisch-Naturwissenschaftlichen Fakultät der Humboldt-Universität zu Berlin.

Berlin, den 05 Mai 2021

Iryna Buchovska